Investigation of Structural and Magnetic Properties in MnBi/FeCo and MnGa/FeCo Exchange Spring Bilayers

Untersuchung der strukturellen und magnetischen Eigenschaften von MnBi/FeCo und MnGa/FeCo Austauschfeder Doppelschichten
Zur Erlangung des akademischen Grades Doktor-Ingenieur (Dr.-Ing.)
genehmigte Dissertation von M.Sc. Sareh EsmaeilySabetRoudsari (Sareh Sabet) aus Tehran, IRAN
Tag der Einreichung: 07.08.2019, Tag der Prüfung: 23.09.2019
Darmstadt 2019 — D 17

1. Gutachten: Prof. Dr. Lambert Alff
2. Gutachten: Prof. Dr. Oliver Gutfleisch

TECHNISCHE
UNIVERSITÄT
DARMSTADT

Fachbereich Material- und Geowissenschaften
Fachgebiet Dünne Schichten

Investigation of Structural and Magnetic Properties in MnBi/FeCo and MnGa/FeCo Exchange Spring Bilayers
Untersuchung der strukturellen und magnetischen Eigenschaften von MnBi/FeCo und MnGa/FeCo Austauschfeder Doppelschichten

Genehmigte Dissertation von M.Sc. Sareh EsmaeilySabetRoudsari (Sareh Sabet) aus Tehran, IRAN

1. Gutachten: Prof. Dr. Lambert Alff
2. Gutachten: Prof. Dr. Oliver Gutfleisch

Tag der Einreichung: 07.08.2019
Tag der Prüfung: 23.09.2019

Darmstadt — D 17

“There is no DARK SIDE of the moon really.
Matter of fact it’s all DARK.
... And each small CANDLE lights a corner of the DARK”.

To ASHKAN,
who has travelled by my side through all the DARKNESS.

To my PARENTS,
who taught me KNOWLEDGE is the one and only true merit.

To my SISTER,
who’s coloured my life.

Erklärung zur Dissertation

Hiermit versichere ich, die vorliegende Dissertation ohne Hilfe Dritter nur mit den angegebenen Quellen und Hilfsmitteln angefertigt zu haben. Alle Stellen, die aus Quellen entnommen wurden, sind als solche kenntlich gemacht. Diese Arbeit hat in gleicher oder ähnlicher Form noch keiner Prüfungsbehörde vorgelegen.

Darmstadt, den October 23, 2019

(S. EsmaeilySabetRoudsari)

Abstract

Due to the economic crisis concerning rare-earth elements, synthesis of rare-earth free permanent magnets has attracted much attention. The Mn-based intermetallic hard magnetic phases such as MnBi and MnGa are promising rare-earth free candidates particularly in the form of exchange spring magnets coupled to a soft magnetic phase. In this thesis, I have investigated the structural and magnetic properties of c-axis textured MnBi and epitaxial (001) MnGa thin films as well as their exchange coupled bilayers with FeCo soft magnetic layer for further enhancement of the magnetic properties.

First, I studied the growth of highly c-axis textured MnBi thin films deposited in magnetron sputtering from alloy targets on quartz glass substrates. Compared to previous thin film studies in which a multilayer approach was used to grow sequential $(\mathrm{Mn/Bi})^n$ layers, in this thesis for the first time I have deposited single layer low-temperature phase (LTP) MnBi thin films with a subsequent annealing step to improve its crystalline texture. Using this approach, the highest degree of crystallinity was achieved at an annealing temperature of 415 °C which significantly improves the saturation magnetization up to 600 emu/cm^3 with a high perpendicular magnetic anisotropy of 1.86 MJ/m^3. The effect of different starting stoichiometries has shown that slightly higher Mn amount ($\mathrm{Mn_{55}Bi_{45}}$ (at.%)) results in the highest saturation magnetization in the MnBi thin films. The LTP-MnBi thin films have shown a high Curie temperature of ∼510 K (237 °C) and a positive temperature coefficient for both magnetic anisotropy and coercivity.

Moreover, I have investigated the exchange coupling effect in MnBi/FeCo exchange spring bilayer system. The effect of soft magnetic layer thickness and two different FeCo stoichiometries (Fe-rich and Co-rich compositions) have been studied in this system. Based on the magnetic measurements, the Co-rich stoichiometry acts in favour of exchange coupling. DFT calculations predicted formation of a polycrystalline FeCo layer with coexisting crystalline (110) and disordered phases. The HR-TEM evaluations confirmed that the FeCo layer grown on MnBi thin film shows crystalline (110) orientation with a disordered region close to the hard/soft magnetic interface. This disordered region resulted in a rough interface which deteriorates the exchange coupling for the FeCo thickness above 1 nm. Micromagnetic simulations showed that thickness of the FeCo layer and the interface roughness both control the effectiveness of exchange coupling in MnBi/FeCo system.

In the second part of this thesis, I have deposited epitaxial (001) MnGa thin films using a single layer growth approach on Cr-buffered MgO(100) substrates. The effect of different substrate temperatures on the resulting structural and magnetic properties has been investigated. A high saturation magnetization of 840 emu/cm^3 and a very high perpendicular magnetic anisotropy of 2.1 MJ/m^3 were achieved for epitaxial $L1_0$-MnGa thin films grown at a substrate temperature of 450 °C which are very close to the theoretically predicted value. The MnGa thin films have shown a Curie temperature of 530 K (257 °C) and a negative temperature coefficient for the magnetic anisotropy and coercivity.

In addition, I have investigated the exchange coupling effect in epitaxial MnGa/FeCo bilayer samples which have shown a stronger coupling effect compared to the MnBi/FeCo case. The effect of epitaxial growth (the hard/soft interface quality) and thickness of the soft magnetic layer have been studied in this system. DFT calculations have shown that a Co-terminated Co-rich FeCo layer is in favour of exchange coupling. In optimized bilayers, the coercivity of MnGa (approximately 6 kOe) is fully conserved while the overall saturation magnetization is increased beyond 1000 emu/cm^3. The TEM evaluations confirmed a (001) epitaxially grown bilayer with a sharp interface resulted from a small lattice misfit between the two layers. This is considered as the reason for a more coherent magnetic exchange coupling with a permissible soft magnetic layer thickness of up to 2 nm in MnGa/FeCo system.

Zusammenfasung

Aufgrund der Kritikalität der Metalle der Seltenen Erden ist die Synthese von seltenerdfreien Permanentmagneten in den Forschungsfokus gerückt. Hartmagnetische intermetallische Phasen auf Mangan-Basis wie MnBi und MnGa sind vielversprechende seltenerdfreie Kandidaten, insbesondere als Bestandteil austauschgekoppelter Systeme in Verbindung mit einer weichmagnetischen Phase. In dieser Arbeit wurden das Wachstum und die magnetischen Eigenschaften von hartmagnetischen texturierten Dünnschichten von MnBi und MnGa sowie deren austauschgekoppelte Doppelschichten mit einer weichmagnetischen FeCo-Phase untersucht, um die magnetischen Eigenschaften weiter zu verbessern.

Zuerst wurde das Wachstum von c-Achse orientierten mittels Magnetronsputterns hergestellter MnBi Dünnschichten untersucht. Diese wurden unter der Verwendung einer neuen Einzelschicht-Wachstumsmethode von einem Legierungs-Sputtertarget auf Quarzglas-Substraten abgeschieden. Bei allen vorhergehenden Studien wurden sequentielle $(\mathrm{Mn/Bi})^n$ Schichten gewachsen. In dieser Arbeit wurde zum ersten Mal das Wachstum von einschichtigen Niedertemperatur-Phasen (LTP) MnBi Dünnschichten mit einem anschließenden Wärmebehandlungsschritt untersucht, durch den eine signifikante Verbesserung der kristallinen Textur erzielen wurde. Dieser neue Ansatz führte zu einer hohen Kristallinität bei einer Glühtemperatur von 415 °C, wodurch die Sättigungsmagnetisierung drastisch auf bis zu 600 $\mathrm{emu/cm^3}$ erhöht wurden konnte. In diesen Schichten wurde eine sehr hohe senkrechte magnetische Anisotropie von 1.86 $\mathrm{MJ/m^3}$ beobachtet. Die Wirkung von verschiedener Ausgangsstöchiometrien des Sputtertargets wurde ebenfalls untersucht. Eine etwas höhere Menge an Mn ($\mathrm{Mn_{55}Bi_{45}}$ (at.%)) führt zu der höchsten Sättigungsmagnetisierung in den betrachteten MnBi Dünnfilmen. Die LTP-MnBi Dünnschichten weisen des Weiteren eine hohe Curie-Temperatur von etwa 510 K und einen positiven Temperaturkoeffizienten sowohl für die magnetische Anisotropie als auch für die Koerzitivkraft auf.

Aufbauend auf den beschriebenen dünnen Schichten von MnBi wurde die Austauschkopplung in MnBi/FeCo Doppelschichtsystemen untersucht. Dabei wurde der Einfluss der weichmagnetischen Schichtdicke und zweier verschiedener FeCo-Stöchiometrien (Fe-reiche und Co-reiche Zusammensetzung) untersucht. Magnetische Messungen zeigten, dass Co-reiche Stöchiometrien sich zugunsten der Austauschkopplung auswirken. Ergänzende DFT-Rechnungen haben die Bildung einer polykristallinen FeCo Schicht mit koexistierenden kristallinen und ungeordneten (110)-Phasen vorhergesagt. HR-TEM Auswertungen zeigten, dass die auf einer MnBi-Dünnschicht aufgewachsenen FeCo Schichten eine kristalline (110) Orientierung mit einem ungeordneten Bereich nahe der hart/weichmagnetischen Grenzfläche zeigen. Dies führte zu einer rauen Grenzfläche, die die Austauschkopplung schon bei einer FeCo Schichtdicke über 1 nm verschlechtert. Mikromagnetische Simulationen zeigen, dass sowohl die Dicke der FeCo-Schicht als auch die Rauheit der Grenzfläche die Wirksamkeit der Austauschkopplung im MnBi/FeCo-System determinieren.

Im zweiten Teil dieser Arbeit wurden epitaktische (001) MnGa Dünnschichten bei verschiedenen Substrattemperaturen auf Cr-gepufferten MgO(100) Substraten abgeschieden. Die $L1_0$-MnGa Dünnschichten, die bei einer Substrattemperatur von 450 °C gewachsen wurden, zeigen den höchsten Wert der Sättigungsmagnetisierung von 840 $\mathrm{emu/cm^3}$ und eine hohe senkrechte magnetische Anisotropie von 2.1 $\mathrm{MJ/m^3}$. Die MnGa Dünnschichten besitzen eine Curie-Temperatur von 530 K und einen negativen Temperaturkoeffizienten für die magnetische Anisotropie und Koerzitivkraft. Im Vergleich zum MnBi/FeCo System zeigt das MnGa/FeCo System eine deutlich verbesserte Austauschkopplung. DFT-Rechnungen zeigen, dass eine Co-terminierte und Co-reiche FeCo-Schicht zu einer Erhöhung der Austauschkopplung führt. TEM-Untersuchungen bestätigen eine (001) epitaktisch gewachsene Doppelschicht mit einer scharfen Grenzfläche. Das epitaktische Wachstum wird durch die geringe Gitterfehlanpassung der beiden Materialien begünstigt. Die atomar scharfe Grenzfläche führt zu einer kohärenten Austauschkopplung bis zu einer maximalen Schichtdicke der weichmagnetischen Schicht von 2 nm.

Contents

1 Introduction 1

2 Theory of Magnetism 5
- 2.1 Origin of magnetic moment . . . 5
- 2.2 Exchange energy . . . 6
  - 2.2.1 Direct exchange . . . 6
  - 2.2.2 Itinerant exchange . . . 9
  - 2.2.3 RKKY exchange . . . 9
  - 2.2.4 Superexchange . . . 10
- 2.3 Origin of hysteresis: intrinsic contributions . . . 10
  - 2.3.1 Magnetocrystalline anisotropy: spin-orbit interaction . . . 12
  - 2.3.2 Shape anisotropy: dipolar interaction . . . 13
  - 2.3.3 Surface anisotropy . . . 14
  - 2.3.4 Induced anisotropy . . . 15
  - 2.3.5 Magnetostrictive anisotropy . . . 15
  - 2.3.6 Total micromagnetic energy . . . 15
- 2.4 Origin of hysteresis: extrinsic contributions . . . 15
- 2.5 Rare-earth free permanent magnets . . . 18
  - 2.5.1 Exchange spring magnets . . . 18
  - 2.5.2 Material system: low temperature phase MnBi . . . 20
  - 2.5.3 Material system: $L1_0$-$\mathrm{Mn}_{1.5}$Ga . . . 22

3 Synthesis and characterization methods 26
- 3.1 Sputtering deposition process . . . 26
  - 3.1.1 DC sputtering . . . 28
  - 3.1.2 Magnetron sputtering . . . 29
  - 3.1.3 RF sputtering . . . 29
  - 3.1.4 Sputtering of alloys . . . 30
- 3.2 Thin film deposition: structural zone model (SZM) . . . 31
- 3.3 Thin film deposition: physical mechanisms of growth . . . 33
- 3.4 Thin film deposition: Thermodynamics of growth . . . 36
- 3.5 Structural characterization . . . 38
  - 3.5.1 X-ray analysis: The $2\theta - \theta$ scan . . . 38
  - 3.5.2 X-ray Analysis: Rocking curve (ω scan) . . . 40
  - 3.5.3 Transmission electron microscopy (TEM) . . . 42
- 3.6 Magnetic characterization . . . 44
  - 3.6.1 Superconducting quantum interference device (SQUID) . . . 44
  - 3.6.2 Torque magnetometry . . . 47
- 3.7 Theoretical investigations of exchange interface . . . 49
  - 3.7.1 Density functional theory calculations . . . 49
  - 3.7.2 Micromagnetic simulation . . . 54

4 Growth of MnBi and MnGa thin films 56
- 4.1 Magnetron sputtering deposition . . . 56
  - 4.1.1 Temperature calibration . . . 58
  - 4.1.2 Stylus surface profiling . . . 59

5 Results and discussion 60
5.1 MnBi polycrystalline c-axis textured thin films . . . 60
5.1.1 Annealing study . . . 60
5.1.2 Effect of measurement temperature . . . 64
5.1.3 Thickness and composition study . . . 67
5.1.4 Magnetic anisotropy . . . 69
5.2 MnBi/FeCo exchange coupled bilayers . . . 72
5.2.1 Transmission electron microscopy (TEM) of MnBi/FeCo exchange interface . . . 75
5.2.2 Theoretical investigations of MnBi/FeCo exchange interface . . . 77
5.3 MnGa epitaxial (001) thin films . . . 82
5.3.1 Growth temperature study . . . 82
5.3.2 Magnetic anisotropy . . . 84
5.4 MnGa/FeCo exchange coupled bilayers . . . 88
5.4.1 Transmission Electron Microscopy (TEM) . . . 91
5.4.2 Theoretical investigations of exchange interface . . . 91

6 Conclusion 96

7 Outlook 98
7.1 Different deposition approach . . . 98
7.2 $L1_0$-MnAl and effect of buffer layers . . . 98
7.3 MnBi epitaxial (001) thin films . . . 98
7.4 MnGa/FeCo/MnGa trilayer exchange spring system . . . 99

8 Scientific Contributions 101
8.1 Publications . . . 101
8.2 Conference contributions . . . 101

References 102

Acknowledgement 115

Curriculum Vitae 116

1.1 Summary of room temperature data on saturation magnetization, M_s, and coercive field, H_c, for LTP MnBi with starting composition of $Mn_{55}Bi_{45}$ (at. %) including values reported for thin films (TF: gray circles), bulk (B: dashed circles), and single crystal (SC: black circle) samples. The numbers in brackets refer to the list of references, figure adapted from Ref. [34]. 2
2.1 Schematic of magnetic moments associated with (a) spin angular moment, and (b) orbital moment of an electron, adapted from Ref. [78]. 5
2.2 Schematic of a spatially symmetric wave function (ψ_s), with electronic charge piled up between atoms, and a spatially antisymmetric wave function (ψ_a) with no charge between atoms in H_2 molecule, adapted from Ref. [78]. 7
2.3 A schematic of Bethe-Slater curve, adapted from Ref. [87]. 8
2.4 Schematic of RKKY oscillations for interaction of a magnetic impurity with a non-magnetic host. 9
2.5 Schematic of a typical superexchange bond, adapted from Ref. [78]. 10
2.6 (a) Schematic directions of easy axis with respect to the external magnetic field, (b) magnetization curves for single crystal of cobalt with hexagonal crystal structure in easy and hard directions, adopted from Ref. [79]. 11
2.7 (a) Schematic of two possible configuration for magnetic dipoles (a) Broadside, and (b) head to tail, adapted from Ref. [78]. 13
2.8 Typical hysteresis loop for ferromagnetic materials. 16
2.9 Schematic of typical hysteresis loops for a hard magnetic phase (e.g. MnBi, blue solid line), a soft magnetic phase (e. g. FeCo, red solid line), and the exchange spring composite magnet (e. g. MnBi/FeCo, green solid line) resulting from hard/soft exchange coupling. The four insets show a one-dimensional configuration of magnetic moments at the hard/soft magnetic interface under varying external magnetic field (H) assuming an out-of-plane easy axis direction. Red open arrows represent the magnetic moments in the soft phase and blue filled arrows represent the magnetic moments in the hard phase. The length of the arrows represents the magnetization and the width of the arrows represents the coercivity. Figure is adapted from Supplemnetal Material provided with Ref. [106]. 19
2.10 Two dimensional model of exchange spring magnet, adapted from Ref. [68]. 19
2.11 Binary phase diagram of Mn-Bi, low temperature phase of MnBi is stable at room temperature and is the ferromagnetic phase, adapted from Ref. [45]. 21
2.12 A schematic of NiAs hexagonal crystal structure for MnBi illustrated with VESTA [115]. 22
2.13 Binary phase diagram of Mn-Ga, tetragonal ordered $L1_0$- $Mn_{1.5}Ga$ which is the ferromagnetic phase and only stable in a narrow range of composition between 49-59 wt.% (56-65 at.%) of Mn, adapted from Ref. [45]. 23
2.14 Schematic unit cell of (a) tetragonally ordered $L1_0$- Mn_xGa ($0.76<x<1.8$) phase with a_0=3.88Å and c_0=3.64Å which shows ferromagnetic properties, and (b) $D0_{22}$- Mn_xGa ($2<x<3$) phase with a_0=3.90Å and c_0=7.10Å which shows anti-ferromagnetic properties, illustrated in VESTA [115]. 24
3.1 Thornton zone model, adapted from Ref. [136]. 32
3.2 Illustrations of the events which happen during a typical vapour-phase thin film growth process. 34
3.3 Illustrations of the three main growth modes at different levels of film coverage (θ). . . . 35
3.4 Free energy as a function of particle radius, adapted from Ref. [152]. 36
3.5 A schematic of elastic X-ray scattering event, adapted from Ref. [158]. 38

3.6 A schematic geometrical derivation of the Bragg law. X-rays strike the successive atomic planes in a crystal which have been separated by the distance of d. In case of constructive interference of all scattered X-rays the extra distance that the X-ray travels from each plane is equal to an integer multiplication of the X-ray wavelength λ, adapted from Ref. [158]. 39
3.7 A schematic representation of $2\theta - \theta$ XRD scan. K_i and K' are incoming and exiting X-ray beams and G is the scattered vector which is parallel to plane normal s_3, adapted from Ref. [158]. 40
3.8 A schematic representation of $2\theta - \omega$ rocking curve scan. K_i and K' are incoming and exiting X-ray beams and G is the scattered vector which is being rocked in vicinity of surface normal vector s_3, adapted from Ref. [158]. 41
3.9 Rocking curve for a thin film with thickness of $t = m.d$, adapted from Ref. [159]. 42
3.10 Schematic of ray diagrams for three main TEM imaging modes: (A) BF image formed from the direct electron beam, (B) displaced-aperture DF image formed with a off-axis scattered beam, and (C) a CDF image for which the incident beam is tilted so that the scattered beam emerges on the optic axis. The area of the DP selected by the objective aperture is shown below each ray diagram, adapted from Ref. [161]. 43
3.11 A schematic of (a) DC Josephson junction, and (b) the SQUID signal in correspondence to the sample movement in a MPMS device from QuantumDesign using the Reciprocating Sample Option (RSO), adapted from Ref. [167]. 47
3.12 A schematic of piesoresistive silicon torque chip used in torque magnetometry setup of PPMS device along with illustration of measurement angles, adapted from Ref. [175]. . . 48
4.1 A schematic of the custom-made magnetron sputtering unit which was used for deposition experiments in current thesis. 57
4.2 Result of temperature calibration: (a) heating curves vs. time for different applied temperatures in the range of 50 °C-600 °C, and (b) the linear relationship between applied temperature, T_set, and substrate temperature, T_sub. 59
5.1 XRD pattern of as-deposited MnBi thin film without annealing. 61
5.2 XRD patterns of MnBi thin films annealed at different temperatures, T_ann, between 365 °C and 430 °C. The spectra are vertically offset for clarity. The peaks originating from residual bismuth in the films are labelled with (*) indexing Bi (003) planes. The inset shows rocking curve collected from MnBi (002) peak for the sample annealed at T_ann =415 °C figuring a wide FWHM, adapted from Ref. [34]. 61
5.3 (a) Out-of-plane and (b) in-plane magnetization data for MnBi thin films annealed at different temperatures (T_ann) between 265 °C and 415 °C and measured at 300 K, adapted from Ref. [34]. 62
5.4 Change in saturation magnetization (M_s), remanent magnetization (M_r), uniaxial anisotropy (K_u), in-plane and out-of-plane coercivity (H_c), and maximum energy product ($(BH)_\mathrm{max}$) for MnBi thin films as a function of annealing temperature, adapted from Ref. [34]. 63
5.5 Change in energy product vs. external magnetic field for MnBi thin films annealed at T_ann=365 °C and T_ann=415 °C. 64
5.6 Out-of-plane magnetization data for the MnBi thin film annealed at T_ann=365 °C measured between 10 K and 350 K. 65
5.7 Temperature dependence of H_c and M_s for the MnBi thin film annealed at 365 °C in out-of-plane and in-plane direction. The inset shows the change of $M_\mathrm{r}/M_\mathrm{s}$ ratio (black solid curve) and calculated MAE (blue dashed curve) with temperature for out-of-plane direction of applied field, adapted from Ref. [34]. 65

5.8 XRD patterns of MnBi thin films deposited with different thickness (10 nm, 20 nm, 35 nm and 50 nm) on glass substrates and post-annealed at T_{ann}= 415 °C. Inset shows changes in FWHM values for MnBi (002) peak as a function of film thickness extracted from rocking curve measurements. 67
5.9 Room-temperature out-of-plane magnetization data collected from MnBi thin films deposited with four different thickness (10 nm, 20 nm, 35 nm and 50 nm) on glass substrates and post-annealed at T_{ann}= 415 °C. 68
5.10 XRD patterns of MnBi thin films deposited from alloy sputtering targets with three different starting Mn:Bi stoichiometries (60:40, 55:45 and 50:50 (at.%)) on glass substrates and post-annealed at T_{ann}= 365 °C. 69
5.11 Room-temperature out-of-plane magnetization data collected from MnBi thin films deposited from alloy sputtering targets with three different starting Mn:Bi stoichiometries (60:40, 55:45 and 50:50 (at.%)) on glass substrates and post-annealed at T_{ann}= 365 °C. . . 69
5.12 Angular dependence of magnetic torque for a MnBi film annealed at 415 °C measured in a torque magnetometer attached to a PPMS device rotating under 9 T magnetic field at 300 K, adapted from Ref. [34]. 70
5.13 Angular dependence of magnetic torque for a MnBi film annealed at 415 °C measured in torque magnetometer under different applied fields 1 T-9 T at 300 K. 71
5.14 Unixaial magnetic anisotropy constant (K_{u}) for a MnBi film annealed at 415 °C, which is proportional to the amplitude of the sine function fitted to the magnetic torque curves, as well as the peak offset from the position of maximum (45°) as a function of applied magnetic field in the range of 1 T-9 T measured at 300 K. 71
5.15 Angular dependence of magnetic torque for a MnBi film annealed at 415 °C measured in torque magnetometer under 9 T magnetic field at different temperatures between 60 K to 300 K. 72
5.16 Dependency of magnetic anisotropy constant on saturation magnetization for a MnBi film annealed at 415 °C measured at different temperatures between 60 K to 300 K. 72
5.17 (a) XRD patterns collected from exchange spring bilayers of $\mathrm{Mn_{55}Bi_{45}/Fe_{35}Co_{65}}$ (at.%) with different thickness of FeCo soft magnetic layer between 1 nm to 3 nm. The LTP-MnBi thin films were annealed at T_{ann}: 365 °C and FeCo layer was deposited at a substrate temperature of T_{sub}: 100 °C. The spectra are vertically offset for clarity. The peaks originating from residual bismuth in the films are labelled with (*) indexing Bi (003) planes. Inset shows a schematic representation of grown bilayers on quartz glass substrate with LTP-MnBi as hard magnetic layer and $\mathrm{Fe_xCo_{100-x}}$ as soft magnetic layer, adapted from Ref. [106]. 73
5.18 Out-of-plane magnetization data for MnBi/FeCo bilayers with different FeCo thickness 0 nm-3 nm measured at 300 K, (a) with a Fe-rich, and (b) with a Co-rich soft magnetic FeCo layer. The dashed line in (b) shows the in-plane magnetization for a single MnBi layer, adapted from Ref. [106]. 74
5.19 (a) Cross-sectional high resolution transmission electron microscopy (HR-TEM) image from MnBi/FeCo bilayer sample (c-axis textured MnBi hard magnetic layer has thickness of ∼ 50 nm and polycrystalline Co-rich FeCo soft magnetic layer has thickness of ∼ 5 nm), (b) STEM image from cross section of the layers along with EDX mapping for each element : Mn, Bi, Fe, Co, Ta, Pt and O across the layers, (c) composition gradient of Mn, Bi, Fe and Co across a 25 nm scan length close to MnBi/FeCo interface, adapted from Ref. [106]. 76
5.20 Schematic of atomic structures after DFT relaxation (a) MnBi (001)/disordered FeCo (110) and (b) MnBi (001)/amorphous FeCo (111) interfaces demonstrated using VESTA [115]. Mn, Bi, Fe and Co are shown with small dark violet, large light violet, gold and blue colours, respectively. The 1×1×1 unit cell of each orientation is indicated with dashed line. Figure is adapted from supplemental material provided with Ref. [106]. 77

5.21 Micromagnetic simulation results of a MnBi/Fe_3Co_5 model system with disordered FeCo (110) (d-(110)) and crystalline FeCo (111) (c-(111)) interfaces. Magnetic reversal curves: (a) without interface roughness using the A^{int} value listed in Tab. 5.1; (b) with interface roughness using the same A^{int} as in (a); (c) with nterface roughness using A^{int} reduced to 10% of that in (a). The external magnetic field $\mu_0 H_{\text{ex}}$ is applied along the z direction. Inset of (a): Model geoemetry with in-plane periodic boundary condition. Inset of (b): Interfacial roughness of MnBi with a maximum dent height of 0.4 nm. a-i and a-ii, b-i and b-ii, and c-i and c-ii present the magnetic configurations (yz surface at $x = 0$) corresponding to the marked circles of reversal curves in (a), (b), and (c), respectively, which belongs to the disordered Fe_3Co_5 (110). Figure is adapted from Ref. [106]. 79

5.22 Hysteresis plots obtained from micromagnetic simulations for MnBi (001) /FeCo (110) double layers (a) without and (b) with interface roughness. (c) Variation of the magnetization with respect to the applied field around zero field for the theoretical and experimental hysteresis plots as a function of FeCo thickness. For the case of interfaces without roughness two regions are evident in which at 1 nm FeCo thickness incoherent coupling between the hard and soft magnetic layers appears. The rough interfaces in both theoretical and experimental cases, behave incoherently for all thicknesses. For comparison, the experimental data for the epitaxial case of MnGa (001)/FeCo (001) bilayer are also presented (see section 5.4.2). Figure is adapted from Ref. [106]. 80

5.23 (a) XRD patterns of MnGa thin films deposited at different substrate temperatures, T_{sub}, between 350 °C and 600 °C (Figure is adapted from Ref. [193]). For clarity, the XRD spectra are shown with a vertical offset. The peaks from Ga or Mn in the MnGa films are labelled with (*) and (+), respectively. (b) Change of c-lattice constant and peak broadening for MnGa (002) peak as a function of substrate temperature. 83

5.24 Out-of-plane magnetization data for MnGa thin films deposited at different substrate temperatures, T_{sub}, between 350 °C and 600 °C. 84

5.25 (a) Out-of-plane magnetization data measured in SQUID magnetometer for $Mn_{1.5}Ga$ thin film grown at T_{sub}= 450 °C at different temperatures between 10 K and 300 K, (b) changes in saturation magnetization (M_s) and coercivity (H_c) upon changing measurement temperature for $Mn_{1.5}Ga$ thin film, the inset to graph (b) shows the changes in anisotropy field (H_s) and the estimated uniaxial magnetic anisotropy constant (K_u) from H_s as a function of temperature. 85

5.26 (a) Out-of-plane and in-plane magnetization data measured in SQUID magnetometer, (b) angular dependence of magnetic field measured in a torque magnetometer attached to a PPMS device rotating under 14 T magnetic field for $Mn_{1.5}Ga$ thin film grown at T_{sub}= 450 °C at 300 K. Figure is adapted from Ref. [193]. 86

5.27 Angular dependence of magnetic torque for a MnGa film grown at 450 °C measured in torque magnetometer under different applied magnetic fields in the range of 1 T-14 T at 300 K. 87

5.28 Summarized graphs showing the trend of changes in uniaxial magnetic anisotropy and peak shift with respect to the maxima in magnetic torque curves measured for a MnGa film grown at 450 °C as a function of different applied magnetic fields in the range of T-14 T at 300 K in torque magnetometer. 88

5.29 Angular dependence of magnetic torque for a MnGa film grown at 450 °C measured in torque magnetometer under applied magnetic field of 14 T at different temperatures in the range of 60 K to 300 K. 88

5.30 The dependence of magnetic anisotropy (K_u) on saturation magnetization (M_s) at different temperatures in the range of 60 K to 300 K for a MnGa film grown at 450 °C. 89

5.31 XRD patterns collected from exchange spring bilayer of $Mn_{1.5}Ga/Fe_{35}Co_{65}$ with 2 nm thickness of FeCo soft magnetic layer. The $L1_0$-$Mn_{1.5}$Ga thin film was deposited at T_{sub}: 450 °C and FeCo layer was deposited at a substrate temperature of T_{sub}: 100 °C. The inset shows schematic of $Mn_{1.5}Ga/Fe_{35}Co_{65}$ bilayer samples deposited on Cr (001) buffered MgO (100) substrate. 89

5.32 Out-of-plane magnetization data for MnGa/FeCo bilayers with $Fe_{35}Co_{65}$ (at.%) thickness between 0 nm-8 nm measured at 300 K. Figure is adapted from Ref. [193]. 90

5.33 (a) High-resolution cross-section TEM image of $Mn_{1.5}$Ga (001)/$Fe_{35}Co_{65}$ (001) epitaxial bilayer sample, with 3 nm FeCo layer thickness, (b) HR-STEM image of the epitaxial MnGa/FeCo interface, and (c) line scan EDS map of the Cr, Mn, Ga, Fe and Co distribution across the bilayer sample. Figure is adapted from Ref. [193]. 92

5.34 Atomic structure of (a) MnGa (001)/Fe_3Co_5 (001) with Ga and Co terminations, and (b) MnGa (001)/Fe_5Co_3 (001) with Ga and Fe terminations demonstrated using VESTA [115]. Mn, Ga, Fe and Co are shown with light pink, magenta, yellow, and blue colors, respectively. Figure is adapted from Ref. [193]. 92

5.35 (a) Simulated hysteresis loops using OOMMF code for a MnGa(001)/Fe_3Co_5(001) bilayer system corresponding to the first row of data in Tab. 5.2 for various thicknesses of FeCo. (b) First derivative plots of both experimental and simulated hysteresis loops for MnGa(001)/Fe_3Co_5(001) bilayers as a function of soft layer thickness. The first derivative at higher temperature is also inculded in the same graph for comparison. For better visualization, the second derivative of the simulated data is shown as well. Figure is adapted from Ref. [193]. 94

7.1 XRD patterns collected from three MnBi thin films grown from $Mn_{55}Bi_{45}$ alloy target onto BaF_2(111) (a) grown at T_s= 400 °C without annealing, (b) grown at T_s= 300 °C with post annealing at T_a= 530 °C for 30 min, and (c) grown at T_s= 300 °C with post annealing at T_a= 530 °C for 1 h. For better visualization, the graphs have a vertical offset. 100

1.1 Summary of magnetic properties for $L1_0$ ordered tetragonal phases of MnGa and MnAl with the highest theoretically predicted magnetic properties. The star(*) values show the highest reported experimental values from previous thin film studies [7, 9, 61]. 3
2.1 Summary of demagnetizing factors (in cgs) for some specimen shapes, values adapted from Ref. [79, 101]. 14
2.2 Summary of physical and magnetic properties for ferromagnetic LTP MnBi. The values are adapted from [23] 20
2.3 Summary of physical and magnetic properties for FM tetragonal $L1_0$- $\mathrm{Mn_{1.5}Ga}$, values adapted from [8, 118, 119] 23
5.1 Calculated values of interface formation energy γ^{int}, interface exchange coupling energy J^{int}, exchange constant A^{int} and lattice misfit (longitudinal and angular) obtained from DFT calculations. The disordered (110) structure is reconstructed and lost its short range order compared to crystalline (110) structure. The amorphous (111) is completely irregular. Table is adapted from Ref. [106]. 78
5.2 Values of interface formation energy γ^{int}, interface exchange coupling energy J^{int}, interface exchange constant A^{int} and lattice mismatch calculated by DFT considering different compositions of $\mathrm{Fe_xCo_{1\text{-}x}}$ layer and different terminations in MnGa/FeCo interface. All the interfaces are perpendicular to the [001] crystallographic direction. Table is adapted from Ref. [193]. 93
7.1 Summarized values of lattice misfit between different substrates (buffer layers) and $L1_0$-MnGa (a= 3.886 Å) or $L1_0$-MnAl (a= 3.920 Å) phases. The lattice parameter values are adapted from ICDD (International centre for diffraction data). The (*) values are calculated with 45° in-plane rotation (a=a/$\sqrt{2}$). 99

1 Introduction

Permanent magnets have application in many modern technologies from renewable energy, e. g. in wind turbines and electric vehicles, to communication and entertainment, e. g. smartphones and other electronic gadgets [1]. Currently, rare-earth permanent magnets, e. g. $Nd_2Fe_{14}B$ as the most prominent phase, are commercially employed for most applications since they show an exceptional energy product $>$ 240 kJ/m^3 (∼30 MGOe)[2] which is a prerequisite to build a highly efficient generator or motor. However, their relatively low Curie temperature (of 585 K in case of Nd-Fe-B) [3] undermines their performance for high temperature applications. Aside from the reduced performance at elevated temperatures, the fragility in the global supply-demand chain for rare-earth elements is the main reason which has made the application of rare-earth permanent magnets critical. Since 97% of the world rare-earth element resources are dominated by China [4], the limited supply makes it both politically and commercially critical to use them for the above-mentioned applications. Therefore, there is a rising demand for synthesis of rare-earth free permanent magnets, or ferromagnetic phases with a reduced amount of rare-earth elements [1, 3]. In order to replace the established materials, the potential rare-earth free permanent magnets must possess high energy density, high anisotropy, and stability at elevated working temperatures [5].

Mn-based intermetallic phases exhibit high perpendicular magnetic anisotropy, K_u, and high Curie temperature, T_c, which qualifies them for a wide range of applications not only as permanent magnets but also in spintronics. Because of their potential application in magnetic devices for high density magnetic recording and as rare-earth free permanent magnets [6], ferromagnetic thin films of MnBi, MnGa and MnAl have recently attracted special attention in research [7, 8, 9, 10, 11, 12]. Synthesis of highly anisotropic thin films with a K_u of at least 10^7 erg/cm^3 as well as a moderate magnetization M_s is necessary to obtain a high density perpendicular magnetic recording in the range of 10 Tb/inch^2 [13, 14]. However, in order to be employed for permanent magnet applications their moderate saturation magnetization needs to be further improved.

The low temperature phase (LTP) of MnBi has recently gained much attention as a relatively inexpensive ferromagnetic compound [15, 16] for applications for permanent magnets, recording media and magneto-optics [17, 18, 19, 20]. The potential use of MnBi as hard magnetic component in an exchange spring magnet is also a new focus in research [21]. MnBi is an intermetallic compound with a NiAs-type hexagonal crystal structure ($P6_3/mmc$, No. 194) with the easy axis of magnetization parallel to the c-axis [22]. Despite its relatively low saturation magnetization (M_s) of 710 emu/cm^3 (0.71 MA/m) as compared to the rare-earth magnets [23], the promising magnetic properties of MnBi such as the large uniaxial anisotropy (K_u) of about 10^7 erg/cm^3 (10^6 J/m^3) [23, 24, 25, 26, 27], the high Curie temperature (T_c) of 711 K (which is limited in practice by its structural transformation temperature of 630 K but is still about 40 K higher than that of $Nd_2Fe_{14}B$)[17], and the outstandingly high coercivity (H_c) with positive temperature coefficient, reaching the maximum value of 25 kOe (2.5 T) at 540 K, make MnBi one of the most interesting candidates to be used as a rare-earth free magnet [27, 28, 29]. The most commonly reported maximum energy product $(BH)_\mathrm{max}$ for a MnBi magnet is only about 7.7 MGOe (61 kJ/m^3) at room temperature [30, 31, 32]. The highest achieved $(BH)_\mathrm{max}$ value of 17 MGOe at 290 K was reported only for a bulk directionally-solidified LTP MnBi magnet [33]. There is obviously room to reach the theoretical value of 17.7 MGOe (140 kJ/m^3) for MnBi thin films either by achieving a higher saturation magnetization through synthesis of pure LTP MnBi, or by improving the coercivity [23]. Aforementioned magnetic properties bring considerable potential to study MnBi as a rare-earth free permanent magnet material specifically for applications at elevated temperatures.

More recently in various studies, the magnetic properties of MnBi in different forms from nanomaterial to single crystals have been investigated. It has been found that the initial elemental composition influences the magnetic properties of the synthesized LTP MnBi. Starting with a slightly higher Mn

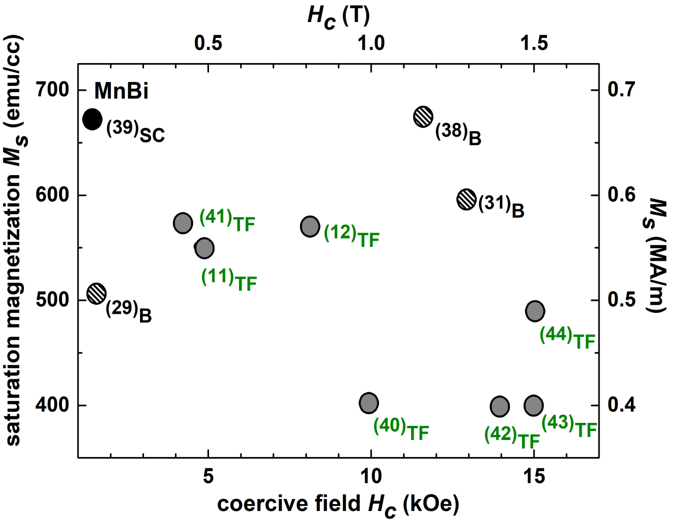

Figure 1.1: Summary of room temperature data on saturation magnetization, M_s, and coercive field, H_c, for LTP MnBi with starting composition of $Mn_{55}Bi_{45}$ (at. %) including values reported for thin films (TF: gray circles), bulk (B: dashed circles), and single crystal (SC: black circle) samples. The numbers in brackets refer to the list of references, figure adapted from Ref. [34].

content ($Mn_{55}Bi_{45}$ at. %) minimizes the amount of unreacted Bi and results in the highest amount of LTP MnBi with the highest magnetization [21, 31, 35, 36, 37]. In Fig. 1.1, the literature values for the saturation magnetization, M_s, and the coercive field, H_c, of LTP MnBi samples with starting composition of $Mn_{55}Bi_{45}$ are summarized [11, 12, 29, 31, 38, 39, 40, 41, 42, 43, 44]. In contrast to a direct deposition approach from one off-stoichiometric target used in the current study, all previous studies reported thin films of LTP MnBi which have been synthesized by stacking subsequent Bi and Mn layers followed by post annealing. The deposition from a single $Mn_{55}Bi_{45}$ (at. %) target provides an easier way to deposit additional layers, e. g. within a spring magnet or spin valve system.

Synthesis of tetragonal $L1_0$-Mn_xGa and $L1_0$-Mn_xAl phases is highly demanded as these perpendicularly magnetized Mn-based intermetallic phases are also promising candidates for a vast range of applications in spintronics, magnetic recording and also as replacement for rare-earth containing permanent magnets. Among several magnetically ordered phases in Mn-Ga and Mn-Al complicated phase diagrams, the $L1_0$-MnAl (τ, Mn: 50-60 at.%) and $L1_0$-Mn_xGa(γ_3, $0.76< x <1.8$) ferromagnetic phases are theoretically predicted to have outstanding magnetic properties [8, 45, 46, 47]. The $L1_0$-MnGa ($D0_{22}$-Mn_3Ga) alloys are theoretically predicted to have K_u of 26 (20) Merg/cm^3 [48, 49], M_s of 845 (305) emu/cm^3 [48, 49, 50, 51], $(BH)_{max}$ of 28 (3.7) MGOe [8, 52], and spin polarization (P) of 71(88) at the Fermi level [8, 49, 52, 53], respectively. Moreover, as another promising rare-earth free ferromagnetic phase $L1_0$-MnAl is theoretically predicted to have a K_u of 15 Merg/cm^3, M_s of 800 emu/cm^3 (or 2.37 μ_B/Mn) and $(BH)_{max}$ of 12.64 MGOe [54, 55, 56].

Since early 1990s when a square perpendicular hysteresis was measured by Krishnan and Tanaka *et al.* for Mn_xGa ($1.2< x <1.5$) grown on GaAs (001) substrates [57, 58], different attempts have been made to grow epitaxial $L1_0$ and $D0_{22}$-Mn_xGa films by magnetron sputtering or molecular-beam epitaxy (MBE) on different types of substrates such as GaN, MgO, GaAs, GaSb, Si, Al_2O_3, $SrTiO_3$ with different buffer layers including Cr and ScN to reduce the lattice misfit and improve crystallinity of the resulting films [8, 7, 50, 59, 60, 61, 62, 63, 64, 65].

Table 1.1: Summary of magnetic properties for $L1_0$ ordered tetragonal phases of MnGa and MnAl with the highest theoretically predicted magnetic properties. The star(*) values show the highest reported experimental values from previous thin film studies [7, 9, 61].

$L1_0$ Phase	K_u [Merg/cm^3]	M_s[emu/cm^3]	$(BH)_{max}$ [MGOe]
$L1_0$-$Mn_{1.5}Ga$	26 (15*)	845 (650*)	28
$L1_0$-$Mn_{48}Al_{52}$ (at.%)	15 (10*)	800 (600*)	12.64

Growth of MnAl (001) epitaxial thin films has also been widely investigated using different methods such as MBE, sputtering, E-beam evaporation and pulsed laser deposition on GaAs (001) single crystal substrates covered by an AlAs buffer layer [54], MgO (001) substrates covered by a Cr buffer layer [9, 10] and glass substrates [66]. Using noble metals such as Pd and Pt as buffer layer could result in the minimum lattice mismatch below 1% which can improve the growth properties. Although, only a few of the resulting films which were grown on MgO or GaAs have shown perpendicular magnetic anisotropy [9, 67].

Despite all the efforts, the highest magnetic properties achieved are not yet as high as the theoretically predicted values. Therefore, there is still room to improve the magnetic properties of MnGa and MnAl tetragonal phases. For an overview, the highest reported values were summarized along with the theoretically predicted values in Tab. 1. In both cases, deposition with sputtering using an alloy target on MgO (100) single crystalline substrates (with lattice misfit of $\sim$ 7.8%) covered by a Cr (100) buffer layer (lattice misfit of $\sim$ 4.6%) has resulted in the highest magnetic properties [7, 9, 61].

For permanent magnet applications, even higher magnetic moments are required for the Mn-based intermetallics to compete with rare-earth containing magnets. As suggested back in 1991 by Kneller and Hawig, one way to overcome this barrier and to further improve the energy product is through the synthesis of exchange spring magnets with coupled hard/soft magnetic phases (see schematics in Fig. 2.9) [68, 69, 70, 71, 72, 73, 74]. Such composite magnets, e. g. coupled bilayers of MnBi or MnGa in combination with FeCo as the soft phase, will possess a much higher saturation magnetization and thus an increased overall energy product.

For exchange spring heterostructures with MnBi as hard magnetic phase, there have been only a few recent studies investigating the synthesis and magnetic properties of the resulting bilayers [44, 75, 76]. Although theoretical calculations have proven the concept of exchange spring magnets to increase the overall magnetic properties, according to the few available studies the coupling between the MnBi and Fe_xCo_{1-x} layers is incoherent for magnetic layers thicker than $\sim$4 nm [44, 75, 76]. This is also evident from the small shoulder observed around zero field on the hysteresis loops measured in all above mentioned studies where the two layers do not behave as a single magnetic phase. It is important to understand the interfacial effects responsible for an incoherent interlayer exchange coupling in order to make further advances in the exchange spring magnets of above-mentioned systems.

Based on the model suggested by Kneller [68], there is a critical thickness (volume) of the soft magnetic phase which is limited by the domain wall width (or exchange length) of the hard magnetic phase [70, 71]. For thicker soft magnetic layers, the coupling between hard and soft magnets begins to deteriorate and hence the layers will switch independently during the magnetic reversal process. However, if the thickness of the soft magnetic layer is less than twice of the domain wall width in the hard magnetic phase, the bilayer is expected to behave as a single phase with increased magnetization in which both soft and hard phases switch coherently during magnetic reversal under opposing field (H<0). Nevertheless, in experiment even for sufficiently thin soft magnetic layers, incomplete exchange coupling is reported indicating that other factors are involved.

Beside the thickness of the soft and hard magnetic layers, structural factors such as degree of crystallinity and growth orientation might affect the strength of exchange coupling. For instance, the hard/soft interface roughness, resulting from the growth quality of the layers, and lattice mismatch at the interface can influence the coupling between the layers. In addition, the effect of composition of the $\mathrm{Fe_xCo_{1\text{-}x}}$ soft magnetic layer has been considered as a controlling factor which influences the interlayer exchange coupling. Based on their calculations, Gao *et al.* have also argued that the formation of a Co-rich $\mathrm{Fe_xCo_{1\text{-}x}}$ layer at the interface with MnBi is beneficial for exchange coupling where according to their experimental data the strongest coupling occurs in MnBi/Co bilayers with an optimum Co thickness of $\sim 3\,\mathrm{nm}$ [75].

For exchange coupled heterostructures with MnGa as hard magnetic layer, only one study has addressed the exchange spring bilayer of MnGa/FeCo system with a 1.5 nm FeCo soft magnetic layer. The MnGa/FeCo Bilayers studied by Ma *et al.* have shown a transition from a ferromagnetic to an antiferromagnetic coupling when the Co contents in FeCo layer was increased [77]. However, in contrary for the MnBi/FeCo system it was shown that not only a Co-rich composition of $\mathrm{Fe_xCo_{1\text{-}x}}$ soft layer is in favour of the ferromagnetic exchange coupling but the thickness of soft magnetic layer also plays a crucial role which was not investigated in the above-mentioned study by Ma *et al.* for MnGa/FeCo system [75].

This thesis is divided into four principal chapters in which I address the above-mentioned issues. In the first chapter, an overview on *magnetism* has been provided along with a short introduction to exchange spring magnets, as well as MnBi and MnGa as the hard magnetic material systems under study. The second chapter is focused on the experimental methods for *synthesis and characterization* of the deposited exchange bilayers. First, a summarized theory of thin film deposition is provided along with a more detailed introduction to magnetron sputtering as the employed thin film growth method in the current study. In addition, the principle behind the *structural and magnetic characterizations methods* as well as *theoretical calculations* are described which have been used to analyse the deposited thin films and the exchange coupling coherency, respectively. In the third chapter, the experimental procedure for the *growth of (001) MnBi and MnGa hard magnetic thin films* and their exchange bilayers with the soft magnetic $\mathrm{Fe_xCo_{1\text{-}x}}$ (x=0.65 and/or 0.35) layer in a magnetron sputtering unit is explained in detail. Finally, in the fourth chapter the experimental results of the growth study of *c*-axis oriented LTP-MnBi and epitaxial $L1_0$-$\mathrm{Mn_{1.5}Ga}$ thin films and their exchange coupled bilayers with $\mathrm{Fe_xCo_{1\text{-}x}}$ (x=0.65 and/or 0.35) soft magnetic layers are discussed. A combined experimental and theoretical method is used to study the exchange coupling behavior at the interface in the MnBi/FeCo and MnGa/FeCo bilayer systems focusing on the structural factors including crystallinity, interface roughness and composition of the soft magnetic phase to identify which of these factors is dominant in controlling the strength and coherency of the exchange coupling effect.

This chapter gives an overview on the important magnetic phenomena which govern the magnetic properties of interest in the current thesis. First of all, a short introduction is given on the origin of magnetism and magnetic moment. Secondly, interatomic exchange interactions are described based on the four main exchange mechanisms in metals and insulators. In the next section, the origin of magnetic hysteresis is discussed. In the first part, as intrinsic contribution to the hysteresis the concept of magnetic anisotropy is introduced along with different anisotropy terms based on crystal structure, shape, reduced symmetry and induced factors. In the second part, basic mechanisms of hysteresis in permanent magnets under applied magnetic field is described along with the concept of domain wall and magnetic reversal process. The final section is dedicated to the rare-earth free permanent magnets and the concept of exchange spring magnets, in particular for the two Mn-based intermetallic material systems under study in this thesis namely low temperature phase MnBi and $L1_0$-MnGa, which are used as the hard magnetic phase for synthesis of exchange coupled bilayers.

2.1 Origin of magnetic moment

Magnetism originates from the total magnetic moment of electrons in atoms which from a microscopic point of view can be explained based on the quantum mechanical definition of electronic angular momentum. The origin of magnetic moment for each electron is initiated by two phenomena, first one is the electron orbiting around the nucleus from which orbital moment is generated, and the second one is according to the Pauli's principles based on which the spin of electrons generates a moment along the spin axis. In Fig. 2.1 a schematic of these two phenomena is shown which are coupled by the spin-orbit interaction. Occupation of electron shells in atoms is governed by Pauli's exclusion principle and Hund's rule [78]. The quantum numbers describe the state of electron levels and are called angular momentum l, spin projection quantum number s and the total angular momentum j. The Pauli's Exclusion Principle states that no two electrons in an atom can have the same four electronic quantum numbers. As an orbital can contain a maximum of only two electrons, the two electrons must have opposing spins. Based on Hund's rule, every orbital in a sublevel is singly occupied before any orbital is doubly occupied and all of the electrons in singly occupied orbitals have the same spin to maximize total spin. If an atom has a fully occupied electron shell then the net magnetic moment would be cancelled out. Therefore, only materials with partly filled electron shells show magnetic properties.

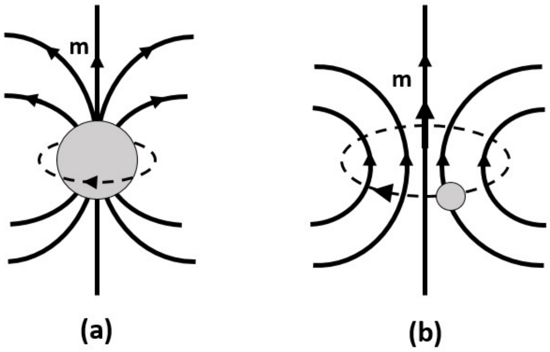

Figure 2.1: Schematic of magnetic moments associated with (a) spin angular moment, and (b) orbital moment of an electron, adapted from Ref. [78].

Depending on the number of unpaired electrons and their orientation in the orbital, magnetic materials behave differently under external applied magnetic field. As a consequence, most materials can be classified as: ferromagnetic, antiferromagnetic, ferrimagnetic, paramagnetic and diamagnetic [79].

Antiferromagnetic materials possess moments with equal magnitude but aligned in opposite directions. This anti-parallel configuration of magnetic moments gives rise to a zero net magnetization in the absence of external magnetic field and below ordering or Néel temperature. In some ceramic materials, another type of magnetic property is observed called *ferrimagnetism*. They are basically made of two sublattices which are antiferromagnetically coupled to each other. Each of these sublattices has unequal magnetic moment which results in a small but non-zero net magnetization. *Diamagnetic* and *paramagnetic* materials are generally considered as "non-magnetic" and they only exhibit magnetic moment under external magnetic field. *Diamagnetism* is similar to the Lenz law in electric field. There is a system of moving charged under external field and their motions change in a way that an opposing field is formed with respect to the original applied field. Because of incomplete cancellation of electron orbital or spin magnetic moments, atoms have permanent dipole moments which adapt random orientation in the absence of external magnetic field. *Paramagnetism* happens when such random orientation of dipole moments changes and aligns toward the direction of externally applied magnetic field. Most importantly, in transition metals and some rare-earth elements, *ferromagnetic* properties are observed. These materials show permanent magnetization as a result of strong interaction of magnetic moments even in the absence of applied magnetic field which is stable up to the Curie temperature and has specific direction [80].

2.2 Exchange energy

Apart from the energies induced by external magnetic field, there is an internal molecular or exchange field in a ferromagnetic material proportional to its magnetization meaning that each spin sees the average magnetization over all other spins in the material [81]. Exchange interaction takes into account the spin-spin interactions on a scale of atomic distance and it tends to order the neighbouring spins.

The electron orbitals of neighbouring atoms in solid overlap which leads to the correlation of electrons. The inter-atomic exchange interaction is resulted from this correlation which means the total energy of crystal will depend on the relative orientation of localized spins on neighbouring atoms. The exchange interaction is responsible for the existence of parallel (i. e. ferromagnetic) and antiparallel (i. e. antiferromagnetic) spin alignment and is the largest magnetic interaction in solids. The exchange interaction results from different mechanisms the main ones are discussed in the following sections [79, 82, 83, 84].

The origin of exchange or molecular field was not discovered until Heisenberg showed in 1928 that it is caused by quantum mechanical exchange forces [85]. The exchange forces can be explained taking into account the effect of spin orientation on repulsive Coulomb's electrostatic interactions between two neighbouring atoms. As a consequence of the Pauli exclusion principle which forbids the two electrons to occupy the same quantum state unless they have opposite spins, the atoms will be attracted to each other and consequently a stable molecule will be formed at specific distance between the constructing atoms [78, 79].

2.2.1 Direct exchange

In ferromagnetic and antiferromagnetic metals the main exchange mechanism involved is overlapping of partly localized atomic orbitals of adjacent atoms. This is because of electrostatic Coulomb's repulsion between two nearby electrons and Pauli principle which forbids electrons with the same spin to occupy same quantum state [78, 86]. Since electrons are indistinguishable, there must be the same electron density resulted from exchange of two electrons which means: $|\Psi(1,2)| = |\Psi(2,1)|$. The only condition under which the last statement is fulfilled would be if the two electrons have antisymmetric wave functions meaning: $\Psi(1,2) = -\Psi(2,1)$. Considering simplest example of hydrogen molecule with one electron in $1s$ orbital of each H atom with wave function $\Psi_i(r_i)$, Schrödinger equation is written as:

$$\mathscr{H}(r_1,r_2)\Psi(r_1,r_2) = \epsilon\Psi(r_1,r_2) \tag{2.1}$$

The total wave function is the product of a space coordinate function $\phi(r_1,r_2)$ and a spin coordinate function $\chi(s_1,s_2)$. There are two molecular orbitals (i) spatially symmetric bonding orbital (Φ_s) where electrons pile up between the atoms (spin singlet state), (ii) spatially antisymmetric antibonding orbital (Φ_a) with a nodal plane without any charge midway between the atoms (spin triplet state):

$$\Phi_\mathrm{s} = \frac{1}{\sqrt{2}}(\Psi_1 + \Psi_2) \tag{2.2}$$

$$\Phi_\mathrm{a} = \frac{1}{\sqrt{2}}(\Psi_1 - \Psi_2) \tag{2.3}$$

The ψ_1 and ψ_2 are spatial components of wave functions of electron 1 and electron 2 with $\psi(r_1)$ and $\psi(r_2)$ as solutions of schrödinger's equation, respectively. As mentioned above, the electrons must have antisymmetric wave functions to be able to occupy same quantum state. Therefore, the wave functions for electron 1 and 2 must be the product of a symmetric space function ($\phi(r_1,r_2)$) and an antisymmetric spin function ($\chi(s_1,s_2)$) or vice versa. In a spin triplet state, there is no chance of finding electrons at the same point of space because of parallel spins which avoid each other. However, in the spin singlet state with antiparallel spins, there can be some probability of finding electrons in the same place because this means that spatial part of the wave function is symmetric under exchange of the electrons.

The two energy states for singlet (ϵ_I) and triplet (ϵ_{II}) spin configuration can be evaluated by Hamiltonian. There is a spin splitting between energies of these two states which is twice of the exchange integral. In the case of hydrogen molecule, bonding singlet state lies below antibonding triplet state and so the exchange energy is negative.

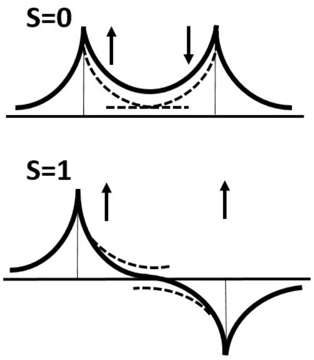

Figure 2.2: Schematic of a spatially symmetric wave function (ψ_s), with electronic charge piled up between atoms, and a spatially antisymmetric wave function (ψ_a) with no charge between atoms in H_2 molecule, adapted from Ref. [78].

In general for two adjacent atoms with electron 1 orbiting around proton 1 and electron 2 orbiting around proton 2, there is a possibility for these two electrons to exchange their places since electrons are indistinguishable in small interatomic distance. This assumption will gives rise to an additional energy term in the total energy of these two electrons caused by the difference in their energy considering two spin configuration of $\uparrow i \uparrow j$ and $\uparrow i \downarrow j$. The exchange energy between two atoms i and j each with electron spin angular momentum of $S.h/2\pi$ is as following where J_ex describes the strength of the exchange coupling between the spins i and j:

$$E_\mathrm{ex} = -2J_\mathrm{ex}\hat{S}_i\hat{S}_j \tag{2.4}$$

Assuming a lattice made of such atoms, a sum over all pairs of atoms on the lattice sites must be considered. The exchange energy of the system is given by the expectation value of the Heisenberg Hamiltonian:

$$\mathscr{H}_{\mathrm{ex}} = E_{\mathrm{ex}} = -2\sum_{i<j} J_{\mathrm{ex}} S_i S_j \tag{2.5}$$

J_{ex} is the exchange integral related to the overlap of charge distribution of atoms i and j. If the exchange interaction is considered the same for each nearest neighbouring pair of atoms, the Eq. 2.5 can be rewritten as below:

$$E_{\mathrm{ex}} = -2J\,cos\Phi \sum_{i<j}^{nn} S_i S_j \tag{2.6}$$

where Φ is the angle between the spins. Therefore, for the case of parallel magnetization orientation in ferromagnetic materials, J must be positive and the exchange energy is minimum ($cos\Phi = 1$) and in case of anti-parallel configuration of spins J must be negative ($cos\Phi = -1$) and exchange energy is maximum in anti-ferromagnetic materials. Fig. 2.3 shows the variation of exchange integral (J) with respect to interatomic distance (ratio of radius of an atom to radius of its $3d$ electron shell: $r_{\mathrm{a}}/r_{\mathrm{3d}}$) which is usually known as the Bethe-Slater curve. When the ratio of $r_{\mathrm{a}}/r_{\mathrm{3d}}$ is large, J_{ex} is small and positive. If r_{3d} stays constant, by bringing two atoms of the same kind closer together, i. e. decreasing the $r_{\mathrm{a}}/r_{\mathrm{3d}}$, the $3d$ electrons approach one another more closely and the positive exchange interaction which is in favour of parallel spins first becomes stronger and then decreases to zero. Further decreasing the interatomic distance brings the $3d$ electrons so close that their spins must become antiparallel, which results in a negative J_{ex}, and the material would become antiferromagnetic.

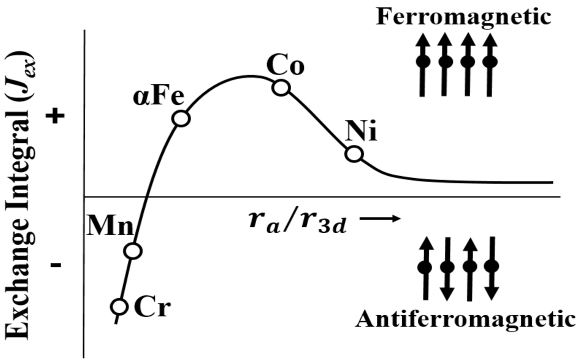

Figure 2.3: A schematic of Bethe-Slater curve, adapted from Ref. [87].

If the angle between neighbour spins is small, it is possible to make a Taylor expansion of the exchange energy. In the continuum approximation we obtain:

$$f_{\mathrm{ex}}(m(r)) = A((\nabla m_{\mathrm{x}})^2 + (\nabla m_{\mathrm{y}})^2 + (\nabla m_{\mathrm{z}})^2) \tag{2.7}$$

where A (exchange stiffness constant) is equal to $A = nJS^2/a$ which is a function of number of atoms in the unit cell (n), lattice constant (a) and $m(r) = M(r)/M_{\mathrm{s}}$ with M_{s} being saturation magnetization. For a hexagonally closed-packed crystal, summation over S_i vectors leads to the same result as in the Eq. 2.7 with $A = 4\sqrt{2}JS^2/a$ where a is the distance between nearest neighbours.

By applying large enough thermal energy, the parallel spins which are held in the same orientation by strong exchange forces can be disordered. Therefore for a positive J_{ex}, the magnitude of exchange energy is proportional to the Curie temperature of that specific element. Such temperature dependency is because of strong dependence on interatomic distance which is affected by thermal energy.

2.2.2 Itinerant exchange

In $3d$ metals such as Fe, Co and Ni, the exchange interaction is due to purely delocalized electrons. Therefore, instead of interatomic exchange interactions, magnetic properties of these metals must be described using the band model of the electrons. Due to Coulomb repulsion and kinetic energy of electrons in the bands with opposite spins, exchange splitting occurs resulting in a non-zero magnetic moment in these materials. According to the Stoner model, the exchange splitting energy (ΔE_{ex}) is proportional to average atomic magnetization (M) with a proportionality constant called Stoner exchange parameter (I) [88]. Based on the Stoner model, the stability of spontaneous magnetic order is limited by the density of states at Fermi level ($N(E_{\mathrm{f}})$) which means that a high density of state at Fermi level and a strong exchange splitting works in favour of metallic ferromagnetism. Since there is an unequal number of electrons with different spin orientations, the magnetic moment is defined by the position of the Fermi level in the conduction band and not by the atomic rules. Therefore, the total magnetic moment in $3d$ metals and their alloys shows a dependency on the number of valence electrons known as the Slater-Pauling dependence [89, 90].

2.2.3 RKKY exchange

An indirect exchange mechanism is observed in metals based on $s-d$ model which happens when there is no direct overlap of the wave functions with unpaired electrons but an interaction between the localized and delocalized electrons [91, 92, 93, 94]. The $s-d$ model describes the coupling of the spins of the conduction electrons S_{e} with core spins S_{core} in a metal and can be expressed by a Hamiltonian as following:

$$H = J_{sd}\Omega|\Psi|^2 S_{core}S_e, \tag{2.8}$$

where Ω is volume of core d shell and $|\Psi|^2$ is s-electron probability density. Whether J_{sd} is positive or negative, it can result in long-range ferromagnetic coupling between the core spins. The interaction between two magnetic moments at sites i is mediated by the uniform spin polarization of the conduction electrons parallel or anti-parallel to the core spins. This model can be applied to rare-earth elements as well in which core spins are from $4f$ shell. In this case, the localized moments in the $4f$ shell interact via electrons in the $5d$–$6s$ conduction band. Ruderman, Kittel, Kasuya and Yosida (RKKY) showed that a single magnetic impurity actually causes a non-uniform oscillatory behaviour of the exchange integral J or spin polarization in the conduction band which changes its sign as a function of distance between the localized moments as r^{-3} leading to a long range oscillatory coupling between core spins. This phenomenon is responsible for the oscillatory interlayer exchange coupling in multilayer giant magnetoresistance (GMR) structures.

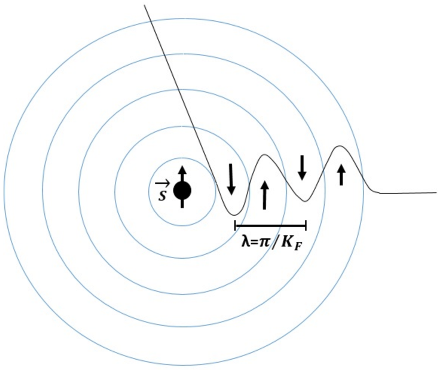

Figure 2.4: Schematic of RKKY oscillations for interaction of a magnetic impurity with a non-magnetic host.

2.2.4 Superexchange

The superexchange is also another type of indirect exchange interaction between localized electrons and is important in insulators specially in ionic solids such as the transition metal oxides. It is a strong coupling between two next-to-nearest neighbour cations via a non-magnetic intermediary anion which is usually antiferromagnetic. Superexchange is a result of the coulping of the electrons from the same donor atom with the receiving ions spins. The interaction can be a ferromagnetic if these two next-to-nearest neighbor cations are connected at 90 degrees with respect to the bridging non-magnetic anion [95, 96].

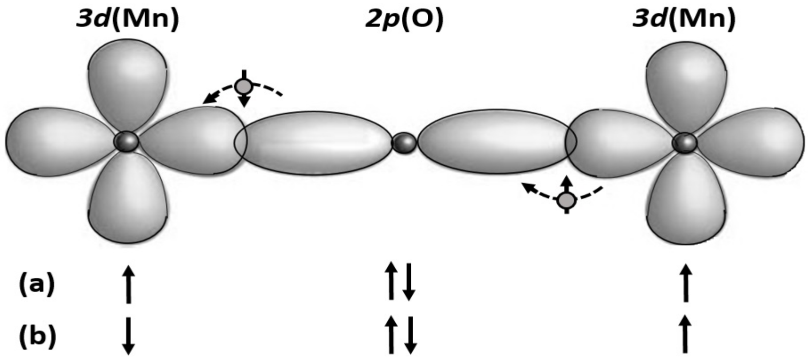

Figure 2.5: Schematic of a typical superexchange bond, adapted from Ref. [78].

As an example in MnO, the $3d$ orbitals of Mn are hybridized with $2p$ orbitals of oxygen and through this the interaction between two Mn atoms is mediated by oxygen. This means both electrons in oxygen $2p$ orbital spread out into unoccupied $3d$ orbitals of Mn. If the orientation of magnetic moments at the metal centres is parallel, no delocalization occurs which is in favour of antiferromagnetic alignment because the overlap integrals are more likely to be larger than zero. The strength of the superexchange depends on the magnitude of the magnetic moments on the metal atom, the overlap between the metal orbitals and the non-metallic element as well as the bond angle. The exchange energy of the adjacent moments increases as the angle between the moments increases varying as $\cos^2\theta$. Another important factor to determine the strength and sign of superexchange is occupancy and orbital degeneracy of the $3d$ states which is summarized in *Goodenough-Kanamori* rules [97, 98, 99]:

(i) If two cations have lobes of singly occupied $3d$ orbitals pointing towards each other, usually in case of 120-180° M-O-M bonds, there would be a large overlap and hopping integrals which results in a strong antiferromagnetic exchange ($J<0$).

(ii) For 90° M-O-M bonds, two cations have an overlap integral between singly occupied $3d$ orbitals which is zero by symmetry. The result is a relatively weak but ferromagnetic exchange.

(iii) In case the two cations have an overlap between singly occupied $3d$ orbitals and empty or doubly occupied orbitals of the same type, the exchange is again ferromagnetic and relatively weak.

2.3 Origin of hysteresis: intrinsic contributions

In general, any material property which depends on direction is considered as anisotropic. In magnetism, anisotropy is attributed to preferential orientation of magnetization in a specific direction (easy axis). It is of great importance to understand possible origins of magnetic anisotropy since it greatly affects the magnetic properties. In the absence of external magnetic field, magnetization lies in the direction of easy axis. However, with increasing the external field applied to an anisotropic ferromagnet, the magnetization vector is pulled more and more towards the direction of the field. The energy per unit volume of magnetization for such a ferromagnetic material with an easy axis of magnetization can be described with the following equation [78, 100]:

$$E = Ksin^2\theta, \tag{2.9}$$

in which, K is anisotropy constant, E is energy per volume (J/m^3), and θ is the angle between the direction of magnetization and easy axis. However, there is another contribution to the energy due to the magnetic field which must also be added to the Eq. 2.9:

$$E = Ksin^2(\theta) - \mu_0 MHcos(\beta - \theta) \tag{2.10}$$

In the second term $(\beta - \theta)$ is the angle between H and M. Taking first derivative of the Eq. 2.10 with respect to the angle θ results in:

$$dE/d\theta = 2Ksin(\theta) - \mu_0 MHsin(\beta - \theta) \tag{2.11}$$

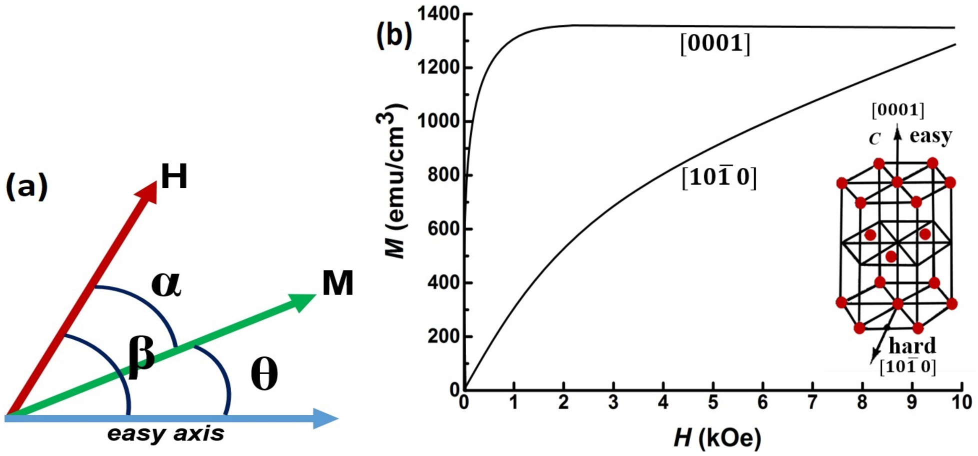

Figure 2.6: (a) Schematic directions of easy axis with respect to the external magnetic field, (b) magnetization curves for single crystal of cobalt with hexagonal crystal structure in easy and hard directions, adopted from Ref. [79].

In order to reach equilibrium, the above derivative must be equal to zero and we must take the value of $\beta = 90°$ as equilibrium angle for the magnetization with respect to the easy axis. Then by taking into account the Eq. 2.10 the following equation is achieved:

$$sin(\theta) = H/H_s \tag{2.12}$$

This relation shows that if the field is zero, the magnetization lies along the easy axis. However, when we apply a field, the magnetization rotates away from the easy axis by a value given for that field from the Eq. 2.12. Finally, if the applied field magnitude reaches H_s, the magnetization will point along the field direction.

The magnetic anisotropy is originated from two interactions on the atomic scale: spin-orbit interaction and magnetic dipolar interaction. Without taking these interactions into account, the total energy of the electron spin system would not depend on magnetization direction. The spin-orbit interaction couples the localized spins to the electron orbitals and the orbits themselves are influenced by the crystal lattice of the material. In this way, spin-orbit interaction induces a small orbital momentum to the atom which couples the total magnetic moment to the crystal axes and so the total energy will also depend on the orientation of the magnetization and the symmetry of the crystal. This is known as the *magnetocrystalline* contribution to the magnetic anisotropy [100].

In the case of thin films, the broken symmetry at the interface also modifies the above mentioned contributions, which is not present in a bulk sample, and leads to another source of anisotropy called *interface anisotropy* [101]. The interface anisotropy is only dominant for fairly thin layers with thickness below $\sim 10\,\mathrm{nm}$ [100]. In a more particular case, a lattice misfit between the layers specifically in multilayer systems results in a strained structure in which a *magnetostrictive anisotropy* will be induced. Here again spin-orbital interactions play a role caused by overlap of wavefunctions in the neighbouring atoms. Depending on the shape of the system, dipolar interaction contributes also to the anisotropy energy. It is of great importance in thin films and is the so-called *shape anisotropy* term. The shape anisotropy forces the direction of magnetization to flip in-plane.

According to the above discussed terms, the total magnetic anisotropy energy (MAE) or effective anisotropy for a thin film sample with thickness of t can be written as following in which K_s represents difference between the anisotropy of interface atoms with respect to the inner bulk atoms. The factor 2 is considered assuming that the layer is bounded by two identical interfaces. The effective magnetic anisotropy can be separated into volume contribution [$\mathrm{J/m^3}$] which is described by the first two terms in the Eq. 2.13 as well as another contribution from interfaces [$\mathrm{J/m^2}$] which is the last term in the following equation [100]:

$$K_\mathrm{eff} = K_\mathrm{MCA} + K_\mathrm{shape} + 2K_\mathrm{s}/t \tag{2.13}$$

The magnitude of the effective uniaxial magnetic anisotropy can be deducted as a rough estimation from the anisotropy field (H_s) which is defined as the magnetic field needed to saturate magnetization of a uniaxial crystal in the direction of its hard axis. A second term must be also included in this equation which represents the opposing effect of demagnetizing field:

$$H_\mathrm{s} = \frac{2K_\mathrm{eff}}{\mu_0 M} - 4\pi M \tag{2.14}$$

2.3.1 Magnetocrystalline anisotropy: spin-orbit interaction

Magnetocrystalline anisotropy refers to the existence of an easy axis or easy plane for specific magnetic materials depending on their crystal structure along which less energy is needed to reorient spin directions and reach saturation when magnetized in external magnetic field. Fig. 2.6-(b) shows anisotropic behaviour of a hexagonal crystal under external field which has a c-axis as easy axis of magnetization. Such a behaviour can be understood by the equation of anisotropy energy in different symmetries [78].

For hexagonal structure:

$$E_\mathrm{a} = K_1 sin^2(\theta) + K_2 sin^4(\theta) + K_3 sin^6(\theta) + K_3' sin^6(\theta) sin(6\phi) \tag{2.15}$$

For tetragonal structure:

$$E_{\mathrm{a}} = K_1 sin^2(\theta) + K_2 sin^4(\theta) + K_2' sin^4(\theta) cos(4\phi) + K_3 sin^6(\theta) K_3' sin^6 \theta sin(6\phi) \tag{2.16}$$

For cubic structure:

$$E_{\mathrm{a}} = K_{1\mathrm{c}}(\alpha_1^2\alpha_2^2 + \alpha_2^2\alpha_3^2 + \alpha_3^2\alpha_1^2) + K_{2\mathrm{c}}(\alpha_1^2\alpha_2^2\alpha_3^2), \tag{2.17}$$

in which θ and ϕ are the polar and azimuthal angles, and α_i is direction of cosines of the magnetization. The $K_{1\mathrm{c}}$ term is equal to: $K_{1\mathrm{c}}$ $(\sin^4(\theta)\cos^2(\phi)\sin^2(\phi)+\cos^2(\theta)\sin^2(\theta))$.

In order for magnetic moment to be anisotropic with respect to a specific crystal direction, there must be a weak interaction involved which would follow the preferential direction upon applying an external field. This interaction is a coupling of spin to orbital motion of electrons. Under external field the spins of electrons reorient themselves and so the orbits try to reorient as well. However, since the orbits are coupled strongly to the lattice they resist this rotation of spins away from the easy axis. The anisotropy energy is defined as the energy needed to overcome such spin-orbit coupling and the anisotropy constant K shows the strength of anisotropy for a specific crystal.

There are two sources for magnetocrystalline anisotropy which are called $single-ion$ and $two-ion$ anisotropy [102]. Considering spin of electrons in the orbitals, first interaction is an electrostatic interaction between the orbitals containing the electrons with the potential which is created at orbital site by the rest of the crystal. This crystal field, which is called spin-orbital interaction, stabilizes specific orbitals, therefore, the magnetic moments are aligned in particular crystallographic direction. There is also a second effect from dipole-dipole interaction resulting from two different possible configuration of magnetic dipoles next to each other, one is head to tail and the other one is broadside (see Fig. 2.7). Since the first configuration has a lower energy, magnets tend to arrange themselves in this configuration. This interaction is also of importance for non-cubic crystals [78].

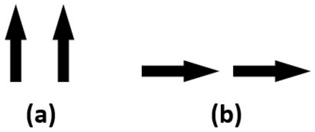

Figure 2.7: (a) Schematic of two possible configuration for magnetic dipoles (a) Broadside, and (b) head to tail, adapted from Ref. [78].

2.3.2 Shape anisotropy: dipolar interaction

The origin of shape anisotropy is the long range dipolar interaction due to asymmetric shape of material which affects the demagnetizing field inside the material and the stray field outside the material. It is of great importance for thin film samples in which one dimension is shorter than the other ones. In an easy case if we consider a ferromagnetic material with the shape of an ellipsoid and magnetization of M with its easy axis along the c-axis, the magnetostatic energy (in SI units) is as follows [78, 79, 82, 102]:

$$E_{\mathrm{m}} = \frac{1}{2}\mu_0 V(N' - N)M_{\mathrm{s}}^2 \tag{2.18}$$

If such an ellipsoid with voulme of V is magnetized along its easy or hard directions, there would be an energy difference (ΔE) which corresponds to the anisotropy energy. In this equation N is the

Table 2.1: Summary of demagnetizing factors (in cgs) for some specimen shapes, values adapted from Ref. [79, 101].

Shape of specimen	N_1	N_2	N_3
`Sphere`	$\frac{4\pi}{3}$	$\frac{4\pi}{3}$	$\frac{4\pi}{3}$
`long cylinder along z-axis`	2π	2π	0
`Infinite plate normal to z-axis`	0	0	4π

demagnetizing factor tensor for easy direction and N$'$ is $(1/2)(1-N)$ which is demagnetizing factor tensor for hard direction. Therefore, we have:

$$\Delta E = \frac{1}{2}\mu_0 V M_s^2[\frac{1}{2}(1-N)-N]$$

$$\Delta E = \frac{1}{4}\mu_0 V M_s^2[1-3N]$$

$$K_{\text{shape}} = \frac{1}{4}\mu_0 M_s^2[1-3N] \tag{2.19}$$

The demagnetizing factor tensor N mentioned above significantly depends on the specimen shape and is given by an integral over the volume (as introduced by Néel 1954) [101]. The demagnetizing factor relates the demagnetizing field with the magnetization in the sample as a function of position:

$$N(r) = -\frac{1}{4\pi}\int\int\int d^3r' \bigtriangledown' (\bigtriangledown'(\frac{1}{r-r'}) \tag{2.20}$$

In many symmetrical shapes the demagnetizing factor tensor only has three principal components:

$$\begin{pmatrix} H_1 \\ H_2 \\ H_3 \end{pmatrix} = -\begin{pmatrix} N_1 & 0 & 0 \\ 0 & N_2 & 0 \\ 0 & 0 & N_3 \end{pmatrix}\begin{pmatrix} M_1 \\ M_2 \\ M_3 \end{pmatrix} \tag{2.21}$$

in which $N_1+N_2+N_3 = 1$ (in SI) and $N_1+N_2+N_3 = 4\pi$ (in cgs). The values of demagnetizing factors for some general sample shapes are summarized in Tab. 2.1 [101]. The shape anisotropy would be zero for a spherical sample with $N = 1/3$ [SI] in all three directions. However, for a thin film specimen with easy axis perpendicular to the film plane demagnetizing factor is equal to 0 for x and y directions and only the z component is effective which is equal to 1 (in SI) or 4π (in cgs). Therefore, by inserting $N = 4\pi$ in equation of magnetostatic energy (Eq. 2.18) the value of shape anisotropy (energy per volume) for such thin film is: $K_{\text{shape}} = -2\pi M_s^2$.

2.3.3 Surface anisotropy

As Néel reported in 1954, in ultra thin films the preferred direction for magnetic anisotropy is controlled by surface magnetic anisotropy [101]. The origin of this type of anisotropy could be attributed to the reduced symmetry at the surface due to the lack of neighbouring atoms, strain induced at the interface by lattice mismatch between film and substrate material, or interface roughness. For such ultra thin films, shape anisotropy and surface anisotropy are in competition and below a critical thickness, surface anisotropy is the dominant effect. The critical thickness and easy direction of surface anisotropy depend on film material and growth conditions such as substrate material and growth temperature [100, 103].

2.3.4 Induced anisotropy

The magnetic anisotropy can be induced to some materials by other means such as growing a film under applied field, heat treatment while applying external magnetic field (field annealing) or by applying a uniaxial stress to the material. This anisotropy is independent of other forms of anisotropy and material might show an easy axis of magnetization after such field treatments. If uniaxial anisotropy is induced by stress into the material, its magnitude depends on magnetostriction [78].

2.3.5 Magnetostrictive anisotropy

Magnetostrictive anisotropy is created in a material by the presence of stress. This type of anisotropy is formed in an isotropic crystal as a result of a change in volume because of magnetic order. Applying tensile or compressive stress can create easy axis parallel or perpendicular to the direction of applied stress in case the magnetostriction constant is positive [78].

2.3.6 Total micromagnetic energy

The total free energy in a ferromagnetic material is given by the equation below which is the sum of all above discussed energy terms:

$$G(M,H) = \int_V g_{\mathrm{tot}}(M(r).H)dV = \int_V (f_{\mathrm{ex}} + f_{\mathrm{mca}} + f_{\mathrm{ms}} + f_{\mathrm{h}})dV \tag{2.22}$$

in which $g_{\mathrm{tot}}(M(r).H)$ is total energy density as the sum of exchange, anisotropy, magnetostatic and external field energies, respectively, where H is applied magnetic field.

2.4 Origin of hysteresis: extrinsic contributions

In ferromagnetic materials, parallel or anti-parallel atomic moment depends on very strong interactions resulted from electronic exchange forces. Therefore, ferromagnetic materials show spontaneous magnetization meaning that even in the absence of external magnetic field, a net magnetization is observed. The magnitude of such a net magnetization depends on spin magnetic moment for electrons as mentioned earlier. Regardless of the strong electronic exchange forces, all ferromagnetic materials show a Curie temperature (T_c) above which thermal energy overcomes exchange energies and results in transition to a paramagnetic state with random moment directions.

Domain theory suggests that regions of uniform magnetization exist in a macroscopic sample separated by planar regions called the domain walls. Within the wall, the magnetization changes direction from that in one domain to that in the next domain. Domains tend to form in the lowest-energy state of a ferromagetic sample in order to minimize the total free energy of the system (see Eq. 2.22). The magnetostatic energy depends on the wall positions and the domain orientations. The domain walls have a finite width that is determined principally by the balance between the exchange energy and the magnetic anisotropy energy. In bulk material Bloch walls are formed, since the system is large enough to include these walls. Magnetization vectors turn through the plane parallel to the wall plane where only small stray fields are present at the rim of the sample. In thin films, Néel walls appear, if the exchange length is larger than the film thickness, where the magnetization rotates within the plane of the domain wall [78].

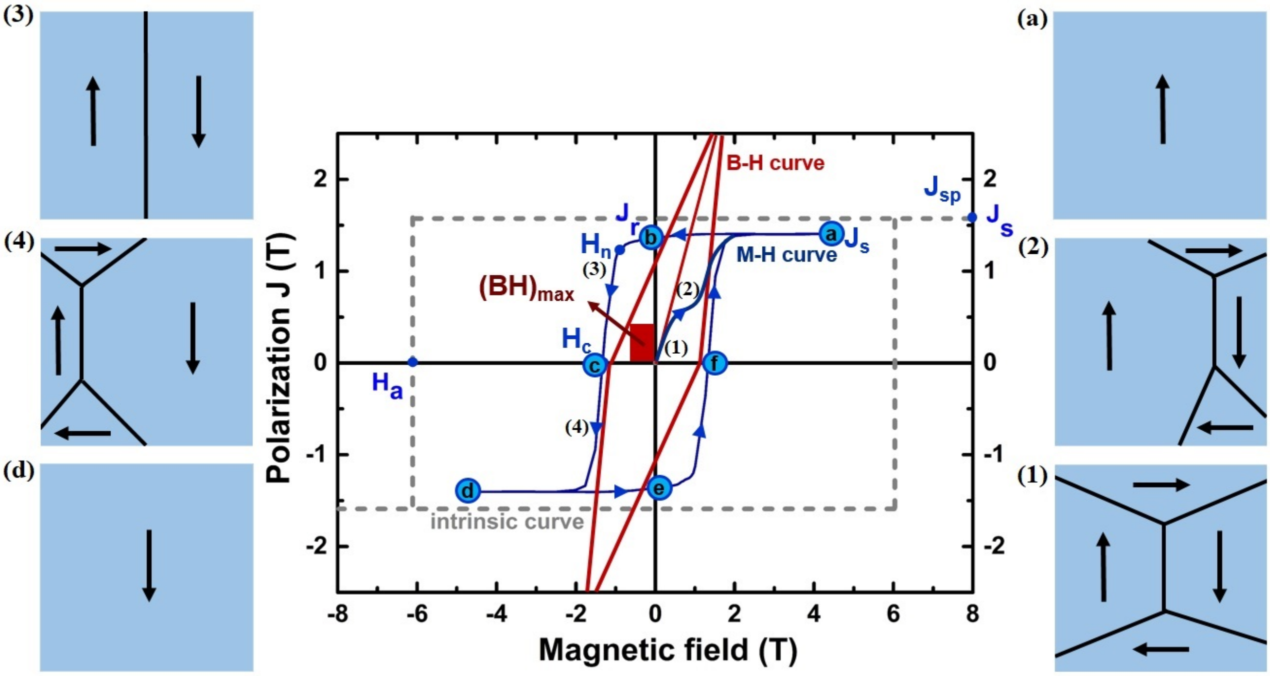

Figure 2.8: Typical hysteresis loop for ferromagnetic materials.

In response to application of external magnetic field, all ferromagnetic materials show a magnetic hysteresis loop which shows a history dependent nature of magnetization in a ferromagnetic material under applied field and can be used as a map to drive different magnetic properties. To acquire such map, one should measure the magnetic flux of ferromagnetic material under continuous change of the external field. An applied magnetic field changes the net magnetization of the sample either by causing wall motion (e. g. when the field is applied along the easy axis), or by making the magnetization in the domains rotate towards the direction of the applied field (e. g. if the applied field has a component perpendicular to the anisotropy axis). The saturation magnetization is achieved mostly through the domain wall motion which is energetically inexpensive compared to magnetization rotation. During the magnetization process, first domain wall motion happens meaning the domains, which are aligned favourably with respect to the direction of applied field, grow at the expense of domains which are aligned differently. At higher field values, domain rotation occurs during which the anisotropy energy can be outweighed and the magnetization can suddenly rotate away from the original direction of magnetization to the crystallographic easy axis that is nearest to the field direction. The final domain process at highest magnetic fields is the coherent rotation of the domains to a direction aligned with the magnetic field (irrespective of the easy and hard axes) [78].

Fig. 2.8 shows a typical form of ferromagnetic hysteresis loop ($M-H$ curve). The origin (1) resembles a ferromagnetic material which has not been yet exposed to any external magnetic field or is fully demagnetized. Starting from the origin, by increasing the magnetic field the material follows the dashed line meaning more and more of magnetic domains in the material will be aligned to the direction of external magnetic field until we reach point (a). At this point, which is the saturation point, all the domains are fully aligned to the direction of applied field. The magnetization measured at this point is also called *saturation magnetization* (M_s). When the field is decreased to zero, instead of demganetizing through the non-linear dashed line the ferromagnetic sample will be demagnetized following the line towards point (b). The most of the magnetic flux remains in the sample even at zero applied magnetic field and the sample retains considerable degree of magnetization. This indicates *remanence* magnetization in the material. Now if we apply the reverse magnetic field, the curve continues from point (b) to reach point (c) and the sample would be then fully demagnetized (similar to point (1)). The applied field which is needed to fully demagnetize a ferromagnetic sample at point (c) is called *coercive force* or *coercivity* (H_c). Upon further increasing the magnetic field in negative direction, the material reaches again a saturation (point d) but this time with opposite direction as that observed in point (a). If we reduce the negative field to zero, the number of domains with their moment parallel to that of external magnetic field will decrease. We will reach point (e) at which a remanence magnetization is observed with its magnitude equal to that observed at point (b) but in opposite direction. Finally to complete this loop, with increasing the applied field in the positive direction we will bring the magnetization first back to zero (point (f) which again shows the coercivity) and then the sample follows a different path from there to reach saturation at point (a). The magnetic properties driven from hysteresis loop (such as saturation magnetization, remanence, coercivity) are characteristics of each material and could depend on different synthesis parameters like temperature, internal stress, domain sizes, etc [79].

As discussed above, a number of primary magnetic parameters can be determined from the hysteresis loop. The most important ones are as follows:

- **Remanence**: It is material's ability to retain certain amount of its magnetization when the magnetizing field is removed after reaching saturation. This is a measure of the residual flux density which corresponds to the saturation induction of a magnetic material.

- **Residual magnetism**: The magnetic flux density that remains in a material when the magnetic field is zero. It should be noted that when the material has been magnetized until the saturation point, the residual magnetism and remanence are the same.

- **Coercive force**: The reverse magnetic field which must be applied to a magnetic material to make the magnetization back to zero is called ceorcive field or coercivity.

- **Permeability**: It is a property of material which describes the ease with which magnetic flux can be established in the material.

- **The maximum energy product (BH)$_{\mathrm{max}}$**: A permanent magnet operates at a point in the second quadrant of the $B-H$ curve where it is subject to the demagnetization field, H_{d}. The direction of this field is opposite to that of the magnetization and it is determined by the shape of the magnet. The magnetostatic energy in a magnet can be defined as:

  $$E = -\frac{1}{2}\int(\vec{B}.\vec{H})dV, \tag{2.23}$$

  in which B is the total magnetic flux in the specimen and $H = H_{\mathrm{applied}} - H_{\mathrm{d}}$. Energy product will be defined then as $-\vec{B}.\vec{H}$ which is energy per volume. The $(BH)_{\mathrm{max}}$ or maximum energy product known as a figure of merit for permanent magnet materials is the largest value for product of B and H in the second quadrant of $B-H$ loop. It is shown as a red rectangular area in Fig. 2.8 and is representative of maximum energy which can be stored in a magnet. If $M-H$ loop is not square and there is some level of random misorientation, this will affect the slope of $B-H$ loop and decreases maximum energy product. In randomly oriented materials, some domains switch at fields smaller than H_{c} which decreases the coercivity of $B-H$ loop and therefore results in a lower $(BH)_{\mathrm{max}}$. Based on the shape of the resulting hysteresis loops, ferromagnetic materials are divided into two groups: *hard* magnetic materials which show a broad hysteresis loop with high coercivity ($> 1\,\mathrm{kOe}$) and *soft* magnetic materials which exhibit a narrow hysteresis loop with low coercivity ($< 100\,\mathrm{Oe}$).

William F. Brown has shown that the coercivity for a homogeneous uniformly magnetized ellipsoid obeys the following inequality which is known as Brown's theorem [78]:

$$H_\mathrm{c} \geq \frac{2K_1}{\mu_0 M_\mathrm{s}} - N M_\mathrm{s}, \tag{2.24}$$

in which, the first term represents anisotropy field and the second term represents demagnetizing field. In reality, the coercivity in bulk material never reaches such a large value which shows that the assumptions of the theory are not met in practice. This contradiction between practice and theory is known as Brown's paradox. The reason behind this contradiction is that all real materials are inhomogeneous, and therefore the magnetization reversal is initiated in a small nucleation volume around an existing defect. A reverse domain can nucleate in the bulk at the position of a defect or at a surface asperity. Surface defects are sources of strong local demagnetizing fields which often act as nucleation centres, because in the second quadrant of the hysteresis loop the reverse magnetic field H is enhanced in the vicinity of such defects. Once a small nucleus is formed, the wall may grow from the nucleation volume and propagate outwards which might become pinned at some other defects [78].

2.5 Rare-earth free permanent magnets

The rising demand for renewable clean energy resources led to inevitable need for strong permanent magnets for the mechanical-electrical energy conversion which is required in wind turbine generators and hybrid electric vehicles. This gave rise to a bigger market for the magnets that are suitable for such applications [104]. However, the rare-earth magnets are critical since the resources of those elements is restricted mostly to China [105]. There was a large increase in prices of rare-earth elements supplied by China in 2009 which caused what is called *rare-earth crisis* because of the cost instabilities due to the monopoly of rare-earth element supply to China. Although the prices have relaxed since then but still remain relatively high [105]. The rare-earth crisis has been brought to international attention specifically for countries such as Germany with no fossil fuel resources in which new clean resources for energy are highly demanded. In this context, synthesis of rare-earth free permanent magnets with comparable magnetic properties as for the rare-earth magnets has attracted much attention recently and so many projects have been funded by the governments to perform research on these material systems [3, 5].

2.5.1 Exchange spring magnets

In 1991, E. F. Kneller and R. Hawig proposed a two phase magnet in which the magnetization of a hard magnet could be increased by the addition of a soft magnetic phase with high saturation magnetization with little reduction in coercivity [68]. If the exchange coupling between the hard and soft magnetic component is strong, such a two phase composite magnet would behave like a single phase magnet but will exhibit a higher overall energy product ($(BH)_\mathrm{max}$). The implication of the exchange spring magnet is that a hard rare-earth free magnet with high coercivity can be coupled to a soft magnet with high M_s in order to form a compound rare-earth free permanent magnet that would have competitive $(BH)_\mathrm{max}$ value compared to that of rare-earth magnets such as Nd-Dy-Fe-B.

Fig. 2.9 shows a schematic of such a magnet with exchange coupled hard and soft layers. The applied field is opposite to the magnetization of the hard phase, but its magnitude is lower than the switching field of the hard magnetic phase. The moments closer to the hard layer are more strongly coupled and thus upon demagnetization the soft layer magnetization resembles a torsional spring.

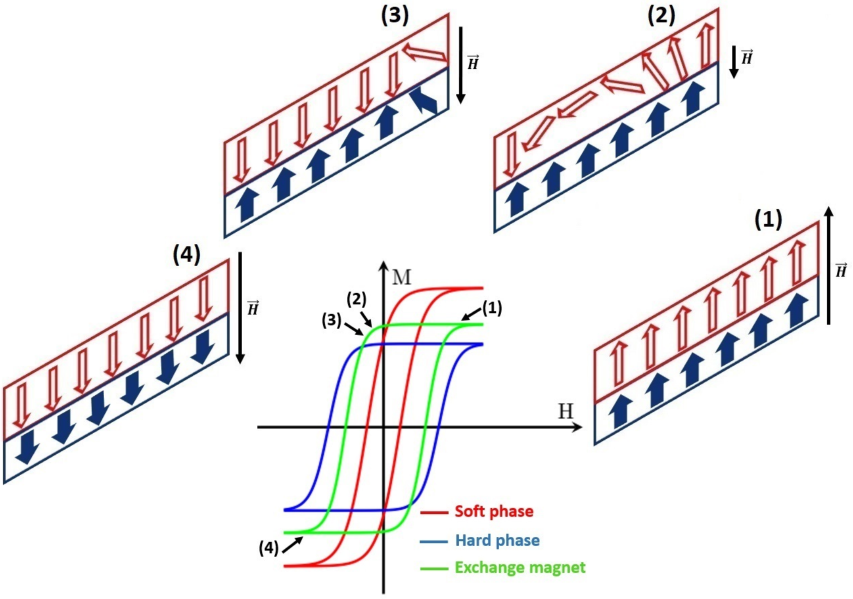

Figure 2.9: Schematic of typical hysteresis loops for a hard magnetic phase (e.g. MnBi, blue solid line), a soft magnetic phase (e. g. FeCo, red solid line), and the exchange spring composite magnet (e. g. MnBi/FeCo, green solid line) resulting from hard/soft exchange coupling. The four insets show a one-dimensional configuration of magnetic moments at the hard/soft magnetic interface under varying external magnetic field (H) assuming an out-of-plane easy axis direction. Red open arrows represent the magnetic moments in the soft phase and blue filled arrows represent the magnetic moments in the hard phase. The length of the arrows represents the magnetization and the width of the arrows represents the coercivity. Figure is adapted from Supplemnetal Material provided with Ref. [106].

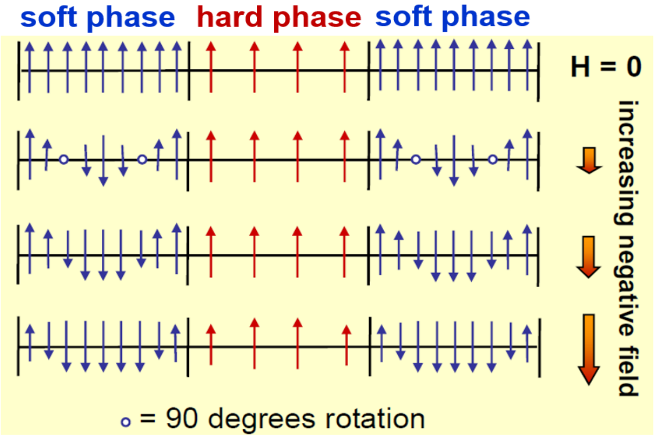

Figure 2.10: Two dimensional model of exchange spring magnet, adapted from Ref. [68].

The exchange spring concept requires the soft phase to be sufficiently small such that domain walls do not form in it upon magnetic reversal. There is a critical thickness for the soft phase which should be about twice as the width of the domain walls in the hard magnetic phase (i.e. 2-4 nm). The smaller the hard phase, the larger the volume fraction of soft phase and thus the larger the M_s and $(BH)_{max}$. The domain wall width for hard magnetic phase can be calculated using the following equation in which A is

Table 2.2: Summary of physical and magnetic properties for ferromagnetic LTP MnBi. The values are adapted from [23]

$m[\mu_\mathrm{B}/\mathrm{f.u.}]$	$M_\mathrm{s}[\mathrm{emu/cm^3}]$	$H_\mathrm{c}[\mathrm{T}]$	$K_\mathrm{u}[\mathrm{MJ/m^3}]$	$T_\mathrm{c}[\mathrm{K}]$	$(BH)_\mathrm{max}[\mathrm{kJ/m^3}]$
3.63	710	2.0 (at 400 K)	1.5	630	140

exchange stiffness constant and K is anisotropy constant of the hard phase [70]:

$$\delta_\mathrm{w} = \pi\sqrt{\frac{A_\mathrm{h}}{K_\mathrm{h}}} \tag{2.25}$$

For such a composite system the magnetic properties, e. g. magnetization, can be calculated by an average over the volume of soft and hard phase [70].

$$M_\mathrm{total} = \frac{(M_\mathrm{h}t_\mathrm{h} + M_\mathrm{s}t_\mathrm{s})}{(t_\mathrm{h} + t_\mathrm{s})} \tag{2.26}$$

2.5.2 Material system: low temperature phase MnBi

In order to compete with the high performance rare-earth based commercial permanent magnets, rare-earth free magnets need to have high energy products, high anisotropy, and stability at increased working temperatures [5]. As a relatively inexpensive ferromagnetic compound, the low temperature phase (LTP) of MnBi is a promising potential candidate [15, 16]. More than fifty years ago, its basic magnetic properties have been studied and still remain of interest for a variety of applications in recording media and magneto-optics [17, 18, 19, 20]. A new focus of research is the potential use of MnBi as hard magnetic component in an exchange spring magnet [21].

Manganese Bismuth (MnBi) intermetallic compound crystallizes in NiAs hexagonal symmetry ($P6_3/mmc$, No. 194) with the easy axis of magnetization parallel to the c-axis [22]. Although it shows a relatively low saturation magnetization (M_s) of 710 emu/cm^3 (0.71 MA/m) compared to the rare-earth magnets [23], it has extraordinary magnetic properties including a large uniaxial anisotropy (K_u) of about 10^7 erg/cm^3 (10^6 J/m^3) [23, 24, 25, 26, 27], a high Curie temperature (T_c) of 711 K (which is limited in practice by its structural transformation temperature of 630 K) [17], and a high coercivity (H_c) with positive temperature coefficient reaching the maximum value of 25 kOe (2.5 T) at 540 K (much larger than that of the Nd-Fe-B magnets) which make MnBi one of the most interesting candidates for rare-earth free permanent magnets [27, 28, 29].

Manganese and bismuth are difficult to alloy because of the large difference in their melting points. The Mn-Bi equilibrium phase diagram, Fig. 2.11, shows that the melting temperatures of Mn and Bi are 1508 K (1235 °C) and 544 K (271 °C), respectively, which means the melting point difference is about 1000 K. Within the 1000 K for MnBi composition, there is about a 700 K span of temperature (the region between the liquids and the peritectic melting temperature at 719 K or 446 °C) where Mn will be segregated from the liquid. The segregated Mn undergoes a series of polymorphous transformations from δ-Mn (Mn ht4) to γ-Mn (Mn ht3) to β-Mn (Mn ht4), and finally to α-Mn at 1411 K (1138 °C), 1373 K (1100 °C), and 1000 K (727 °C), respectively. Two other unknown phase transformations at 1316 K and 870 K had also been detected from cooling curves [107]. The five transformations fill in the region with

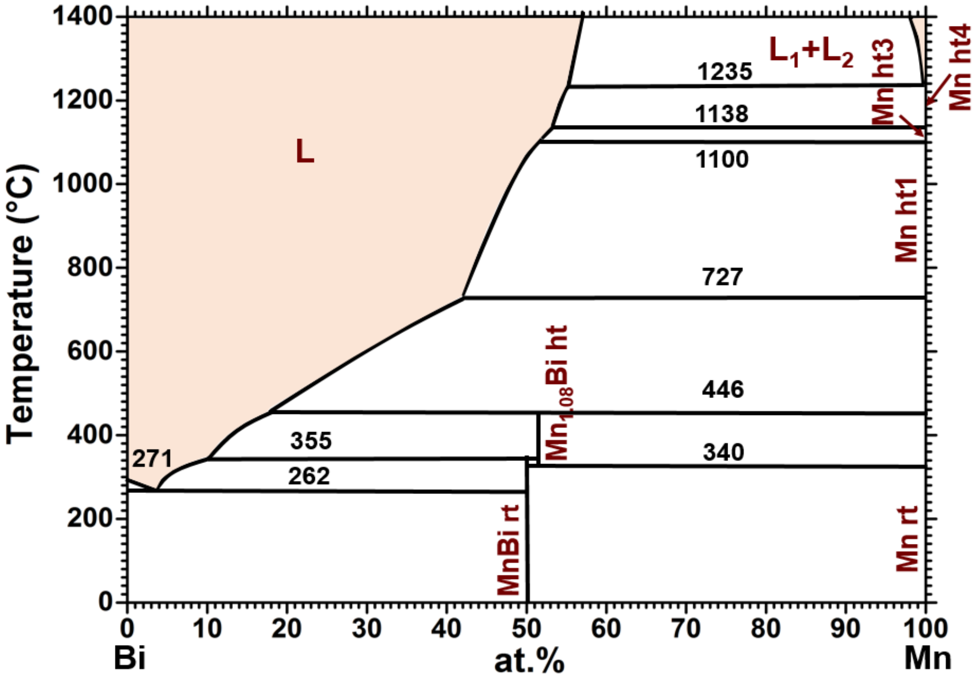

Figure 2.11: Binary phase diagram of Mn-Bi, low temperature phase of MnBi is stable at room temperature and is the ferromagnetic phase, adapted from Ref. [45].

a sequence of horizontal lines. By cooling below this coexistence region of $\mathrm{Mn}_{\text{solid}}$ and liquid, the MnBi high temperature phase (HTP) can be formed, at 719 K, by the peritectic reaction:

$$Liquid + Mn_{\text{solid}} \rightarrow MnBi_{\text{solid}}(HTP) \tag{2.27}$$

Upon further cooling, the HTP transforms into MnBi low temperature phase (LTP) at 613 K. However, the peritectic reaction is difficult to complete. Above 719 K, if cooling rate is slow, the segregated Mn floats on the top of the liquid because of its lower density and results in inhomogeneous distribution of Mn in the liquid which causes diffusion problems for peritectic reaction. Moreover, the diffusion of the Mn and Bi through MnBi is also found to be extremely slow [22, 108, 109], so that the formation of MnBi at the interface impedes any further reaction. As a result, pure Mn and Bi might remain after the system is solidified [26, 38]. Usually to eliminate the unreacted Mn and Bi from magnetic LTP MnBi, the resultant mass will be broken out into fine powder in a ball mill and then the magnetic particles will be separated using a magnetic separator. Up to now, several methods have been used for preparation of high purity MnBi bulk samples, including arc-melting, sintering and meltspin rapid solidification [22, 31, 110, 111, 112, 113, 114]. Among these methods, only with rapid solidification it was possible to reproducibly produce over 90% pure MnBi single phase. However it is much preferred to use a conventional method such as casting and heat treatment because of its compatibility with current industrial processes. In a recent study, Rao *et al.* shows that the conventional cast annealing method can also be used to achieve 90 % single phase MnBi [113, 114].

According to Mn-Bi binary phase diagram, in addition to the above mentioned peritectic reaction, there is a eutectic reaction at 535 K (262 °C), Liquid $\leftrightarrows$ Bi+MnBi. This reaction limits the maximum temperature to which the LTP MnBi can be exposed. Although the eutectic temperature is about 62 K higher than the desired working temperature of 473 K (200 °C), still for bulk magnet fabrication methods such as sintering and hot pressing it is rather low.

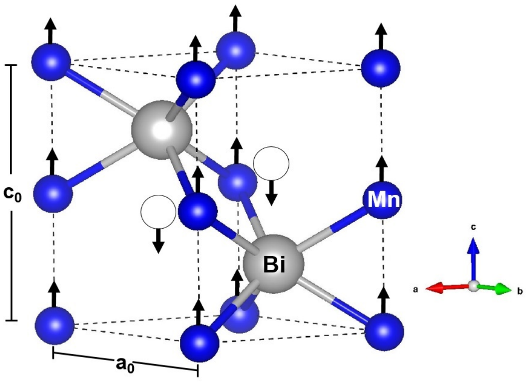

Figure 2.12: A schematic of NiAs hexagonal crystal structure for MnBi illustrated with VESTA [115].

In all previously reported bulk samples, the final powder always contains several percents of Bi metal as the result of the peritectic reaction. During the fabrication process, as soon as the temperature exceeds the eutectic temperature of 535 K, Bi and part of the MnBi will transform to a Bi-rich liquid. If sample is exposed to any amount of oxygen, it may result in oxidation of Mn atoms in the liquid and formation of MnO. Once the oxide forms, it cannot be reduced even in a hydrogen environment at a temperature of $<$ 535 K (262 °C). This leads to some leftover Bi which results in further dissolution of MnBi. The presence of unreacted Bi and MnO is the main reason that deteriorates the magnetic properties of resulting MnBi samples and it can only be controlled either by limiting the processing temperature during the production to less than 473 °C or synthesis under high vacuum level with a precise control over oxygen content in the production chamber [38].

The equilibrium low temperature phase of MnBi (LTP) adopts the hexagonal NiAs type ($P6_3/mmc$) structure as shown in Fig. 2.12 with lattice parameters of a_0=0.4290 nm and c_0=0.6126 nm at room temperature. There is a hexagonal close-packed Bi sublattice with Mn^{3+} ions occupying the octahedral interstices which form a simple hexagonal sublattice [116]. Both above and below, these octahedral sites share common faces along the c-axis and the cations are positioned in linear chains. The tetrahedral interstices of the anion sublattice also share a common face and each tetrahedral site pair forms a trigonal bipyramidal hole, which is fivefold coordinated. These bipyramidal interstices are large enough to take in additional cations. An evidence of the presence of interstitials in MnBi is the fact that in an ideal hexagonal close-packed lattice the c/a ratio is 1.633 which is larger than that of MnBi$\sim$1.40.

Upon heating above its structural transformation temperature of $\sim$360 °C, e. g. during the magneto-optical recording process, the MnBi high-temperature phase (HTP) is formed by a combined magnetic and first-order lattice transition which shows paramagnetic or antiferromagnetic properties [108, 117]. Throughout this transformation, 15% of the Mn cations migrate from the octahedral lattice sites to the bipyramidal sites [22, 108]. Neutron diffraction measurements has indicated a magnetic moment of 3.95 μ_B for the low-temperature phase and 1.90 μ_B for the quenched high-temperature phase of MnBi [22, 108].

2.5.3 Material system: $L1_0$-Mn$_{1.5}$Ga

As another rare-earth free ferromagnetic phase, $L1_0$-Mn$_{1.5}$Ga has also attracted much attention for its theoretically predicted high magnetic properties which make it remarkably desirable for many applications in ultrahigh-density magnetic recording, high performance spintronic devices, and economical permanent magnets. Among several other magnetically ordered phases in Mn-Ga complicated phase diagram, the $L1_0$-Mn$_x$Ga(γ_3) ($0.76<x<1.8$) ferromagnetic phase and $D0_{22}$-Mn$_x$Ga ($2<x<3$) ferrimag-

Table 2.3: Summary of physical and magnetic properties for FM tetragonal $L1_0$- $Mn_{1.5}Ga$, values adapted from [8, 118, 119]

$m[\mu_B/\mathrm{f.u.}]$	$M_s[\mathrm{emu/cm^3}]$	$H_c[\mathrm{T}]$	$K_u[\mathrm{MJ/m^3}]$	$T_c[\mathrm{K}]$	$(BH)_{max}[\mathrm{kJ/m^3}]$
2.5	845	1.0	> 2.0	697	223

netic phase are theoretically predicted to show outstanding magnetic properties. The $L1_0$-Mn_xGa ($D0_{22}$ Mn_3Ga) alloys are theoretically expected to have high K_u of 26 (20) Merg/cm^3 [48, 49], M_s of 845 (305) emu/cm^3 [48, 49, 50, 51], $(BH)_{max}= (2\pi M_s)^2$ of 28 (3.7) MGOe [8, 52], P of 71 (88) at the Fermi level [8, 49, 52, 53] and Gilbert damping constant (alpha) of 0.0003 (0.001) [48], respectively. Despite all the efforts to synthesize above mentioned phases with magnetic properties close to the theoretical limits, the highest achieved magnetic properties are not yet as high as the theoretically predicted values. This shows that the magnetic properties of MnGa tetragonal phase can still be improved using a more successful synthesis method. The theoretically predicted values for $L1_0$- $Mn_{1.5}Ga$ are summarized in Tab. 2.3.

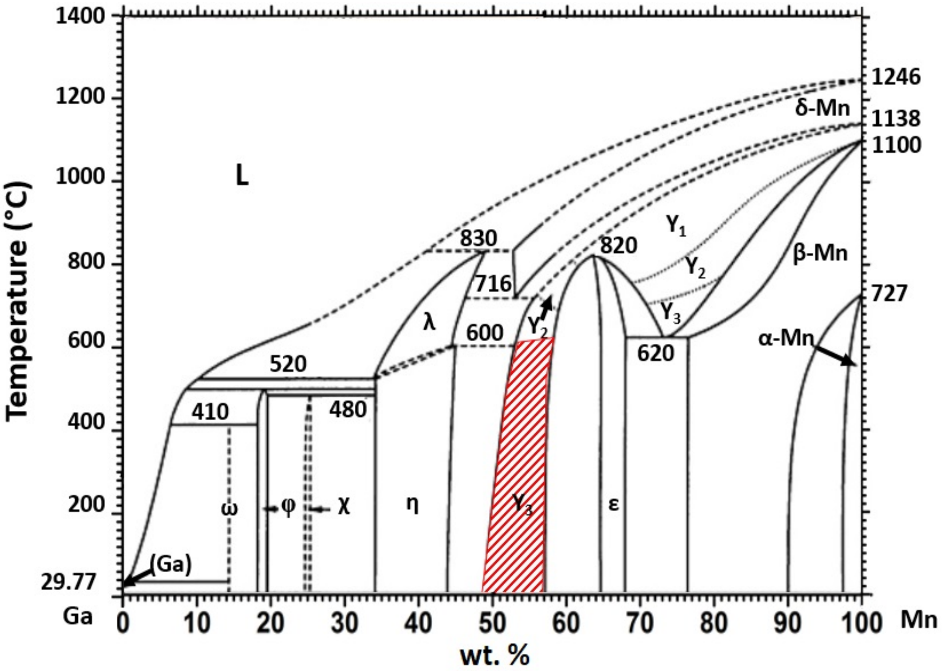

Figure 2.13: Binary phase diagram of Mn-Ga, tetragonal ordered $L1_0$- $Mn_{1.5}Ga$ which is the ferromagnetic phase and only stable in a narrow range of composition between 49-59 wt.% (56-65 at.%) of Mn, adapted from Ref. [45].

Mn-Ga binary phase diagram is complicated (Fig. 2.13) containing several magnetically ordered phases, each stable at certain composition and temperature range [46, 47, 120]. As mentioned above, for magnetic applications the main focus is only on the two most interesting tetragonal phases which show strong magnetism and high Curie temperatures. The ferromagnetic tetragonally ordered phase which is called $L1_0$ (γ_3) is formed in the composition range of 56-66 at.% (Mn_xGa with 0.76<x<1.8) [8, 121]. The ferrimagnetic tetragonally ordered phase is called $D0_{22}$ (ϵ) which is stable in a Mn to Ga ratio of 2<x<3 [7, 53, 119, 122, 123]. Fig. 2.14 shows schematic lattice structures of both $L1_0$-MnGa and $D0_{22}$-Mn_3Ga magnetic phases. The unit cell of $L1_0$-MnGa has space group of $P4/mmm$ and is consisted of alternative Mn and Ga atomic layers along the c-axis. The reported bulk lattice constants of $L1_0$-MnGa are a_0=3.88-3.90 Å and c_0=3.64-3.69 Å [121]. The $D0_{22}$-Mn_3Ga crystal structure, on the other hand, has space group of $I4/mmm$ with bulk lattice constants of a_0=3.90-3.94 Å and c_0=7.10-7.17 Å [119, 122, 123].

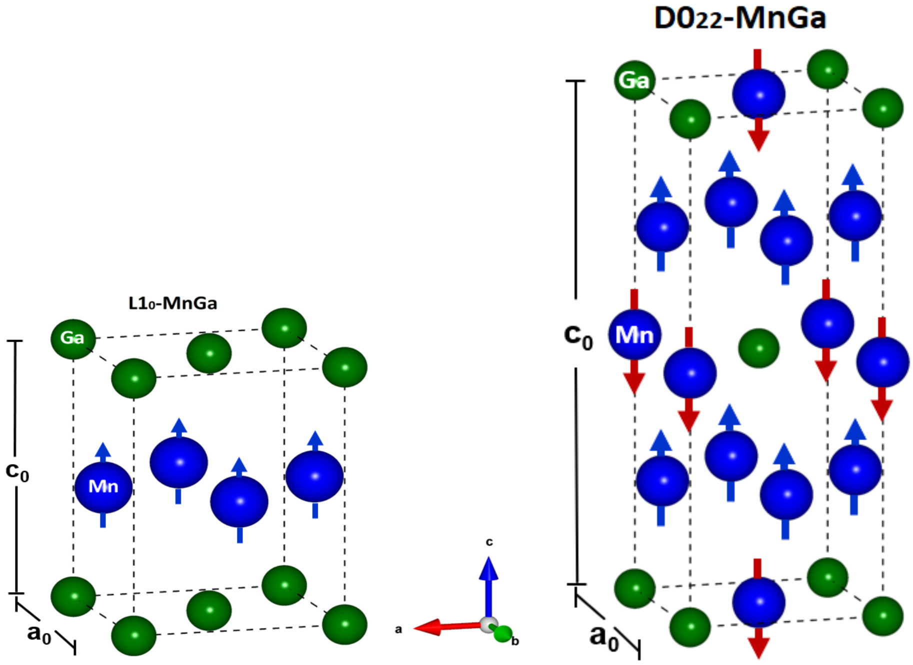

Figure 2.14: Schematic unit cell of (a) tetragonally ordered L1$_0$- Mn$_x$Ga (0.76<x<1.8) phase with a_0=3.88Å and c_0=3.64Å which shows ferromagnetic properties, and (b) D0$_{22}$- Mn$_x$Ga (2<x<3) phase with a_0=3.90Å and c_0=7.10Å which shows anti-ferromagnetic properties, illustrated in VESTA [115].

In stoichiometric $L1_0$-MnGa, each Mn atom will contribute a magnetic moment of 2.51 μ_B which corresponds to a total magnetization of 845 emu/cm^3. Both magnetism and coercivity of $L1_0$ phase are strongly dependent on crystallinity, composition and strain in the synthesized structures [7, 8, 50, 53, 121]. According to the theoretical predictions, excess Mn atoms in $D0_{22}$-Mn$_3$Ga non-stoichiometric phase will result in a decreased magnetization as the additional Mn atoms will align anti-parallel to the rest of Mn atoms. Therefore, the $D0_{22}$ shows ferrimagnetic properties and has a reduced magnetism compared to $L1_0$ phase. By increasing the number of Mn atoms, c lattice constant will monotonically decrease while a lattice constant shows only a slight increase or stays constant [7, 51, 119, 121, 122, 123]. In experiment, it has been observed that increasing Mn to Ga ratio can lead to higher Curie temperature for Mn$_x$Ga nano-ribbons [124]. In 1965 Bither *et al.* reported synthesis of bulk polycrystalline samples with $L1_0$-Mn$_x$Ga (1.2<x<1.5) phase [121]. Samples were prepared by melt fusion of mixtures of electrolytic Mn (99.99%) and Ga (99.999%) in alumina crucibles under an argon atmosphere in a spiral graphite resistance furnace. Then the solids were reduced in particle size to pass through a 100-mesh screen by either filing or crushing in a mortar. These powders were then pelleted and sealed off under vacuum in silica tubes, annealed at 560-570 °C for one week, and then quenched in ice water. Subesequently, the samples were investigated using X-ray diffraction and magnetic measurements [121].

In 1970 Krén and Kádár have obtained $D0_{22}$-Mn$_{2.5}$Ga bulk samples by annealing a hexagonal $D0_{19}$-Mn$_x$Ga phase at 350-400 °C for 1-2 weeks. According to neutron diffraction measurements, the samples show ferrimagnetic properties with Mn atoms having magnetic moment of 2.8 ± 0.3 μ_B at site I and 1.6 ± 0.2 μ_B at site II [119]. For the first time in early 1990s, Krishnan and Tanaka *et al.* each has reported a square perpendicular hysteresis for Mn$_x$Ga (1.2<x<1.5) films grown on GaAs(001) substrate [57, 58]. Ever since, other studies have investigated growth of $L1_0$-Mn$_x$Ga on various substrates including GaN, GaSb, Si, Al_2O_3 and MgO with different buffer layers (such as ScN and Cr). Only few of the resulting films which were grown on GaAs or MgO substrates have shown perpendicular magnetic anisotropy. The $D0_{22}$-Mn_xGa films, on the other hand, have been mostly deposited on MgO (001) substrate [7, 8, 48, 50, 59, 60, 61, 62, 63, 64, 65, 123, 125, 126]. It has been shown in the previous studies that the structural and magnetic properties of Mn_xGa films can be engineered by controlling growth temperature (T_s) [50], composition (x) [7, 8], even with proper annealing temperature [8], and choosing different substrates for the growth [62, 63]. Despite the vast research to synthesize the MnGa thin films with excellent magnetic properties, the highest reported values for the resulting films are still far from the theoretically predicted values. This leaves room for further improvement of the magnetic properties by synthesis of highly epitaxial phase pure films.

3 Synthesis and characterization methods

This chapter provides an overview over the experimental techniques which were used to synthesize and characterize the thin film samples as well as a brief description on the theoretical methods used to investigate exchange coupling effect in bilayer samples. In the first section, a general background is given on the sputtering as the experimental deposition method which was used to synthesize the thin film samples. In addition, different mechanisms governing the film growth were discussed in the next three sections including structural zone model, physical mechanisms and thermodynamics of growth process. Finally, a short introduction is given on different characterization methods used in the current thesis to analyse sample properties. For structural analysis, a brief description is provided for X-ray diffraction methods (XRD and rocking curve) and transmission electron microscopy (TEM). For magnetic characterization, basics of SQUID and torque magnetometry measurement techniques are discussed. Finally, density functional theory (DFT) and micromagnetics are briefly described as theoretical calculation and simulation methods employed to investigate exchange coupling properties in the bilayers.

3.1 Sputtering deposition process

Sputtering is a physical vapour deposition method in which the ions in a plasma are used for bombardment of a target material to deposit a thin film from the removed material on the surface of a substrate. It is a process based on momentum transfer and is of special importance for deposition of compound or alloy films. The reason is that the composition transfer by sputtering from an alloy target is more accurate than that by thermal evaporation of alloy materials since the melting separates the constituting elements and there might be a large difference in vapour pressures of elements which both can lead to non-stoichiometric films [127, 128].

Plasma contains large number of mobile species with both negative and positive charges. If we have the space between two parallel capacitor plates filled with a neutral gas like argon, the plasma can be sparked by applying a sufficient potential across these plates which ionizes some of the gas molecules. Then the resulting positively charged ions will be accelerated towards the cathode (target plate) and simultaneously the electrons will be forwarded to the anode side (substrate). These accelerating particles will collide with more of the gas molecules on their way to the electrodes which leads to more scattering events ionizing the major part of the inert gas molecules. The rate of their collision is defined by their mean free path which depends on the inert gas pressure and scattering cross section of species involved. The resulting current density (i) between the two plates is given by the well-known Townsend equation [129, 130, 131]:

$$i = i_0 \frac{e^{\alpha d}}{1-\gamma_e(e^{\alpha d}-1)} \tag{3.1}$$

where α represents the probability by which collision of an electron and a gas molecule results in ionization, meaning number of ions per unit length produced by electrons, and i_0 is the primary electron current density from external source. α itself depends on the potential applied to electrodes (E), ionization potential of gas species involved (V_i in [eV]) and the mean free path in the gas (λ). The electrons must gain sufficient energy between scattering events to surpass the ionization potential of gas molecules. The probability of ionization (α) has following relation with above mentioned parameters [129, 130]:

$$\alpha = \frac{1}{\lambda} e^{\frac{-V_\mathrm{i}}{qE\lambda}} \tag{3.2}$$

Here q is the electron charge and E is the electric field applied to the electrodes and is equal to V/d.

The parameters d and γ_e in Eq. 3.1 are the distance between the electrodes and the Townsend secondary electron emission coefficient, respectively. The secondary electrons are caused by collision of positive gas ions to the cathode and γ_e is a measure of how many secondary electrons are released per each positive gas ion striking the cathode (target surface). The secondary electrons increase the ionization of the gas molecules and generate a self-sustained discharge. The contribution of the secondary electrons in the current density between the electrodes is more important in the presence of reactive gas molecules in a reactive sputtering process. For breakdown of gas into the plasma, the current must go to infinity and the denominator of the Eq. 3.1 goes to zero. With this assumption and inserting α into the Eq. 3.1 the breakdown voltage (V_B) can be written as following [129, 130]:

$$V_\mathrm{B} = \frac{\frac{V_\mathrm{i}}{q} \times \frac{d}{\lambda}}{ln(\frac{d}{\lambda}) - ln(ln(\frac{\gamma_\mathrm{e}+1}{\gamma_\mathrm{e}}))} \tag{3.3}$$

Since mean free path is inversely related to the gas pressure $(1/P)$ the Eq. 3.3 can be written as what is known as Paschen's law [129, 130]:

$$V_\mathrm{B} = \frac{A_1 P.d}{ln(P.d) + A_2} \tag{3.4}$$

The Paschen's Law can predict that there must be a minimum in the V_B versus the product of the pressure and the electrode distance $(P.d)$. If the value of $P.d$ is low, only a few collisions happen between electrons and gas molecules so the breakdown voltage will increase. By increasing $P.d$, V_B is reduced until the point that due to the mean free path in the gas it becomes necessary to apply a greater electric field so that electrons have enough energy to ionize gas molecules. Therefore we can say V_B rises with increasing $P.d$.

There are three stages of plasma according to the applied discharge current density. During the initial stage of plasma formation, we are in the "Townsend discharge" region where space charge is formed but not dominant. Once the breakdown voltage is reached because of impact ionization with secondary electrons, the plasma becomes self-sustaining. This is called "normal glow regime" since the plasma has a characteristic glow due to photons generated as a result of recombination of electrons with ions and is sustained at higher current and lower voltage. In the normal glow regime, the current through the plasma is almost independent of the voltage. By increasing power through the plasma, the "abnormal discharge regime" is reached where current and voltage increase together which is the regime used for sputtering process. By further increasing the power, heating of the electrodes (e.g. in case of improper cooling) and thermionic emission will cause arcing and low voltage current transport. The plasmas formed in laboratory systems are often cold which means that the electron, ion, and gas subsystems are not in thermal equilibrium. The effective temperature of electrons are higher than that of ions and neutrals (with characteristic temperatures of 20,000 K, 500 K and 293 K , respectively). As a result electrons will have velocities up to three times more than ions. Both ions and electrons will hit the chamber walls but because of higher electron velocity the surfaces in contact to the plasma receive more electron current than ion current. This gives rise to the formation of a lower potential at chamber site compared to the body of plasma grounding the chamber walls. Afterwards, the plasma becomes self-biased to a positive potential which encourages ion current and prohibits further charging of the chamber walls. The self biasing voltage for a DC plasma can be obtained using the following relation [129, 130]:

$$V_\mathrm{P} = \frac{k_\mathrm{B} T_\mathrm{e}}{q} \ln(\sqrt{\frac{m_\mathrm{g}}{2\pi m_\mathrm{e}}}), \tag{3.5}$$

in which T_e is the electron temperature (in K), k_B is the Boltzmann's constant, m_g and m_e are gas atomic mass and electron mass, respectively. Considering T_e of 20000 K and Ar atomic mass, Eq. 3.5 will give a plasma potential of 8 Volts.

The transition region between the plasma and the wall with lower potential is called the "*sheath*". The width of sheath region is in relation with the Debye length (screening length) for isolated charge in a plasma which in turn is proportional to the square root of the effective temperature of involved species [129, 130, 132]:

$$\lambda_D = \sqrt{\frac{\epsilon_0 K_\mathrm{B} T}{n_\mathrm{i} q^2}} \tag{3.6}$$

For a constant number of positive ions, n_i, the screening happens by high concentration of electrons around the charge. The sheath width can be calculated with the following equation:

$$d_\mathrm{sheath} = \frac{\sqrt{2}}{3}\lambda_\mathrm{D}\left(\frac{2q(V_\mathrm{P}-V)}{k_\mathrm{B}T}\right)^{\frac{3}{4}} \tag{3.7}$$

The edge of the glowing plasma and the electrode effectively form parallel plates separated by a distance d_s. When the mean free path in the gas is longer than the distance between electrodes, the Child-Langmuir equation can be used to drive current-voltage relations in DC plasma at low pressure [129, 130]:

$$\frac{I}{A} = \frac{4\epsilon_0}{9d_\mathrm{s}^2}\sqrt{\frac{2q}{m}}(V_\mathrm{P}-V)^{\frac{3}{2}}, \tag{3.8}$$

in which I is total current, A is electrode area, q is electron charge and m is mass of charge carrier.

3.1.1 DC sputtering

In a common laboratory DC sputtering machine, a metallic target sits in the cathode place and we put a substrate in the anode place. The chamber is filled with argon gas at a pressure higher than the deposition pressure to make it possible to spark a plasma by lowering the breakdown voltage to a level accessible by normal power supplies. Then a plasma can be established by applying a DC power to the electrodes. After plasma ignition, the pressure is reduced and sputtering takes place at the cathode site. First, Ar gas molecules in glowing region will collide with high energy electrons and become ionized. Afterwards, these ions with starting potential V_P at plasma are accelerated towards the cathode by facing the sheath between the target and the plasma. When they reach the target they have a new potential V and so their potential has decreased by the amount of $|(V-V_\mathrm{P})q|$. They will transfer some of this energy to the target while striking the surface and this impingement will remove some atoms from the target, part of which will be deposited on the substrate. The number of atoms reaching the substrate per impinging ion is defined by the *sputtering yield*.

The sputtering yield depends on the mass and energy of the bombarding ions as well as the mass of material in the target. Other factors such as crystallinity and the angle of incidence also affect the sputtering yield. The impinging ions must have sufficient energy higher than the binding energy of the target material in order for sputtering to happen (it can be up to 50 eV). When the ion energy is low, the sputtering yield will increase with square root of the ion energy [132].

This increase will continue until energies are around ∼ 10 keV. By further increasing the ion energy, ions will be implanted in the target and the yield first settles and then will even start to decrease. In addition, the angle at which the ions impinge the target also affects the sputtering yield. If θ would be the angle between ion velocity vector and the surface normal of the target, the yield is a function of $\frac{1}{cos\theta}$. The energy of sputtered particles is described by Thompson's formula and does not depend on the ion energy [133]. By increasing the sputtering voltage the yield will increase but it has no effect on the energy of the sputtered particles. However, the energy of sputtered material depends on the surface binding energy (U_b) and it is maximum at a value reaching half of the surface binding energy [133].

The currently accepted theory for the sputtering yield (S_Y) from collision cascades is suggested by Sigmund and predicts the sputtering yield for two different ranges of threshold energy as in the following equations [131, 133, 134]:

$$S_\mathrm{Y} = \frac{3\alpha}{4\pi^2}\frac{4M_\mathrm{i}M_\mathrm{t}}{(M_\mathrm{i}+M_\mathrm{t})^2}\frac{E_\mathrm{th}}{U_\mathrm{b}}(E_\mathrm{th} < 1\,keV) \tag{3.9}$$

$$S_\mathrm{Y} = 3.56\alpha\frac{Z_\mathrm{i}Z_\mathrm{t}}{Z_\mathrm{i}^{\frac{2}{3}}+Z_\mathrm{t}^{\frac{2}{3}}}(\frac{M_\mathrm{i}}{M_\mathrm{i}+M_\mathrm{t}})\frac{S_\mathrm{n}(E)}{U_\mathrm{b}}(E_\mathrm{th} > 1\,keV) \tag{3.10}$$

where M_i and M_t are the atomic mass, and Z_i and Z_t are atomic numbers of the incident ion and target atom, respectively. E_th is the threshold energy and U_b is the surface binding energy. The factor α is a measure of momentum transfer efficiency during collision. It is a function of $M_\mathrm{i}/M_\mathrm{t}$ ratio and also embeds the effect of ion impact angle (relative to surface normal of target). The factor $S_\mathrm{n}(E)$ is called "reduced stopping power" and is a measure of energy loss per unit length due to nuclear collisions. At low energies, it depends on the energy, mass and atomic number of involved atoms. To reach reasonable deposition rates, it is necessary to apply high pressure during DC sputtering process. This is an issue since high pressure can lead to random motions and severe energy loss by scattering for both ions and sputtered particles; specifically if the pressure is so high that the cathode sheath width exceeds the mean free path of ions. This can deteriorate film morphology and decreases the deposition rate.

3.1.2 Magnetron sputtering

Magnetron sputtering is the most widely used commercial sputtering method and it is designed to overcome the issue with necessity of high gas pressure in DC sputtering to have high deposition rate. As the name stands for, a magnetron is involved by which a field is applied perpendicular to the direction of electric field between the electrodes. To do so, a magnet or electromagnet is placed on the back of the sputtering target. In the absence of such magnetic field, electrons would be accelerated towards anode taking a straight path. However, under the field they will follow a helical path which increases the probability of collision ionization and will trap the secondary electrons in target (cathode) vicinity. Under magnetic field, the electrons move perpendicular to both the magnetic field and the electric field. This leads to a higher current density between the electrodes at a specific pressure and target voltage, or in the other word, it is possible to establish the same current as for the DC sputtering but at a lower pressure. It preserves energy of sputtered particles because of the low necessary pressure and it brings advantages including extending the operating vacuum level and a reduced electron bombardment at the substrate [131]. On the other hand, the secondary electron yield is essentially reduced since these electrons are confined to the target vicinity and can be recaptured by the magnetron at the cathode. However, because of the presence of the magnetron, a higher plasma density is achieved and so more ions are produced per each secondary electron compensating for the lower secondary electron yield.

3.1.3 RF sputtering

For metallic targets, it is possible to drive a DC current through the target, although if we need to sputter from an insulator target which has low conductivity, it does not work because of the positive ions (Ar^+) accumulation on the surface of insulating target. To avoid this issue, an AC power must be used instead of DC power, so that during each cycle with positive electric field the positive ions are accelerated toward the surface of target and sputter it. This is followed by a cycle with negative field where the charged positive ions on the surface of target will be removed. In RF sputtering, the plasma ignition is easier since RF oscillating fields can more efficiently transfer energy to the electrons and there is no need for secondary electrons to maintain the plasma. Moreover, the oscillating electrons are more efficient for ionization of the gas molecules and so the RF sputtering is capable of running in lower pressure (1-15 mTorr) meaning fewer gas collisions are needed.

If applied frequencies are less than 50 kHz, both electrons and ions can follow the switching of the anode and cathode, and therefore it leads to DC sputtering of both surfaces. On the other hand, if the applied frequencies are well above 50 kHz, ions which are heavy can no longer follow the switching. Thus, electrons can neutralize positive charge build-up on each electrode during each half cycle. Therefore, due to the AC nature of applied RF voltage both electrodes will be sputtered, if we have a symmetric target-substrate configuration. To tackle this issue, insulating sputtering target must be capacitively coupled to the RF generator. In this way, we have two series capacitors, one in sheath region of target and the other one at the substrate. Since capacitive reactance is inversely proportional to capacitance which in turn is proportional to area, thus more voltage drop happens at the capacitance with smaller area. Consequently, the target electrode must be made smaller in area than the other electrode attached to the substrate, chamber wall and the system ground. There is a fourth power dependence between the ratio of area for the two electrodes and the ratio of voltages across them [131]:

$$\frac{V_\mathrm{t}}{V_\mathrm{s}} = (\frac{A_\mathrm{s}}{A_\mathrm{t}})^4, \tag{3.11}$$

which means a large A_s is required in order to effectively increase the voltage drop at target sheath and decrease the ion bombardment at the substrate site.

3.1.4 Sputtering of alloys

One advantage of the sputtering method compared to evaporation is that sputtering allows to preserve the starting stoichiometry of the alloy target material in the deposited film. The first reason is that although each element in the alloy starting material will evaporate with different vapour pressure and will be sputtered with different yield, the difference in the vapour pressure is more significant than the slight difference in the sputtering yield. The more important reason is that due to the rapid atomic diffusion and convection the melts homogenize readily while in sputtering the minimal solid state diffusion enables maintaining of the targeted composition [131].
If we consider a binary alloy target containing n_A of A atoms and n_B of B atoms with total number of atoms $n = n_\mathrm{A} + n_\mathrm{B}$, the concentration of A and B elements in the alloy target would be $C_\mathrm{A} = \frac{n_\mathrm{A}}{n}$ and $C_\mathrm{B} = \frac{n_\mathrm{B}}{n}$, respectively. The ratio of initial atomic flux (Ψ) would be [131]:

$$\frac{\Psi_\mathrm{A}}{\Psi_\mathrm{B}} = \frac{C_\mathrm{A} S_\mathrm{A}}{C_\mathrm{B} S_\mathrm{B}} \tag{3.12}$$

If during the sputtering process the target is impinged by n_g gas atoms, the total number of ejected A and B atoms from the target surface would be $n_\mathrm{g} C_\mathrm{A} S_\mathrm{A}$ and $n_\mathrm{g} C_\mathrm{B} S_\mathrm{B}$, respectively. This results in a target surface composition modification of:

$$\frac{C'_\mathrm{A}}{C'_\mathrm{B}} = \frac{C_\mathrm{A}}{C_\mathrm{B}} \frac{1 - n_\mathrm{g} S_\mathrm{A}/n}{1 - n_\mathrm{g} S_\mathrm{B}/n} \tag{3.13}$$

If $S_\mathrm{A} > S_\mathrm{B}$, the concentration of atom B is greater at the target surface and therefore it will be sputtered more:

$$\frac{\Psi_\mathrm{A}}{\Psi_\mathrm{B}} = \frac{C'_\mathrm{A} S_\mathrm{A}}{C'_\mathrm{B} S_\mathrm{B}} = \frac{C_\mathrm{A} S_\mathrm{A}}{C_\mathrm{B} S_\mathrm{B}} \frac{1 - n_\mathrm{g} S_\mathrm{A}/n}{1 - n_\mathrm{g} S_\mathrm{B}/n} \tag{3.14}$$

The sputtered flux ratio will change with the continuous change in the target surface composition and alters until it is equal to $\frac{C_\mathrm{A}}{C_\mathrm{B}}$, same as the starting target composition. At the same time the target surface composition reaches $\frac{C'_\mathrm{A}}{C'_\mathrm{B}} = \frac{C_\mathrm{A} S_\mathrm{B}}{C_\mathrm{B} S_\mathrm{A}}$ which is maintained thereafter. This creates a steady-state transfer of atoms from the bulk of the target to the plasma which results in stoichiometric film deposition until the whole target is consumed. The above discussed circumstance necessitates conditioning of the target surface before the deposition to establish a steady state of composition by sputtering a few hundred atom layers [131].

3.2 Thin film deposition: structural zone model (SZM)

The first attempts toward characterization of coatings deposited by PVD process was taken by Movchan and Demchishin in 1969 which helped them to discover the effect of ad-atoms mobility as a function of deposition temperature on microstructure of deposited films [135]. They have developed the basic ideas behind what is today called *structural zone model* (SZM). Based on the SZM, morphology and microstructure of deposited films can be predicted regardless of type of elements involved only by taking into account the energy supplied to the ad-atoms by different mechanisms such as thermal energy, ionic bombardment or chemical reactions at the substrate. The structural zone model based on Movchan and Demchishin's research on Ti, Ni, ZrO_2 and Al_2O_3 films suggested that there are three different structure zones as a function of normalized deposition temperature ($\frac{T_\mathrm{s}}{T_\mathrm{m}}$ where T_s is substrate temperature and T_m is melting temperature of target material).

In the low-temperature zone or zone 1 with $\frac{T}{T_\mathrm{m}}$<0.3, the film structure consists of tapered columns with porous morphology and weakly bonded grains which corresponds to a low ad-atom mobility. This means that not only the diffusion is low, but also the varying velocity and incident angle of the ad-atoms on the substrate leads to some atomic shadow effects. In zone 2 with 0.3<$\frac{T}{T_\mathrm{m}}$<0.5, the surface diffusion becomes dominant and the resulted film contains straight columnar grains with smooth surface topography and better binding to other columnar grains. At zone 3 with higher temperatures ($\frac{T}{T_\mathrm{m}}> 0.5$), bulk diffusion is the dominant process and the produced structure consists of equiaxed grains caused by grain growth and re-crystallization [137].

In 1974 Thornton modified the model considering the effect of final working pressure into the zone classification. The reason is that this growth parameter has a twofold effect on the film structure. First, working pressure of sputtering gas will change kinetic energy of ions arriving at the substrate. Secondly, it can also affect the mean free path of particles decreasing or increasing the bombardment of the substrate surface which in turn can control mobility of ad-atoms on the substrate. In Thornton's model, a transitional zone (T zone) has been added between the first and second structural zones for which the resulting grain are denser and their surfaces are less rough than the two other zones [136].

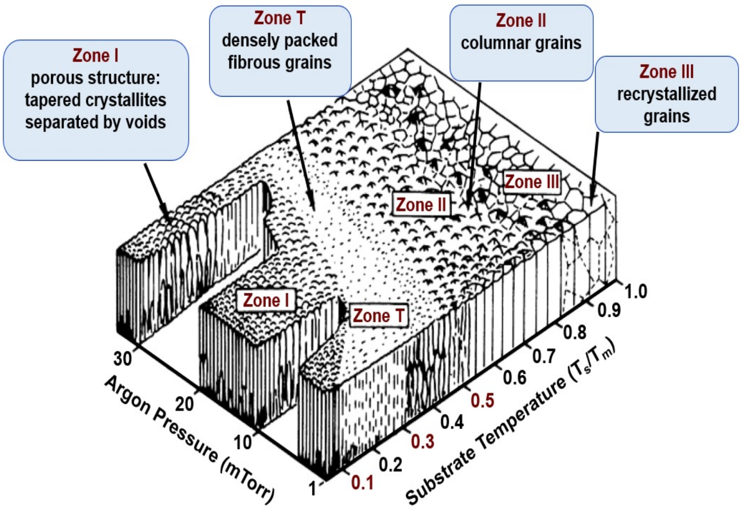

Figure 3.1: Thornton zone model, adapted from Ref. [136].

Moreover, in 1984 Messier and Giri realized that in thin films of TiB_2, BN and SiC a non-linear limit must be considered between the first zone and T zone, which is a function of the bias voltage applied to the substrate. Such a bias voltage plays the same role as for the substrate temperature and so by increasing the bias voltage the first zone shrinks and the transition (T) zone expands which leads to having denser films with higher crystallinity. In addition, they have replaced the pressure axis of Thornton model with the net bombardment energy from sputtered material, reflected neutral species and ion bombardment. They claimed that the bombardment energy encloses the effects of higher pressure and allows for other considerations like intentional bombardment as well [138].

For alloy films if the composition of one of the elements is sufficiently high compared to the other element, the structural zone model is as described for high purity one-component films [139]. Barna *et. al.* has shown that alloying elements (impurities) play important role in structure formation of polycrystalline films and to describe effect of impurities on film structure they developed a so called "real structural zone model" [139]. In this model, both zone 1/zone T and zone T/zone 2 boundaries are shifted to higher temperatures due to limited grain boundary mobility caused by impurities which can result in disappearance of both zone 2 and zone 3 in case of high impurity concentrations.

In case of reactive sputtering, effect of power and gas flow on the resulting texture in the grown film is also considerable. Generally, the degree of crystallinity will increase with applying higher power to the target during growth of sputtered films [128]. There are three models suggested to explain the preferential growth direction in thin films: a) the thermodynamic model [140], b) the kinetic model [141], and c) the atomic model [142]. In the first model, the preferential orientation is defined by the thermodynamic equilibrium reached by minimizing the total energy of the system. The total energy (W_{hkl}) is considered as the sum of the surface energy (S_{hkl}), deformation energy (U_{hkl}) and passivation energy (S_{hk}) as a result of unsaturated bonding at the surface. The surface energy can be calculated as as function of the sublimation energy (ΔH), the number of unsaturated bondings per atom at (hkl) plane (N_{hkl}), and the amount of coordination among neighbours (Z) (excluding the effect of impurities) [143]:

$$S_{\mathrm{hkl}} = \frac{\Delta H N_{\mathrm{hkl}}}{Z} \tag{3.15}$$

Considering only two dimensions, deformation energy U_{hkl} is related to intrinsic phenomena in the film and can be calculated by:

$$U_{\mathrm{hkl}} = \epsilon_{\mathrm{hkl}}^{2} E_{\mathrm{hkl}}(1-\mu) \tag{3.16}$$

where $\epsilon_{\mathrm{hkl}}^{2}$ shows elongation along the (hkl) plane of the film, E_{hkl} is the elastic module along the (hkl) plane, and μ is the Poisson's ratio. Depending on the material system, one of this energy terms (S_{hkl} or U_{hkl}) can be dominant for one specific orientation (hkl) and the other direction could be favourable based on the other energy term; however, the minimum total energy (W_{hkl}) resulted from their competition finally determines the resulting texture of the grown thin film. This minimum energy can be affected also by the thickness of grown film since the deformation energy (U_{hkl}) will change as a function of thickness which could affect the final texture in the film.

Kinetic model suggests that the kinetic energy and flow of the ions are also involved in the orientation of the grown film. For example in case of TiN [111], the [111] orientation is resulted from the low mobility of ad-atoms. Therefore, if the ad-atoms mobility is increased, either by substrate temperature or increasing ion to atom flow rate ratio, the texture could change to [200] orientation [141].

There is also an atomistic model which proposes that in thin films which are deposited at high temperatures the thermodynamics control the orientation of the grown film in favour of the planes with low energy, i.e. the (200) planes. According to this model, the degree of ion bombardment is influenced by the flow ratio between the density current of the ions and the density current of the atoms ($\frac{J_{\mathrm{i}}}{J_{\mathrm{a}}}$) and the ion energy ($E_{\mathrm{i}}$) which both are dependent on the pressure, substrate target distance and substrate bias [144, 145, 146, 147]. There is an energy parameter E_{P} suggested as the energy deposited per dense particle which combines both the ion energy and the flow. This mobility parameter is defined as follows with the E_{i} as the incident energy of the ions [143]:

$$E_{\mathrm{P}} = \frac{J_{\mathrm{i}}}{J_{\mathrm{a}}} \times E_{\mathrm{i}} \tag{3.17}$$

The incident energy of the ions can be calculated from the plasma potential (V_{p}) and substrate bias (V_{s}) and the elementary charge (e) as: $E_{\mathrm{i}} = e(V_{\mathrm{s}} - V_{\mathrm{p}})$.

3.3 Thin film deposition: physical mechanisms of growth

The whole deposition process in general can be divided into six steps [148]. In the first step, all the species (atoms and molecules) reaching the surface must be adsorbed to the surface (i). In the next step, these adsorbed species follow a surface diffusion to meet other adsorbed species and cluster to start the film growth (ii). Adsorption of species can happen in two different ways, either by physisorption or chemisorption. By physisorption the atom forms weak bond to the surface and can easily diffuse on the surface to minimize its surface energy. The second possibility is a chemisorbed atom which will form stronger bond to the surface. The initial stage of growth starts with the meeting species either reacting with the substrate surface or one another (iii), and the subsequent formation of agglomerates or nucleation (iv). Proceeding with the film growth, the formed aggregates or nuclei connect to each other and form a network and finally coalesce and show a new rough crystal structure (v). The resulting film can be amorphous, polycrystalline or single crystalline depending on the growth conditions and more importantly the crystallinity and lattice fitting of substrate with respect to the film. If the film imitates the crystal order of a single crystal substrate, it is called "epitaxial growth". In the last step bulk diffusion occurs (vi) which can be improved by post-annealing of the film at higher temperatures either in vacuum or a certain atmosphere to enhance the film properties. The film quality can be improved also by application of other energy sources such as ion bombardment to increase the reactivity between film and substrate material [149, 150].

A summary of these processes is schematically illustrated in Fig. 3.2. When an atom in the plasma is adsorbed on the substrate surface (a), it will first diffuse on the surface (b). If there has been already an island formed on the surface the arriving atom can hop on this island atoms (c). Another possibility is that the adsorption happens directly on the island (d) which can cause an atom in the island to be desorbed from the surface (e). The additional energy needed for last event can be provided to the film by thermal energy or ion bombardment. If the energy is enough, atoms can also diffuse into the substrate (f).

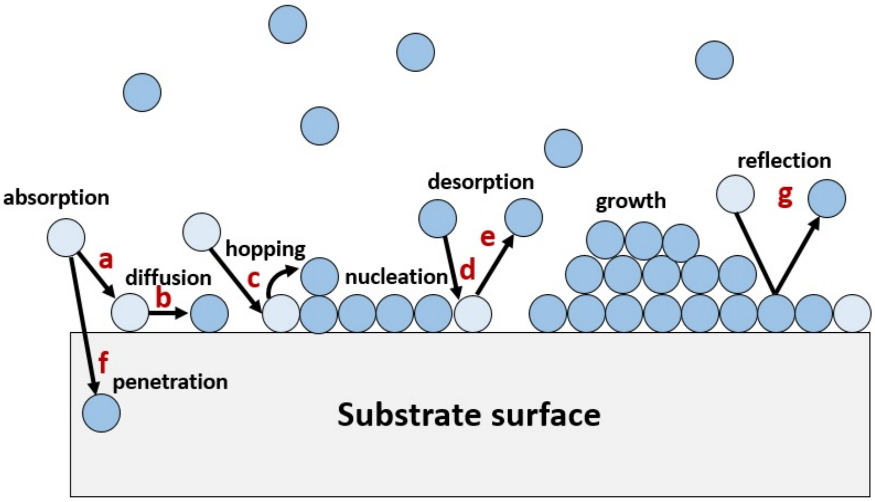

Figure 3.2: Illustrations of the events which happen during a typical vapour-phase thin film growth process.

With the help of X-ray diffraction, optical diffraction and mainly electron diffraction studies, it is feasible to establish three main physical mechanisms involved in the nucleation and growth of thin films over the substrate. These three categories are assigned based on the thermodynamic parameters of the growth and the surface interaction between the ad-atoms and the substrate material [151, 152]. The three basic modes are: (1) Frank-Van der Merwe model (2D layer by layer growth), (2) Volmer-Weber model (island growth), and (3) Stranski-Krastanov model (3D growth). Fig. 3.3 summarizes each of these growth modes schematically. The film growth starts with nucleation of ad-atoms (deposited material) onto the substrate followed by nucleation or agglomeration of particles by formation of chemical bonds to each other on the substrate. As this nuclei grows, an interface is formed between the substrate and deposited film particles. The growth of nuclei is governed by surface energies of substrate, film, the interface between them as well as a misfit energy derived from lattice mismatch between the substrate and film material [152].

The Frank and Van der Merwe growth mode happens if the misfit energy is small and sum of the surface energies of the film and the interface are smaller than the surface energy of the substrate. In this case, substrate is fully wetted by the film material deposited on top of it. At the beginning of the nucleation a monolayer island of the deposit forms on the substrate. Afterwards, the monolayers grow together and a complete continuous monolayer is formed. This growth process is repeated in a layer by layer manner. This is because the interaction between the substrate and the ad-atoms is stronger than that between the neighbouring ad-atoms [152].

In the second model suggested by Volmer and Weber, which includes also effect of the misfit energy, the surface energy of the substrate is less than the sum of the surface energies of the film, and the interface plus the misfit energy. This means that for an equilibrium of the total surface energy, the nucleation of film material on the substrate happens in the form of separate islands to minimize the interface energy resulting in a three-dimensional growth, while the rest of the substrate is devoid of any condensed phase. The number of nuclei and the size of a given nucleus increase until the nuclei grows in size and they intersperse with each other to form a continuous film [152].

The third growth model suggested by Stransky and Krastanov (S-K) is a combination of the two first growth modes. The S-K nucleation is common with metal on metal deposition and at low temperatures where the surface mobility is low. In this model, the sum of the surface energies of the film and the interface plus the misfit energy is less than the substrate surface energy at the beginning of growth. This leads to the nucleation and growth in the layer by layer manner, so that a finite number of monolayers are produced. However, as the film grows in thickness the lattice misfit energy also grows, which results in increasing of the sum of energies over the surface energy of the substrate, therefore the three-dimensional growth follows the layer by layer growth at a critical thickness. Subsequently, formation of the film continues by formation of the separate nuclei [152].

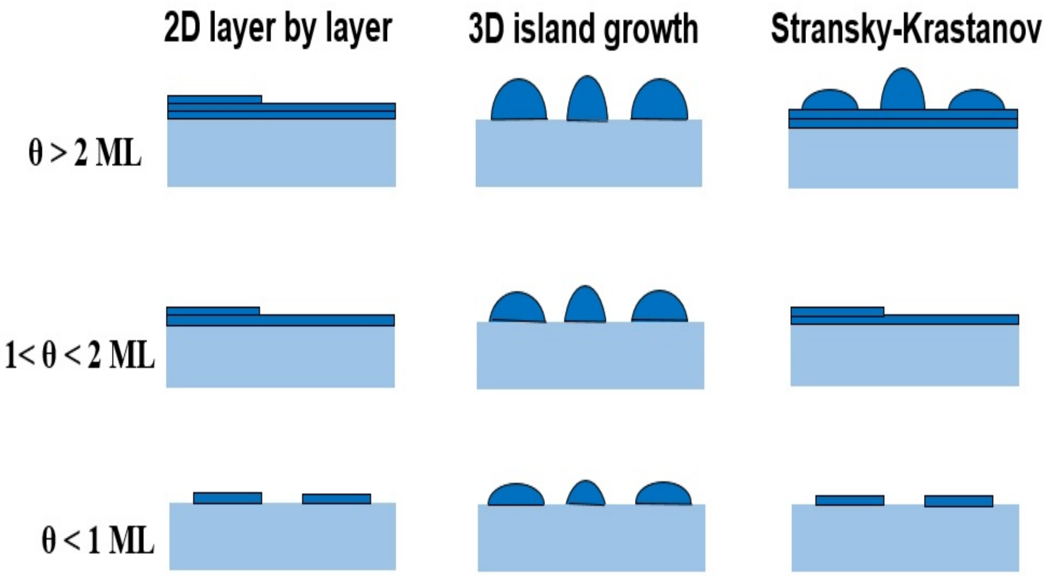

Figure 3.3: Illustrations of the three main growth modes at different levels of film coverage (θ).

Depending on the governing surface energies of the growing film and the used substrate, the film can grow in different ways. Although among the three different growth modes described above normally the most desired growth mode is the 2D or the layer-by-layer mode since it will result in the least amount of structural defects in the sample. Based on this, the grown films can be classified into following categories according to the different resulting crystal morphologies and atomic order:

- Epitaxial: In this case, there is a definite orientation relationship between the film grains and the substrate which results in a long range structural order in the film grains. A perfect epitaxial growth means the growth of an ideal single crystalline layer with no defects which is perfectly fixed to lattice registry on the single crystal substrate beneath. However, in most real cases the film might have slight deviations from this ideal case showing some defects in the form of dislocations or small tilts between different crystalline grains with the same orientation.

- Textured: In this case, while growing the structurally ordered grains align themselves along a certain preferential orientation.

- Polycrystalline: In this case, the grown layer consists of randomly oriented grains with a certain crystalline order within each grain.

- Amorphous: In this case the film does not show any long range order.

3.4 Thin film deposition: Thermodynamics of growth

To discuss the thermodynamics of the film growth we first assume the clusters to be spherical for simplicity. Considering spherical clusters with ΔG_{v} as free energy of nuclei per unit volume, and γ as the surface tension, the total energy to create a surface is equal to $4\pi r^2\gamma$ and the total energy to form a stable phase is $\frac{4}{3}r^3\Delta G_{\mathrm{v}}$. Thus the total free energy can be written as following [151, 152]:

$$\Delta G_{\mathrm{total}} = 4\pi r^2\gamma + \frac{4}{3}r^3\Delta G_{\mathrm{v}} \tag{3.18}$$

To find the critical cluster size needed for the maximum free energy change we need to plot $\Delta G_{\mathrm{total}}$ vs. cluster radius (r) (see Fig. 3.4) and look for $d(\Delta G_{\mathrm{total}})/dr = 0$. This gives a critical radius proportional to $\frac{\gamma}{|\Delta G_{\mathrm{v}}|}$ as shown below [151, 152]:

$$r^* = \frac{-2\gamma}{\Delta G_{\mathrm{v}}} \tag{3.19}$$

The resulting nucleation barrier can be estimated by substituting r^* into the Eq. 3.18 as [151, 152]:

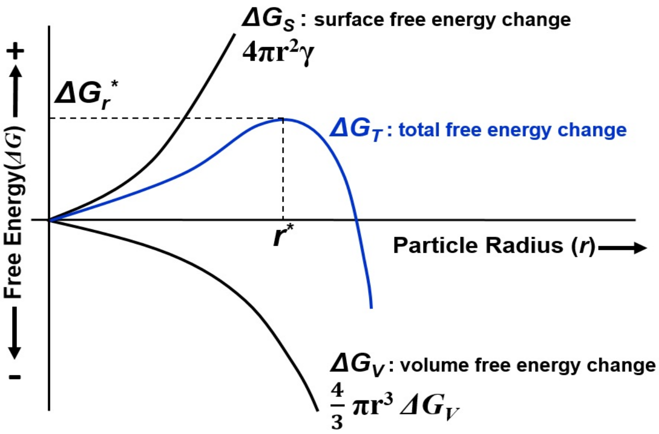

Figure 3.4: Free energy as a function of particle radius, adapted from Ref. [152].

$$\Delta G^* = \frac{16\pi\gamma^3}{3(\Delta G_{\mathrm{v}})^2} \tag{3.20}$$

This means that a cluster with its radius larger than the critical radius (r^*) is stable and can form a nuclei. In case of a cubic nuclei with size X since the surface to volume ratio of atoms is larger, the above extracted formulas will change as following [151, 152]:

$$\Delta G_{\text{total}} = 6X^2\gamma + X^3\Delta G_{\text{v}} \tag{3.21}$$

$$X^* = \frac{-4\gamma}{\Delta G_{\text{v}}} \tag{3.22}$$

$$\Delta G^* = \frac{32\gamma^3}{(\Delta G_{\text{v}})^2} \tag{3.23}$$

If we consider nucleation on a surface as a thermodynamic equilibrium process between the vapor phase with pressure P and the forming cluster, the first and second law of thermodynamics can be combined together and $d\Delta G$ can be written as following relation for addition of one adatom to this cluster with respect to the pressure and temperature of equilibrium system [151, 152]:

$$d\Delta G = Vdp - SdT \tag{3.24}$$

In this equation S is entropy and V is the volume. If we apply a constant substrate temperature T_{s} then the second term of above equation SdT would be equal to zero. Then the ΔG is only a function of volume and pressure of the system. According to the ideal gas law at constant temperature, T_{s}, we have $PV = nkT_{\text{s}}$. Substituting this in the Eq. 3.24 gives [151, 152]:

$$d(\Delta G)_{T_s} = nkT_s(\frac{dP}{P}) \tag{3.25}$$

By the addition of one atom to the cluster we overcome the energy barrier by increasing the size over the critical radius and increased volume of cluster will be equal to the volume of this additional atom (ΔV). Then ΔG_{v} is $\frac{\Delta G}{\Delta V}$ and we get [151, 152]:

$$d(\Delta G_{\text{v}})_{T_s} = \frac{KT_s}{\Delta V}(\frac{dP}{P}) \tag{3.26}$$

$$d(\Delta G_{\text{v}})_{T_s} = \frac{KT_s}{\Delta V}\ln(\frac{P}{P_{\text{vp}}}) \tag{3.27}$$

In which P_{vp} is the vapour pressure of solid phase in substrate temperature of T_{s}. The ratio of $\frac{P}{P_{\text{vp}}}$ is proportional to the ratio of fluxes $\frac{J}{J_{\text{vp}}}$ of the atoms which arrive at the surface and the atoms which are desorbed from the surface. We can replace this ratio in the Eq. 3.19 with a new quantity ζ (supersaturation) and then derive an equation to calculate the critical radius [151, 152]:

$$r^* = \frac{2\Delta V\gamma}{kT_s\ln(\zeta)} \tag{3.28}$$

This equation shows that the critical radius is inversely proportional to the substrate temperature and to $\ln(\zeta)$. So if substrate temperature T_s increases, the critical radius decreases which means that small clusters are easy to dissociate due to their low E_{coh}. Besides, increasing the substrate temperature will increase the surface diffusion or nucleation length. If substrate temperature stays constant and J increases because of an increased supersaturation the critical radius decreases.

3.5.1 X-ray analysis: The $2\theta - \theta$ scan

For X-ray diffraction analysis a beam of X-rays, i. e. electromagnetic waves, are generated in an X-ray source. The resulting X-ray mainly interacts with the electrons in the specimen either by an elastic or inelastic scattering event, or the photon can be fully absorbed by the material [153]. The X-ray wavelengths are in the order of sub-atomic distances, i. e. $\lambda \sim$ a few tenth of Å. A simplified assumption would be to exclude all other interactions and assume that X-rays only interact with the electron density of the atoms in the sample via elastic scattering. Measuring scattering events using X-ray waves gives patterns which can be correlated to the ordering of atoms within the material or the crystal lattice structure of the sample.

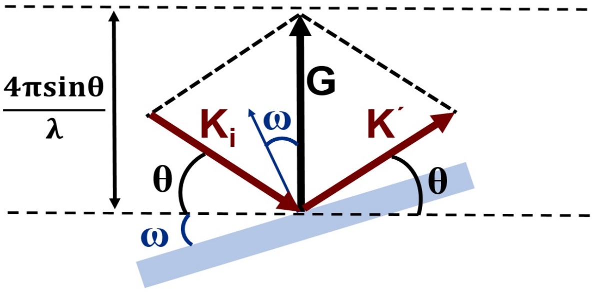

Figure 3.5: A schematic of elastic X-ray scattering event, adapted from Ref. [158].

Fig. 3.5 shows a schematic of an X-ray beam involved in an elastic scattering event with geometrical relationship between the incident wave vector, the scattered wave vector and the scattering wave vector. The wave vector K resembles X-ray beam in space which can be related to X-ray wavelength (λ) through $K = 2\pi/\lambda$ neglecting the magnetic field effect. During and elastic scattering event, the X-ray photon will keep the same momentum and only adopts a different direction. The change in the momentum of the scattered x-ray photon G in case of an elastic scattering is as below:

$$G = K' - K_i, \tag{3.29}$$

in which K_i is the incident vector and K' is the scattered vector. Since the scattering is an elastic one, the momentum is conserved: $|K_i| = |K'|$. Therefore, the relation between the G (scattering vector) and θ (scattering angle) becomes:

$$|G| = \frac{4\pi sin\theta}{\lambda} \tag{3.30}$$

Only if the scattering vector is equal to a reciprocal space vector of the crystal system it will result in a constructive interference of the incident wavevectors with the crystal lattice [154]. Such a constructive interference was first discussed by W. L. Bragg (in 1912) who has shown that the necessary condition for occurrence of constructive interference is when [155, 156]:

$$n\lambda = 2d_{\mathrm{hkl}} sin\theta, \tag{3.31}$$

where, as illustrated in Fig. 3.6, d is the distance between the neighbouring atomic planes, λ is the wavelength of the X-ray, n is the order of the diffraction, and θ is the angle of incident of the wavevector with respect to the atomic plane.

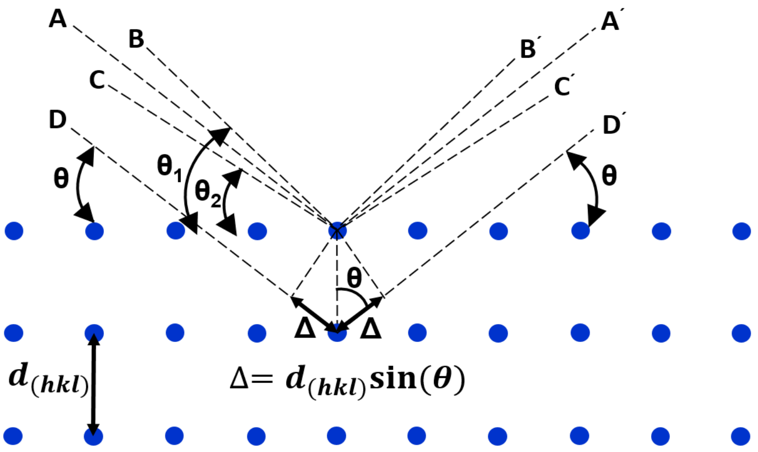

Figure 3.6: A schematic geometrical derivation of the Bragg law. X-rays strike the successive atomic planes in a crystal which have been separated by the distance of d. In case of constructive interference of all scattered X-rays the extra distance that the X-ray travels from each plane is equal to an integer multiplication of the X-ray wavelength λ, adapted from Ref. [158].

There is also a general relation to predict the diffraction angle for any set of planes which is obtained combining the Bragg law and the plane-spacing equation which is applicable to the specific crystal structure. If the crystal is *cubic* we have [157]:

$$\frac{1}{d^2} = \frac{h^2 + k^2 + l^2}{a^2} \tag{3.32}$$

combining the above equation with the Bragg equation will give [157]:

$$sin^2\theta = \frac{\lambda^2}{4a^2}(h^2 + k^2 + l^2) \tag{3.33}$$

With this equation, we can predict all the possible Bragg angles at which diffraction can occur from the planes (hkl) for a specific incident wavelength, λ, and a specific cubic crystal of unit cell size, a.

If the crystal is *tetragonal* with axes a and c, the corresponding general equation would be as follows [157]:

$$sin^2\theta = \frac{\lambda^2}{4}(\frac{h^2 + k^2}{a^2} + \frac{l^2}{c^2}) \tag{3.34}$$

And in case of a *hexagonal* crystal structure with a and c axes we have [157]:

$$sin^2\theta = \frac{\lambda^2}{3}(\frac{h^2 + hk + k^2}{a^2}) + \frac{\lambda^2}{4}(\frac{l^2}{c^2}) \tag{3.35}$$

The 2θ-θ specular scan according to Eq. 3.31 is the most conventional X-ray measurement using the Bragg geometry. The incident and diffraction angles are both altered simultaneously so that the scattering vector stays always perpendicular to the sample surface. The incident and diffracted angles are conventionally called θ and 2θ, respectively. A schematic of such a scan is shown in Fig. 3.7. Typically in X-ray machines, the sample stage stays stationary and X-ray beam and detector are moved simultaneously or independently. Since the detector has to move by the angle that is twice that of the incident

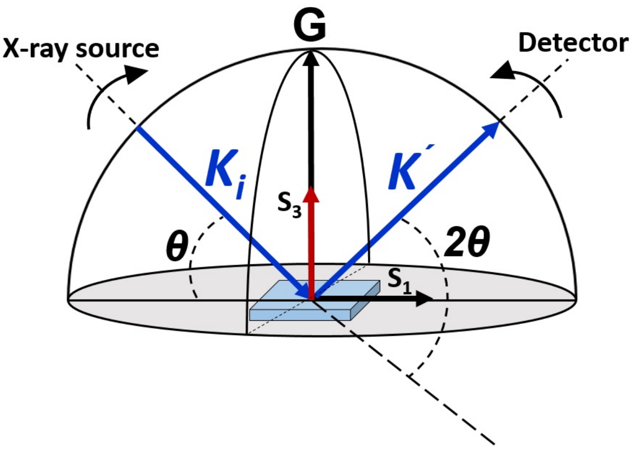

Figure 3.7: A schematic representation of $2\theta - \theta$ XRD scan. K_i and K' are incoming and exiting X-ray beams and G is the scattered vector which is parallel to plane normal s_3, adapted from Ref. [158].

beam, it moves two times faster than the incident beam and the scattering vector remains normal to the sample surface. The 2θ-θ scan can be performed in two main modes. First one is "out-of-plane" measurement to investigate lattice planes parallel to film surface. The second type of 2θ-θ scan is called "in-plane" scan for lattice planes perpendicular to film surface. Moreover, a mixed out-of-plane and in-plane scan is also possible to investigate lattice planes which are neither parallel nor perpendicular to sample surface [158].

Using the out-of-plane scan, we can detect only diffractions from the planes parallel to the film surface and therefore it is mostly used for epitaxially grown or out-of-plane textured films. The quantity measured is intensity of scattered X-rays at position of detector and results of measurement is normally presented in the form of $I(2\theta)$. We are interested in position, intensity and shape of diffracted peaks to gain structural information [158].

3.5.2 X-ray Analysis: Rocking curve (ω scan)

The measurement of a rocking curve is performed in a way that the detector on the 2θ circle is fixed to the center position of $2\theta_0$ for the investigated Bragg peak, while the sample is tilted (rocked) on the θ circle in the vicinity of the Bragg angle (θ_0). Therefore, the θ and 2θ circles are decoupled and θ angle is now called ω which is defined as the deviation from half the scattering angle and is related to the surface normal (s_3) vector as: $\omega = \theta - 2\theta_0/2$. Setting a fixed $2\theta_0$, the scan angle ω is restricted to the range between $-\theta_0$ and $+\theta_0$. If ω angles exceeds this limit, there would be no scattering information because the incoming or exiting beam would decline below the sample surface. The result of such a scan is I(ω) measured at constant scattering angle of $2\theta_0$ varying the ω. Since s_3 remains in the same plane as K_i and K', similar to symmetric $2\theta-\theta$ scan, the rocking curve scan also operates in coplanar geometry [158].

The $2\theta - \omega$ scan is performed to determine the lattice constant as well as the degree of crystal orientation or mosaicity for polycrystalline films. Fig. 3.9 gives an example of rocking curve measurement for a thin film sample with thickness of $t = m.d$. The intensity is maximum at angle θ_0 and will reach zero at both limit angles of θ_1 and θ_2. The width of such broad peak (B) observed between angles θ_1 and θ_2 is usually measured in radians at half of the peak maximum intensity and that is why it is normally referred to as "full width at half maximum" (FWHM). As rough measure, B has following relation with θ_1 and θ_2 [159]:

$$B = \frac{1}{2}(2\theta_1 - 2\theta_2) = \theta_1 - \theta_2 \tag{3.36}$$

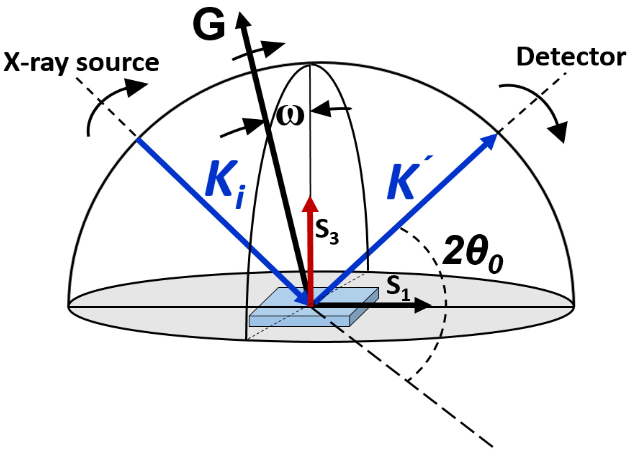

Figure 3.8: A schematic representation of $2\theta - \omega$ rocking curve scan. K_{i} and K' are incoming and exiting X-ray beams and G is the scattered vector which is being rocked in vicinity of surface normal vector s_3, adapted from Ref. [158].

These two different angles have the following path-differences:

$$2tsin(\theta_1) = (m+1)\lambda \tag{3.37}$$
$$2tsin(\theta_2) = (m-1)\lambda \tag{3.38}$$

By subtracting these two equations, we will have:

$$\lambda = t(sin\theta_1 - sin\theta_2) \tag{3.39}$$
$$\lambda = 2tcos(\frac{\theta_1+\theta_2}{2})sin(\frac{\theta_1-\theta_2}{2}) \tag{3.40}$$

Considering that both θ_1 and θ_2 are so close to θ_0, we can make the following approximations:

$$2\theta_0 = \theta_1 + \theta_2 \tag{3.41}$$
$$sin(\frac{\theta_1-\theta_2}{2}) = \frac{\theta_1-\theta_2}{2} \tag{3.42}$$

Using which we can reform the Eq. 3.39 as below:

$$\lambda = 2t\frac{\theta_1-\theta_2}{2}cos\theta_0 \tag{3.43}$$
$$t = \frac{\lambda}{Bcos\theta_0} \tag{3.44}$$

A more exact equation was suggested by Scherrer formula (in 1916) considering a factor K in the nominator of previous equation which for most of the cases is equal to 0.9 as follows [160]:

$$t = \frac{0.9\lambda}{B cos\theta_0} \tag{3.45}$$

This equation is used to estimate particle size of small crystals using the measured width (FWHM(B)) of their diffraction patterns collected by a conventional $2\theta - \omega$ scan. Generally, the lower the FWHM of the Bragg reflection of a ω scan the lower the film mosaicity which relates to a better crystallinity. On the other hand, observation of a peak with larger FWHM relates to a lower crystallinity.

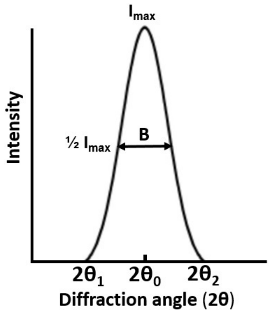

Figure 3.9: Rocking curve for a thin film with thickness of $t = m.d$, adapted from Ref. [159].

In this thesis, symmetrical out-of-plane $2\theta - \theta$, and $2\theta - \omega$ measurements were performed in a Rigaku SmartLab X-ray diffractometer with Cu K_α radiation. A schematic illustration of the diffractometer setup is presented in Fig. 3.7 and Fig. 3.8, labeling the different available degrees of freedom for each measurement. All the measurements were done with parallel beam geometry with an X-ray mirror for the sake of parallelization and primary monochromatization of the initial X-ray beam. A secondary graphite monochromator has been mounted prior to the scintillation counter on the secondary optic side in flat mode equipped with a K_β slit for further monochromatization to increase the resolution.

3.5.3 Transmission electron microscopy (TEM)

Transmission electron microscopy (TEM) is one of the most valuable tools to investigate crystalline thin films. Different information regarding crystal structure, grain size and shape as well as interface characteristics including shape, thickness and composition can be obtained from this micro-structural evaluation. However, TEM is a complicated technique and needs accurate data collection and interpretation. For the purpose of structural investigations with TEM, a beam of electrons is transmitted through an ultrathin section of the specimen (less than 100 nm thick) called lamella and from the interaction of the electrons with the specimen as the beam is transmitted through the lamella an image is formed. The thin lamella is irradiated by a primary electron beam and the scattered or diffracted electrons in transmission geometry are detected by CCD arrays. Through the interaction of the primary electrons with the sample, there is a forward scattering which deflects the electron beam. The sample can either be scanned with a focused beam (scanning transmission electron microscopy, STEM) or a complete picture can be taken in a parallel beam (transmission electron microscopy, TEM).

There are three main imaging modes used in TEM (see Fig. 3.10), (i) bright-field (BF) images obtained from a direct electron beam, (ii) dark-field (DF) images obtained by an off-axis scattered beam using a displaced-aperture, and (iii) centred dark-field images obtained for a tilted primary beam for which the diffracted beam goes through an on-axis aperture. The resulting diffraction pattern is displayed on a phosphor screen below the objective aperture. The corresponding areas of diffraction pattern are schematically presented in Fig. 3.10. A brief overview of the utilized TEM modes for this thesis is given in the following. A detailed description of TEM principles is beyond the scope of this work and can be

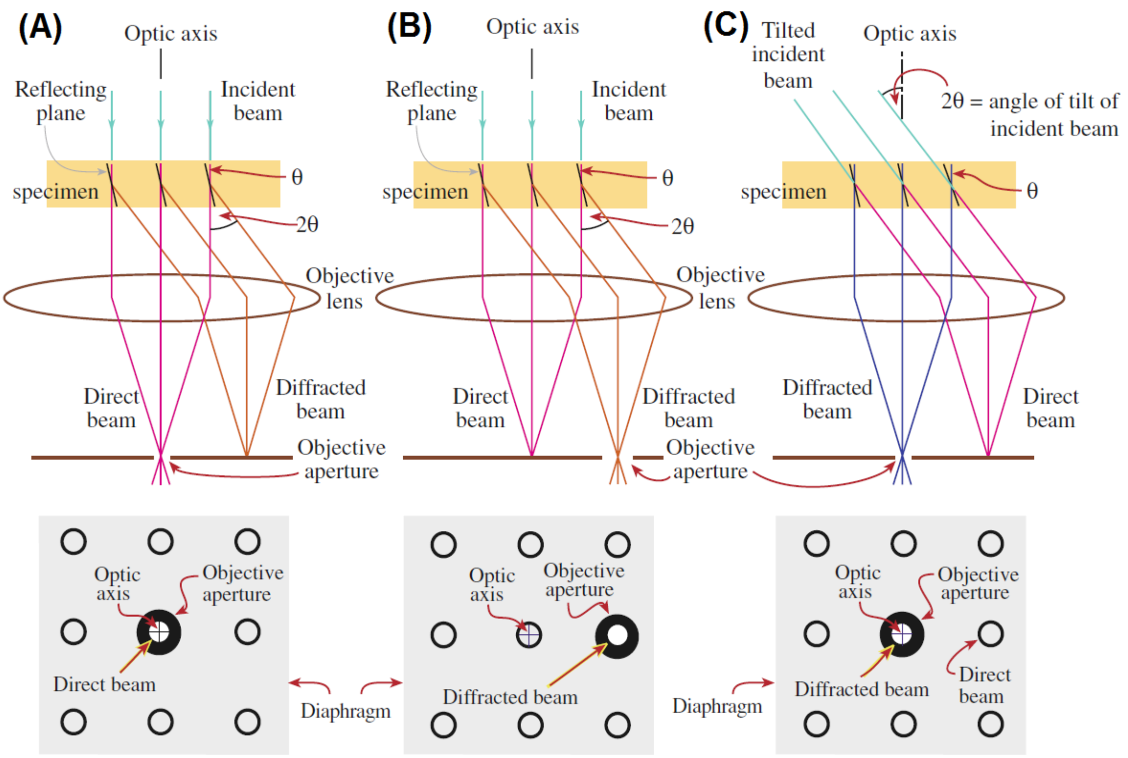

Figure 3.10: Schematic of ray diagrams for three main TEM imaging modes: (A) BF image formed from the direct electron beam, (B) displaced-aperture DF image formed with a off-axis scattered beam, and (C) a CDF image for which the incident beam is tilted so that the scattered beam emerges on the optic axis. The area of the DP selected by the objective aperture is shown below each ray diagram, adapted from Ref. [161].

found in ref [161].

BF − STEM: In the bright field, the elastically scattered electrons are detected with a small deflection angle. The difference in contrast is due to the different orientation of the crystals and the constructive interference at parallel beam planes.

HAADF − STEM: In the dark field (high angle annular dark field, HAADF) the elastically scattered electrons are detected with a large deflection angle. At the high scattering angles, the signal is mostly dominated by the Rutherford scattering and higher order elements lead to greater deflections and therefore to higher intensities due to their larger atomic masses which is why this contrast is also called "z-contrast".

STEM − EDX: The EDX signal in the STEM is similar to SEM (scanning electron microscopy). In contrast to the SEM, the excitation volume in TEM is much lower due to the focused electron beam and investigation of thin samples with a lateral resolution of less than 1 nm is possible. However, the thicker the lamella the higher would be the EDX signal. For a thicker lamella, we have a larger excitation volume and broadening of interfaces if they are tilted against the primary electron beam axis.

HR − TEM: In the high-resolution TEM, the elastically scattered electrons in the Parallel beam are used for imaging. If the lamella is thin enough and a grain is located in a zone axis, a constructive interference occurs by which the potential differences below the sample can be mapped and interpreted in the form of the atomic structure. From these FFT (fast Fourier transformation) images with the Gatan digital micrograph software the corresponding diffraction reflections in the reciprocal space can be extracted. These diffraction reflections correspond to the phase shift produced by the scattering of the electrons at the periodic lattice of the crystal structure. In contrast, the scattering amplitudes are measured during electron or X-ray diffraction. Thus the information from the electron diffraction and the HRTEM are complementary and can be used together to solve crystal structures. In this work, only the distances between the reflections from the FFT images and the angles between them were evaluated to verify a phase out of the ICCD data (The international centre for diffraction data).

In this thesis, the TEM investigations were carried out at Karlsruhe institute of technology (KIT) in the group of Prof. Dr. Christian Kübel. The lamella was prepared by Dr. Mohammad H. Fawey and the TEM measurements were performed by M.Sc. Saleh Gorji. For cross-sectional high resolution transmission electron microscopy (HR-TEM) investigations, TEM lamella was prepared by focused ion beam (FIB) using a FEI Strata 400S equipped with an OmniProbe 200 micromanipulator for *in-situ* lift-out. The lamella was prepared in a way that an observation plane perfectly perpendicular to the film cross-section is obtained. TEM sample preparation was initially performed at 30 kV with an ion beam current of 16 nA, followed by cleaning with a 6.5 nA ion beam current. The final thinning step of the area of interest at the interface was performed at a low-voltage/low-current regime starting from 8 kV to 2 kV with ion beam current ranging from 56 pA to 3 pA. An aberration (image) corrected FEI Titan 80-300 operating at 300 kV acceleration voltage and equipped with a US1000 slow-scan CCD camera (Gatan Inc.), a high-angle annular dark-field (HAADF) detector (Fischione), and an SUTW (super ultra-thin window) EDX detector (EDAX Inc.) were used to evaluate the crystallinity, interface quality and composition.

3.6 Magnetic characterization

3.6.1 Superconducting quantum interference device (SQUID)

Because of reduced scattering of free electrons for almost all conductors, the resistance decreases at low temperatures. However, for superconducting materials a different conducting mechanism happens which leads to conductivity even at lower temperatures. The mechanism involves pairs of electrons with opposite moments and spins which are called *Copper pairs*. These two mutually bound electrons acting as one elementary particle with electric charge of $q = 2e$ and mass of $m = 2m_e$ constituting a copper pair incorporate to electric conductivity at low temperature. This phenomenon results in quantum effects such as *Josephson effect*, conduction through a thin insulator barrier, which is used in magnetic measurement.

Back in 1962, Josephson predicted that in a Josephson junction made of two superconductors which are separated by a very thin insulator barrier (0.1-2 nm) due to the existence of Cooper pairs, a flow of extraordinary current can be observed. The DC current in the junction, i_s, is proportional to the critical current, i_c, of the junction (above which the superconductivity vanishes) as well as the angle θ representing the phase difference between wave functions of electrons in pair at each side of the junction [162].

$$i_s = i_c sin\theta \tag{3.46}$$

$$f = \frac{d\theta}{dt} = \frac{2e}{h}V = C_i V \tag{3.47}$$

If we supply a DC voltage, V, to the Josephson junction an alternating supercurrent flows through the junction, oscillating with frequency of $2eV/h$. The $2e/h$ is called the Josephson constant, C_i, which depends only on the physical constants and is known to be equal to $\sim$ 483.6 GHz/V. The standard volt is now defined as the voltage required to produce a frequency of 483.6 GHz. Under high frequency magnetic field, voltage versus current relationship in the Josephson junction changes with n quantized steps of the value:

$$V(n) = nf\frac{h}{2e} = nf\frac{1}{C_\mathrm{i}} \tag{3.48}$$

This equation shows that the voltage across the junction depends only on Planck's constant (h), electron charge (e) and microwave frequency (f), three of which can be accurately measured. The voltage drop is equal to zero in superconducting state until the current reaches the critical current (I_c). Above the critical current, both normal electrons and the Cooper pairs incorporate to the conduction and so the superconductor would behave like a normal conductor.

The superconducting quantum interference device (SQUID) is made of a superconducting ring with one (RF) or two (DC) Josephson tunnelling junctions. The SQUID combines two effects; one is quantization of magnetic flux and the other one is tunnelling by a weak link (Josephson effect). The quantized flux in one ring with Josephson junction Φ_{in} is expressed as following:

$$\theta + 2\frac{\Phi_\mathrm{in}}{\Phi_0} = 2\pi n \tag{3.49}$$

In this relationship Φ_0 is the magnetic flux quantum (fluxon) which depends only on physical constants h and e:

$$\Phi_0 = \frac{h}{2e} = 2.07 \times 10^{-15}\mathrm{Wb} \tag{3.50}$$

If cross section of the Josephson junction ring is $1\,\mathrm{cm}^2$ there would be a flux density of 2.067×10^{-11} T which is sensitive enough for measurement of extremely small magnetic fields. The current in the ring can be calculated as [163]:

$$i_\mathrm{s} = i_\mathrm{c}\sin\frac{2\pi\Phi_\mathrm{in}}{\Phi_0} \tag{3.51}$$

Two years after the Josephson discovery, Jaklevic presented a quantum interference effect in two Josephson junctions connected in parallel [164]. We can supply such device directly by a DC voltage. The device is called DC SQUID with two Josephson junctions in a superconducting loop. In the absence of external magnetic field, by establishing a constant input biasing current (I_b) it will split equally into the two branches. However, If we apply a small external magnetic field to the superconducting loop, a screening current (I_s) start to flow in the loop generating a magnetic field to cancel the applied external magnetic flux. The induced current is in the same direction as input current in one branch of the loop and is opposite to input current in the other branch. Thus, we have interference between two different currents in two branches of the ring. The screening current (I_s) induced by external magnetic flux is $I_\mathrm{s} = -\Phi_\mathrm{ex}/L$ with L being self inductance of the superconducting ring. The total current in the branches becomes $I_\mathrm{b}/2 - I_\mathrm{s}$ and $I_b/2 + I_s$, respectively. As soon as the current in either branch exceeds the critical current I_c of the Josephson junction, a voltage appears across the junction.

If the external flux is further increased, exceeding half of the magnetic flux quantum, Φ_0, since the flux in the superconducting loop must be an integer number of flux quanta, instead of screening the flux the SQUID starts to increase it to Φ_0. Under these circumstances, I_s now flows in the opposite direction and therefore every time the flux increases by half integer multiples of Φ_0, I_s changes its direction. This leads to oscillation of critical current as a function of the applied flux which acts as a flux to voltage converter. If I_b is more than I_c, the SQUID operates in the resistive mode and the voltage is a function of the applied magnetic field and the period equal to Φ_0. The $I-V$ curve of the DC SQUID shows hysteresis and because of this, a shunt resistance R is connected across the junction to eliminate the hysteresis.

According to the above discussion, the measured voltage will oscillate with the changes in phase at the two Josephson junctions (consisting of two half-ring devices shunted by a resistor R and a capacitor C), depending on the change in the magnetic flux. We can evaluate the resulting flux change by counting these oscillations. The change in the flux can be estimated from the change in the voltage:

$$\Delta V = R\Delta I \tag{3.52}$$

$$\Delta V = \frac{R}{L}\Delta\Phi \tag{3.53}$$

The current flowing in such a device depends on the external magnetic flux as following relation [165]:

$$I = 2I_0 |\cos\frac{\pi\Phi_\mathrm{ex}}{\Phi_0}| \tag{3.54}$$

In low-temperature SQUID normally niobium layers are used as the superconducting material which are separated by niobium oxide or aluminium oxide films. Since the SQUID sensor is highly sensitive to any magnetic and electric noise, it is not used directly to measure magnetic flux. Instead, practically the SQUID sensor is kept in a superconducting box held at temperatures below its T_c so that the box acts as diamagnet and can protect the SQUID from any source of noise. This box is then connected to the magnetic source by a coil made of superconducting wire which is often used as a flux transformer in the form of a gradiometer for SQUID signal read-out and coupling with external voltage. There is a second derivative detector array with two first order gradiometer coils mounted parallel to the field direction (Z) within superconducting magnet so that the magnetic flux is homogeneous and the gradiometer is relatively insensitive to field drift. Both the flux transformer and the SQUID device are in special vacuum flask known as "dewar". This cryostat is filled with liquid helium with boiling point of 4.2 K for low temperature measurements.

Applying a homogeneous magnetic flux B in the z-direction leads to a zero voltage drop between the coils, however, a field gradient along the z direction for example by moving a sample through the pick-up coils will produce a voltage drop. Such change in the magnetic flux will induce a voltage which is coupled by a flux transformer to the input inductance placed next to the SQUID. A screening current is then induced by the change in magnetic flux in the SQUID. The biasing current in the SQUID is optimised in a way that the highest amplitude and sensitivity can be achieved for the resulting oscillating voltage drop across the SQUID. In order to determine the magnetic moment of the measured sample, the measurement software provides a non-linear least-square fitting routine which can be used to fit the resulting voltage. This fitting correlates the speed of sample, its position, and the SQUID voltage. Since the gradiometers are vertically mounted in the setup used for my experiments, only Z component of the magnetization vector, M_z, is achieved for the sample.

In the MPMS setup used for my experiments, the sample is mounted on a reciprocating sample option (RSO) head which allows high magnetic moment measurement resolution of 5×10^{-9} emu electromagnetic unit ($1\,\mathrm{Am}^2=10^3$ emu). The sample is located in a plastic straw and is moved sinusoidally through the center of the second order gradiometer. This sinusoidal movement combines the SQUID voltage measurement setup with lock-in techniques and reduces the external noise from the measurement signal. A schematic overview of the sample movement and SQUID voltage correlation with a RSO head is shown

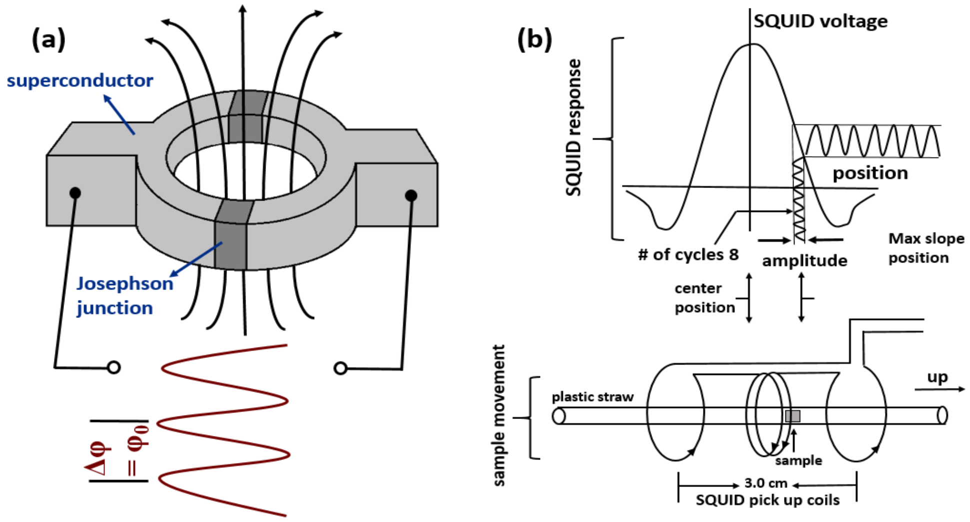

Figure 3.11: A schematic of (a) DC Josephson junction, and (b) the SQUID signal in correspondence to the sample movement in a MPMS device from QuantumDesign using the Reciprocating Sample Option (RSO), adapted from Ref. [167].

in the Fig. 3.11. The voltage versus position plot shows perfect symmetry which is rarely the case since the thin film samples have at least two different phases of substrate and the film material with different magnetic properties in case of a Quartz glass substrate and MnBi thin film on top, one is diamagnetic and the other one is ferromagnetic. Under these circumstances, there are two centres of magnetic moment with different magnetic nature in the z direction which leads to superposition of two measurement signals and an asymmetric SQUID-signal so the observed SQUID voltage could be distorted. To avoid such distortion, one could choose the substrate as thin as possible and measure the bare substrate signal to be later substituted from the overall measurement. Choosing the proper magnitude of applied field during centring process allows a stronger signal for the ferromagnetic film material so that only film contribution are obtained in the measurement. Inserting the sample in the plastic straw with its plane parallel or normal to the z or applied field direction in case of MnBi and MnGa which both have an easy axis of magnetization out-of-plane, will obtain in-plane and out-of-plane measured hysteresis loops, respectively.

All the SQUID measurements were performed in a commercial QuantumDesign magnetic property measurement system (MPMS) device with applicable fields up to ± 7 Tesla and the measurement temperature capability from liquid helium temperature (∼4.2 K) up to 350 K. Sample size is limited by the inner diameter of the sample bore which is 8.5 mm. A more detailed description of MPMS measurement principles can be found in Ref. [165, 166, 167].

3.6.2 Torque magnetometry

As the most powerful method to investigate the magnetic anisotropy in ferromagnetic materials, torque magnetometry can be used to determine different characteristics of the system. From the periodicity of the measured torque curve, the symmetry of the magnetic anisotropy can be directly observed. Using Fourier analysis [168] or the Myajima method [169] the first and second order anisotropy constants can be determined and by analysing the field dependency of the rotational hysteresis the anisotropy field can be precisely measured. Moreover, we can analyse competing anisotropies [170] and define spin reorientation temperature in case such characteristics are applicable to the magnetic system under investigation. A more thorough investigation can derive information on magnetic instability and magnetic reversal processes as well [171, 172].

The torque measurements for the samples studied in the current thesis were performed by Dr. Iliya Radulov (in group of Prof. Gutfleisch, institute of functional materials, TU Darmstadt) using the torque magnetometry option attached to the commercial QuantumDesign physical property measurement system (PPMS) device. Similar to the SQUID machine discussed above, the PPMS system is a cryostat inside a superconducting magnet as well but with a wider diameter of dewar which can accommodate the torque setup. Moreover, the PPMS system is capable of applying magnetic fields up to 14 T while the applicable temperature range is 10-400 K. This is of great importance since for the torque measurement high magnetic fields, sufficiently higher than the anisotropy field of under study material ($H >> H_{\mathrm{K}}$), are necessary to ensure the magnetization is parallel to the applied field in all measurement steps [168]. The sample holder of the PPMS torque setup consists of a Wheatstone bridge and a piezoresistive micro fabricated silicon torque lever chip. It measures the angular dependency of the magnetic torque τ with respect to the applied field B (torque $\tau = m \times B$) in a sample with magnetic moment of m (see Fig. 3.12). The sample is mounted on this chip in PPMS rotator, and piezoresistive technique is used to detect twisting (deflection) of the torque lever about the lever's symmetry axis when the sample is subject to torque. Due to the mechanical stress caused by the magnetic torque there will be a change in resistance $\Delta(R_1 - R_2)$ in piezoresistive torque chip proportional to the torque which can be very accurately measured by the Wheatstone bridge. The resulting curve plots the torque required to rotate the saturation magnetization away from the easy axis as a function of the angle of rotation. The measurement starts with zero rotation while the field is applied perpendicular to the film plane and then the rotation angle monotonically changes up to 360° [84, 173, 174]. The sample mass and size must be limited to 10 mg and 1.5 mm × 1.5 mm × 0.5 mm to prevent the torque signal greater than 5×10^{-5} N.m and prevent the torque-lever chip from breakage. The on-chip current loop is used to provide known magnetic moment and accurate calibration of change in resistance as a function of torque. The moment and torque sensitivity of the setup is 1×10^{-7} emu and 1×10^{-8} N.m, respectively [175].

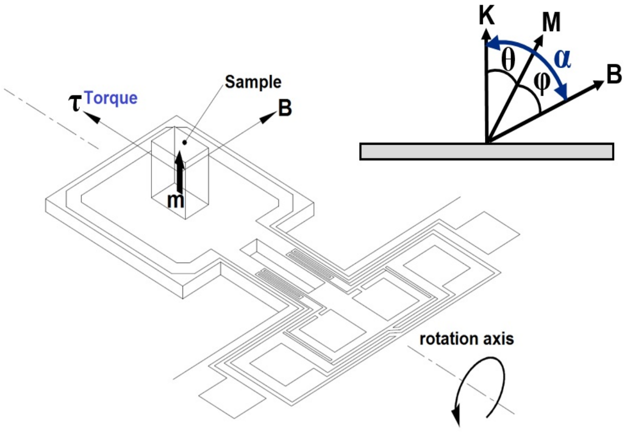

Figure 3.12: A schematic of piesoresistive silicon torque chip used in torque magnetometry setup of PPMS device along with illustration of measurement angles, adapted from Ref. [175].

The uniaxial magnetocrystalline anisotropy energy (E_{K}) can be expressed with the first two coefficients of a power $sin(\theta)$ series in which θ is the angle between anisotropy (or c-axis which is the easy axis and lies out-of-plane for the films under study) and magnetization direction, and all the terms with odd powers are zero because of the hexagonal crystal symmetry [79]. Considering the effect of shape anisotropy E_{s} energy which acts opposite to the uniaxial anisotropy energy as well as the magnetostatic energy E_{MS} due to the angle between the field and direction of magnetization (Φ), the total anisotropy energy per volume of the sample V is given as [168]:

$$E_{\mathrm{total}} = E_{\mathrm{K}} - E_{\mathrm{S}} + E_{\mathrm{MS}} \tag{3.55}$$

$$\frac{E_{\mathrm{total}}}{V} = K_1 sin^2\theta + K_2 sin^4\theta - 2\pi M_{\mathrm{s}}^2 sin^2\theta + M_{\mathrm{s}} H cos\Phi \tag{3.56}$$

The torque L is expressed as [168]:

$$\frac{L}{V} = -M_{\mathrm{s}} H sin\Phi \tag{3.57}$$

Differentiating the E_{total} with respect to θ to find the direction of M_{s} for the minimum energy, we find L as a function of angle θ [168]:

$$\frac{L}{V} = Asin(2\theta) + Bsin(4\theta) \tag{3.58}$$

$$A = K_1 + K_2 - 2\pi M_{\mathrm{s}}^2 \tag{3.59}$$

$$B = -\frac{1}{2} K_2 \tag{3.60}$$

If the applied field is high enough ($H >> H_{\mathrm{K}}$) we can make sure that the magnetization is always parallel to the field and the angles between anisotropy and magnetic field (α) would be nearly the same as the angle between anisotropy and magnetization (θ). The saturation magnetization (M_{s}) can be measured in SQUID or PPMS device. By Fourier expansion of the measured torque curve, K_1 and K_2 can be easily calculated. In the Eq. 3.58, A and B are first and second Fourier coefficients of the sinusoidal torque curve $L(2\theta)$, respectively [168].

3.7 Theoretical investigations of exchange interface

In this section the theoretical methods which were employed to investigate exchange interactions at the interface of hard/soft magnetic phases in the exchange coupled (MnBi/FeCo and MnGa/FeCo) bilayer samples, were shortly discussed. The corresponding models and packages which were used to simulate the structures close to the hard/soft interface and calculate the exchange energies involved are also mentioned along with the exchange parameters applied in the calculations. More details regarding the theoretical procedure can be found in the supplemental material provided with Ref. [106].

3.7.1 Density functional theory calculations

Density functional theory (DFT) was first introduced by P. Hohenberg and W. Kohn [176] and afterwards it was developed further by W. Kohn and L. J. Sham [177]. Using DFT, the energy (and hence other properties) of a system in the ground state can be predicted as a “functional” of its electron density ($\rho(\vec{r})$) [178]. In this theory, instead of using the wave function as the primary variable, the electron density ($\rho(\vec{r})$) which itself is a function of coordinates ($\vec{r}$) is used in the calculation of the ground state energy. That is the reason it is called density functional theory. In the following, a few basic definitions and theorems regarding DFT are shortly reviewed.

The total energy of a system of atoms or molecules can be calculated using the Schrödinger equation which is defined as [179, 180]:

$$\hat{H}\Psi_i(\vec{r}_1, \vec{r}_2, ..., \vec{r}_{\mathrm{n}}, \vec{R}_1, \vec{R}_2, ..., \vec{R}_{\mathrm{m}}) = E_i \Psi_i(\vec{r}_1, \vec{r}_2, ..., \vec{r}_{\mathrm{n}}, \vec{R}_1, \vec{R}_2, ..., \vec{R}_{\mathrm{m}}). \tag{3.61}$$

In this equation, $\hat{H}$ is the Hamiltonian operator for any atomic and/or molecular system consisting of n electrons and m nuclei, $\vec{r}_\mathrm{n}$ and $\vec{R}_\mathrm{m}$ represent coordinates of electron and nuclei, respectively, Ψ_i is the overall wave function of the system and E_i are the energy eigenvalues, which results from the Hamiltonian operator acting on the wave function of the system.

In practice, calculating the precise wave function and hence the total energy of a system is not feasible, however, using high level quantum chemistry approaches for small systems, obtaining a very good (almost accurate) approximation of the wave function is possible. Thus, a more efficient approach is required for larger systems. The above-mentioned Hamiltonian can be written in atomic unit as the following expression [178]:

$$\hat{H} = \underbrace{-\frac{1}{2}\sum_{i=1}^{\mathrm{n}}\nabla_i^2}_{T_\mathrm{e}} \underbrace{-\frac{1}{2}\sum_{\mathrm{A}=1}^{\mathrm{m}}\frac{1}{m_\mathrm{A}}\nabla_\mathrm{A}^2}_{T_\mathrm{nu}} \underbrace{-\sum_{i=1}^{\mathrm{n}}\sum_{\mathrm{A}=1}^{\mathrm{m}}\frac{Z_\mathrm{A}}{r_{i\mathrm{A}}}}_{V_\mathrm{e-nu}} + \underbrace{\sum_{i=1}^{\mathrm{n}}\sum_{j>i}^{\mathrm{n}}\frac{1}{r_{ij}}}_{V_\mathrm{e-e}} + \underbrace{\sum_{\mathrm{A}=1}^{\mathrm{m}}\sum_{\mathrm{B}>\mathrm{A}}^{\mathrm{m}}\frac{Z_\mathrm{A}Z_\mathrm{B}}{r_\mathrm{AB}}}_{V_\mathrm{nu-nu}}. \tag{3.62}$$

In the above Hamiltonian, m_A, Z_A, $r_{i\mathrm{A}}$, r_{ij} and r_AB are the mass of nuclei, atomic number, distance between electron-nuclei, distance between electron-electron and distance between nuclei-nuclei, respectively. T and V stand for the kinetic and potential energies, respectively ("e" and "nu" subscripts refer to electrons and nuclei, respectively) [178].

In order to simplify the general Hamiltonian in Eq. 3.62, it is assumed that the electrons motions can be considered in the field of static nuclei since the mass of nucleus is much larger than that of the electron, the movement of nuclei in an atom is much slower than that of electrons. This approach is known as the **Born-Oppenheimer approximation** [181]:

$$\hat{H}_\mathrm{elec}\psi_\mathrm{elec}(\vec{r}_\mathrm{n};\vec{R}_\mathrm{m}) = E_\mathrm{elec}(\vec{R}_m)\psi_\mathrm{elec}(\vec{r}_\mathrm{n};\vec{R}_\mathrm{m}), \tag{3.63}$$

Therefore, to calculate the total energy it is essential to solve Eq. 3.63 and then using the Born-Oppenheimer approximation the contribution of the nuclei to the total energy of the system can be added to the electronic contribution as a parameter. Although the Born-Oppenheimer approximation to some extent facilitates the problem of solving the Schrödinger equation, the difficulty still remains for large systems [178].

The electron density in a volume element ($d\vec{r}_1$) for a **n**-electron system over the spin coordinates is defined as:

$$\rho(\vec{r}_1) = n\int\cdots\int|\Psi\{(\vec{r}_1),(\vec{r}_2),...,(\vec{r}_\mathrm{n})\}|^2 ds_1 d\vec{r}_2...d\vec{r}_\mathrm{n}, \tag{3.64}$$

which is the core of density based methods for calculation of ground state energy. Based on the Eq. 3.64, the total number of electrons in the system (n) over the entire space can be obtained using [178]:

$$n = \int\rho(\vec{r})d\vec{r}. \tag{3.65}$$

Hohenberg and Kohn first proved that the electron density of a system can uniquely determine the Hamiltonian and the ground state energy and other properties of that system [176]. Therefore, the following relation can be written [178]:

$$\rho_0(\vec{r}) \rightarrow \hat{H} \rightarrow E_0. \tag{3.66}$$

Based on this theorem, the total energy as a functional of electron density can be written as [178]:

$$E_0[\rho_0(\vec{r})] = T[\rho_0(\vec{r})] + E_{\text{e-nu}}[\rho_0(\vec{r})] + E_{\text{e-e}}[\rho_0(\vec{r})] = \underbrace{\int \rho_0(\vec{r})V_{\text{ext}}(\vec{r})d\vec{r}}_{\text{particular system}} + \underbrace{T[\rho_0(\vec{r})] + E_{\text{e-e}}[\rho_0(\vec{r})]}_{\text{every system}=F_{\text{HK}}[\rho_0(\vec{r})]}. \tag{3.67}$$

The second term, the system independent energy ($F_{\text{HK}}[\rho_0(\vec{r})]$), includes the contributions of kinetic and electron-electron repulsion energies. If it was possible to accurately solve this energy term, one could obtain the exact answer to the Schrödinger equation. Although, so far only approximations are made to deal with this problem. The repulsive electron-electron term can be written as [178]:

$$E_{\text{e-e}}[\rho_0(\vec{r})] = \underbrace{\frac{1}{2}\int\int \frac{\rho_0(\vec{r}_1)\rho_0(\vec{r}_2)}{\vec{r}_{12}}d\vec{r}_1 d\vec{r}_2}_{J[\rho_0(\vec{r})]} + E_{\text{qm}}[\rho_0(\vec{r})], \tag{3.68}$$

in which the term $E_{\text{qm}}[\rho_0(\vec{r})]$ refers to all the quantum mechanical contributions including the electron-electron correlations, exchange and self interactions, while $J[\rho_0(\vec{r})]$ is the classical Coulomb interaction. Kohn and Sham [177] proposed a method to solve the kinetic energy contribution in Eq. 3.67 since it can introduce large deviations in the total energy. They assumed that since it is not possible to obtain the exact kinetic energy of an interacting system ($T[\rho_0(\vec{r})]$), this term can be divided into two parts: the kinetic energy of a "non-interacting" system (T_{S}) and the remaining effects corresponding to the interacting system ($T - T_{\text{S}}$). The proposed kinetic energy by Kohn-Sham can be written as [178]:

$$T_{\text{S}} = -\frac{1}{2}\sum_{i=1}^{\text{n}} \langle \phi_i^{\text{KS}} | \nabla^2 | \phi_i^{\text{KS}} \rangle, \tag{3.69}$$

in which n is the number of electrons in the system and ϕ_i^{KS} represents one-electron Kohn-Sham spin orbitals. Therefore, the Hohenberg-Kohn functional, $F_{\text{HK}}[\rho(\vec{r})]$, can be written as [178]:

$$F_{\text{HK}}[\rho(\vec{r})] = T_{\text{S}}[\rho(\vec{r})] + J[\rho(\vec{r})] + E_{\text{XC}}[\rho(\vec{r})]. \tag{3.70}$$

In this important formula, $E_{\text{XC}}[\rho(\vec{r})]$ is the sum of ($T - T_S$), electron-electron self-interaction, exchange and correlation effects, all of which are unknown. Therefore, the total energy can be written as [178]:

$$E[\rho(\vec{r})] = T_{\text{S}}[\rho(\vec{r})] + J[\rho(\vec{r})] + E_{\text{XC}}[\rho(\vec{r})] + \underbrace{\int \rho(\vec{r})V_{\text{ext}}(\vec{r})d\vec{r}}_{E_{\text{e-nu}}[\rho(\vec{r})]}. \tag{3.71}$$

Now the V_{eff} should be defined so that the resulting one-electron Kohn-Sham spin orbitals exactly provide the density of the real system. For this, we refer to Eqs. 3.69 and 3.71 and expand Eq. 3.71 as [178]:

$$\begin{aligned} E[\rho(\vec{r})] = &\underbrace{-\frac{1}{2}\sum_{i=1}^{n}\langle \phi_i^{\text{KS}} | \nabla^2 | \phi_i^{\text{KS}} \rangle}_{T_{\text{S}}[\rho(\vec{r})]} + \underbrace{\frac{1}{2}\sum_{i=1}^{n}\sum_{j=1}^{n} |\phi_i^{\text{KS}}(\vec{r}_1)|^2 \frac{1}{r_{12}} |\phi_j^{\text{KS}}(\vec{r}_2)|^2 d\vec{r}_1 d\vec{r}_2}_{J[\rho(\vec{r})]} \\ &+ E_{\text{XC}}[\rho(\vec{r})] \underbrace{- \sum_{i=1}^{n} \int \sum_{A=1}^{m} \frac{Z_A}{r_{1A}} |\phi_i^{\text{KS}}(\vec{r}_1)|^2 d\vec{r}_1}_{E_{\text{e-nu}}[\rho(\vec{r})]}. \end{aligned} \tag{3.72}$$

Finally, the variational principle is applied to the total Hamiltonian and minimum energy eigenvalues (ϵ_i) can be obtained as [178]:

$$\left[-\frac{1}{2}\nabla^2+\overbrace{\left(\int\frac{\rho(\vec{r}_2)}{r_{12}}d\vec{r}_2-\underbrace{\sum_{A=1}^{M}\frac{Z_\mathrm{A}}{r_{1\mathrm{A}}}}_{V_\mathrm{ext}}+V_\mathrm{XC}(\vec{r}_1)\right)}^{V_\mathrm{eff}}\right]\phi_i^\mathrm{KS}=\epsilon_i\phi_i^\mathrm{KS}, \tag{3.73}$$

where the electron density of the real system can be expressed from the Kohn-Sham spin orbitals as [178]:

$$\rho(\vec{r})=\sum_{i=1}^{\mathrm{n}}|\phi_i^\mathrm{KS}(\vec{r})|^2, \tag{3.74}$$

with n equals to the number of electrons. Eqs. 3.73 and 3.74 are referred to as the Kohn-Sham equations. In Eq. 3.73, V_eff is the effective potential in which only $V_\mathrm{XC}(\vec{r})$ (potential due to the exchange-correlation energy equal to $\frac{\delta E_\mathrm{XC}[\rho(\vec{r})]}{\rho(\vec{r})}$) term is unknown. Unlike the Hartree-Fock scheme where the approximations are entered from the first step because of the nature of the Slater determinant [182, 183], in the Kohn-Sham formulations it is only after Eq. 3.73 where the approximations are introduced. If finding the exact value for E_XC was possible, the ground state energy obtained from DFT would be close to the exact value.

To sum up, the overall procedure to solve the Kohn-Sham equations for a fixed geometry (single-point calculation) is as the following sequence [178]:

- Starting with an initial $\rho(\vec{r})$,
- Obtaining the V_eff and determining a new $\rho(\vec{r})$ using Eqs. 3.73 and 3.74,
- Using the obtained Kohn-Sham orbitals from Eq. 3.73 to calculate the kinetic energy via Eq. 3.69,
- Continuing this cycle until $\rho(\vec{r})$ is converged within a certain criterion and then total energy can be calculated using Eq. 3.72.

Density functional theory (DFT) calculations were performed by Dr. Ashkan Moradabadi from Freie Universität Berlin using the projected augmented wave method as implemented in the VASP code [184] for both MnBi/FeCo and MnGa/FeCo bilayer systems. The exchange correlation functionals were parameterized using the generalized gradient approximation (GGA) as in Ref. [185]. The effect of the GGA+U approximation was also investigated for MnBi since it is important to understand the bulk anisotropy [186] but it had no significant influence on the interface properties.

Two MnBi/FeCo models with different FeCo orientations were considered in the DFT calculations, MnBi (001)/FeCo (110) and MnBi (001)/FeCo (111), which are used as the starting structures in both of their crystalline and amorphous states. The corresponding crystalline lattice parameters were then used to generate the above-mentioned amorphous structures using *ab initio*-based molecular dynamics (AIMD) calculations implemented in VASP at 500 °C (773 K) after 10 ps run for the FeCo (111) and 2 ps run for the FeCo (110) surfaces, respectively. All models were constructed as symmetric and non-stoichiometric slabs so that their interface formation energies would be comparable. To study the influence of chemical composition on the interfacial properties, $\mathrm{Fe_xCo_{(1\text{-}x)}}$ layers with two different stoichiometries, i. e. $\mathrm{Fe_3Co_5}$

and Fe_5Co_3, were considered. The thickness of the MnBi layer in MnBi (001)/FeCo (110) and MnBi (001)/FeCo (111) interfaces was $\sim$ 1 nm and $\sim$ 1.5 nm, respectively. The modelled FeCo layer had a thickness of $\sim$ 1 nm.

For the MnGa/FeCo system, similar *ab initio*-based DFT calculations were performed using the VASP code [184]. For the bulk structures, tetragonal MnGa ($P4/mmm$, a=b=2.711 Å and c=3.663 Å) and alloy structures of cubic Fe_3Co_5 and Fe_5Co_3 ($Im\bar{3}m$, a=b=c=5.741 Å) were considered. After the full geometry optimization for bulk MnGa and FeCo, two MnGa/FeCo interface models were constructed, MnGa (001)/Fe_3Co_5 (001) and MnGa (001)/Fe_5Co_3 (001), using a 2×2 supercell of MnGa (001) and a 1×1 supercell of FeCo (001) with 88 atoms in total. Symmetric and non-stoichiometric slabs were constructed so that their corresponding interface formation energies would be comparable. The thickness of the MnGa and FeCo layers in these models were $\sim$ 1.5 nm and $\sim$ 1.8 nm, respectively. To resemble the experimental conditions, $\frac{1}{3}$ of the bottom layers for MnBi (MnGa) were fixed. At least 14 Å vacuum was considered when constructing the supercells using slab models to minimize the interaction between periodic images and minimize any artificial interactions.

In order to compare the thermodynamic stability of different interfaces, interface formation energy γ_{int}, which is a measure of the stability of the corresponding interface, was calculated for both MnBi/FeCo and MnGa/FeCo systems using the following equation:

$$\gamma_{\text{int}} = \frac{1}{2S}\left[E_{\text{int}} - n_1 E_{\text{bulk}}^{\text{MnBi(MnGa)}} - n_2 E_{\text{bulk}}^{\text{FeCo}} + \sum_i \mu_i\right], \tag{3.75}$$

where S and E_{int} are the area and the total energy of the whole interface, $E_{\text{bulk}}^{\text{MnBi(MnGa)}}$ and $E_{\text{bulk}}^{\text{FeCo}}$ are the total energies per formula unit of MnBi (MnGa) and FeCo, and n_1 and n_2 are the number of bulk units of MnBi (MnGa) and FeCo in the models, respectively. The μ_{i} is the chemical potential of any missing atoms summation of which maintains the stoichiometry. The chemical potential corresponds to any missing atoms in this model which is obtained from total energies per atom in metallic bulks of Mn, Bi (Ga), Fe and Co. It should be noted that for the interface formation energies of the amorphous and disordered phases, the reference $E_{\text{bulk}}^{\text{FeCo}}$ of the crystalline FeCo phase is used. Using reference $E_{\text{bulk}}^{\text{FeCo}}$ of amorphous FeCo phase would result in even smaller (more favorable) interface formation energies for amorphous and disordered cases. The result of these calculations are shown in Tab. 5.1 and Tab. 5.2.

The interface exchange coupling energy J^{int} was obtained using the following relation:

$$J^{\text{int}} = (E^{\text{AFM}} - E^{\text{FM}})/S, \tag{3.76}$$

where E^{AFM} and E^{FM} are the DFT total energies for antiferromagnetic (antiparallel) magnetization alignment (AFM), and ferromagnetic (parallel) magnetization alignment (FM), respectively. To obtain E^{AFM} and E^{FM}, the final relaxed structures of the interfaces has been used and then DFT relaxation were performed with antiparallel and parallel magnetizations for FeCo, respectively. This expression of J^{int} is widely used to estimate the interface exchange coupling energy by using the first-principles results as input, as shown in other exchange-spring magnetic system [187, 188].

Based on the optimized lattice parameters using DFT calculations, the lattice mismatch between the MnBi (001) and FeCo (110) is 4.8% with a 10.5° angular misfit while the lattice mismatch between MnBi (001) and FeCo (111) is 7.1% with zero angular misfit. The implemented MnBi (001)/ FeCo(111) model consisted of a 2×2 supercell of MnBi (001) and a 1×1 supercell of FeCo (111) with 96 atoms in total. In the MnBi (001)/FeCo (110) model modelled here, a 6×6 supercell of MnBi (001) together with a 5×5 supercell of FeCo (110) with 752 atoms in total were used to achieve the 4.8% lattice misfit. For the calculation of MnBi (001)/FeCo (111) interface, 3×3×1 k-point mesh was used and the calculation of MnBi (001)/FeCo (110) was performed with gamma-point. The energy cutoff for all the calculations was 360 eV. The convergence tests of the energy cutoff and k-point mesh with respect to the magnetic moments of the elements in their bulk states and energy per atom were conducted. The lattice mismatch between MnGa (001) and FeCo (001) after cell optimization was ∼ 4.2%. For the MnGa (001)/FeCo (001) interface, a 3×3×1 k-points mesh was used. The energy cutoff for all the calculations was 500 eV. Convergence tests of the energy cutoff and k-point mesh with respect to the force of 0.03 eVÅ^{-1} per atoms were also performed.

3.7.2 Micromagnetic simulation

Using the results from DFT calculations as input, micromagnetic simulations were performed by Dr. Min Yi from TU Darmstadt and Dr. Ashkan Moradabadi from Freie Universität Berlin within a simplified model based on single crystalline structures to investigate the mechanism of exchange coupling in MnBi/FeCo and MnGa/FeCo magnets using the 3D NIST OOMMF (object oriented micromagnetic framework) code [189]. For this model, the thickness of the hard MnBi layer was set as 40 nm, and the thickness of the FeCo soft layer was varied in the range of 0.5-8 nm. The lateral size was chosen as 8×8 nm^2 and an in-plane periodic boundary condition was applied. The model was discretized by 0.4 nm×0.4 nm×0.1 nm cuboid cells. Magnetic reversal curves were calculated by setting the initial magnetization along a positive z axis and changing the external magnetic field along z axis from 2.5 T to –2.5 T. To model MnGa/FeCo bilayers, the thickness of the hard MnGa layer were set as 40 nm. The thickness of the soft FeCo layer was varied in the range of 0.5-8 nm. The lateral size was chosen as 8×8 nm^2 and an in-plane periodic boundary condition was applied. The model was discretized by 0.4 nm×0.4 nm×0.1 nm cuboid cells. Magnetic reversal curves were calculated by setting the initial magnetization along the positive z axis and changing the external magnetic field along z from 3.5 T to –3.5 T.

In order to characterize the degree of exchange coupling between MnBi (MnGa) and FeCo layers through the interface, the exchange stiffness constant A^{int} was estimated according to the method presented in the OOMMF code [189]. According to this approach, the contribution of exchange energy density is numerically expressed as [189]:

$$E_{\mathrm{i}} = \sum_{j \epsilon N_{\mathrm{i}}} A_{\mathrm{ij}} \frac{\vec{m}_{\mathrm{i}} \cdot (\vec{m}_{\mathrm{i}} - \vec{m}_{\mathrm{j}})}{\Delta_{\mathrm{ij}}^2}. \tag{3.77}$$

Here, E_{i} is the exchange energy density of cell i, A_{ij} is the exchange parameter between two cells, $\vec{m}_{\mathrm{i}}$ and $\vec{m}_{\mathrm{j}}$ are the magnetization unit vectors of the two i and j cells and Δ_{ij}^2 is the discretization steps between two cells. Thus, the variation of micromagnetic exchange energy density can be approximated by $\delta E_{\mathrm{i}} \cong 2A^{\mathrm{int}}/\Delta z^2$, in which $\Delta z = 0.1$ nm is the distance between the two adjacent grid cells along the z direction.

The energy density difference (δE_{i}) from numerical approximation is assumed to be equal to that obtained from DFT calculations:

$$\delta E_i \approx I^{\mathrm{vol}} = J^{\mathrm{int}}/\Delta d, \tag{3.78}$$

where I^{vol} is the volumetric energy density from *ab initio*-based calculations, and J_{int} is the interface exchange energy (with one interface) as explained in Eq. 3.76. The Δd is the average distance at the interface estimated from the relaxed interface structures.

Finally, the interface exchange stiffness constant (A^{int}), which characterizes the exchange coupling between MnBi (MnGa) and FeCo layers through the interface, can be estimated using the following equations:

$$2A^{\mathrm{int}}/\Delta z^2 = I^{\mathrm{vol}} = J^{\mathrm{int}}/\Delta d, \tag{3.79}$$

thus,

$$A^{\mathrm{int}} \approx \frac{I^{\mathrm{vol}}\Delta z^2}{2} \approx \frac{J^{\mathrm{int}}\Delta z^2}{2\Delta d}. \tag{3.80}$$

in which I^{vol} is the volumetric energy density resulted from dividing of J^{int} by the average interface distance obtained from the crystal structures after DFT relaxation. The $\Delta z = 0.1$ nm is the cell size in the z direction. The resulting values of γ^{int}, J^{int} and I^{int} for MnBi/FeCo and MnGa/FeCo systems are shown in Tab. 5.1 and Tab. 5.2 in “Results and discussion” section, respectively.

The bulk parameters for exchange stiffness, A, and uniaxial anisotropy constant, K, for MnBi/FeCo bilayer system were set as: A^{FeCo}=10 pJ/m, A^{MnBi}=8 pJ/m, K^{FeCo}=0 MJ/m^3, and K^{MnBi}=1.86 MJ/m^3 (using my experimental data measured with torque magnetometer) [34, 190]. The saturation magnetizations, $M_{\mathrm{s}}^{\mathrm{FeCo}}$ and $M_{\mathrm{s}}^{\mathrm{MnBi}}$, were also obtained from the DFT calculation results.

The bulk parameters for exchange stiffness A, K_{u}, and M_{s} for MnGa/FeCo bilayer system were set as the following values: A^{FeCo}=10 pJ/m [190], A^{MnGa}=10 pJ/m [191], K^{FeCo}=0 MJ/m^3 [190], K^{MnGa}=2.1 MJ/m^3 (using my experimental data measured with torque magnetometer), $M_{\mathrm{s}}^{\mathrm{FeCo}}$=2.47 T and $M_{\mathrm{s}}^{\mathrm{MnGa}}$=1.05 T. The last two values of M_{s} were obtained from the DFT calculations.

4 Growth of MnBi and MnGa thin films

This chapter is dedicated to the growth process of the thin film and bilayer samples studied in current thesis. First, the technical details are provided for radio frequency (RF) magnetron sputtering unit used in this study for thin film deposition. In addition, the details regarding the deposition process and heat treatment parameters used for growth of c-axis textured LTP-MnBi (001) and epitaxial $L1_0$-$Mn_{1.5}Ga$ (001) thin films are given. Moreover, the growth process of the exchange coupled MnBi/FeCo and MnGa/FeCo bilayer samples are described in detail.

4.1 Magnetron sputtering deposition

The films studied in this thesis were deposited in a custom-made RF magnetron sputtering system with water cooled chamber walls and three sputtering sources. The sputtering system is equipped with a load lock and the base pressure of the vacuum chamber is maintained at approximately 5.0×10^{-6} Pa by a S40B TRIVAC turbomolecular pump from LEYBOLD-HERAEUS GmbH with pumping speed of 40 cubic meter per hour and an ultimate vacuum of less than 2.5 Pa. The load lock is used to ensure that the system could be kept at high vacuum without interruption by loading the samples into the chamber, thus minimizing the presence of residual gases during deposition. In order to do so, the load lock is evacuated using a rotary pump. The chamber is also equipped with a 250 W halogen heating lamp which was used to heat the substrate holder and the substrate to a maximum of 650 °C for heating of the substrate during the deposition or for post annealing heat treatment.

The sputtering chamber had three different independent sputtering sources all equipped with a magnetron beneath them providing a magnetic flux of $\sim$ 160 G. All three sputtering guns are attached to a RF/DC power supply (Advanced Energy (AE) CESAR or MDX 500). For deposition of MnBi films, alloy sputtering targets with two inch diameter and $\frac{1}{4}$ inch thickness of 99.95% purity prepared by powder metallurgy (Alineason Materials Technology GmbH) were used inside of a shuttered magnetron sputtering gun. For the most part of the MnBi deposition experiments, a target with $Mn_{55}Bi_{45}$ (at.%) composition was used since it has shown the optimum magnetic properties (see section 5.1.3). However, for composition verification experiments two other MnBi targets with the same dimension as for the main target but with different stoichiometries of $Mn_{50}Bi_{50}$ (at.%) and $Mn_{60}Bi_{40}$ (at.%) were also used. To deposit MnGa thin films, an alloy target with starting stoichiometry of $Mn_{60}Ga_{40}$ (at.%) was used. For a better heat conductivity, all alloy targets were bonded to a Cu plate ($\sim$ 1 mm thick) using Indium paste. This is also to prevent the target from cracking as a result of thermal shock caused by heat generation due to the applied power to the sputtering gun during deposition. Argon was flown into the chamber from bottom of the chamber. The flow rate of gas was controlled by mass flow controller manufactured by MKS Instruments attached to a multichannel flow ratio/pressure controller type 647 C from MKS instruments. The working pressure of the system was monitored by a vacuum cold cathode ion gauge manufactured by LEYBOLD, model COMBIVAC CM31, while the pressure during the deposition was monitored by a Baratron capacitance manometer from MKS instruments.

The process for deposition of MnBi films followed the general procedure described below. First, the substrate (Quartz glass) with dimension of $5\times5\times0.5\,\mathrm{mm}^3$ (two side polished from CrysTec GmbH) was fixed onto a disk-shaped substrate holder made of stainless steel ($\sim$ 3 cm diameter and $\sim$ 2 cm height) using silver paste (TED PELLA, INC.). A second substrate was also mounted in a similar way close to the first substrate at the centre of the holder, part of which was covered with a small shadowing plate screwed to the holder, for subsequent thickness and rate determination in profilometer. The holder was heated to $\sim$ 30 °C for 10 min using a lamp heater (Philips, 40 W) in order to cure the paste. Before loading the substrate into the load lock, the surface was blown with high purity N_2 gas to dislodge any dust or particulate that had developed during substrate preparation. Afterwards, the holder is

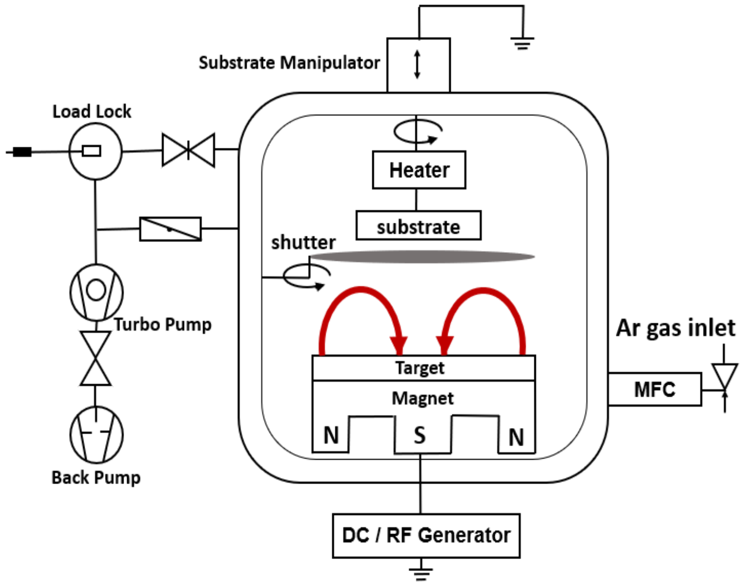

Figure 4.1: A schematic of the custom-made magnetron sputtering unit which was used for deposition experiments in current thesis.

placed face down on the transfer arm into the N_2-vented load lock. After pre-pumping of the load lock with the rotary pump followed by pumping with turbo-molecular pump down to 2.0×10^{-4} Pa, the gate valve is opened and the substrate holder is transferred to the main chamber and mounted on the manipulator column connected to the heater assembly. Subsequently, the gate valve is closed and the substrate holder and heater assembly are lowered into place above the sputtering source with a distance of 15 cm (throw distance). The chamber was evacuated with turbo-molecular pump for minimum 8 hours to reach the base pressure of 5.0×10^{-6} Pa before the start of deposition. Argon gas is then flown into the chamber through the gas inlet connected to the bottom of the chamber. The flow rate is controlled with a multi channel flow ratio controller (MKS type 647 C) and the system pressure is maintained by an automated butterfly valve that throttled the turbopump connected to a exhaust valve controller (MKS type 152G). Argon was flown into the system at a rate of 4 sccm with a pressure of $\sim$ 4 Pa. At these settings, the DC power supply (Advanced Energy (AE), DC: MDX 500, RF: CESAR 136) connected to the source containing the MnBi target was turned on to spark the plasma. For MnBi alloy target at $\sim$ 4 W the plasma was ignited and then the power is increased to 20 W. Afterwards, the target surface was pre-sputtered for 15 minutes to remove possible oxide monolayers on top.

Before the deposition starts, argon gas flow rate is reduced to 0.40 sccm followed by automatic opening of the butterfly valve connected to the turbo pump to set a reduced pressure of $\sim$ 0.7 Pa. After the pressure is stabilized, the shutter on top of the sputtering source is opened to allow deposition of MnBi onto the substrate. The optimized growth parameters of 0.7 Pa Ar gas pressure at 20 W sputtering power leads to a growth rate of 0.04 nm/s. Once the sufficient time has passed to deposit a film with desired thickness, the source shutter is once again closed. Then the argon gas is turned off and the turbopump main gate valve is fully opened to return the system to the base pressure.

MnBi thin films were typically grown at room temperature but they must be annealed *in situ* to form LTP MnBi phase. At this point, the substrate heater is turned on to start the post-annealing process. The annealing program can be set either manually on the temperature controller itself (Eurotherm, Invensys 3500) or via the temperature controller software (iTools) installed on the computer connected to the sputtering unit. The temperature of the substrate holder is inferred by a thermocouple located inside of the heater assembly right below the heating lamp. The films are subsequently annealed for 1 hr (dwelling time) *in situ* under vacuum ($\sim 2.0{\times}10^{-5}$ Pa) at the annealing temperature, T_{ann}, which was varied for different samples in the range of T_{ann} = 250 °C to 450 °C. The temperature was ramped up and down with a rate of 20 °C/min and 10 °C/min, respectively.

In case of MnGa thin films a growth temperature must be applied and a single crystalline MgO (100) substrate (from CrysTec GmbH) is used which must be preheated before the deposition. For the preheating process, the substrate is heated to 650 °C and maintained at this temperature for half an hour. During the substrate heating, the ion gauge pressure reading after 30 minutes of heating at 650 °C is roughly $\sim 1.0{\times}10^{-5}$ Pa. After cooling down to room temperature and heating again to 350 °C, a chromium (Cr) buffer layer with a typical thickness of ∼ 25 nm was deposited from a 3 mm thick Cr target (99.99%) onto the MgO (100) substrate. The optimum growth parameters for chromium buffer layer in the sputtering setup used in these experiments were 2.5 Pa Ar gas pressure at 20 W sputtering power with substrate to source distance of 15 cm leading to a growth rate of 0.017 nm/s. The MnGa layer was deposited onto the Cr buffer layer using an alloy target with a composition of $Mn_{60}Ga_{40}$ (at.%) at different substrate temperatures varied from 350 °C to 600 °C to find the optimized growth temperature in order to achieve the highest degree of crystallinity. The optimum growth parameters in the sputtering system used in these experiments for deposition of MnGa layer with minimized deposition rate of 0.04 nm/s were found to be 0.8 Pa Ar gas pressure, using 450 °C substrate temperature, at 20 W sputtering power with a target to substrate distance of 15 cm. The temperature was ramped up and down with a rate of 20 °C/min and 10 °C/min, respectively.

For synthesis of exchange coupled bilayers of MnBi(MnGa)/FeCo, the exact same procedures mentioned above were followed to deposit the hard magnetic layers. Only after deposition of MnBi or MnGa thin films a soft magnetic FeCo layer was also deposited on top. The optimum growth parameters found for FeCo layer were as follows: 2.5 Pa Ar gas pressure, at 80 W sputtering power with a target to substrate distance of 8 cm at a substrate temperature of 100 °C which leads to a slow deposition rate of 0.008 nm/s. In case of MnBi/FeCo exchange spring bilayers, the FeCo layer was deposited using two alloy sputtering targets with two different stoichiometries. A Fe-rich target with composition of $Fe_{65}Co_{35}$(at.%) and a Co-rich target with composition of $Fe_{35}Co_{65}$ (at.%). In case of MnGa/FeCo exchange spring bilayers, only a Co-rich FeCo layer was deposited as the soft magnetic layer, since based on the theoretical calculations it was known that this is in favour of exchange coupling. The thickness of the FeCo layer has been varied for MnBi/FeCo and MnGa/FeCo bilayer samples between 1-3 nm and 2-8 nm, respectively.

At the final step, after cooling down the sample to room temperature a thin tantalum, aluminium or chromium capping layer was deposited on the MnBi, MnGa or FeCo thin film following the general deposition steps as mentioned above to prevent oxidation when the samples are removed from the vacuum chamber. The deposition parameters for capping layer are 1 sccm of argon flow, 3 Pa of argon pressure, 20 W sputtering power, throw distance of 15 cm, and the growth temperature of 120 °C which resulted in a growth rate of 0.5 nm/min. At this point, the plasma is turned off and the substrate holder is then left in argon atmosphere for one hour to cool down before the sample is removed from the system for subsequent tests.

4.1.1 Temperature calibration

In the magnetron sputtering unit used for my experiments, the original thermocouple wire is positioned right below the heater lamp. There is roughly a 4 cm gap to the backside of the substrate holder when it sits face down at the end of the heater column attached to the manipulator. The existence of this gap makes it necessary to calibrate the temperature at the beginning and realize how much the actual temperature at the substrate position differs from the set temperature of the heater lamp.

For this purpose, a second thermocouple wire was inserted into the vacuum chamber and screwed to the front side of the substrate holder. The wire tip was attached to the holder at the exact sitting position of the substrates by means of silver paste. Different temperatures were applied in the range of 50 °C to 600 °C and the reading of actual temperatures was done at both thermocouples every 10 s.

Fig. 4.2 summarizes the result of temperature calibration study. Fig. 4.2-(a) shows that even with the applied temperature as high as 600 °C, it will take only around 20 min for the temperature to reach the set value and settle. The higher the value of set temperature, the shorter the settlement time. On the other hand, for higher T_{set} values there would be bigger difference between the set temperature and the actual temperature reading at the substrate position which means the actual growth temperature would be lower than the set value.

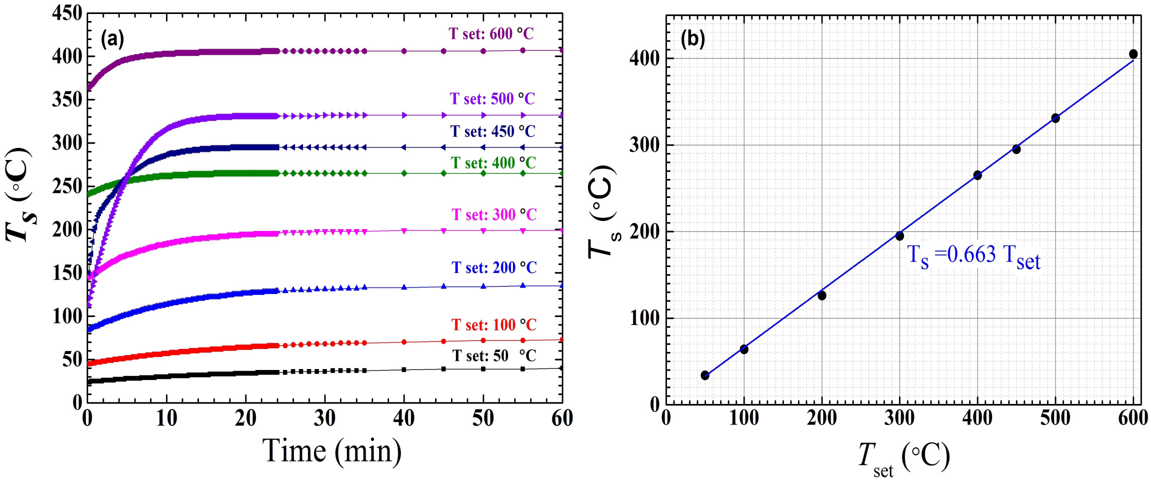

Figure 4.2: Result of temperature calibration: (a) heating curves vs. time for different applied temperatures in the range of 50 °C-600 °C, and (b) the linear relationship between applied temperature, T_{set}, and substrate temperature, T_{sub}.

The graph in Fig. 4.2-(b) shows the relation between set temperature (reading the main thermocouple) and actual temperature at substrate position (reading the additional thermocouple). Although there is a fairly linear relationship between T_{set} and T_{sub} a linear fitting to the data points shows that the T_{sub}=0.663 T_{set}. From this point onward in this thesis all the mentioned temperatures are in reference to the actual temperature or the substrate temperature.

4.1.2 Stylus surface profiling

To directly measure the thickness of the films with a stylus profiling system, the film had to exhibit a step structure on a plane substrate. For that, during each deposition a second substrate was placed along with the main substrate on the substrate holder part of which was covered by a shadowing plate screwed to the substrate holder. This half-deposited layer then was used for thickness determination by profilometry. The measurements were done using a Bruker Dektak-XT stylus surface profiling system. A diamond stylus (with tip curvature of ∼ 10 μm) is pulled along the surface at constant velocity and the step height is measured by a pick-up system. A suitable hardness of the film and the plane substrate is necessary for precision. The load applied on the stylus tip was reduced to ∼ 10 μN to prevent destruction of the sample surface. The measurement range varies from some 5 nm to some 10 μm with a resolution of some Å in highest sensitivity.

5 Results and discussion

In this section, I present the result of growth and characterization studies of MnBi/FeCo and MnGa/FeCo bilayer systems. In the first part, I discuss the growth optimization of "MnBi polycrystalline c-axis textured thin films". Effect of growth conditions such as annealing temperature, film thickness and composition of sputtering target on the degree of crystallinity and resulting magnetic properties including saturation magnetization, coercivity and magnetic anisotropy has been investigated. The result of this growth study has been published in Ref. [34]. In the second part, "the exchange coupling effect in bilayer system of MnBi/FeCo" has been investigated. Effect of thickness and composition of FeCo soft magnetic layer on the degree of interlayer exchange coupling have been experimentally studied. To have a better understanding of the structural and interfacial factors such as growth orientation and interface roughness which control the exchange coupling, HR-TEM evaluations along with DFT calculations and micromagnetic simulations have been performed. The result of these two studies have been published in Refs. [192] and [106]. The third part of this section is dedicated to the growth of "MnGa epitaxial (001) thin films" as the hard magnetic phase in the exchange coupled MnGa/FeCo bilayers. Here, the effect of substrate temperature on the degree of crystallinity and the resulting magnetic properties including saturation magnetization, coercivity and magnetic anisotropy has been investigated in MnGa thin films. Finally, "the exchange coupling in MnGa/FeCo epitaxial bilayers" has been studied both experimentally and theoretically considering the effect of soft layer thickness and composition. The result of these studies has been published in Ref. [193].

5.1 MnBi polycrystalline c-axis textured thin films

5.1.1 Annealing study

As it can be observed from XRD spectrum shown in Fig. 5.1, for as-deposited MnBi films without annealing only Bi peaks were observed. The fact that Mn peaks could not be observed can be explained by the amorphous state of Mn after room temperature deposition. Fig. 5.2 shows room-temperature XRD patterns of MnBi thin films as a function of T_{ann}. Peak indexing shows hexagonal MnBi with space group of $P63/mmc$ and traces of residual bismuth for some films. When T_{ann}>360 °C, MnBi (002) and (004) peaks appear indicating the formation of LTP MnBi with c-axis texture. The residual Bi (003) peaks disappear for T_{ann}>400 °C. Note that the unreacted Bi is also c-axis oriented. The highest X-ray intensity of the MnBi peaks was observed for T_{ann}=415 °C. The calculated c-axis lattice parameter from the (002) peak is c=6.115±0.003 Å, which is in agreement with the reported value for single crystalline LTP MnBi [39]. There is an improvement in crystallinity and degree of texture upon increasing annealing temperature, i. e., highest crystallinity is achieved only at the highest possible annealing temperature before reaching the thermodynamic decomposition temperature. Once the annealing temperature is increased above $T_{\text{ann}} \sim 420$ °C, the MnBi film decomposes to Bi and Mn and all reflections disappear pointing towards an amorphous state. As a result, the highest degree of crystallinity is obtained close to the stability phase boundary beyond which the compound becomes unstable.

Room-temperature magnetization data for both out-of-plane and in-plane directions for MnBi thin films annealed at different temperatures (T_{ann}) between 265 °C and 430 °C are shown in Fig. 5.3. For a better overview of the important trends, the relative values for saturation magnetization M_{s}, remanent magnetization M_{r}, magnetic anisotropy K_{u}, maximum energy product $(BH)_{\text{max}}$, and coercivity for out-of-plane and in-plane direction as a function of annealing temperature are summarized in Fig. 5.4 (a) - (f), respectively. The volume saturation magnetization increases with increasing the annealing temperature. This is clearly related to the increasing amount of the LTP MnBi phase in the sample. A maximum of M_s=600±22 emu/cm^3 (0.60 MA/m) is obtained for the film annealed at 415 °C. On the other hand, the coercive field shows a maximum at 365 °C reaching 12 kOe (1.2 T) and 14 kOe (1.4 T) in out-of-plane and in-plane direction, respectively. A further increase in annealing temperature decreases

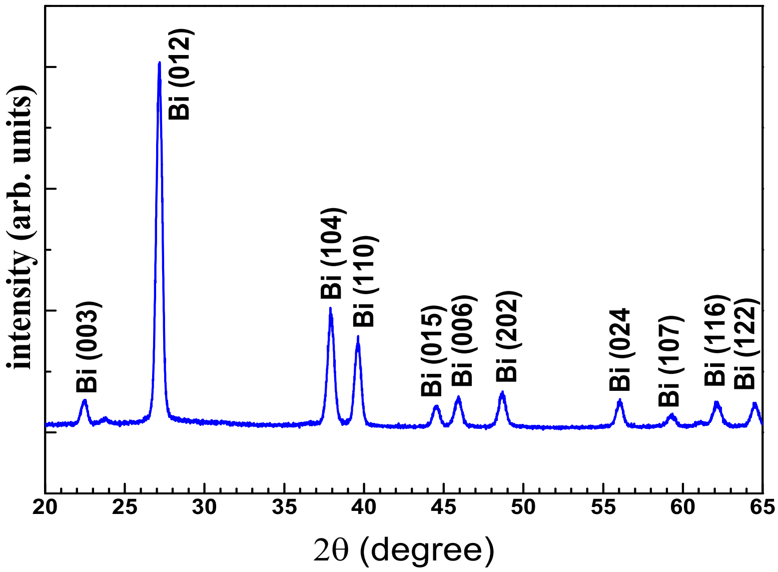

Figure 5.1: XRD pattern of as-deposited MnBi thin film without annealing.

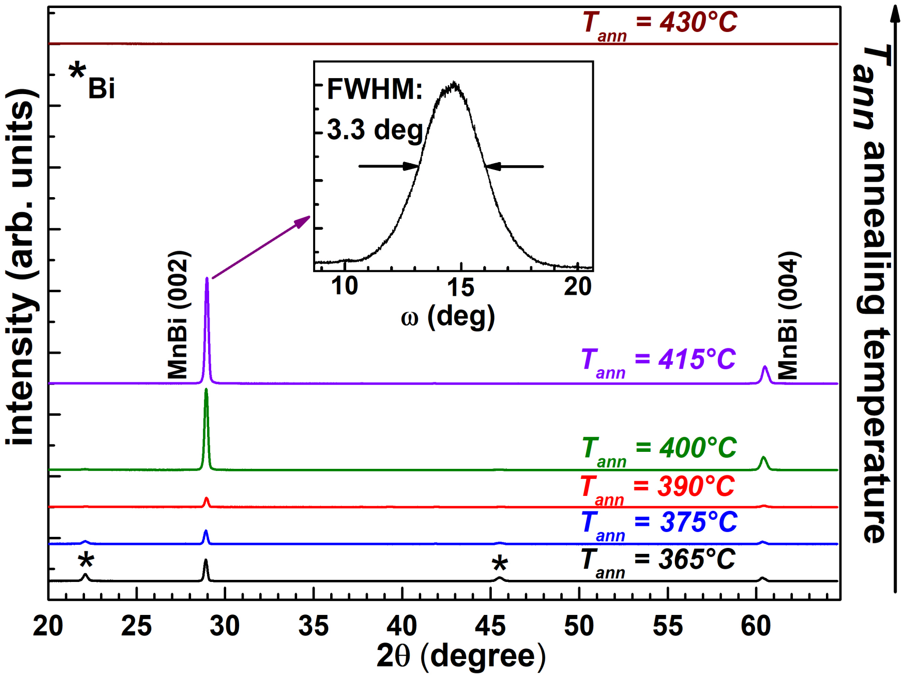

Figure 5.2: XRD patterns of MnBi thin films annealed at different temperatures, T_{ann}, between 365 °C and 430 °C. The spectra are vertically offset for clarity. The peaks originating from residual bismuth in the films are labelled with (*) indexing Bi (003) planes. The inset shows rocking curve collected from MnBi (002) peak for the sample annealed at T_{ann} =415 °C figuring a wide FWHM, adapted from Ref. [34].

the coercivity to 3.5 kOe (0.35 T) in out-of-plane and 10 kOe (1 T) in in-plane direction until the sample starts to decompose.

Such a maximum in coercivity was previously observed for different magnetic materials and has been attributed to the grain size distribution [194]. A single crystal sample has been shown to have a vanishing coercivity [39], while in bulk polycrystalline materials much higher values are obtained due to

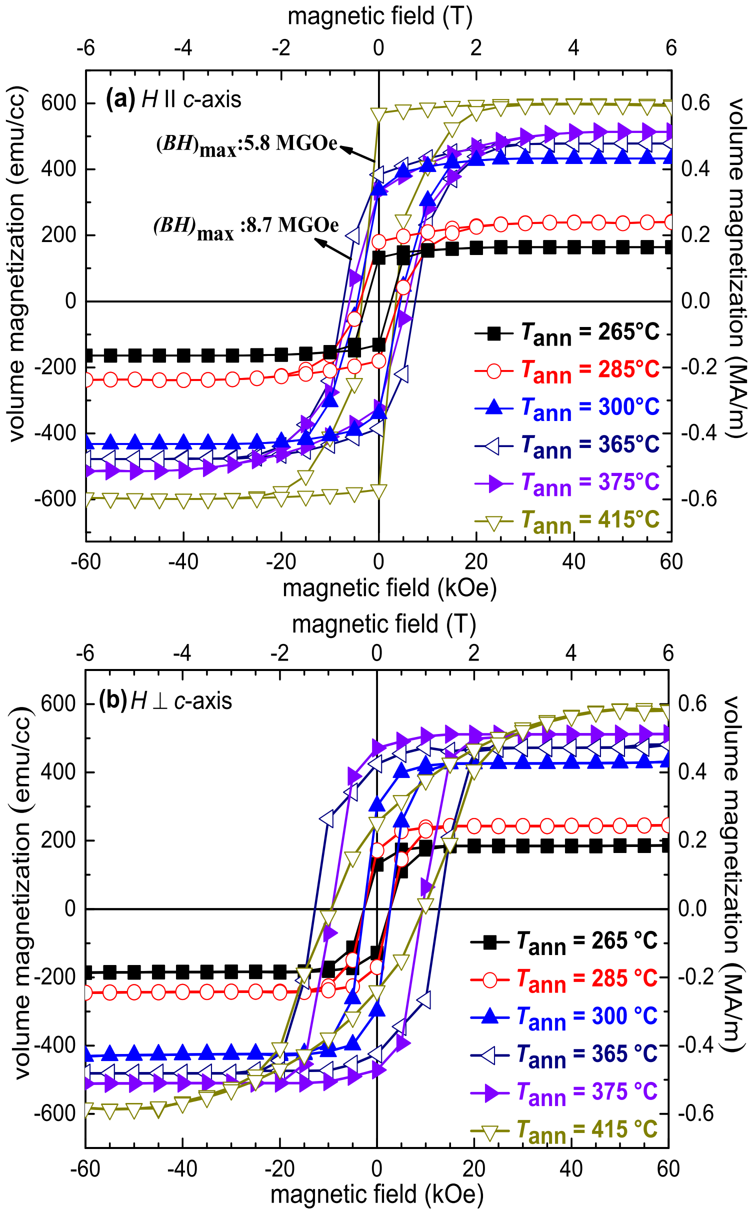

Figure 5.3: (a) Out-of-plane and (b) in-plane magnetization data for MnBi thin films annealed at different temperatures (T_{ann}) between 265 °C and 415 °C and measured at 300 K, adapted from Ref. [34].

extrinsic effects such as domain wall interaction with multiple grain boundaries [29, 30, 38]. The increase in coercivity up to 365 °C annealing temperature is due to both, the improvement of the crystal quality, and the presence of unreacted Bi (see the XRD patterns in Fig. 5.2 for Bi reflections) and likely some residual Mn-O. With further increasing of the annealing temperature, the resulting grain growth reduces the coercivity. The combination of both effects leads to a nearly constant coercivity of 10 kOe (1 T) for T_{ann} above 365 °C.

The large in-plane coercivity is related to the columnar grain growth via the preferential orientation of grain boundaries parallel to the *c*-axis. This leads to strong domain wall pinning when the magnetization direction is in-plane. Such a grain growth is expected according to the zone classification suggested by Thornton (see section 3.2.) [136]. The columnar grain growth is often associated with a large full width at half maximum (FWHM) of the rocking curve ($\sim$ 3.3 degrees)(e. g. see inset of Fig. 5.3-(b)).

The moderate growth temperature used for MnBi leads to a moderate surface diffusivity, but a largely suppressed bulk diffusivity. Under these conditions, the sputtered films tend to show columnar grain growth with voided boundaries. These grains may slightly tilt when relaxed resulting in a large full width of half maximum of the rocking curve.

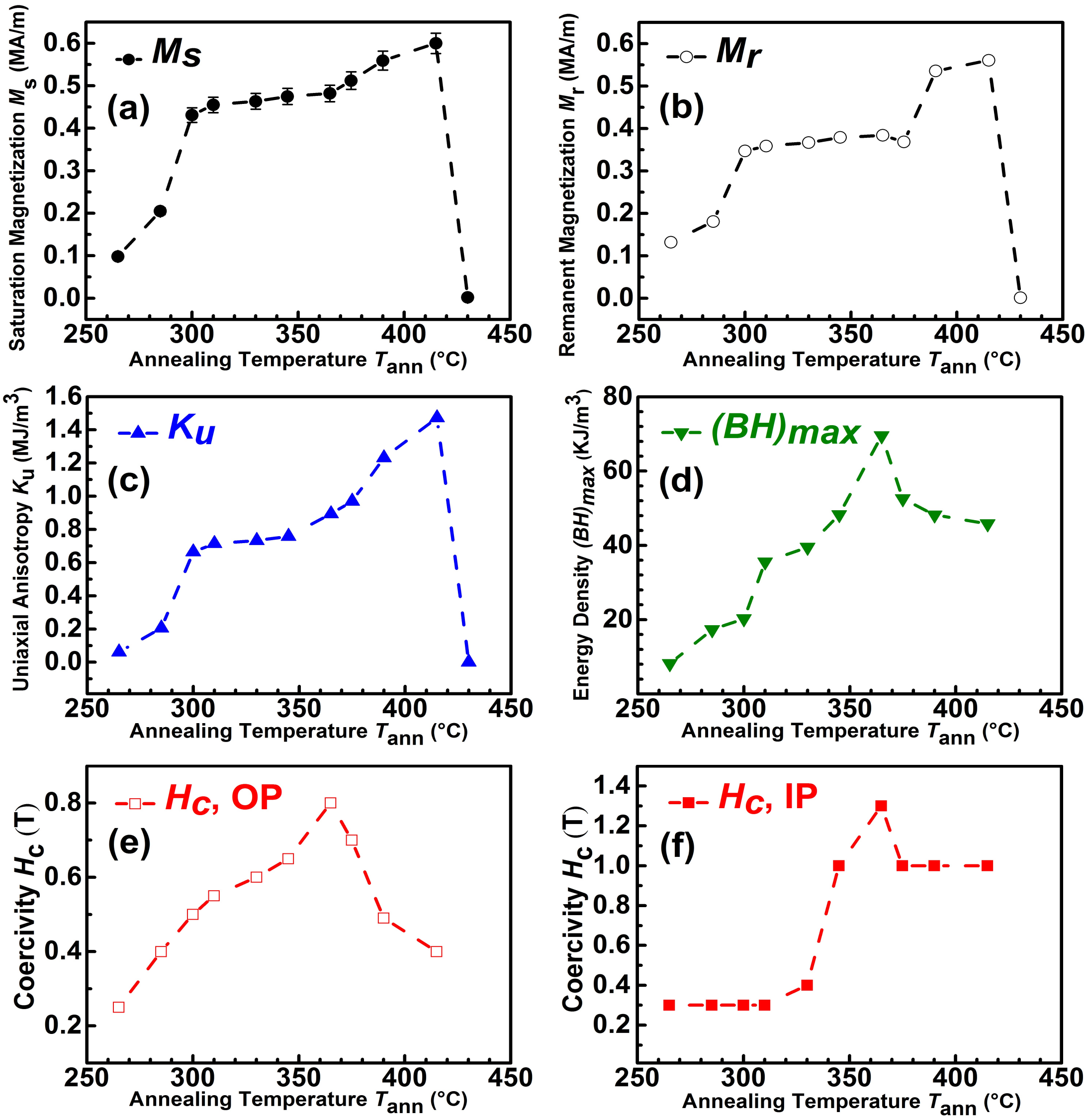

Figure 5.4: Change in saturation magnetization (M_s), remanent magnetization (M_r), uniaxial anisotropy (K_u), in-plane and out-of-plane coercivity (H_c), and maximum energy product ($(BH)_{\text{max}}$) for MnBi thin films as a function of annealing temperature, adapted from Ref. [34].

The total effective magnetic anisotropy, K_{eff}, in thin films can be expressed as $K_{\text{eff}} = K_u - 2\pi M_s^2$ (neglecting the surface anisotropy, see Eq. 2.13) [100]. The second term in this equation represents the negative contribution from shape anisotropy for a thin film with demagnetization factor of $N = 4\pi$ (cgs) which tends to force the magnetization direction away from the easy axis towards the film plane. Using $M_s = 600\,\text{emu/cm}^3$, the shape anisotropy is estimated to be $-2\pi M_s^2 = -2.2\,\text{Merg/cm}^3$ ($\sim -0.226\,\text{MJ/m}^3$). On the other hand, K_{eff} can be estimated using the equation $H_s = 2K_{\text{eff}}/M_s - 4\pi M_s$ where H_s is the saturation field extracted from the hard axis hysteresis loops, and $4\pi M_s$ represents the shape anisotropy field (demagnetizing field) (see Fig. 5.3-(b) and Eq. 2.14). The positive total magnetic anisotropy of $K_{\text{eff}}=12.46\,\text{Merg/cm}^3$ ($1.246\,\text{MJ/m}^3$) indicates that K_u is large enough to overcome shape anisotropy and to stabilize an out-of-plane magnetization direction. As it can be also seen in Fig. 5.4-(a) and -(c),

M_s and K_u show a similar temperature dependence. K_u reaches a maximum value of 14.72 Merg/cm^3 (1.472 MJ/m^3) for the sample annealed at 415 °C. Similarly, M_s is maximal for the same sample (having the highest degree of c-axis texture).

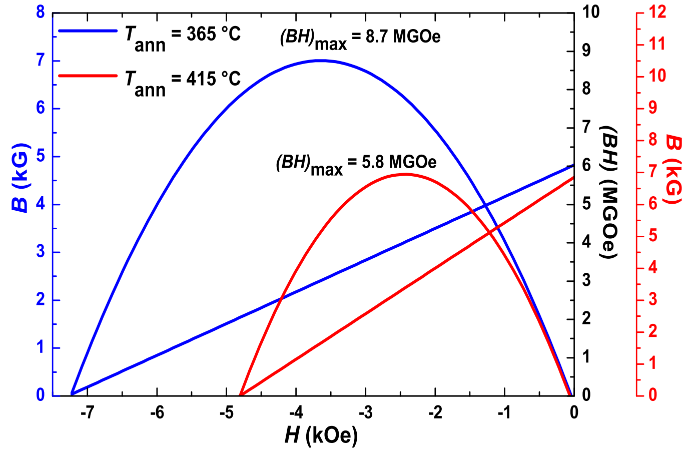

Figure 5.5: Change in energy product vs. external magnetic field for MnBi thin films annealed at T_{ann}=365 °C and T_{ann}=415 °C.

The general trend of the changes in $(BH)_{\mathrm{max}}$ with annealing temperature is shown in Fig. 5.4-(d). To extract the $(BH)_{\mathrm{max}}$ value, first using $B = H + 4\pi M$ equation, the measured $M - H$ curves from the hysteresis data in Fig. 5.3-(a) have been converted to $B - H$ curves. Then using a spline interpolation of the magnetization data in the 2nd quadrant and from the area of rectangles that could be inscribed under the transformed B-H curve, the maximum energy product $(BH)_{\mathrm{max}}$ [KJ/m^3] was calculated for different annealing temperatures (as illustrated also in Fig. 5.5). The sample annealed at 415 °C shows a low $(BH)_{\mathrm{max}} \sim$ 5.8 MGOe (46 kJ/m^3). Considering the high degree of c-axis texture resulting in a saturation magnetization close to a single crystal which reduces the extrinsic anisotropy effects, such a relatively low value for the energy density is expected. The sample which was annealed at a lower temperature of 365 °C and contains unreacted Bi has shown a higher energy density value close to 8.7 MGOe (70 kJ/m^3). This can be attributed to Bi precipitates (likely at MnBi grain boundaries as suggested by TEM images shown in Ref. [43]) which act as pinning centres and increase H_c. From the trends presented in Fig. 5.4, it can be seen that apparently $(BH)_{\mathrm{max}}$ follows the same trend as the coercivity upon increasing the annealing temperature, while the increasing saturation magnetization seems to play a less significant role. Therefore, to further improve the maximum energy density for LTP MnBi samples free of unreacted Bi contents, one needs to achieve higher coercivity through single domain particles with larger grain sizes closer to the critical particle diameter [33, 194].

5.1.2 Effect of measurement temperature

The out-of-plane magnetization data for the MnBi thin film annealed at 365 °C which has shown the highest coercivity among all samples is measured at different working temperatures to investigate the temperature dependence of coercivity and magnetic moment (Fig. 5.6). Due to limitations in the technical measurement setup, temperatures higher than 350 K were not accessible. The results is summarized in Fig. 5.7.

The temperature dependence of coercivity and saturation magnetization for both, out-of-plane and in-plane directions, for the MnBi thin film sample annealed at 365 °C are plotted in Fig. 5.7. The corresponding data points for the graphs were extracted from the hysteresis loops measured at different

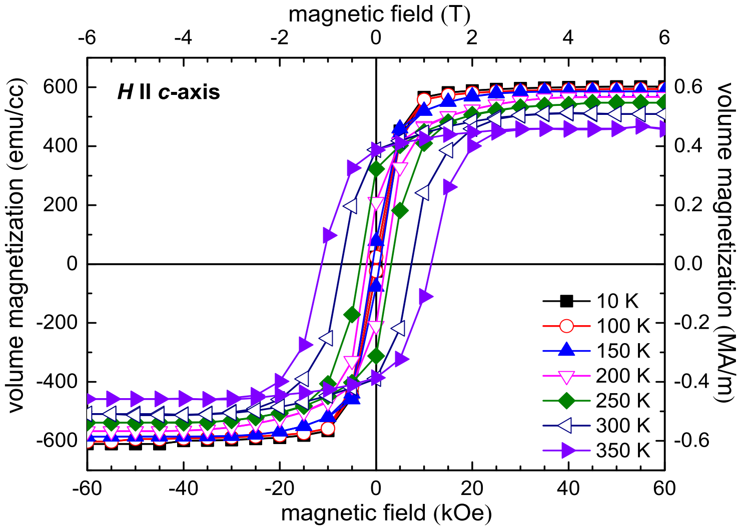

Figure 5.6: Out-of-plane magnetization data for the MnBi thin film annealed at T_{ann}=365 °C measured between 10 K and 350 K.

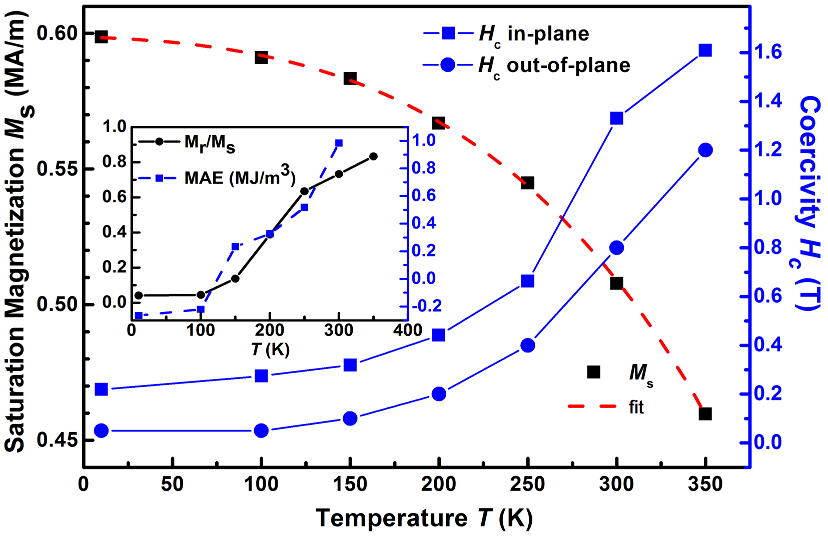

Figure 5.7: Temperature dependence of H_c and M_s for the MnBi thin film annealed at 365 °C in out-of-plane and in-plane direction. The inset shows the change of M_r/M_s ratio (black solid curve) and calculated MAE (blue dashed curve) with temperature for out-of-plane direction of applied field, adapted from Ref. [34].

working temperatures between 10 K and 350 K. As the temperature is decreased, both out-of-plane and in-plane coercivity decrease. For working temperatures lower than 100 K, the coercivity starts to saturate below 1 kOe. Above 100 K, the coercivity shows a positive temperature coefficient and increases drastically from only 1 kOe (0.1 T) at 100 K to almost 12 kOe (1.2 T) at 350 K.

The inset to Fig. 5.7 shows the temperature dependence of the ratio of the remanent magnetization to the saturation magnetization, M_r/M_s, in out-of-plane direction (black solid curve) as well as the temperature dependence for the calculated magnetocrystalline anisotropy energy (blue dashed lines, see below for explanations on the DFT calculations). Both quantities are not related but indicate the spin reorientation temperature at 100 K. Since below 100 K, the M_r/M_s ratio becomes negligible while above 100 K it increases rapidly with increasing temperature to 0.85 at 350 K. For LTP-MnBi as a ferromagnetic phase with uniaxial anisotropy, the relation of $M_{\mathrm{r}}= M_{\mathrm{s}}cos(\theta)$ applies between remanent magnetization and saturation magnetization with θ as the angle between the applied field and easy axis of magnetization. Therefore, it can be concluded that below 100 K, the easy axis is flipping nearly fully into the basal plane corresponding to a spin reorientation.

In previous studies, spin canting was detected around 110 K by neutron diffraction [30], and a confinement of the magnetization direction into the ab-plane was found in a single crystalline LTP-MnBi sample [39]. To shed light on the origin of the spin-reorientation transition, density functional theory (DFT) calculations were performed by Jun. Prof. Dr. Hongbin Zhang from TU Darmstadt using the pseudo-potential plane waves method as implemented in the VASP code [184]. The calculations were performed on a 28×28×20 k-mesh to guarantee good convergence of the magnetocrystalline anisotropy energy (MAE). The d-orbitals of the Mn atoms were treated using the generalized gradient approximation (GGA) plus U (on site Coulomb interaction) method, with U=3.2 eV which leads to a uniaxial anisotropy for MnBi at 100 K. The U value is chosen such that the spin reorientation transition occurs at 100 K. This spin reorientation corresponds to a sign change of magnetic anisotropy from positive to negative showing that the magnetic anisotropy flips from out-of-plane direction into the ab-plane with decreasing temperature. All the calculations were done with the experimental c-lattice parameters deduced from XRD measurements, and the corresponding a-lattice parameters were extracted from Ref. [28] with all other parameters fixed. As shown in the inset of Fig. 5.7, it can be seen that the MAE value from the performed DFT calculations reaches $\sim$ 1.10 MJ/m^3 at 300 K which is consistent with the experimental value measured for MnBi thin film in the current study (1.86 MJ/m^3). The lower calculated value can be attributed to the a-lattice parameters which were used for DFT calculations and could differ from the actual a-lattice constant in the film grown in this study. The positive temperature coefficient obtained for MAE from the calculation is in agreement with the increasing coercivity which was observed for the experimental samples upon increasing temperature. It also agrees with previous calculations [196, 197, 198].

It was shown from previously reported DFT calculations, that even small changes in the a and c lattice parameters have a strong influence on MAE, leading to a decrease in both anisotropy and coercivity at lower temperatures [196, 197]. The effect of temperature on the unit cell volume was also experimentally investigated for both single crystalline bulk and polycrystalline thin film samples previously, showing that the c/a lattice constant ratio will increase with temperature [39, 42]. The reduction in MAE is further enhanced in thin films because the in-plane shape anisotropy grows quadratically with increasing magnetization upon cooling [100]. This reduces the effective anisotropy which in turn will result in a further decrease in coercivity.

The magnetization vs. temperature data in Fig. 5.7 was fitted using a combination of Bloch's law at low temperatures and a mean field type transition close to the Curie temperature as suggested by Guo *et al.* [199, 200]:

$$M_s(T) = M_0(T)[(1-p)(1-B(\frac{T}{T_c})^{\frac{3}{2}}) + p(1-(\frac{T}{T_c})^{\frac{1}{2}})] \tag{5.1}$$

where $p = (\frac{T}{T_c})^n$ is a weight function in a way that spin-wave behavior, $(1-B(\frac{T}{T_c})^{\frac{3}{2}})$, and critical point behavior, $(1-(\frac{T}{T_c})^{\frac{1}{2}})$, are recovered at low and high temperatures, respectively. Since highest possible measurement temperature in MPMS device is 350 K, the significance of the parameters is low. It is not possible to differentiate between a mean field exponent $(1-\frac{T}{T_c})^{\frac{1}{2}}$ or a Heisenberg critical behaviour with exponent $\frac{1}{3}$ [200]. Best fit to the data has been achieved using M_0= 600 emu/cm^3, B=0.3 and n=2 (i. e., with weight function $p \approx (T/T_c)^2$). The estimated Curie temperature from this fit is $\sim$ 510 K which is lower than the reported value for single crystalline LTP MnBi (∼630 K) [39]. This could be due to slight off-stoichiometry.

5.1.3 Thickness and composition study

Thickness and composition study was briefly performed with a few samples to check the effect of MnBi layer thickness and starting composition of sputtering target on crystallinity and magnetization for the resulting c-axis textured MnBi thin films.

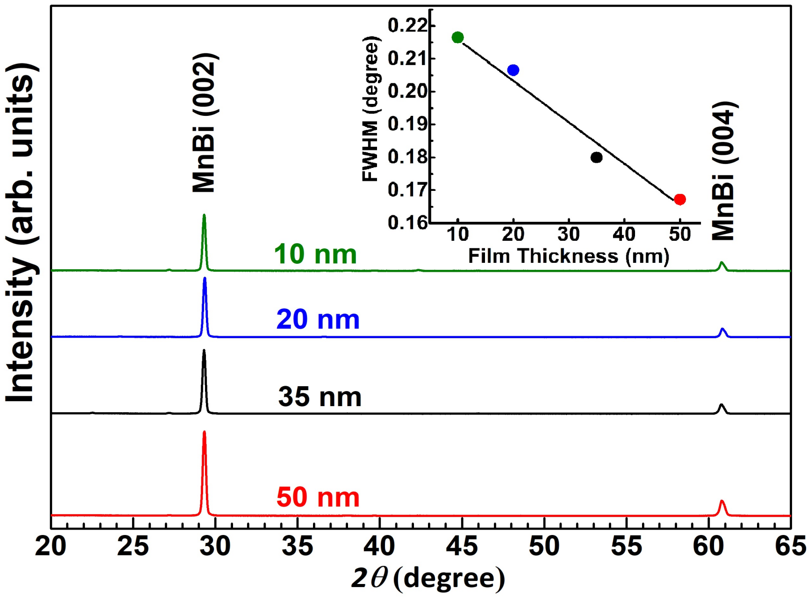

Figure 5.8: XRD patterns of MnBi thin films deposited with different thickness (10 nm, 20 nm, 35 nm and 50 nm) on glass substrates and post-annealed at T_{ann}= 415 °C. Inset shows changes in FWHM values for MnBi (002) peak as a function of film thickness extracted from rocking curve measurements.

To study the effect of thickness on crystalline quality and magnetic properties of resulting MnBi thin films, four $Mn_{55}Bi_{45}$ (at.%) thin films were deposited with different thicknesses of 10 nm, 20 nm, 35 nm and 50 nm on glass substrates. All of these films were annealed at the same annealing temperature, T_{ann}, of 415 °C and then *ex situ* measured by XRD and SQUID to evaluate their structural and magnetic properties. Fig. 5.8 shows XRD patterns collected for these MnBi samples with different thickness. According to the XRD patterns, only strong (002) peaks from MnBi can be observed on these patterns, the intensity of which will increase upon increasing thickness as expected. The inset to Fig. 5.8 represents the change in FWHM value for MnBi (002) peak upon increasing the film thickness obtained from rocking curve measurements. As shown on this plot, the FWHM value will decrease with increasing the thickness of MnBi film which implies that the thicker films have a higher degree of crystallinity compared to the thinner films.

Fig. 5.9 shows out-of-plane hysteresis loops measured for these four MnBi films with different thicknesses at 300 K. One hysteresis loop measured with the applied field in direction of hard axis was also included as a reference. According to the magnetization data presented in this graph, the MnBi layer with higher thickness shows higher saturation magnetization while the MnBi layer with the lowest thickness shows a more rectangular hysteresis loop with higher coercivity meaning a higher energy product. The lower the thickness, the lower the degree of crystalinity according to the XRD patterns and FWHM exctracted from MnBi (002) peak. On the other hand, the thinner the layer, the higher the coercivity which could be attributed to existence of more defects, areas with less degree of crystallinity and some secondary phases such as unreacted Bi or Mn in the first grown monolayers close to the substrate. This can increase the coercivity while resulting in less volume of LTP-MnBi magnetic phase and less density compared to the ideal value of volume used in the magnetization calculations which leads to a slightly lower saturation magnetization.

The effect of different starting stoichiometries of MnBi alloy sputtering targets on the structural and magnetic properties of the resulting MnBi thin films were also briefly investigated using three different compositions: One stoichiometric target with composition of $Mn_{50}Bi_{50}$ and two off-stoichiometric targets with compositions of $Mn_{55}Bi_{45}$ and $Mn_{60}Bi_{40}$ (at.%). Three MnBi thin films were deposited with 50 nm thickness using each of the above mentioned sputtering targets and annealed at $T_{\text{ann}} = 365\,^{\circ}\text{C}$. The crystallinity and magnetization were investigated for these films using XRD and SQUID measurements. As it is shown in XRD patterns in Fig. 5.10, the highest intensity of MnBi (002) peak belongs to the film grown from $Mn_{55}Bi_{45}$ (at.%), the higher or lower amount of Mn in the sputtering targets both resulted in lower degree of crystallinity in the grown films after annealing. This is more significant for the film grown from $Mn_{60}Bi_{40}$ (at.%) alloy target.

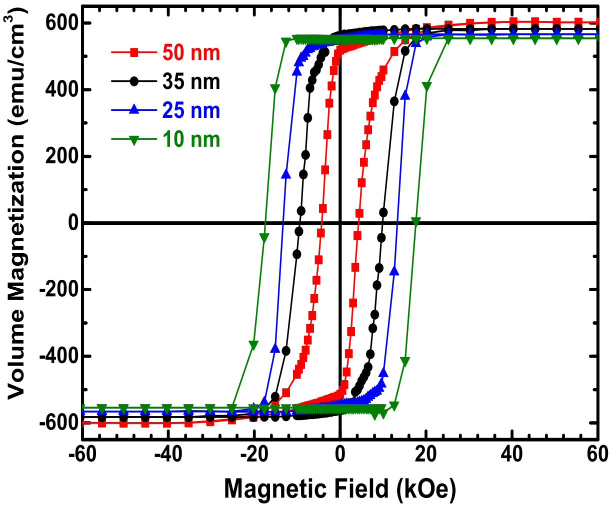

Figure 5.9: Room-temperature out-of-plane magnetization data collected from MnBi thin films deposited with four different thickness (10 nm, 20 nm, 35 nm and 50 nm) on glass substrates and post-annealed at $T_{\text{ann}} = 415\,^{\circ}\text{C}$.

The room-temperature out-of-plane magnetization data measured for the films grown from the alloy targets with different compositions were presented in hysteresis loops in Fig. 5.11. In accordance with the XRD patterns, the MnBi film grown from $Mn_{55}Bi_{45}$ (at.%) alloy target shows the highest saturation magnetization and a more rectangular hysteresis loop. The two other starting stoichiometries both resulted in lower total saturation magnetizations which was even smaller in the case of MnBi film with starting stoichiometry of $Mn_{60}Bi_{40}$ (at.%). Since the measured coercivity values for all three films are nearly the same, it can be concluded that the composition is mostly affecting the magnetization and not the coercivity. This shows that the coercivity is governed by annealing temperature and presence of unreacted Bi in all of these films. This suggests that deposition using an alloy sputtering target with optimized composition of $Mn_{55}Bi_{45}$ (at.%) leads to the highest magnetization and energy product.

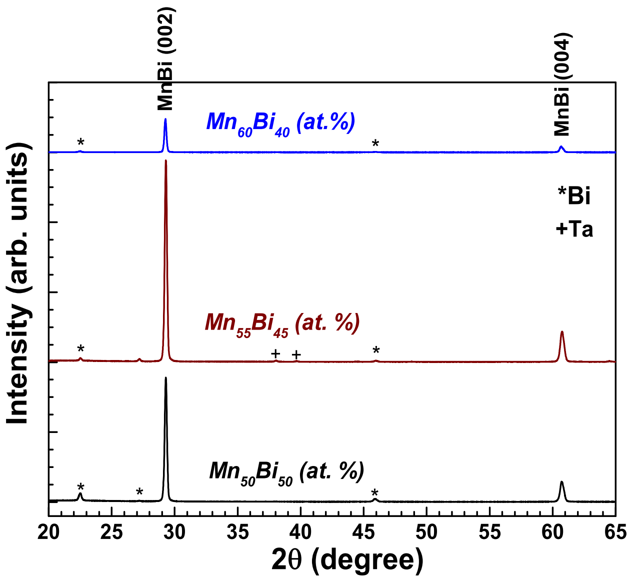

Figure 5.10: XRD patterns of MnBi thin films deposited from alloy sputtering targets with three different starting Mn:Bi stoichiometries (60:40, 55:45 and 50:50 (at.%)) on glass substrates and post-annealed at T_{ann}= 365 °C.

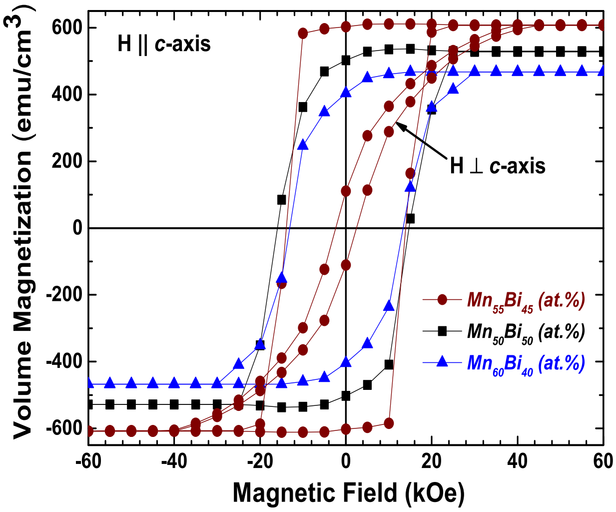

Figure 5.11: Room-temperature out-of-plane magnetization data collected from MnBi thin films deposited from alloy sputtering targets with three different starting Mn:Bi stoichiometries (60:40, 55:45 and 50:50 (at.%)) on glass substrates and post-annealed at T_{ann}= 365 °C.

5.1.4 Magnetic anisotropy

To investigate the temperature dependence of perpendicular magnetic anisotropy constant K_{u}, torque measurements were performed on a LTP MnBi thin film sample after being cut into 1.2 mm × 1.2 mm piece under different applied fields in the range of 1 T to 9 T, and at different temperatures in the range of 10 K-300 K. All the torque curves measured over the temperature range of 110 K to 300 K mainly consist of a two-fold symmetry which indicates the uniaxial magnetic anisotropy mode.

Fig. 5.12 shows the angular dependence of the magnetic torque ($T(\phi)$) measured for the MnBi thin film annealed at 415 °C while rotating under an applied field of 9 T at 300 K. From the data refinement and fitting of a $A\sin(2\theta) + B\sin(4\theta)$ function to the measured torque data using Eqs. 3.58-3.60 [168], a uniaxial magnetic anisotropy constant (K_u) of 18.60 Merg/cm^3 (1.86 MJ/m^3) is obtained. As expected, the value obtained from torque curves is higher than the estimated value using the anisotropy field (H_s) extracted from the intersection of easy and hard magnetization data (which has a large error).

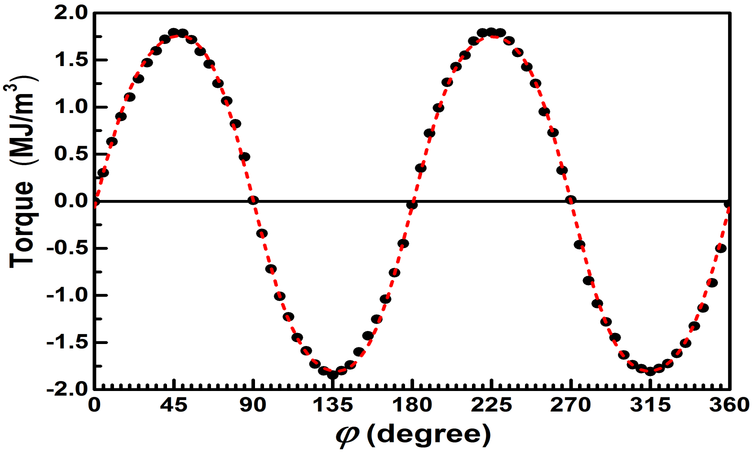

Figure 5.12: Angular dependence of magnetic torque for a MnBi film annealed at 415 °C measured in a torque magnetometer attached to a PPMS device rotating under 9 T magnetic field at 300 K, adapted from Ref. [34].

Fig. 5.13 shows the field dependency of measured magnetic torque curves for the MnBi thin film annealed at 415 °C. The applied field was varied from 1 T to 9 T measured at 300 K. As it can be seen from the measured torque curves on Fig. 5.13, by increasing the applied magnetic field both amplitude of the torque signal and peak offset from 45° are improved. For clarity, the graphs in Fig. 5.14 summarize the calculated unixaial magnetic anisotropy constant (K_u), which is proportional to the amplitude of the sine function, as well as the peak offset from the position of maximum (45°) as a function of applied magnetic field. The plots in Fig. 5.14 are indicative that as applied field increases up to 8 T there is a constant increase observable for the magnetic anisotropy which saturates to $\sim$ 1.8 MJ/m^3 and the maximum peak position moves towards 45° showing a smaller offset. Applying a minimum magnetic field of $\sim 2{\times}H_s$ is necessary to make sure the magnetization is always parallel to the applied field. This means in order to achieve a proper torque signal from which the precise magnetic anisotropy constant in the film can be obtained, the angle between anisotropy and magnetic field must be kept equal to the angle between anisotropy and magnetization.

Fig. 5.15 shows the development trend of collected torque curves at different measurement temperatures under 9 T applied magnetic field. The amplitude of torque signal is constantly increasing upon increasing temperature which proves a positive temperature coefficient for uniaxial magnetic anisotropy constant in MnBi thin film. Below 110 K, the perpendicular magnetic anisotropy vanishes into what could be considered as a small in-plane component and the two-fold symmetry of the graphs turns into a four-fold symmetry which is a sign of competing anisotropies. The improvement of measured uniaxial magnetic anisotropy with temperature is in agreement with what has been observed for the measured hysteresis loops in Fig. 5.6. The graphs in the inset to Fig. 5.7 show a spin reorientation temperature of ~110 K which has been observed also for the measured torque curves.

Fig. 5.16 shows the relation between the uniaxial magnetic anisotropy constant, K_u, and the saturation magnetization, M_s, for the same LTP-MnBi thin film sample in a temperature range from 110 K to 300 K.

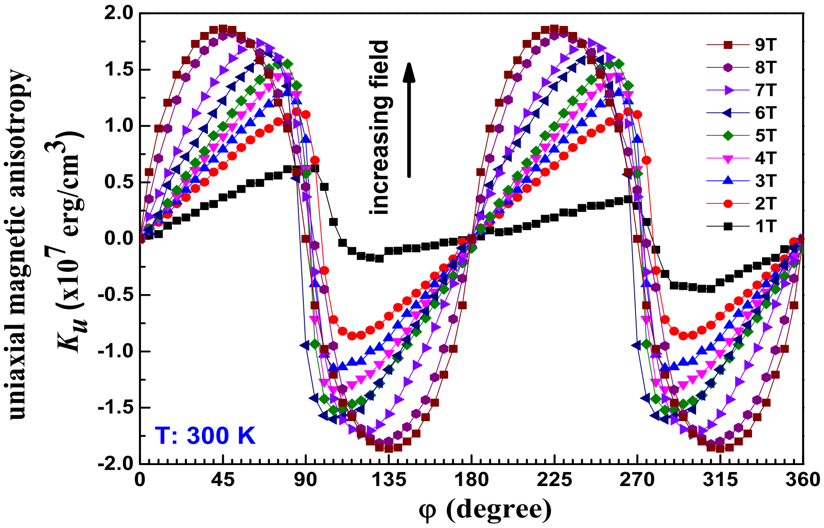

Figure 5.13: Angular dependence of magnetic torque for a MnBi film annealed at 415 °C measured in torque magnetometer under different applied fields 1 T-9 T at 300 K.

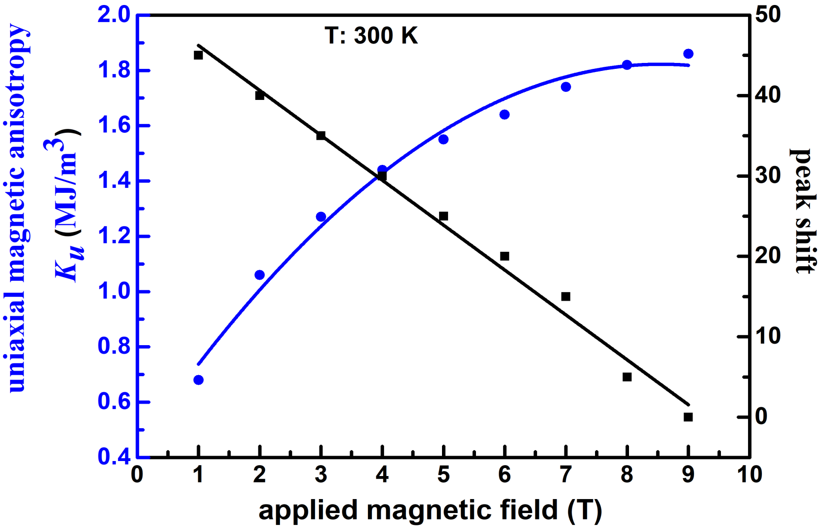

Figure 5.14: Unixaial magnetic anisotropy constant (K_u) for a MnBi film annealed at 415 °C, which is proportional to the amplitude of the sine function fitted to the magnetic torque curves, as well as the peak offset from the position of maximum (45°) as a function of applied magnetic field in the range of 1 T-9 T measured at 300 K.

The values for saturation magnetization have been extracted from the hysteresis loops in Fig. 5.6. The values of uniaxial magnetic anisotropy constant are the measured values obtained from amplitude of the sine function fitted to the torque curves in Fig. 5.15 for different temperatures between 110 K and 300 K. By fitting a polynominal function to the K_u vs. M_s plot, it is found that the K_u is inversely proportional to the tenth power of M_s which shows a very strong dependency. The exponent achieved for MnBi thin film is larger than expected and has an opposite (negative) sign while K_u is expected to be directly proportional to M_s^n with $n = 3$ for uniaxial magnetic anisotropy [79]. However, this is in agreement with the expected positive temperature coefficient for magnetic anisotropy in MnBi. Such a strong dependency of K_u on M_s in the MnBi thin film is important for better understanding of the mechanism of the magnetic anisotropy which implies that other contributions to the anisotropy should also be considered.

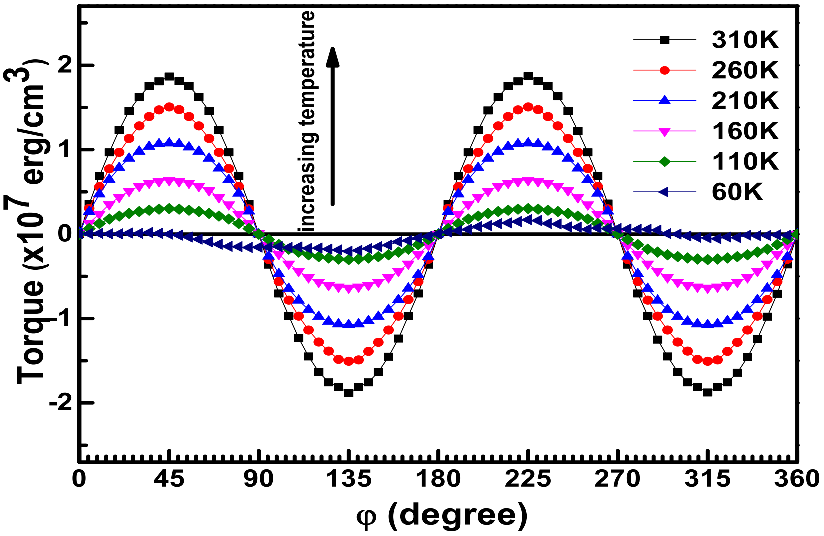

Figure 5.15: Angular dependence of magnetic torque for a MnBi film annealed at 415 °C measured in torque magnetometer under 9 T magnetic field at different temperatures between 60 K to 300 K.

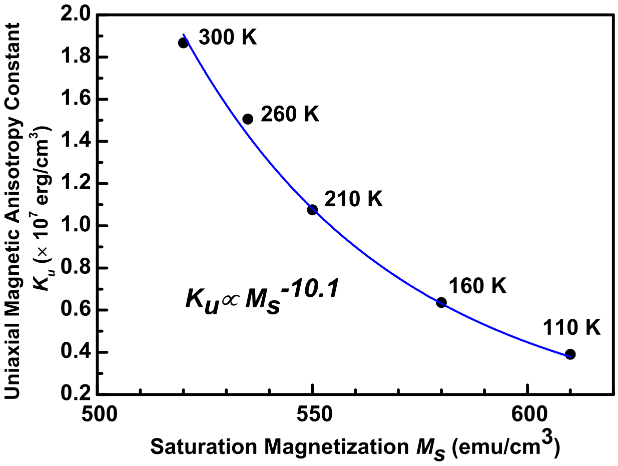

Figure 5.16: Dependency of magnetic anisotropy constant on saturation magnetization for a MnBi film annealed at 415 °C measured at different temperatures between 60 K to 300 K.

5.2 MnBi/FeCo exchange coupled bilayers

To investigate the exchange coupling effect in MnBi/FeCo exchange spring system, bilayer samples with LTP-MnBi film as hard magnetic layer and Fe_xCo_{100-x} (x: 65 or 35 at.%) film as soft magnetic layer have been deposited on glass substrates. More details on deposition process can be found in chapter 4.1. A schematic of such a bilayer is presented in inset to Fig. 5.17. First a LTP-MnBi hard magnetic layer was deposited with ∼ 40 nm thickness and then the FeCo layer was deposited on top of the c-axis textured MnBi layer with varying thickness of 1 nm to 3 nm (in different samples) and different FeCo stoichiometries (Fe-rich or Co-rich phase) to evaluate the exchange coupling effect as a function of thickness and composition of soft magnetic layer.

Fig. 5.17-a shows the XRD patterns collected from $Mn_{55}Bi_{45}/Fe_{35}Co_{65}$ (at.%) exchange spring bilayers with different thicknesses of Co-rich soft magnetic FeCo layer. The peak indexing shows hexagonal

MnBi (002) and (004) peaks with space group of $P63/mmc$ along with some small traces of residual bismuth, caused by the low post-annealing temperature of T_{ann}=365 °C for the MnBi films, indicating the formation of LTP MnBi with strong c-axis texture. The residual Bi (003) peaks observed show that the unreacted Bi is also c-axis oriented. No peaks are observed from FeCo layer as expected from the very low thickness of FeCo thin films. Comparing the intensities of MnBi (002) and (004) peaks in bilayers samples to that of single layer MnBi thin film, it can be observed that all the XRD patterns show nearly the same intensities implying that the crystalline quality of the hard magnetic layer for all bilayer samples is similar.

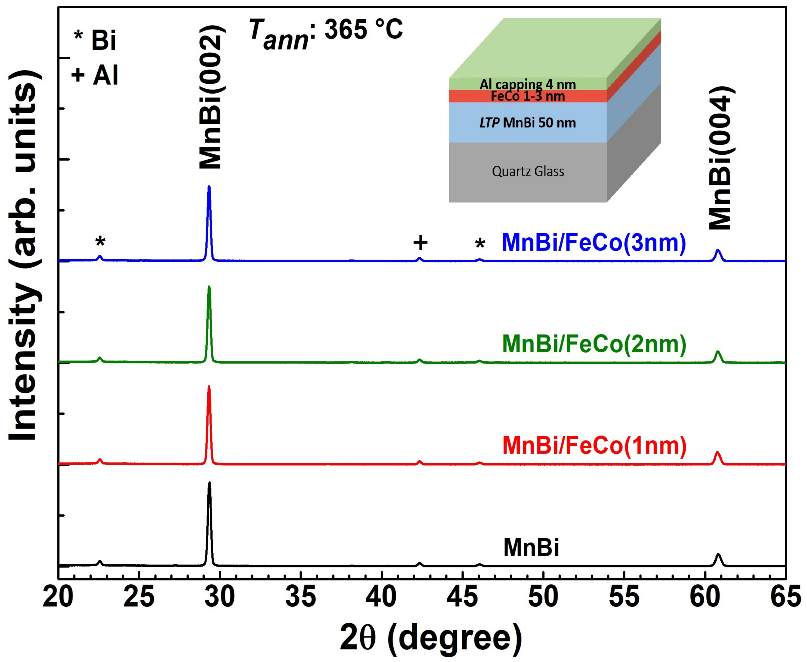

Figure 5.17: (a) XRD patterns collected from exchange spring bilayers of $Mn_{55}Bi_{45}/Fe_{35}Co_{65}$ (at.%) with different thickness of FeCo soft magnetic layer between 1 nm to 3 nm. The LTP-MnBi thin films were annealed at T_{ann}: 365 °C and FeCo layer was deposited at a substrate temperature of T_{sub}: 100 °C. The spectra are vertically offset for clarity. The peaks originating from residual bismuth in the films are labelled with (*) indexing Bi (003) planes. Inset shows a schematic representation of grown bilayers on quartz glass substrate with LTP-MnBi as hard magnetic layer and Fe_xCo_{100-x} as soft magnetic layer, adapted from Ref. [106].

Room-temperature out-of-plane magnetization data measured for MnBi/FeCo bilayer samples in easy direction of magnetization are shown in Fig. 5.18. For the comparison, the out-of-plane hysteresis loop for a single layer MnBi thin film sample has also been included in the same graph. The exchange spring system should reach the higher saturation magnetization adapted from addition of the soft magnetic layer while preserving the coercivity of the hard magnetic phase. The exchange coupling effect between the hard and soft magnetic layers is strong when the bilayer sample shows a magnetically single phase behaviour. As expected by the addition of 1 nm, 2 nm and 3 nm FeCo layer, the saturation magnetization of the bilayer sample monotonously increases while the coercivity stays nearly constant and close to that for the single MnBi layer. According to the graphs in Fig. 5.18, addition of Fe-rich soft magnetic FeCo layer has improved the saturation magnetization more than the addition of Co-rich FeCo layer since $Fe_{65}Co_{35}$ (at.%) phase has a ∼ 20% larger saturation magnetization than the $Fe_{35}Co_{65}$ (at.%) phase [201] and the total magnetization for the bilayer, as mentioned in section 2.5.1., is the volume average of magnetization in hard and soft magnetic layers. The deposition of 1 nm and 2 nm soft magnetic layer on top of MnBi retains the coercivity of hard magnetic phase (∼ 15 kOe with a slight increase), while regardless of the composition of the soft magnetic layer, the addition of 3 nm FeCo decreases the coercivity to 12 kOe.

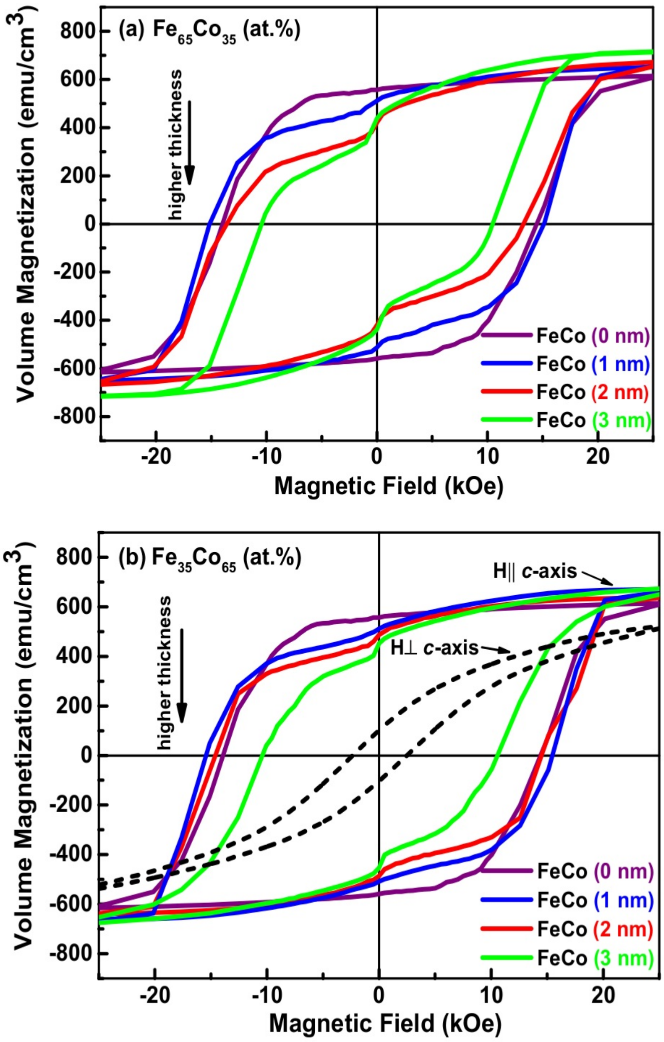

Figure 5.18: Out-of-plane magnetization data for MnBi/FeCo bilayers with different FeCo thickness 0 nm-3 nm measured at 300 K, (a) with a Fe-rich, and (b) with a Co-rich soft magnetic FeCo layer. The dashed line in (b) shows the in-plane magnetization for a single MnBi layer, adapted from Ref. [106].

As mentioned above, the exchange coupling effect between the hard and soft magnetic layers can be considered complete when the bilayer sample shows a magnetically single phase behaviour. The small shoulder with an increasing slope which is observed on the measured out-of-plane hysteresis curves of the double layers during the demagnetization process around zero field indicates that the exchange coupling between the layers is incoherent. Comparing the graphs in Fig. 5.18-(a) and -(b) for a specific thickness, it can be seen that the observed shoulder at zero magnetic field is always more significant with a larger slope in the case of a Fe-rich FeCo layer showing that a Co-rich layer results in a more coherent exchange coupling.

From the hysteresis loops in Fig. 5.18 it can be seen that the degree of coupling decreases with increasing thickness of the soft magnetic layer, as the depth of observed shoulder at zero field crossing increases for a thicker soft magnetic layer. This implies that the layers are behaving more like two separate layers instead of a one single phase bilayer by increasing the FeCo layer thickness. A coherent exchange coupling is only observed for FeCo thickness of 1 nm. However, it is expected that the critical soft layer thickness above which the exchange coupling begins to deteriorate is roughly twice of the domain wall width for hard magnetic layer (see Eq. 2.25), $2 \times \delta_w = \sqrt{\frac{A_h}{K_h}}$) [68, 70, 71], in which δ_{w} is domain wall width, A_{h} is exchange stiffness constant and K_{h} is magnetocrystalline anisotropy for the hard magnetic phase. In case of MnBi/FeCo exchange system with A_{h} (exchange stiffness constant) of $\sim 0.8\times10^{-6}$ erg/cm [190] and K_{h} of $\sim 1.84\times10^{7}$ erg/cm^3 [34], the critical thickness should be as high as $\sim$ 13 nm.

The coupling behaviour in general is not strong for MnBi/FeCo bilayers; specifically in case of a Fe-rich soft magnetic FeCo layer. This shows the optimum thickness of FeCo layer in MnBi/FeCo exchange spring bilayers is only 1 nm which is much lower than the predicted critical thickness of 13 nm. Although, it is observed that a Co-rich FeCo layer is in favour of exchange coupling. Such weak coupling effect in MnBi/FeCo exchange spring system can be attributed to different structural factors including (i) a non-epitaxial hard magnetic layer which most likely results in subsequent growth of a polycrystalline soft magnetic layer on top, (ii) high interface roughness or defects and inhomogeneities present at the interface which could also be a side effect of non-epitaxial growth of the layers, (iii) composition gradient of FeCo layer in the vicinity of the interface. In addition, according to Fig. 5.18-(b), there exists a finite in-plane component of total magnetization in the MnBi hard magnetic layer. The in-plane components of the magnetization, when incompletely or not coupled, lead to a shoulder at the coercive field of the soft magnetic layer (H close to zero).

Using a proper single crystal substrate with a small lattice misfit, it should be possible to grow epitaxial MnBi layer and improve the exchange coupling effect in this system. Not only it will result in a better quality of exchange interface but also the total magnetic properties could be improved by obtaining a higher degree of crsytallinity in both of the hard and soft magnetic layers. Unfortunately, finding a single crystalline substrate which matches the crystalline structure and lattice constant of LTP-MnBi hexagonal phase was not straightforward. Therefore, the effect of a single crystalline hard magnetic layer was studied in section 5.3. by deposition of MnGa (001) epitaxial films and investigating the exchange coupling effect in MnGa/FeCo exchange spring system. Nevertheless, to examine the exchange interface for MnBi/FeCo bilayers and realize which of the above mentioned structural or interfacial factors are playing major role in deteriorating exchange coupling between MnBi and FeCo layers, TEM investigations are performed on one MnBi/FeCo bilayer sample which has shown incoherent ferromagnetic coupling.

5.2.1 Transmission electron microscopy (TEM) of MnBi/FeCo exchange interface

Cross-sectional HR-TEM images have been captured from a MnBi/FeCo bilayer sample to examine the interface between the MnBi and FeCo layers and to investigate the crystalline structure of each layer using the collected diffraction patterns. Moreover, the distribution of different elements across the layer was evaluated in scanning transmission electron microscopy (STEM) mode using energy dispersive x-ray spectrometry (EDX) maps. Fig. 5.19-(a) shows a cross-sectional HR-TEM image of the layers along with fast Fourier transforms (FFTs) collected from each layer in the bilayer sample with a Co-rich soft layer. The HR-TEM image and the sharp diffraction spots in FFTs collected from the MnBi layer confirm the high crystallinity with out-of-plane orientation. The FeCo layer, in contrary, shows a polycrystalline structure. Three different areas have been analyzed in the FeCo layer which are all crystalline, but the examined areas in the upper and lower FFTs (FFT-A1 and -A3, inset of Fig. 5.19-(a)) are slightly misoriented. The reflections in the middle FFT pattern (FFT-A2, inset of Fig. 5.19-(a)) in FeCo layer can be indexed as (110) lattice planes.

As it can be seen in the cross-section HR-TEM image of the MnBi/FeCo bilayer, a few atomic layers of FeCo layer grown on MnBi at the interface are disordered. This was expected since the (001) textured MnBi layer has not grown epitaxially and, in addition, FeCo and MnBi layers have different crystalline structures, i. e., hexagonal structure in MnBi and bcc structure in FeCo. Therefore, the MnBi and FeCo layers show a lattice misfit which results in the growth of a polycrystalline FeCo layer.

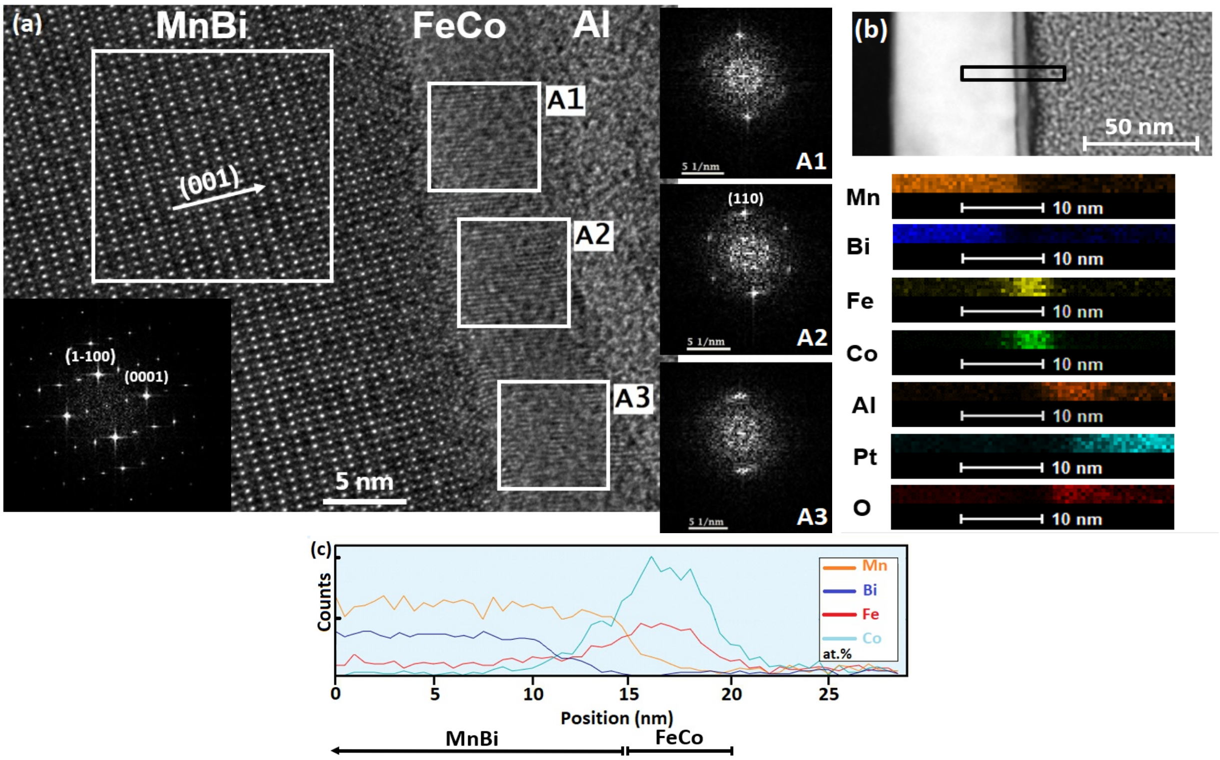

Figure 5.19: (a) Cross-sectional high resolution transmission electron microscopy (HR-TEM) image from MnBi/FeCo bilayer sample (c-axis textured MnBi hard magnetic layer has thickness of ∼ 50 nm and polycrystalline Co-rich FeCo soft magnetic layer has thickness of ∼ 5 nm), (b) STEM image from cross section of the layers along with EDX mapping for each element : Mn, Bi, Fe, Co, Ta, Pt and O across the layers, (c) composition gradient of Mn, Bi, Fe and Co across a 25 nm scan length close to MnBi/FeCo interface, adapted from Ref. [106].

EDX mapping is performed on the enclosed area in Fig. 5.19-(b) to analyse the elemental distribution in the bilayer sample. The result of the EDX mapping is consistent with the phases present in each layer. Close to the interface between the two layers, the Bi concentration starts to decrease earlier than the Mn concentration, resulting in a ∼ 3 nm thick Mn-rich layer at the interface. Fig. 5.19-(c) shows the composition change for Mn, Bi, Fe and Co elements measured across the two layers. As expected at the area close to the MnBi/FeCo hard/soft magnetic interface, the distribution of elements starts to vary meaning that the Mn and Bi contents are both continuously decreasing while the Fe and Co contents in the film are increasing. However, it can be seen that the composition gradient for Mn at the interface shows a steeper slope compared to Bi, and a small amount of Mn is still present until ∼ 3 nm close to FeCo layer. This suggests that there has been diffusion of Mn towards the interface most probably as a result of annealing. The measured elemental composition gradient also confirms the expected stoichiometries for each layer. According to the quantitative EDX analysis from this specific area on the cross-section of the bilayer sample, the MnBi layer shows a stoichiometry of Mn:Bi ratio of 1.4 corresponding to a composition of $Mn_{58}Bi_{42}$ (at.%), which varies across the layer. The measured stoichiometry for the FeCo layer shows a Co:Fe ratio of 1.84, which nearly corresponds to a composition of $Fe_{35}Co_{65}$ (at.%).

5.2.2 Theoretical investigations of MnBi/FeCo exchange interface

In order to shed light on the possible mechanism which affects the performance of the MnBi/FeCo exchange spring magnets, density functional theory (DFT) calculations and micromagnetic simulations (see the next section) were carried out with a focus on the interface properties. Tab. 5.1 summarizes the result of DFT calculations for interface formation energy (γ^{int}), interface exchange coupling energy (J^{int})[187, 188], and interface exchange constant (A^{int}) as the measures to compare differences in thermodynamic stability and exchange coupling at the hard/soft interface by changing the crystalline structure and orientation.

To calculate above-mentioned values, a MnBi (001) layer with either a crystalline or an amorphous (disordered) FeCo layer on top is modelled using VESTA code [115]. Fig. 5.20 shows the atomic structures of the most favorable configurations after the atomic relaxation for MnBi (001)/ crystalline FeCo (110) (which after DFT atomic relaxation becomes MnBi (001)/disordered FeCo (110)), and MnBi (001)/amorphous FeCo (111) interfaces. During the atomic relaxation of the MnBi (001)/ crystalline FeCo (110) interface, the FeCo layer undergoes an atomic reconstruction with a peculiar spiral fashion which has the minimum energy configuration. Moreover, the final structure of the MnBi (001)/amorphous Fe_3Co_5 (110) interface is not stable and during the atomic relaxation transforms into a more ordered (almost crystalline) state which is opposite to the case of the MnBi (001)/amorphous Fe_3Co_5 (111) interface. In case of a crystalline FeCo layer, two different cases one with (111) and one with (110) crystalline orientation are considered which show different interfacial lattice misfits with respect to MnBi layer.

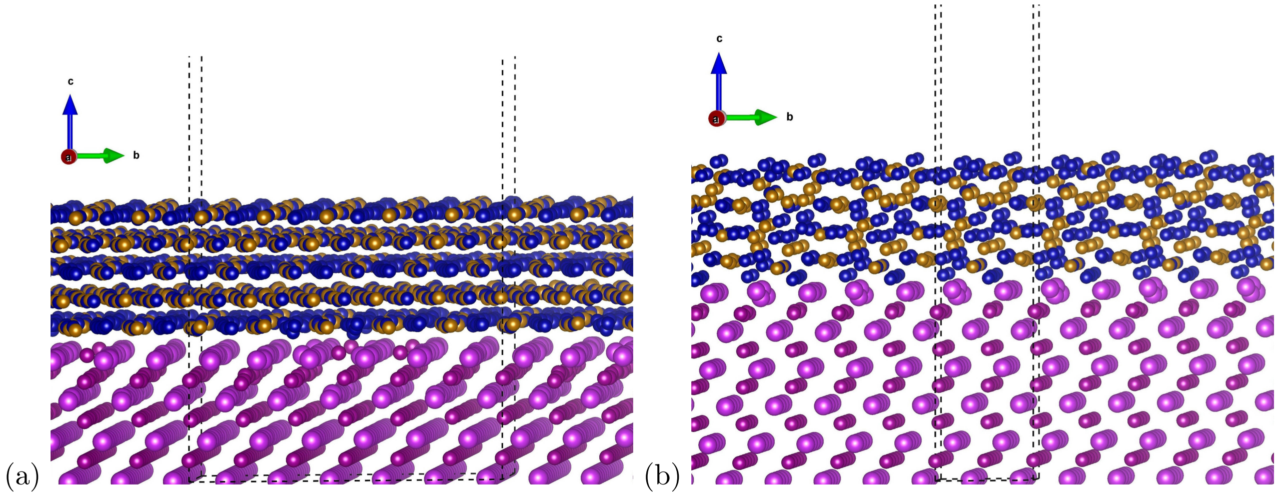

Figure 5.20: Schematic of atomic structures after DFT relaxation (a) MnBi (001)/disordered FeCo (110) and (b) MnBi (001)/amorphous FeCo (111) interfaces demonstrated using VESTA [115]. Mn, Bi, Fe and Co are shown with small dark violet, large light violet, gold and blue colours, respectively. The 1×1×1 unit cell of each orientation is indicated with dashed line. Figure is adapted from supplemental material provided with Ref. [106].

According to the DFT calculation results shown in Tab. 5.1, the interface formation energy of the MnBi (001)/crystalline Fe_3Co_5 (110) interface is lower than that of the MnBi (001)/crystalline Fe_3Co_5 (111) case. This can be related to the fact that MnBi (001)/ Fe_3Co_5 (110) interface has a lower lattice mismatch compared to MnBi (001)/ Fe_3Co_5 (111) case and therefore is more probable to form. However, the rather similar interface formation energies (in the range of 127-130 meV/Å^2) suggest the possible coexistence of the crystalline (110) and disordered structures at the interface. In the cross-sectional HR-TEM image (Fig. 5.19-(a)) at the FeCo side, a crystalline FeCo (110) region (with slight misorientation

Table 5.1: Calculated values of interface formation energy γ^{int}, interface exchange coupling energy J^{int}, exchange constant A^{int} and lattice misfit (longitudinal and angular) obtained from DFT calculations. The disordered (110) structure is reconstructed and lost its short range order compared to crystalline (110) structure. The amorphous (111) is completely irregular. Table is adapted from Ref. [106].

Composition	Lattice misfit	Surface termination	Orientation	Final phase after relaxation	γ^{int} (eV/Å^2)	J^{int} (J/m^2)	A^{int} (pJ/m)
MnBi/Fe_3Co_5	7.1%, 0°	Bi-Co	(111)	crystalline	0.137	0.129	5.4
MnBi/Fe_3Co_5		Mn-Co	(111)	crystalline	0.180	0.127	5.3
MnBi/Fe_3Co_5		Bi-Co	(111)	amorphous	0.130	0.082	2.9
MnBi/Fe_3Co_5	4.8%, 10.5°	Bi-Co	(110)	crystalline	0.129	0.260	5.9
MnBi/Fe_3Co_5		Bi-Co	(110)	disordered	0.127	0.082	1.9

in some areas) along with disordered regions close to the interface are observed which is in agreement with the result of the DFT calculations.

Moreover, it was found that in the MnBi/FeCo bilayers the most favourable atomic configuration at the interface at 0 K temperature forms with Bi-termination in MnBi layer and Co-termination in FeCo layer which is obtained with symmetric non-stoichiometric slab models. These findings are in agreement both with the previous study by Gao *et al.* [75], and with the cohesive energies of these elements [202]. Nevertheless, one case of Mn-termination in MnBi (001) layer with Co-termination in FeCo (111) was also modelled to investigate the effect of Mn excess at the interface which resulted in slightly lower interface exchange constant (see Tab. 5.1). This finding shows that presence of Mn at the interface region does not significantly deteriorate the exchange coupling properties.

Due to the higher values of J^{int} and A^{int} for the interface with crystalline Fe_3Co_5 (110) compared to other configurations, its formation is in favour of a more coherent interfacial exchange coupling. However, the coexistence of disordered phases with lower values of J^{int} and A^{int} in the experimental sample can be considered as one reason for the deterioration of the magnetic exchange coupling at the hard/soft interface which results in a quasi-discontinuous magnetization in the experimental magnetic measurements (see Fig. 5.18) [203].

Apart from the interface exchange energy which was investigated by DFT calculations, the effect of interface roughness and thickness of the soft layer on the exchange interactions are also evaluated by the micromagnetic simulations (see Fig. 5.21-(b) and -(c) for the interface roughness and Fig. 5.22 for thickness analysis of the FeCo layer). The following cases are considered in the micromagnetic simulations the results of which is summarized in Fig. 5.21:

(i) Perfect flat interface with the interface exchange stiffness $A^{\text{int}}_{(111)}$=5.4 pJ/m for crystalline Fe_3Co_5 (111) orientation and $A^{\text{int}}_{(110)}$=1.9 pJ/m for disordered Fe_3Co_5 (110) orientation, as shown in Fig. 5.21-(a),

(ii) Rough interface with a random distribution of dent height (maximum 0.4 nm, inset of Fig. 5.21-(b)) in MnBi and the same values of A^{int} as in the case (i) as shown in Fig. 5.21-(b),

(iii) The same rough interface as in the case of (ii), but with reduced $A^{\text{int}}_{(111)}$=0.54 pJ/m and $A^{\text{int}}_{(110)}$=0.19 pJ/m as shown in Fig. 5.21-(c).

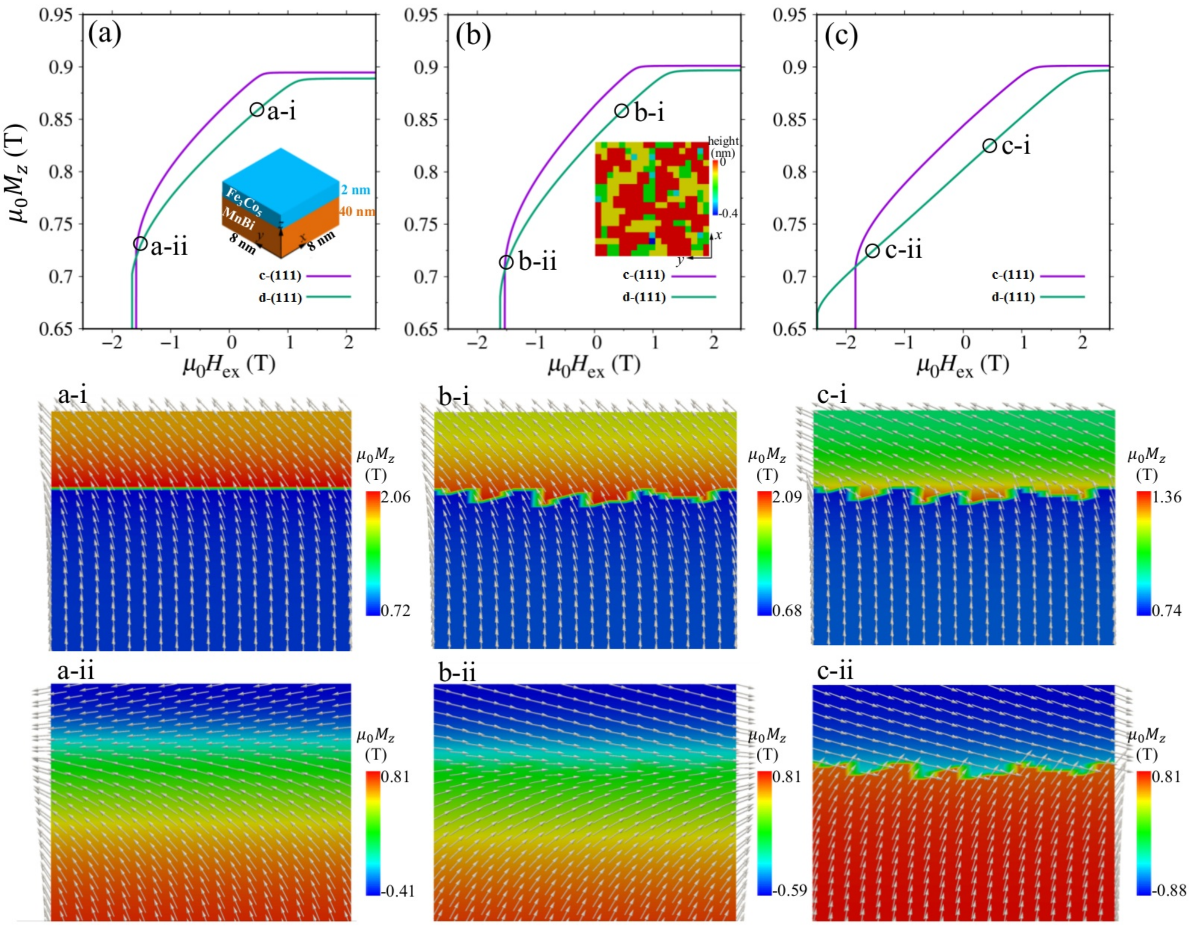

Figure 5.21: Micromagnetic simulation results of a MnBi/Fe_3Co_5 model system with disordered FeCo (110) (d-(110)) and crystalline FeCo (111) (c-(111)) interfaces. Magnetic reversal curves: (a) without interface roughness using the A^{int} value listed in Tab. 5.1; (b) with interface roughness using the same A^{int} as in (a); (c) with nterface roughness using A^{int} reduced to 10% of that in (a). The external magnetic field $\mu_0 H_{\text{ex}}$ is applied along the z direction. Inset of (a): Model geoemetry with in-plane periodic boundary condition. Inset of (b): Interfacial roughness of MnBi with a maximum dent height of 0.4 nm. a-i and a-ii, b-i and b-ii, and c-i and c-ii present the magnetic configurations (yz surface at $x = 0$) corresponding to the marked circles of reversal curves in (a), (b), and (c), respectively, which belongs to the disordered Fe_3Co_5 (110). Figure is adapted from Ref. [106].

It should be also noted that the simulated magnetic reversal curves in Fig. 5.21 do not show the shoulder which was observed in the measured hysteresis loops of the experimental samples. As mentioned earlier, this shoulder could be due to the residual in-plane magnetization component of the hard magnetic phase which is not considered in the micromagnetic simulations but rather a full out-of-plane magnetization vector is assumed.

Using micromagnetic simulations, the magnetic configuration and its evolution around the interface was examined at different external fields, as shown in the second and third rows of Fig. 5.21. When the interface is assumed to be perfect and $A^{\text{int}}_{(110)}$=1.9 pJ/m from Tab. 5.1 is used, the magnetization vectors near the interface in FeCo tend to rotate coherently with those in MnBi, as shown in Figs. 5.21-(a)-i and (a)-ii. This indicates a rather strong interface exchange coupling.

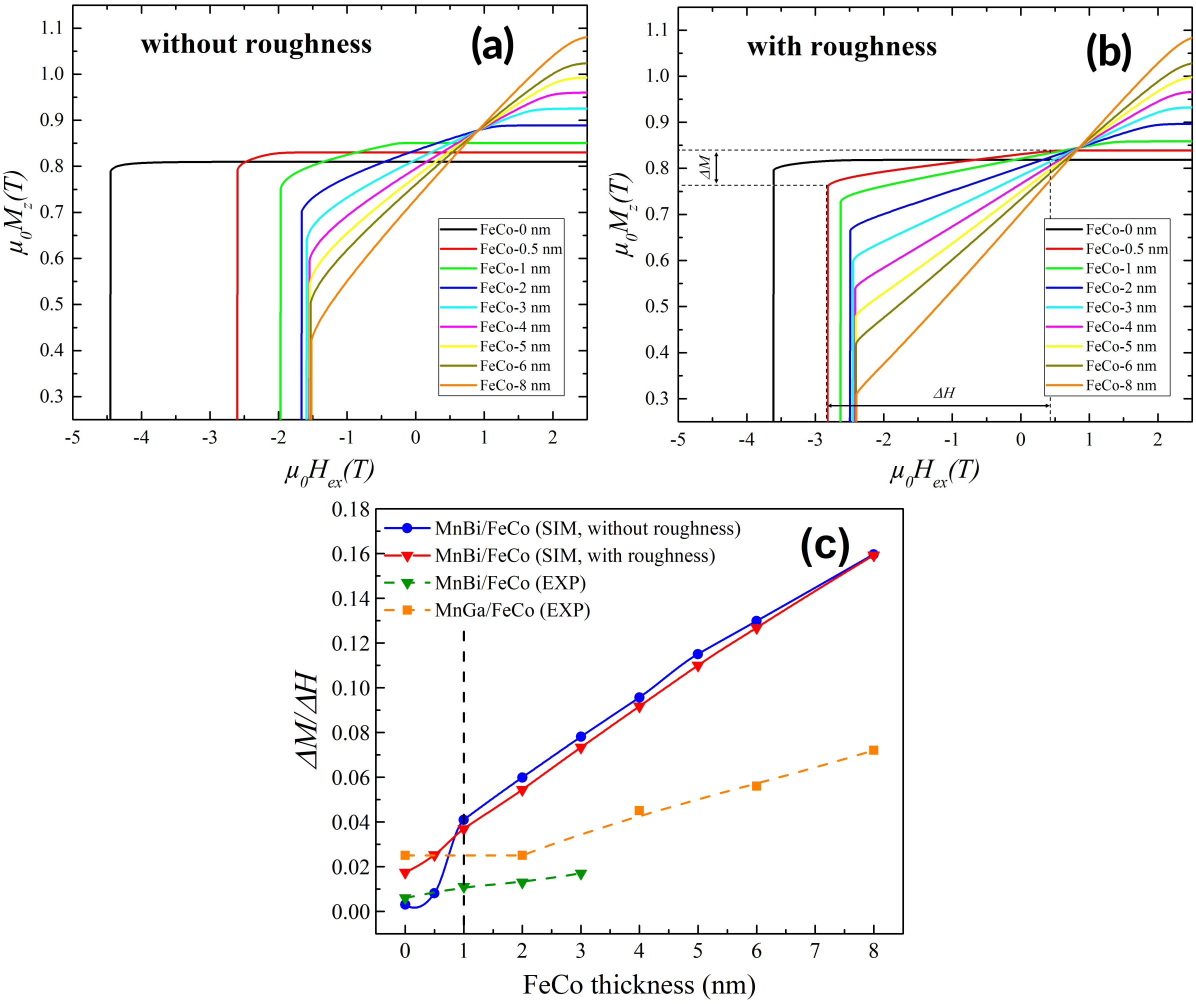

Figure 5.22: Hysteresis plots obtained from micromagnetic simulations for MnBi (001) /FeCo (110) double layers (a) without and (b) with interface roughness. (c) Variation of the magnetization with respect to the applied field around zero field for the theoretical and experimental hysteresis plots as a function of FeCo thickness. For the case of interfaces without roughness two regions are evident in which at 1 nm FeCo thickness incoherent coupling between the hard and soft magnetic layers appears. The rough interfaces in both theoretical and experimental cases, behave incoherently for all thicknesses. For comparison, the experimental data for the epitaxial case of MnGa (001)/FeCo (001) bilayer are also presented (see section 5.4.2). Figure is adapted from Ref. [106].

When a rough interface was assumed and $A^{\text{int}}_{(110)}$ was kept the same, Figs. 5.21-(b)-i and (b)-ii still suggest strong interface exchange coupling. However, the interface magnetization vectors are much easier to be reversed. This can be verified by comparing the distribution of the z component of magnetization ($\mu_0 M_z$). For instance, at $\mu_0 H_{\text{ex}}$=0.5 T, the model with rough interface showed a minimum $\mu_0 M_z$ ($\mu_0 M_z^{\text{min}}$) of 0.68 T around the interface (Fig. 5.21-(b)-i), but the model without roughness showed a little higher $\mu_0 M_z^{\text{min}}$ (Fig. 5.21-(a)-i). The premature reversal in Fig. 5.21-(b)-i and (b)-ii could be attributed to the local higher demagnetization field induced by the sharp corners or irregularities in the rough interface [204, 205]. Accordingly, the simulated coercivity in Fig. 5.21-(b) was also slightly smaller than that of Fig. 5.21-(a).

When the interface roughness was assumed to reduce $A^{\mathrm{int}}_{(110)}$ to 0.19 pJ/m, the magnetic reversal curve was a simple straight line, as shown in Fig. 5.21-(c). From the magnetic configurations in Fig. 5.21-(c)-i and (c)-ii, it can also be found that the magnetization vectors around the interface cross each other and the magnetization in FeCo almost rotates freely, indicating a very poor interface exchange coupling. From Fig. 5.21 we realize that the interface exchange coupling strength evaluated from DFT calculations of smooth interfaces provides useful insight into the atomistic design of the MnBi/FeCo system. In addition, the micromagnetic modelling reveals that the interface roughness and irregular occurrence of defects are also important parameters since it can induce locally premature reversal and, as a consequence, deteriorates the interface exchange coupling.

Fig. 5.22 summarizes the results of thickness analysis based on both experimental measurements and theoretical modelling for MnBi (001)/FeCo (110) interface. In Fig. 5.22-(a) and -(b), hysteresis plots are shown as a function of FeCo layer thickness for two cases one without (-(a)), and one with interface roughness (-(b)) based on the information provided in Fig. 5.21 for MnBi (001)/disordered Fe_3Co_5 (110). As a descriptor to quantitatively evaluate the changes in degree of exchange coupling caused by interface roughness and increasing the soft layer thickness, first derivative of the corresponding hysteresis loops in Fig. 5.22-(a) and -(b) (using simulation data) as well as the experimental hysteresis loops in Fig. 5.18-(b) has been calculated. The slope of each hysteresis curve around zero-field crossing, which shows the variation of magnetization with respect to the applied field ($\frac{\Delta M}{\Delta H}$), has been also plotted in Fig. 5.22-(c) as a function of FeCo layer thickness. This slope increases with thickness of FeCo layer in both simulation and experiment which implies that the exchange coupling becomes more incoherent and bilayers behave more and more like two separate magnetic layers.

From plots in Fig. 5.22-(c), it can be seen that for structures without interface roughness (blue circles), two regions with different slopes are observable, with a borderline at 1 nm FeCo thickness. It is found that for the sample with less than 1 nm FeCo thickness without interface roughness, the first derivatives are close to zero (the hysteresis loop is more rectangular with slope of ∼0), and therefore the hard and soft layers are coherently exchange coupled. However, in the case of a rough interface (red triangles) as the slope is continuously increasing, the exchange coupling is incoherent regardless of the soft layer thickness.

In addition, the first derivatives of the experimental hysteresis curves for MnBi/FeCo bilayers (green triangles with dashed line) as well as epitaxial MnGa (001)/FeCo (001) bilayers (orange square with dashed line) as a function of FeCo thickness have also been included in Fig. 5.22-(c). As can be seen from the plots in Fig. 5.22-(c), the theoretical and experimental findings for the case of MnBi/FeCo bilayer are in agreement and show that the effect of interface roughness on the incoherency of exchange coupling is significant. Moreover, it can be concluded that the effect of the lattice misfit between the hard and soft layers is decisive since even in the case of the interfaces without roughness (blue solid line) using a single crystalline model, the coherent coupling is only observed up to 1 nm FeCo thickness.

Comparing the trend of derivative plots for MnBi/FeCo and MnGa/FeCo bilayer systems, it can be seen that since MnGa/FeCo bilayers show much decreased interface roughness due to epitaxial growth, a coherent exchange coupling can be obtained up to 2 nm FeCo thickness. Therefore, it can be concluded that not only interface roughness is limiting the interfacial exchange coupling but also epitaxial growth and a reduced lattice misfit at the interface will greatly improve the coupling behavior. More details on growth and characterization of MnGa/FeCo exchange bilayers can be found in the following sections.

5.3.1 Growth temperature study

Fig. 5.23-(a) shows the room-temperature XRD patterns collected from the $Mn_{1.5}Ga$ thin films deposited on Cr(001) buffered MgO(100) single crystal substrates at different substrate temperatures (T_{sub}). The two strongest reflections observed aside from the MgO(200) substrate peak at $2\theta = 41.2°$ are indexed to the $L1_0$-$Mn_{1.5}Ga$ crystal structure with space group of $P4/mmm$ with its (001) peak at 2θ= 24.90° and its (002) peak at 2θ= 50.10°. Moreover, the (002) reflection from chromium buffer layer deposited underneath the MnGa layer can be observed as an intense peak. Only the MnGa film deposited at T_{sub} of 450 °C is phase-pure, and for all the other films grown at lower or higher substrate temperatures some traces of Ga and/or Mn are present as additional small reflections. Therefore, the highest crystallinity can be obtained for the film grown at a substrate temperature of 450 °C. The lattice constant c was calculated for MnGa thin film grown at T_{sub} of 450 °C with tetragonal crystal structure using (002) peak position. The corresponding c lattice constant is 3.6258±0.003 Å which is close to the reported bulk value of 3.69 Å or 3.642 Å [58, 121].

The out-of-plane magnetization data for the MnGa thin films deposited at different substrate temperatures are shown in Fig. 5.24. All of the magnetization curves reach a saturation magnetization at a field below 20 kOe with a coercivity in the range of 7 kOe to 9 kOe which shows a hard magnetic behaviour with out-of-plane easy axis of magnetization. According to the measured hysteresis loops, by increasing substrate temperature from 350 °C to 450 °C, the saturation magnetization continuously increases from 705 emu/cm^3 to 840 emu/cm^3. A further increase in the growth temperature will decrease the saturation magnetization again down to $\sim$ 700 emu/cm^3. The coercivity does not change strongly and shows the opposite trend. It has its maximum of 9 kOe for the MnGa film deposited at T_{sub}= 350 °C and upon increasing the T_{sub} to 450 °C, the coercivity decreases to $\sim$ 6 kOe and remains nearly constant for higher substrate temperatures up to T_{sub}= 600 °C (with a slight increase). In accordance to the XRD patterns, the highest saturation magnetization and the lowest coercivity belong to the sample which was grown at T_{sub}= 450 °C showing highest degree of crystallinity. The above-mentioned trends in saturation magnetization and coercivity can be attributed to partial presence of Ga and/or Mn in all MnGa thin films except for the phase-pure MnGa film deposited at T_{sub}= 450 °C.

The change in c-lattice constant and full width half maximum (FWHM) values for the MnGa films grown at different substrate temperatures have been plotted in Fig. 5.23-(b). As it is shown in this graph, by increasing the substrate temperature from 350 °C to 450 °C, the c-lattice constant increases until it reaches the value of 3.6258±0.003 Å which is close to the 3.69 Å or 3.642 Å values reported for bulk MnGa [58, 121]. Further increasing the substrate temperature will result in subsequent decrease of c-lattice constant. This along with a shift in position of MnGa (002) peak first slightly to the left and then to the right, suggests that in both temperature ranges lower and higher than 450 °C the MnGa structure in the films is under tensile or compressive strain, or shows some composition change. The FWHM values measured for (001) peaks in MnGa thin films does not significantly change by increasing the substrate temperature up to 450 °C ($\sim$ 0.1°), but higher substrate temperatures result in broadening of MnGa (002) peak with a larger FWHM value reaching ($\sim$ 0.5°) at 600 °C showing that the crystallinity of MnGa thin film is degrading at substrate temperatures higher than 450 °C. The position of MnGa (002) peak (value of c-lattice constant) as well as FWHM value suggest that the film grown at T_s=450 °C has the best crystalline quality and minimum amount of residual phases among all the different films grown at various substrate temperatures.

The out-of-plane hysteresis loops were measured for MnGa thin film sample grown at T_{sub}= 450 °C at different temperatures to investigate the effect of temperature on saturation magnetization (M_s) and coercivity (H_c). Fig. 5.25-(a) shows the hysteresis loops measured at various temperatures in the range of 10 K

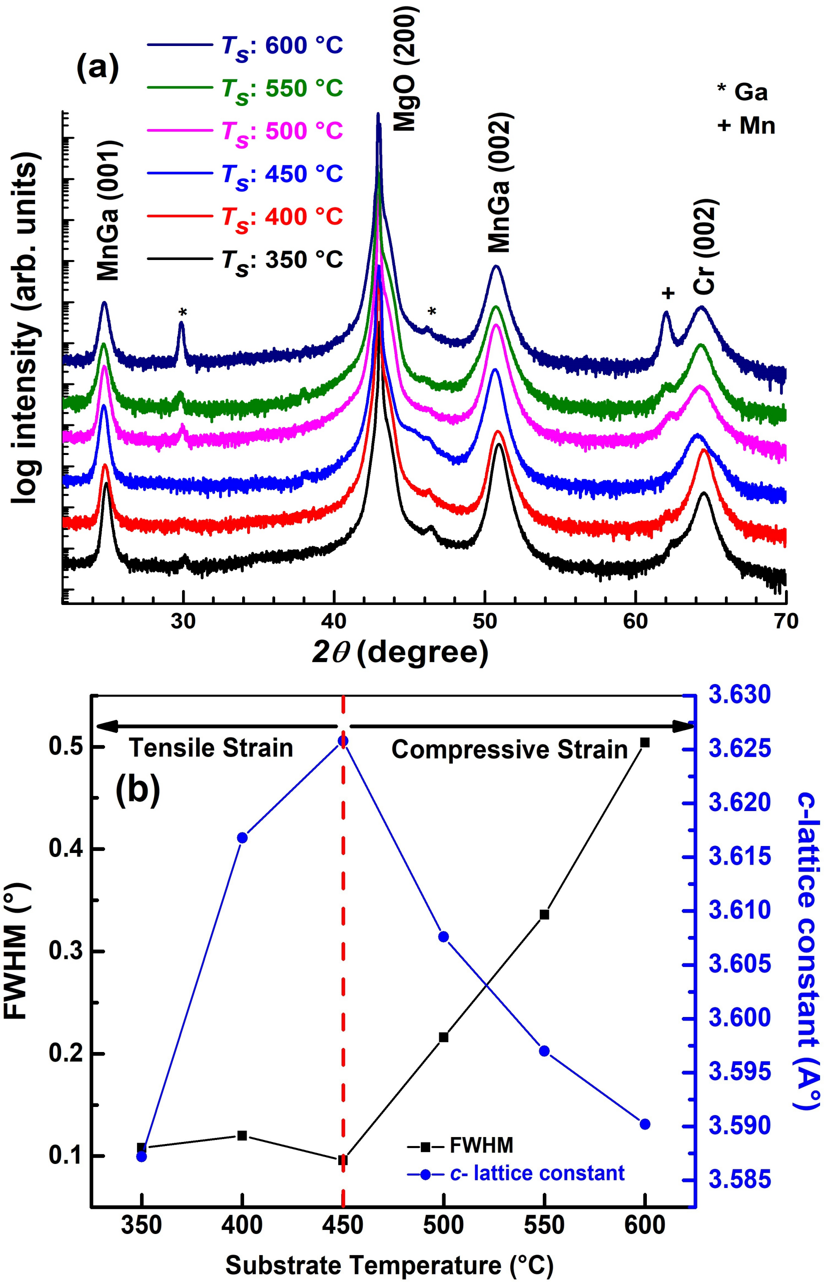

Figure 5.23: (a) XRD patterns of MnGa thin films deposited at different substrate temperatures, T_{sub}, between 350 °C and 600 °C (Figure is adapted from Ref. [193]). For clarity, the XRD spectra are shown with a vertical offset. The peaks from Ga or Mn in the MnGa films are labelled with (*) and (+), respectively. (b) Change of c-lattice constant and peak broadening for MnGa (002) peak as a function of substrate temperature.

to 350 K. Due to temperature limitation of SQUID magnetometer, the maximum applicable temperature was 350 K. For clarity, the change in saturation magnetization (M_{s}) and coercivity (H_{c}) (extracted from these hysteresis loops) upon temperature is summarized in the graphs in Fig. 5.25-(b). As it can be seen from the plots in Fig. 5.25-(b), by increasing the temperature from 10 k to 350 K, the saturation magnetization decreases from 1225 emu/cm^3 to 701 emu/cm^3. The coercivity (H_{c}) also shows the same trend and decreases from 8.75 kOe to 5.9 kOe which shows a negative temperature coefficient for Mn$_{1.5}$Ga thin film.

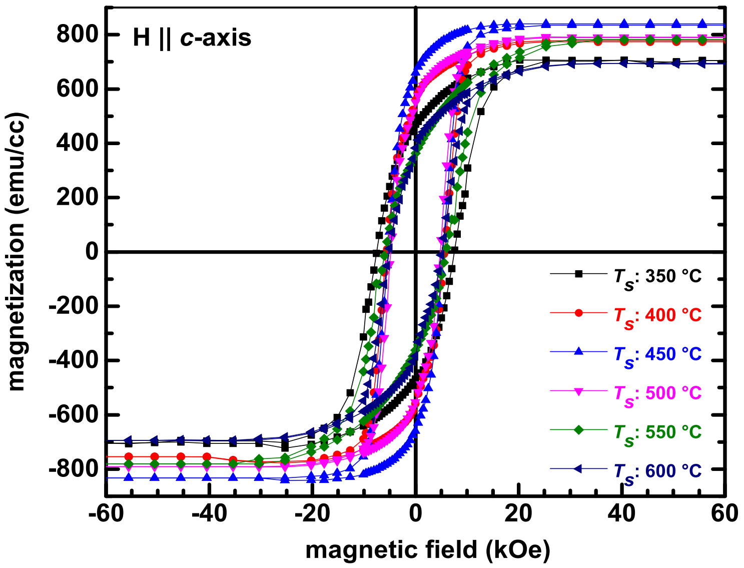

Figure 5.24: Out-of-plane magnetization data for MnGa thin films deposited at different substrate temperatures, T_{sub}, between 350 °C and 600 °C.

The magnetization vs. temperature data in Fig. 5.25-(b) have been fitted using a combination of Bloch's law at low temperatures and a mean field type transition close to the Curie temperature as suggested by Guo *et al.* with a weight function $p \approx (T/T_c)^{1.3}$ [199]. The estimated Curie temperature from this fit (n=1.3 and B=0.44) is about 530 K which is lower than the reported theoretical value for crystalline $\mathrm{Mn_{1.5}Ga}$ (~697 K) [118]. This could be due to slight off-stoichiometry or fitting inaccuracy. A wider temperature range up to the theoretical Curie temperature is needed for the measurement in order to achieve more accurate result. Thus, the significance of the parameters is low. Therefore, it is not possible to differentiate between a mean field exponent $(1-T/T_c)^{1/2}$ or a Heisenberg critical behaviour with exponent 1/3 [200].

The inset to Fig. 5.25-(b) shows the change in anisotropy field H_{s} and uniaxial magnetic anisotropy constant K_{u} as a function of temperature. The anisotropy field values were extracted from the intersection of easy and hard magnetization loops measured at different temperatures for MnGa thin film sample. The uniaxial magnetic anisotropy constants were estimated using Eq. 2.13 by substituting M_{s} and H_{s} values for each measurement temperature (for more details see section 5.1.1). Similar to both saturation magnetization and coercivity, anisotropy field and therefore the estimated uniaxial magnetic anisotropy decrease with increasing temperature. Since small changes in lattice constant of MnGa unit cell can affect both coercivity and anisotropy, this reduction in H_{c} and K_{u} can be attributed to a decrease in tetragonality and c/a ratio in MnGa unit cell upon applying higher temperatures.

5.3.2 Magnetic anisotropy

Fig. 5.26-(a) shows the room-temperature magnetization data for $\mathrm{Mn_{1.5}Ga}$ thin film grown at T_{sub}= 450 °C measured in MPMS device with the magnetic field applied both in out-of-plane (easy axis) and in-plane (hard axis) directions. Similar to the MnBi thin films, for MnGa thin films the K_{u} values have been also estimated from the relation $K_{\mathrm{eff}} = K_{\mathrm{u}}$ - $2\pi M_{\mathrm{s}}^2$ in which K_{eff} is the effective perpendicular magnetic anisotropy constant and $2\pi M_{\mathrm{s}}^2$ is the shape anisotropy of the thin film. The effective perpendicular

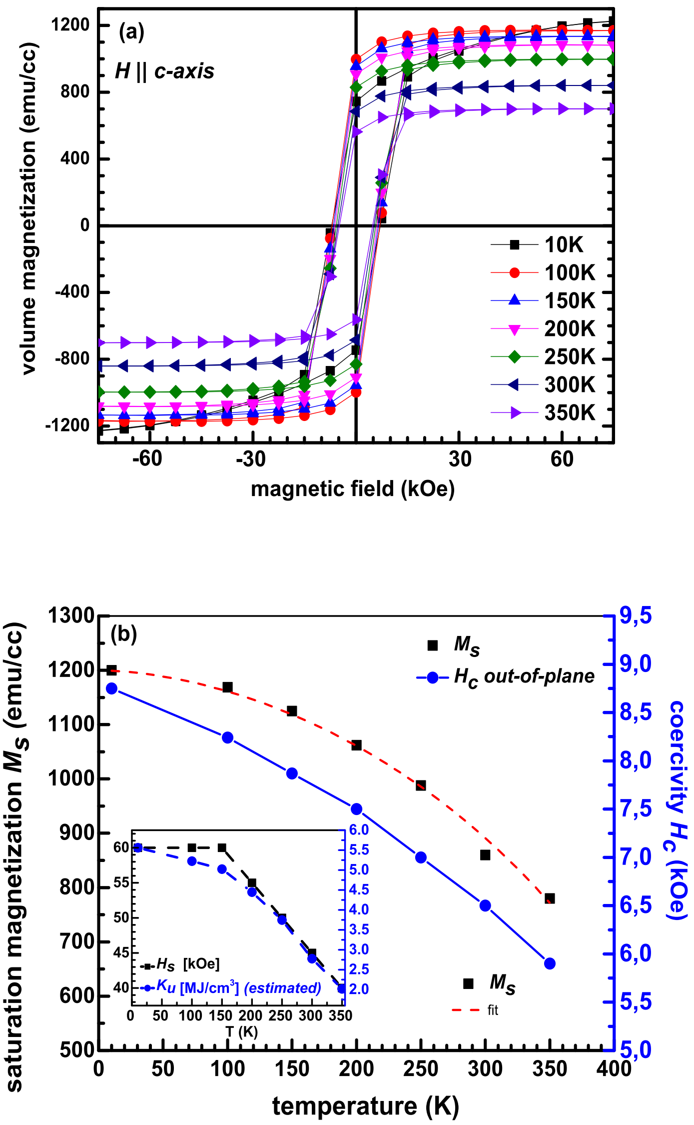

Figure 5.25: (a) Out-of-plane magnetization data measured in SQUID magnetometer for $Mn_{1.5}Ga$ thin film grown at T_{sub}= 450 °C at different temperatures between 10 K and 300 K, (b) changes in saturation magnetization (M_s) and coercivity (H_c) upon changing measurement temperature for $Mn_{1.5}Ga$ thin film, the inset to graph (b) shows the changes in anisotropy field (H_s) and the estimated uniaxial magnetic anisotropy constant (K_u) from H_s as a function of temperature.

magnetic anisotropy constant, can be itself calculated from the relation: $H_s = 2K_{eff}/M_s$- $4\pi M_s$ in which the anisotropy field (H_s) is extracted from the interception of the out-of-plane and in-plane magnetization curves at saturation with their applied fields in parallel and perpendicular direction with respect to the film plane, respectively. The opposing contribution from demagnetizing field must be added to the anisotropy field for a more accurate estimation of K_{eff}. The interception of magnetization curves in Fig. 5.26-(a) results in a high anisotropy field of 45 kOe (4.5 T). Using 45 kOe as H_s and a M_s value of 840 emu/cm^3, the contribution of demagnetizing field is calculated to be ∼ 10.55 kOe which results in a K_{eff} of 23.33 Merg/cm^3 (2.33 MJ/m^3). Adding the value of shape anisotropy ($2\pi M_s^2$=4.43 Merg/cm^3 (0.443 MJ/m^3)) to the K_{eff}, the uniaxial magnetic anisotropy is estimated to be as high as 2.77 MJ/m^3

which is slightly higher than the theoretically predicted value of $2.60\,\mathrm{MJ/m^3}$ due to the large error from this estimation method [49].

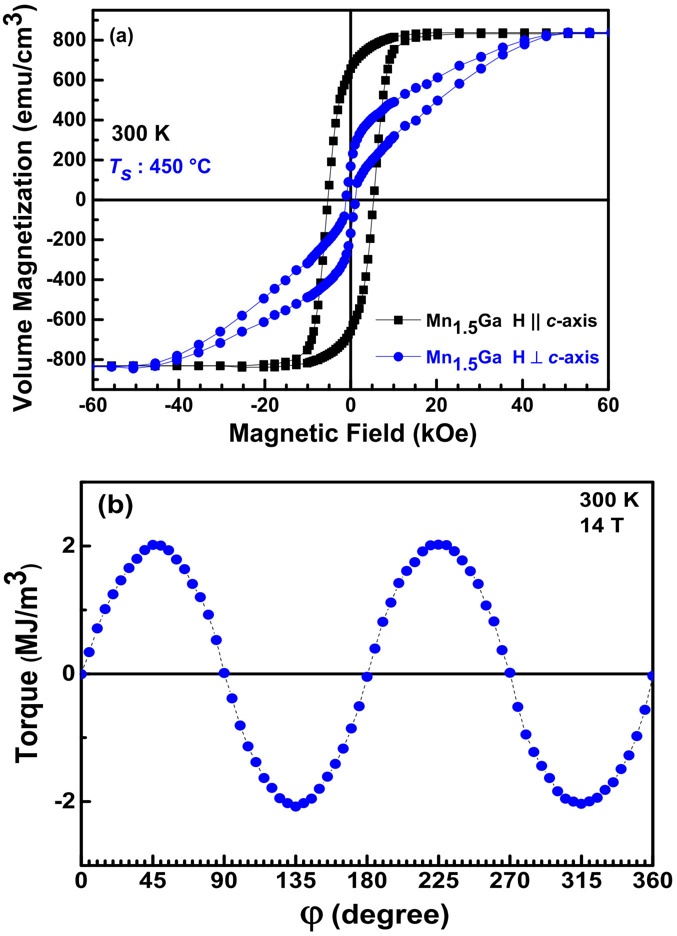

Figure 5.26: (a) Out-of-plane and in-plane magnetization data measured in SQUID magnetometer, (b) angular dependence of magnetic field measured in a torque magnetometer attached to a PPMS device rotating under 14 T magnetic field for $Mn_{1.5}Ga$ thin film grown at $T_{\mathrm{sub}}=$ 450 °C at 300 K. Figure is adapted from Ref. [193].

Fig. 5.26-(b) shows the angular dependency of the magnetic torque ($T(\phi)$) measured for the same MnGa thin film grown at 450 °C in a torque magnetometer attached to a PPMS device. First the film was cut into 1.5 mm × 1.5 mm piece and then the $T(\phi)$ for this small piece was measured while rotating under an applied field in torque magnetometer. The torque measurement was performed in applied field range of 2 T-14 T at different temperatures between 60 K and 300 K. All the torque curves measured over the temperature range of 60 K to 300 K consist mainly of a two-fold symmetry which indicates the uniaxial magnetic anisotropy mode. From the data refinement and fitting of a $A\sin(2\theta)+B\sin(4\theta)$ function to the measured torque curves using Eqs. 3.58-3.60 [168], a uniaxial magnetic anisotropy constant (K_{u}) of $\sim$ 21.00 $\mathrm{Merg/cm^3}$ (2.10 $\mathrm{MJ/m^3}$) is obtained which is lower than the estimated value using the anisotropy field (H_{s}) extracted from easy and hard magnetization data. Similar to the case for MnBi thin film there is considerable difference between the two values which once again proves that there is a large error in estimating the uniaxial anisotropy constant from anisotropy field.

Fig. 5.27 shows the field dependency of measured magnetic torque curves for the MnGa thin film deposited at 450 °C. The applied field was varied from 2 T to 14 T and all the curves were measured at room-temperature. As it can be seen from the measured torque curves on Fig. 5.27, by increasing the applied magnetic field the amplitude of the torque signal is increasing and the peak position moves further toward 45°. For clarity the graphs in Fig. 5.28 summarize the calculated uniaxial magnetic anisotropy constant (K_u), which is proportional to the amplitude of the sine function fitted to the measured magnetic torque data, as well as the peak offset from the position of maxima (45°) as a function of applied magnetic field. The plots in Fig. 5.28 indicate that as applied magnetic field increases up to 14 T, there is a constant increase observable for the magnetic anisotropy which saturates to $\sim 2.10\,\mathrm{MJ/m^3}$ and the maximum peak position moves towards 45° showing smaller offset. Applying a minimum magnetic field of $\sim 3 \times H_s$ seems to be necessary to keep the magnetization always parallel to the applied magnetic field. This means that in order to achieve a proper torque signal and obtain the precise magnetic anisotropy in the film, the angle between anisotropy and magnetic field must be the same as the angle between anisotropy and magnetization.

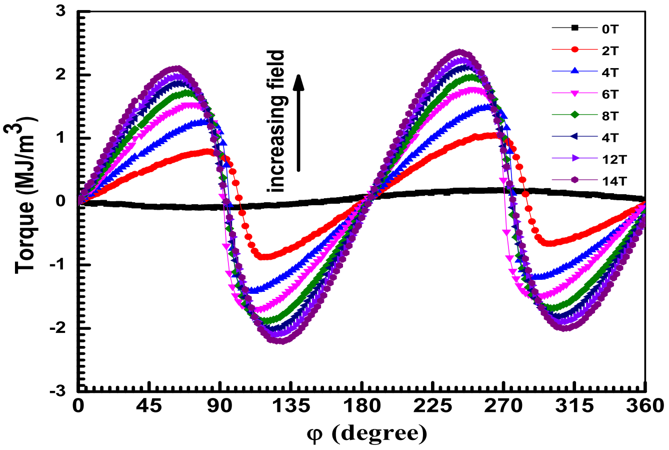

Figure 5.27: Angular dependence of magnetic torque for a MnGa film grown at 450 °C measured in torque magnetometer under different applied magnetic fields in the range of 1 T-14 T at 300 K.

Fig. 5.29 shows the change in collected torque curves at different measurement temperatures under 14 T applied magnetic field for MnGa thin film. Upon increasing the measurement temperature, the amplitude of torque signal which is proportional to the uniaxial magnetic anisotropy constant K_u is slightly decreasing showing a small negative temperature dependency for K_u. The perpendicular magnetic anisotropy remains even at temperatures down to 60 K and for the whole measured temperature range the two fold symmetry of the graphs lasts. The slight deterioration of the measured uniaxial magnetic anisotropy with increasing temperature is in agreement with what has been observed for the measured hysteresis loops in Fig. 5.25 where the magnetization curves show a slight decrease in coercivity upon increasing the measurement temperature.

Fig. 5.30 represents the correlation obtained between uniaxial magnetic anisotropy constant K_u and saturation magnetization M_s for the same MnGa thin film sample in a temperature range from 60 K to 300 K. The values for saturation magnetization have been extracted from the hysteresis loops in Fig. 5.25-(a). The values of uniaxial magnetic anisotropy constant are the measured values obtained from fitting a sine function to the torque curves in Fig. 5.29 measured at different temperatures between 60 K and 300 K. From fitting a polynominal function to the plotted K_u as a function of M_s, it

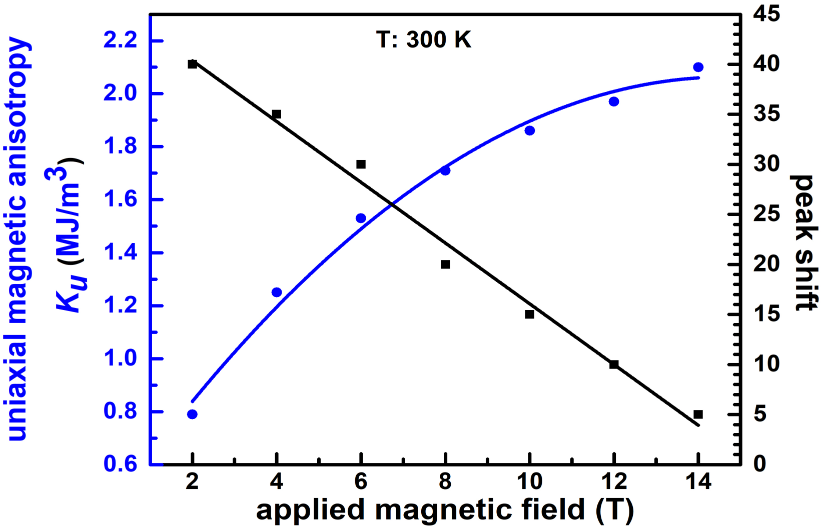

Figure 5.28: Summarized graphs showing the trend of changes in uniaxial magnetic anisotropy and peak shift with respect to the maxima in magnetic torque curves measured for a MnGa film grown at 450 °C as a function of different applied magnetic fields in the range of T-14 T at 300 K in torque magnetometer.

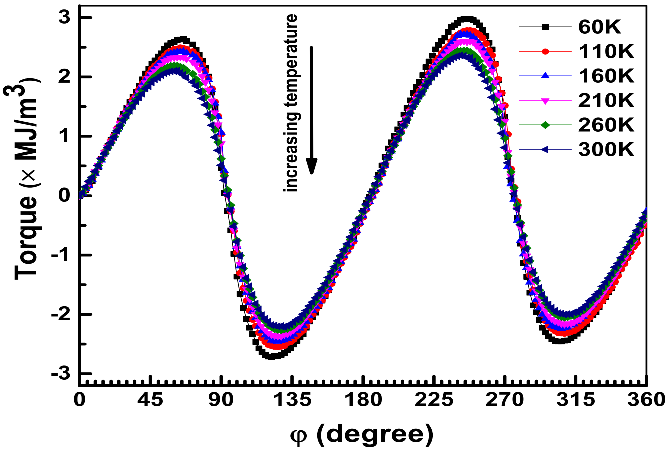

Figure 5.29: Angular dependence of magnetic torque for a MnGa film grown at 450 °C measured in torque magnetometer under applied magnetic field of 14 T at different temperatures in the range of 60 K to 300 K.

was found that the K_u is proportional to the third power of M_s. Since K_u should be directly proportional to M_s^n with $n = 3$ for uniaxial magnetocrystalline anisotropy [79], the exponent achieved for MnGa thin film is in agreement with the expected value and confirms a uniaxial magnetic anisotropy in the films.

5.4 MnGa/FeCo exchange coupled bilayers

To investigate the exchange coupling effect in MnGa/FeCo exchange spring system, bilayers with $L1_0$-$Mn_{1.5}Ga$ film as hard magnetic layer and $Fe_{35}Co_{65}$ (at.%) film as soft magnetic layer have been deposited on Cr (001) buffered MgO (100) substrate. The details of the deposition process is provided in section 4.1. A schematic of such a bilayer is presented in inset to Fig. 5.31. First a $L1_0$-$Mn_{1.5}Ga$ hard magnetic layer was deposited with ~ 40 nm thickness and then the FeCo layer was deposited on top of the (001)

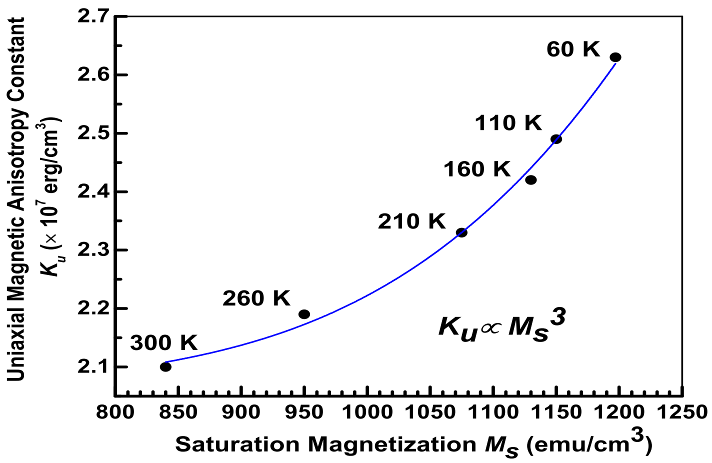

Figure 5.30: The dependence of magnetic anisotropy (K_u) on saturation magnetization (M_s) at different temperatures in the range of 60 K to 300 K for a MnGa film grown at 450 °C.

epitaxial $L1_0$-$Mn_{1.5}Ga$ layer with different thicknesses of 2 nm to 8 nm (in different samples) to evaluate the exchange coupling effect as a function of thickness of the soft magnetic layer.

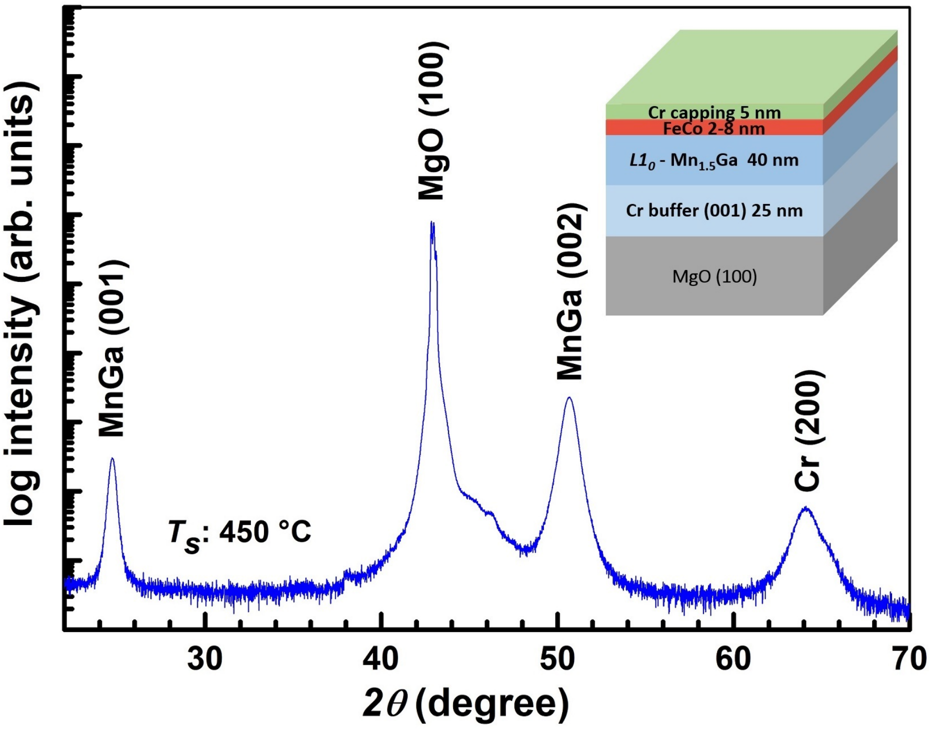

Figure 5.31: XRD patterns collected from exchange spring bilayer of $Mn_{1.5}Ga/Fe_{35}Co_{65}$ with 2 nm thickness of FeCo soft magnetic layer. The $L1_0$-$Mn_{1.5}Ga$ thin film was deposited at T_{sub}: 450 °C and FeCo layer was deposited at a substrate temperature of T_{sub}: 100 °C. The inset shows schematic of $Mn_{1.5}Ga/Fe_{35}Co_{65}$ bilayer samples deposited on Cr (001) buffered MgO (100) substrate.

Fig. 5.31 shows the XRD patterns collected from $Mn_{1.5}Ga/Fe_{35}Co_{65}$ exchange spring bilayers with 2 nm thickness of Co-rich soft magnetic FeCo layer. The peak indexing shows tetragonal MnGa (001) superlattice and (002) peaks with space group of $P4/mmm$, along with the (001) peak of Cr buffer layer underneath the MnGa film and the high intensity MgO substrate peak. As expected no peaks have been observed from FeCo layer because of its very low thickness. Comparing the intensities of MnGa (001) and (002) peaks in bilayers sample to that of the single layer MnGa thin film in Fig. 5.23-(a), the XRD patterns show nearly the same intensities implying that the crystalline quality of hard magnetic layer for all bilayer samples is nearly the same.

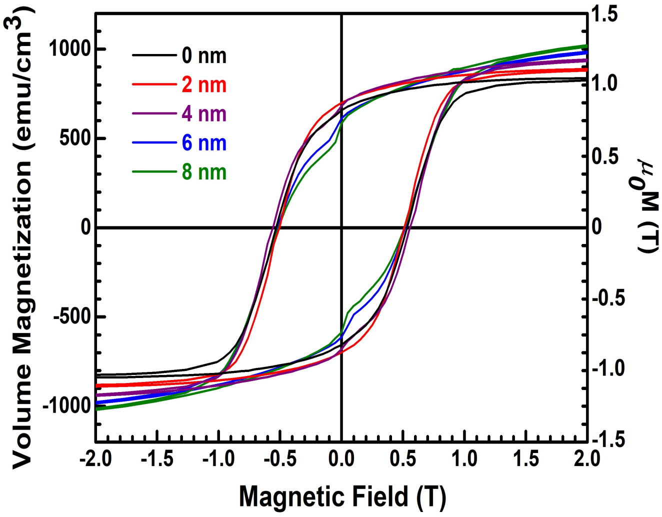

Figure 5.32: Out-of-plane magnetization data for MnGa/FeCo bilayers with $Fe_{35}Co_{65}$ (at.%) thickness between 0 nm-8 nm measured at 300 K. Figure is adapted from Ref. [193].

Room-temperature out-of-plane magnetization data (volume magnetization vs. applied magnetic field) measured in easy direction of magnetization for $Mn_{1.5}Ga/Fe_{35}Co_{65}$ epitaxial bilayers with different thicknesses of the FeCo layer are shown in Fig. 5.32. For the comparison, the out-of-plane hysteresis loop for a single layer MnGa thin film sample has also been included in the same graph. The exchange spring system should reach the higher saturation magnetization by addition of the soft magnetic layer while preserving the coercivity of the hard magnetic phase. The exchange coupling effect between the hard and soft magnetic layers is considered strong when the bilayer sample shows a magnetically single phase behaviour. As expected, by addition of 2 nm, 4 nm and 6 nm and 8 nm FeCo layer, the saturation magnetization of the bilayer sample has monotonously increased while the coercivity stays nearly constant and close to that for the single MnGa layer. The total magnetization for the bilayer, as mentioned in Eq. 2.26, is the volume average of magnetization in hard and soft magnetic layers.

According to the out-of-plane hysteresis loops, the bilayer shows strong exchange coupling with single-phase behavior for a soft magnetic layer thickness of $\sim$ 2 nm resulting in a $\sim$ 20% increase in volume magnetization from 840 emu/cm^3 to 1000 emu/cm^3 while the coercivity is preserved at $\sim$ 6 kOe. A further increase in the soft layer thickness deteriorates the coherency of the exchange interaction as can be seen from the small shoulder in the magnetization data around zero field which shows that the two layers are not behaving as a single phase under demagnetizing field. Although such a decrease in degree of coupling was predicted with increasing thickness of the soft magnetic layer, it is also expected that the critical soft layer thickness is proportional to the domain wall width for hard magnetic layer as: $(2 \times \delta_{\mathrm{w}} = \sqrt{\frac{A_{\mathrm{h}}}{K_{\mathrm{h}}}})$ (see Eq. 2.25) in which δ_{w} is domain wall width, A_{h} is exchange stiffness constant and K_{h} is magnetocrystalline anisotropy for the hard magnetic phase [68, 70, 71]. In case of MnGa/FeCo exchange system with A_h of $\sim 1.0.\ 10^{-6}$ erg/cm [191], the critical thickness should be as high as ∼13.7 nm.

In comparison to the previous exchange spring bilayers in MnBi/FeCo system, the coherency of exchange coupling has been improved for the MnGa/FeCo system resulting in a higher critical soft layer thickness. This can be attributed to the epitaxial growth of both hard and soft magnetic layers leading to an improved hard/soft interface quality [192, 106]. TEM investigations have been performed on a MnGa/FeCo bilayer sample with 3 nm FeCo layer thickness to evaluate the epitaxial growth and crystallinity of the hard and soft magnetic layers and to examine the improved exchange interface for MnGa/FeCo bilayers.

5.4.1 Transmission Electron Microscopy (TEM)

Cross-sectional high-resolution transmission electron microscopy (HR-TEM) images were collected to investigate the hard/soft interface in the exchange spring MnGa/FeCo bilayer. As shown in Fig. 5.33-(a), the layers are epitaxially grown along the (001) out-of-plane orientation leading to the formation of a smooth interface between MnGa and FeCo layers with a roughness of a few unit cells. The formation of a well-defined interface between MnGa and FeCo layers can also be observed from the HR-STEM image in Fig. 5.33-(b). Moreover, EDX analysis was performed in STEM mode to measure the elemental composition for Cr, Mn, Ga, Fe and Co in the bilayer sample. The EDX data in Fig. 5.33-(c) shows distributions of these elements across the different layers. The measured composition distribution is in good agreement with the different crystalline phases present in each deposited layer. The compositions from EDX analysis correspond to a stoichiometry of $\mathrm{Mn_{1.6}Ga}$ and $\mathrm{Fe_{37}Co_{63}}$.

5.4.2 Theoretical investigations of exchange interface

The results of *ab initio*-based DFT calculations for the MnGa/FeCo interface are summarized in Tab. 5.2. The values for interface formation energy, interface exchange coupling energy and interface exchange constant were calculated for $\mathrm{MnGa/Fe_xCo_{1\text{-}x}}$ with different compositions of x = 0.375, 0.5, 0.625 and 1.0 in soft magnetic FeCo layer. Based on the table of cohesive energies [202] as well as the current calculations, the surface termination of Ga atoms in the hard magnetic side is energetically more favorable than a termination with Mn atoms. Nevertheless, both Fe and Co terminations at the interface from the soft magnetic side have been considered to compare their effect on the interlayer magnetic exchange coupling. For each atomic termination at the interface, the number of Fe and Co atoms differ.

Fig. 5.34 shows the atomic structure of MnGa (001)/$\mathrm{Fe_3Co_5}$ (001) with Ga and Co terminations as well as MnGa (001)/$\mathrm{Fe_5Co_3}$ (001) with Ga and Fe terminations at the interface. Fig. 5.34 indicates that after DFT atomic relaxation, despite 4.2% strain in the *ab*-plane at the interfaces, no significant surface reconstruction or irregularity occurs and the experimentally-observed epitaxial feature of the interface is preserved in both termination cases. It is noted that the results of the DFT calculations which are obtained at 0 K are in agreement with the HR-TEM observations (see Fig. 5.33).

In general, the interface from Co-rich alloys enhances thermodynamic stability since the interfaces with Co termination have lower interface formation energies compared to the ones with Fe termination. Moreover, the calculations show that Co termination at the interface results in significantly improved exchange coupling. On the other hand, the presence of Fe atoms at the interface is in favor of antiferromagnetic coupling. Therefore, by increasing the number of Fe atoms at the interface the values of J^{int} and A^{int} both become more negative.

In the previous study by Ma *et al.* [77], it is shown that by increasing the Co content in FeCo layer above 25 %, there is an abrupt transition from FM to AFM for the interface exchange coupling. How-

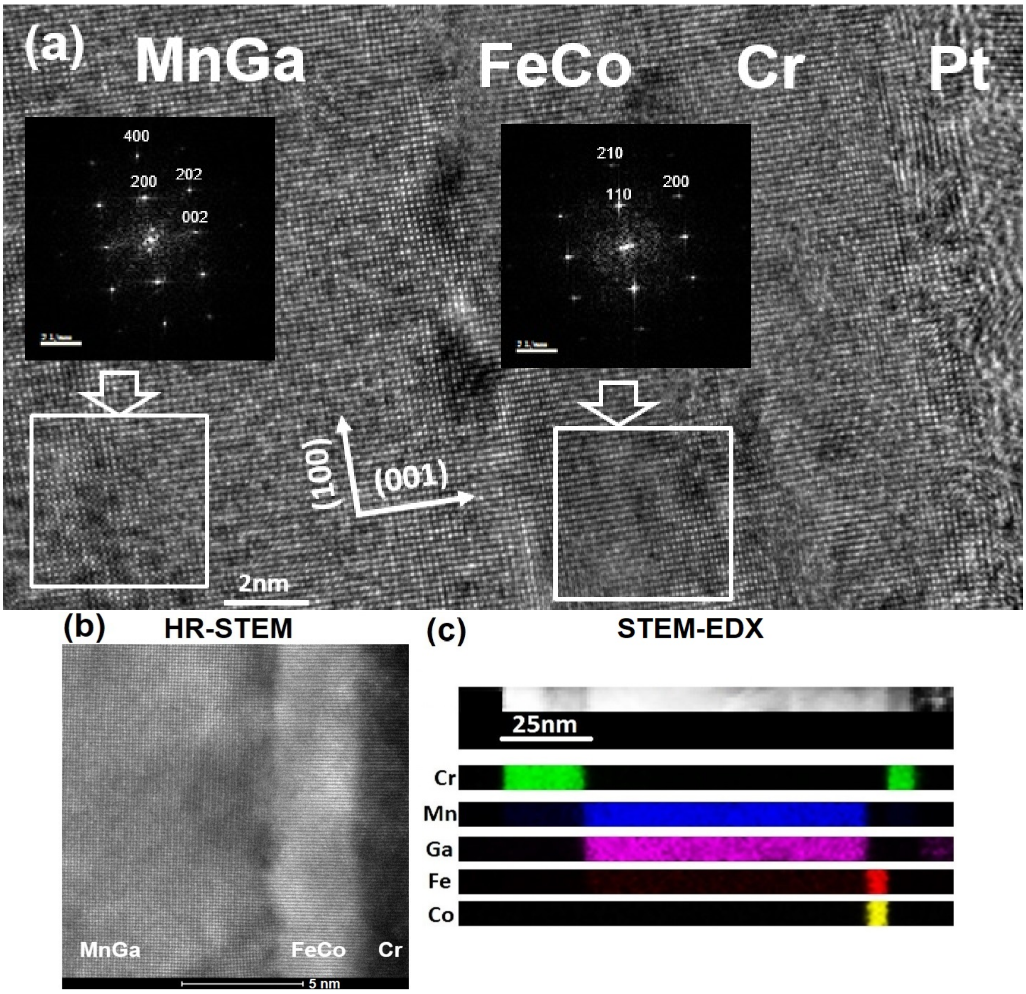

Figure 5.33: (a) High-resolution cross-section TEM image of $Mn_{1.5}Ga$ (001)/$Fe_{35}Co_{65}$ (001) epitaxial bilayer sample, with 3 nm FeCo layer thickness, (b) HR-STEM image of the epitaxial MnGa/FeCo interface, and (c) line scan EDS map of the Cr, Mn, Ga, Fe and Co distribution across the bilayer sample. Figure is adapted from Ref. [193].

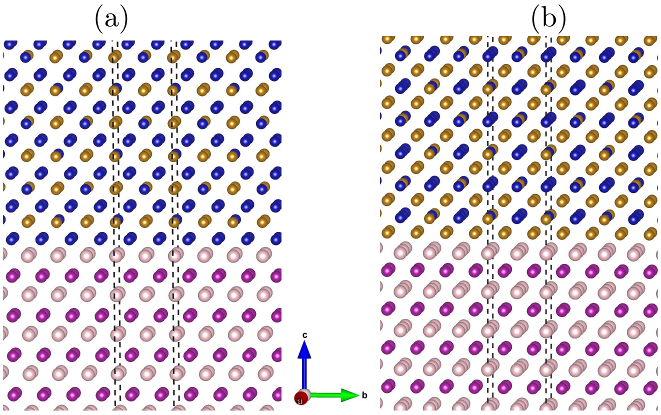

(a) (b)

Figure 5.34: Atomic structure of (a) MnGa (001)/Fe_3Co_5 (001) with Ga and Co terminations, and (b) MnGa (001)/Fe_5Co_3 (001) with Ga and Fe terminations demonstrated using VESTA [115]. Mn, Ga, Fe and Co are shown with light pink, magenta, yellow, and blue colors, respectively. Figure is adapted from Ref. [193].

Table 5.2: Values of interface formation energy γ^{int}, interface exchange coupling energy J^{int}, interface exchange constant A^{int} and lattice mismatch calculated by DFT considering different compositions of $\text{Fe}_{\text{x}}\text{Co}_{\text{1-x}}$ layer and different terminations in MnGa/FeCo interface. All the interfaces are perpendicular to the [001] crystallographic direction. Table is adapted from Ref. [193].

Composition	Interfacial strain	Interface termination of soft layer	γ^{int} (eV/Å^2)	J^{int} (J/m^2)	A^{int} (pJ/m)
MnGa/Fe_3Co_5	4.2%	4 out of 4 Co atoms	0.128	0.081	2.54
MnGa/Fe_3Co_5		3 out of 4 Fe atoms	0.135	−0.034	−1.05
MnGa/FeCo		1 out of 1 Co atom	0.131	0.066	2.01
MnGa/FeCo		1 out of 1 Fe atom	0.143	−0.029	−0.87
MnGa/Fe_5Co_3		3 out of 4 Co atoms	0.166	0.075	2.28
MnGa/Fe_5Co_3		4 out of 4 Fe atoms	0.173	−0.037	−1.12
MnGa/Fe		Only Fe	0.159	0.049	1.49

ever, it should be noted that the samples in the study by Ma *et al.* were annealed at 350 °C for 30 min after deposition while the samples in the current study were not annealed. According to the DFT calculations (Tab. 5.2) it is evident that the interface exchange coupling is strictly related to the type and concentration of atoms from the soft layer at the interface. Therefore, it is concluded that in the study by Ma *et al.* due to the annealing process, possible diffusion of Fe atoms from the interior layers towards the interface took place which results in a Fe-rich interface (with small amount of Co) on the soft magnetic layer side of the exchange interface [206]. This leads to a negative interface exchange coupling for samples with more than 25 % Co [77] (see Tab. 5.2, rows 2, 4 and 6). For samples with less than 25 % Co, on the other hand, same thermally induced diffusion results in presence of only Fe atoms at the vicinity of the interface (Fe termination on the soft layer side). Therefore, based on the last row in Tab. 5.2 for pure Fe, the exchange interaction is completely in favor of ferromagnetic coupling.

Moreover, interface intermixing is also of great importance in the samples which have been under heat treatment [207, 208]. However, this is not the case in the current study. Intermixing is again resulted from the selective inter-diffusion of atoms from interior toward the exchange interface. Depending on the new phase(s) which can form at the interface and the resulting magnetic properties, this newly formed interface region can act either against or in favor of exchange interaction. For instance Liu *et al.* have shown that in the SmCo/Fe (10 nm) bilayer system such inetrmixed interface improves the exhcange coupling since the magnetic properties change gradually at the length scale of 8 nm [208].

In order to elucidate the effect of soft magnetic layer thickness on the coherency of exchange coupling, scale-bridging micromagnetic simulations were performed using the input data of the DFT calculations. As the first step, using OOMMF code, hysteresis graphs for MnGa/FeCo bilayers with various thicknesses of the Fe_3Co_5 layer were simulated. Fig. 5.35-(a) shows the hysteresis loops for a range of FeCo thicknesses from 0 nm (pure MnGa) to 8 nm. It is found that by increasing the thickness of the FeCo layer, the hysteresis loops no longer show a perfect rectangular shape similar to the pure MnGa layer.

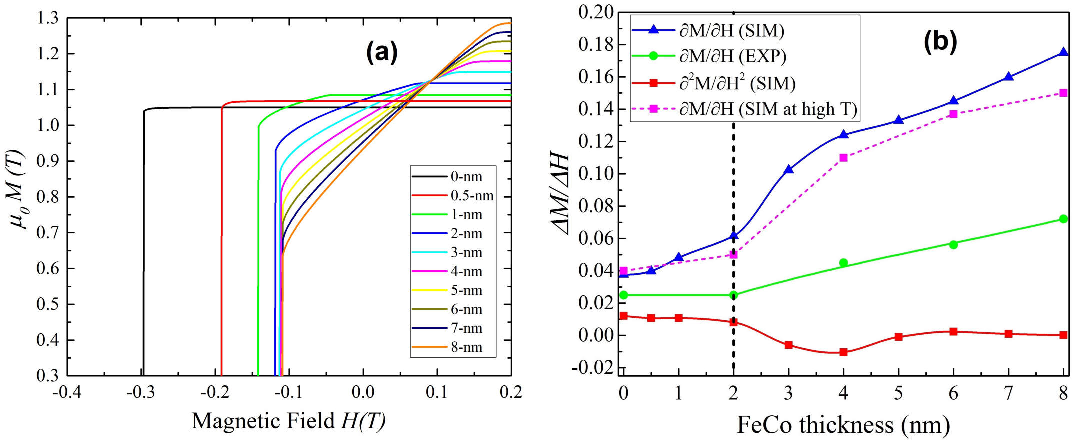

Figure 5.35: (a) Simulated hysteresis loops using OOMMF code for a MnGa(001)/Fe_3Co_5(001) bilayer system corresponding to the first row of data in Tab. 5.2 for various thicknesses of FeCo. (b) First derivative plots of both experimental and simulated hysteresis loops for MnGa(001)/Fe_3Co_5(001) bilayers as a function of soft layer thickness. The first derivative at higher temperature is also inculded in the same graph for comparison. For better visualization, the second derivative of the simulated data is shown as well. Figure is adapted from Ref. [193].

To accurately characterize the effect of increasing soft layer thickness on the degree of exchange coupling, the first and second derivatives of the hysteresis loops in Fig. 5.35-(a) are plotted in Fig. 5.35-(b) as a function of the FeCo layer thickness. For comparison, the first derivative of the experimental hysteresis loops from Fig. 5.32 is also included. From the first derivatives, a critical thickness can be defined below which the hysteresis loop for the exchange coupled bilayer becomes incoherent. The second derivative is shown for a better representation of the incoherency in case of the simulated hysteresis loops. As it can be observed from Fig. 5.35-(b), at 2 nm thickness of the FeCo layer the slope of the first derivative is rather abruptly increased which implies a significant decrease in the coherency of exchange coupling. This jump in the plot at 2 nm FeCo thickness can also be observed in the the second derivative plot.

Due to the assumption of a perfect single crystalline structure in the micromagnetic simulations at either side of the exchange interface, the simulated graphs generally show lower coercivity values compared to the experimentally measured hysteresis loops. The higher value of coercivity in the experimental samples, which is beneficial as it leads to a higher energy product, is attributed to the possible defects/inhomogeneities present in the experimental samples (e. g., thickness variations, phase segregation, secondary phases, chemical gradients, etc). Such imperfections result in higher coericivity due to domain wall pinning. Not only such inhomogeneities can smear the sharpness of the hysteresis curves but also can cause a quasidiscontinuous magnetization (not included in the simulation) which appears as a shoulder around zero field in the experimental data [203]. Since the MnGa/FeCo bilayer samples in current study are epitaxially grown, as also confirmed by HR-TEM/STEM images, the hard/soft interface is smooth with a roughness of only a few unit cells and therefore interface roughness is not considered as a factor affecting the coercivity in MnGa/FeCo bilayers [193]. However, it should be noted that interface roughness is considered as the dominant factor deteriorating the exchange coupling in non-epitaxial or polycrystalline bilayers [106].

Based on the micromagnetic simulation data in Fig. 5.35-(a), the coercivity of bilayers decreases as a function of FeCo layer thickness (i. e., increasing volume of soft the magnetic layer) although this effect is only significant for a soft layer thickness below 2 nm (below the exchange length of hard magnetic MnGa layer $\sim 2.0\,\mathrm{nm}$). Such thickness dependency of coercivity in epitaxial bilayers has been previously reported by Patra *et al.* [209]. This shows that the simulation model used in this study with the assumption of single crystalline epitaxial bilayers can accurately predict the expected exchange coupled hysteresis loops for MnGa/FeCo bilayer system and therefore can be reliably used to predict critical thickness of 2 nm for this system. In comparison, the hysteresis loops collected from the experimental bilayers (in Fig. 5.32) show nearly no thickness dependency of coercivity. The inconsistency suggests that the simplified micromagnetic model used in current study can only simulate the coercivity values observed in the experimental bilayers with high accuracy in case defects/inhomogeneities are implemented into the simulated structures.

In addition, the simulations have been performed at 0 K while the experimental data were collected at room-temperature. Since at higher temperatures both saturation magnetization and anisotropy decrease, additional micromagnetic simulations were performed using slightly decreased values (by only 10%) of saturation magnetization (M_s), magnetic anisotropy (K_u) and interface exchange energy (J_{int}) to roughly estimate the effect of slightly higher temperature on the value of critical thickness. As it can be seen in the derivative graphs in Fig. 5.35-(b), at this slightly higher temperature the resulted derivative graph shows similar trend as for the 0 K only with slightly smaller derivative values which lie closer to the experimental values (magenta dashed line). Therefore, it is concluded that the higher temperature does not affect the critical thickness of 2 nm observed in both experiment and simulation.

The 2 nm critical thickness of the FeCo layer observed for the MnGa/FeCo system is twice the value of 1 nm in the case of MnBi/FeCo system [106]. The improved exchange coupling can be attributed to the similar cubic crystal structure of both MnGa and FeCo with low interfacial strain which results in epitaxial growth of FeCo layer. The smooth interface between hard/soft magnetic layers resulting from epitaxial growth improves exchange interactions. Considering the fact that values of bulk anisotropy and exchange stiffness are rather similar for MnGa and MnBi, the results of current study shows that microstructural factors such as crystalline structure and orientations, interface roughness, and epitaxial growth strongly affect the degree of exchange coupling in multilayer systems. The 2D model nanostructures presented in the current study can be employed to investigate the controlling structural factors which allow for engineering of exchange properties in exchange spring magnets.

The purpose of this study was synthesis of rare-earth free Mn-based ferromagnetic thin films, in particular MnBi and MnGa. Since these phases theoretically show moderate saturation magnetization, exchange coupled bilayers of MnBi/FeCo and MnGa/FeCo systems have been synthesized to achieve higher energy density. For this purpose, I have used magnetron sputtering as a cost-efficient industrial deposition method for thin film growth. The results of this study are divided into four main parts.

In the first part of this work, I have shown that it is possible to sputter high-quality LTP MnBi thin films from an alloy $Mn_{55}Bi_{45}$ (at. %) target on quartz glass substrates, but a subsequent heat treatment under vacuum at annealing temperature of T_{ann}=415 °C was necessary to achieve a high degree of c-axis texture in the resulting thin films. These highly textured phase-pure MnBi films have shown a high saturation magnetization of 600 emu/cm^3 and a high uniaxial anisotropy of $\sim 1.86\,MJ/m^3$, as measured by torque magnetometry, which are one of the highest values ever reported for this phase in thin film form. The observed positive temperature coefficient of coercivity and anisotropy field is in good agreement with the results of performed DFT calculations. The coercivity of the MnBi films depends on the annealing temperature in a way that slightly lower annealing temperature of T_{ann}=365 °C results in a slight decrease in saturation magnetization but a higher out-of-plane coercivity of 12 kOe. This is attributed to the presence of some unreacted Bi in the films which results in a large room-temperature maximum energy product close to 8.7 MGOe. Slightly higher amount of Mn ($Mn_{55}Bi_{45}$ (at.%)) leads to the highest saturation magnetization in the MnBi thin films. In addition, it was shown that the Curie temperature of LTP-MnBi film is as high as $\sim$510 K with a positive temperature coefficient for both coercivity and magnetic anisotropy. Moreover, I have found that alloy sputtering targets with a pre-defined starting stoichiometry can be reliably used to deposit single layer thin films of these Mn-based alloy phases due to a fairly precise stoichiometry transfer from sputtering targets to the deposited films. This straightforward approach is of special importance, since based on the equilibrium phase diagrams, composition is an important factor which influences the resulting magnetic properties in Mn-based intermetallic alloys.

In the next part, exchange spring MnBi/Fe_xCo_{1-x} (x=0.65 and 0.35) bilayers with different soft magnetic layer thicknesses (0-4 nm) were fabricated by DC magnetron sputtering from alloy targets. The magnetic measurements revealed that a Co-rich FeCo soft magnetic layer results in more coherent exchange properties with an optimum soft layer thickness of 1 nm leading to $\sim$3% increase in the saturation magnetization, however, a complete single-phase hysteresis cannot be obtained for higher FeCo thickness. the DFT calculations performed by Dr. Ashkan Moradabadi from the group of Jun. Prof. Hongbin Zhang at TU Darmstadt showed that in the MnBi(001)/FeCo exchange bilayers a combination of crystalline (110) and disordered FeCo phases are formed. The HR-TEM evaluations have confirmed the presence of disordered region close to the exchange interface which considerably limits the exchange coupling effect. Moreover, a (110) orientation for FeCo layer was revealed by HR-TEM. The STEM-EDX elemental mapping was in good agreement with the phases present in each layer and confirmed the stoichiometry of the deposited layers, which slightly varies across the layer. The micromagnetic simulations by Dr. Min Yi from the group of Prof. Dr. Bai-Xiang Xu at TU Darmstadt showed that the thickness of the soft magnetic layer and the interface roughness between the hard and soft magnetic layers control the effectiveness of exchange coupling. Both experiment and simulation have shown that above 1 nm FeCo thickness, the exchange coupling deteriorates. The incomplete exchange coupling observed in MnBi/FeCo bilayers can be correlated with the high interfacial roughness which reduces the exchange constant.

In the third part, I have shown that it is possible to grow phase-pure highly epitaxial $L1_0$-$Mn_{1.5}Ga$ thin films directly from a stoichiometric sputtering target on top of Cr-buffered MgO(100) substrates at an optimum substrate temperature of 450 °C. The resulting films showed a high saturation magnetization of 840 emu/cm^3 and a very high perpendicular magnetic anisotropy of 2.1 MJ/m^3 both of which are in a very good agreement with the theoretically predicted values for $Mn_{1.5}Ga$ phase and to my knowledge are the highest experimental values so far reported for $Mn_{1.5}Ga$ thin films. The coercivity of $Mn_{1.5}Ga$ thin film is 6 kOe and, as expected, it shows a negative temperature coefficient. A Curie temperature of 530 K and a negative temperature coefficient for the coercivity and magnetic anisotropy have been observed.

Finally, the exchange coupling effect was investigated in $Mn_{1.5}Ga$/FeCo bilayer system. The exchange coupling is coherent for a soft layer thickness up to 2 nm leading to a $\sim$ 20% increase in total magnetization, and an enhanced total energy product. The DFT calculations, by Dr. Ashkan Moradabadi from the group of Jun. Prof. Hongbin Zhang at TU Darmstadt, considering different FeCo compositions, revealed that a Co-rich soft magnetic layer with Co termination is in favour of coherent ferromagnetic exchange coupling. In addition, pure Fe layer on top of MnGa also indicated a ferromagnetic exchange coupling, although compared to FeCo, the exchange constant in pure Fe case is smaller. The TEM evaluations confirmed epitaxial growth of both hard and soft magnetic layers with a smooth interface which is responsible for the coherent exchange coupling effect between the layers. The EDX elemental mapping confirmed the stoichiometry of MnGa and FeCo layers. Microstructural analysis of the interface using both HR-TEM and micromagnetic simulations showed that hard/soft interface properties such as roughness and epitaxial growth are critical to achieve strong exchange coupling. The epitaxial growth of the MnGa/FeCo bilayers resulted in a better interface quality and therefore a more coherent exchange coupling compared to the MnBi/FeCo system. Both experiment and modelling showed that coherent exchange coupling is restricted to a critical FeCo thickness of 2 nm. The model used in this thesis provides useful guidelines to synthesize efficient exchange coupled rare-earth free permanent magnets with applications in renewable energy and spintronics through interface engineering of the hard/soft magnetic phases.

The result of current study shows that MnBi and MnGa are both promising rare-earth free candidates; however, it also emphasizes on the criticality of high interface quality in their exchange coupled bilayers which can be achieved only through pronounced growth properties. Among the two investigated candidates, namely MnBi and MnGa, the former shows lower magnetization but is more cost-efficient. The latter, on the other hand, is easier to be grown epitaxially due to the crystallographic characteristics of the phase. Nevertheless, as rare-earth free ferromagnetic phases both candidates are considered cost-efficient. In any case, further improvement of crystallinity of the grown layers are of paramount importance.

7.1 Different deposition approach

Since it is a cost-effective method, in this thesis I have performed the thin film growth using sputtering deposition. However, inability to perform ***in-situ*** growth characterization in our custom-made system either by the means of QCM (quartz crystal microbalance) to monitor the growth rate, or using RHEED (reflection high-energy electron diffraction) to monitor the layer-by-layer growth of epitaxial films brought about additional difficulties. Moreover, a precise control over the growth rate and investigating the effect of lower growth rates was not possible in the current sputtering setup. Therefore, searching for a suitable single crystalline substrate, in case of MnBi thin films, and growth study using a more precise growth method with lower growth rates, e.g. molecular beam epitaxy (MBE), is necessary in order to further improve the growth properties of the resulting layers. Due to time limitation for the experiments, a vast thickness study combined with investigation on the effect of different buffer layers is also remained of question for further work. This can also affect the quality of grown thin films and therefore can improve the resulting crystalline and magnetic properties.

7.2 $L1_0$-MnAl and effect of buffer layers

As shortly mentioned in the introduction section, tetragonal τ-MnAl is also another promising Mn-based intermettalic phase which was not studied in this thesis. Based on the literature review, the τ-MnAl epitaxial thin films with highest magnetization has been reported by Hosoda ***et al.*** [9]. In their experiment, they have grown the MnAl (001) epitaxial thin films using sputtering deposition and a $Mn_{48}Al_{52}$ (at.%) alloy target on Cr-buffered MgO (100) single crystalline substrates at T_s=200 °C followed by post annealing at higher temperature of 450 °C. The resulting films show a M_s of $\sim$ 600 emu/cm^3 and K_u of 10 Merg/cm^3 which are still only $\sim$ 75% and 66% of the predicted theoretical values reported for $L1_0$-MnAl phase [56]. A full growth study with different growth temperatures, various annealing temperatures and effect of composition would be necessary to further improve the quality of MnAl epitaxial thin films. As the next step, investigation of exchange coupling effect in MnAl/FeCo bilayer system would be of great interest. Moreover, as summarized in Tab. 7.1 effect of different buffer layers with various thicknesses on the quality of the epitaxially grown MnAl and MnGa thin films can be evaluated. Based on the values in Tab. 7.1, noble metals such as Pd and Pt are promising candidates resulting in a lattice misfits below 1% which can lead to significant improvement in growth properties of these films [56].

7.3 MnBi epitaxial (001) thin films

Finding a suitable single crystalline substrate among the standard commercially available substrates which allows for epitaxial growth of MnBi layer was challenging due to the hexagonal crystal structure of MnBi and its lattice constant. However, I have finally found a hint in an old article from Schoenes ***et al.*** where epitaxial growth of MnBi layer on BaF_2 (111) substrate was shortly studied [210]. Although due to time limitation I was not able to fully investigate the growth properties of MnBi film deposited on this

Table 7.1: Summarized values of lattice misfit between different substrates (buffer layers) and $L1_0$-MnGa (a= 3.886 Å) or $L1_0$-MnAl (a= 3.920 Å) phases. The lattice parameter values are adapted from ICDD (International centre for diffraction data). The (*) values are calculated with 45° in-plane rotation (a=a/$\sqrt{2}$).

Buffer	a[Å]	$L1_0$-MnGa [%]	$L1_0$-MnAl[%]
MgO	4.21	-7.8	-7.0
GaAs	4.00*	-2.7	-1.9
STO	3.91	0.8	0.3
InAs	4.28*	-9.1	-8.4
AlAs	4.00*	-2.7	-1.9
Cr	4.07*	-4.6	-3.8
Pd	3.89	-0.1	0.8
Pt	3.92	0.9	0
Au	4.08	-4.8	-3.9
Ag	4.09	-5.0	-4.2
Si	3.94	-1.4	-0.5
Al	4.05	-4.0	-3.2
Cu	3.61	7.6	8.6

single crytsalline substrate, I have performed preliminary experiments to shortly evaluate the possibility of out-of-plane growth. Fig. 7.1 shows XRD patterns collected from three different MnBi films which were grown on BaF_2(111) substrates. First film was grown at a substrate temperature of 400 °C without any post annealing. Beside the two strongest peaks which belong to BaF_2 (111) substrate, the peak indexing only shows small individual diffraction peaks from Bi and Al cap layer. The second film was grown at lower substrate temperature of 300 °C but was annealed after deposition for 30 min at 530 °C. The XRD patterns show appearance of two additional peaks which can be indexed to MnBi (002) and MnBi (004) planes although some other small peaks which belong to unreacted Bi are also present. The third sample was grown again at substrate temperature of 300 °C but was annealed after deposition for longer duration of 1 h at 530 °C. Based on the measured XRD patterns, long annealing time caused significant decrease in the intensity of MnBi (002) and (004) peaks. This shows that applying only substrate temperature does not result in epitaxial growth, and a combination of a lower substrate temperature and a higher annealing temperature is more helpful. A magnetization of $\sim$ 540 emu/cm^3 was measured for the sample annealed for 30 min at 530 °C and the two other samples have shown significantly lower magnetization ($<$ 50 emu/cm^3). This preliminary study proves that the epitaxial growth of MnBi (002) films on top of the single crystalline BaF_2(111) substrate is possible in our costume-made sputtering unit. However, a full growth and thickness study evaluating effect of different substrate and annealing temperatures as well as different growth rates is necessary to optimize the growth process and to find the suitable growth window for deposition of epitaxial phase-pure LTP-MnBi films with high crystallinity and magnetic properties.

7.4 MnGa/FeCo/MnGa trilayer exchange spring system

As mentioned, for high performance permanent magnets exchange coupling of a hard magnetic phase with high anisotropy to a soft magnetic phase with high polarization can lead to enhanced energy density ($(BH)_{\max}$). The result of this thesis by modelling of exchange coupled bilayers has shown that epitaxial growth with optimum texture, which leads to both excellent magnetic properties and less roughness of

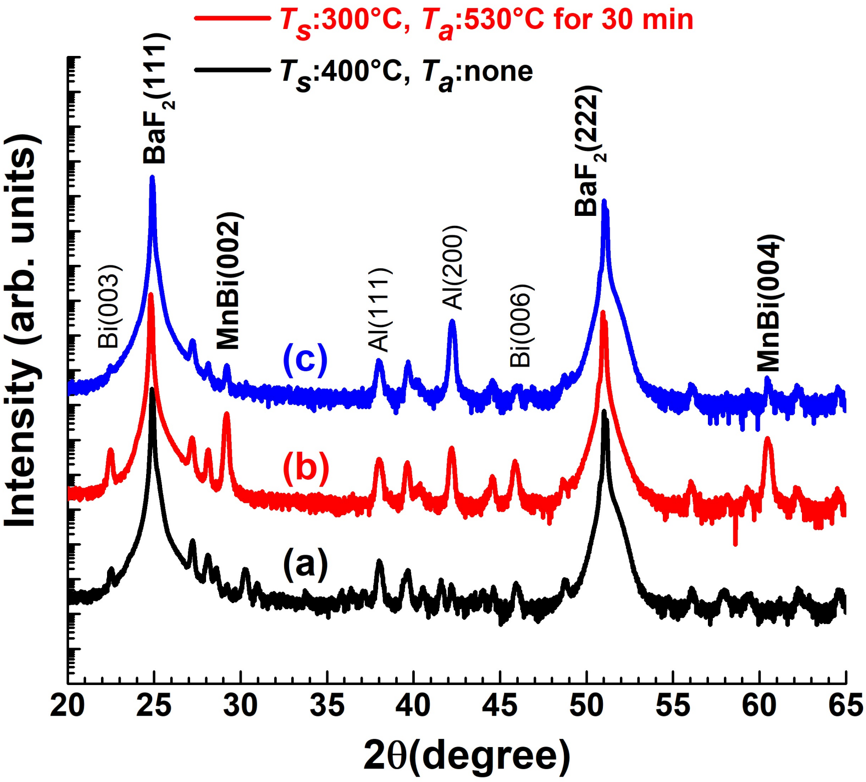

Figure 7.1: XRD patterns collected from three MnBi thin films grown from $Mn_{55}Bi_{45}$ alloy target onto BaF_2(111) (a) grown at T_s= 400 °C without annealing, (b) grown at T_s= 300 °C with post annealing at T_a= 530 °C for 30 min, and (c) grown at T_s= 300 °C with post annealing at T_a= 530 °C for 1 h. For better visualization, the graphs have a vertical offset.

exchange interface, is necessary to achieve strong exchange coupling. In this case due to epitaxial growth the excellent magnetic properties could be maintained for different thicknesses of hard magnetic layer and will not change as a function of film thickness. In exchange systems such as MnGa/FeCo where successful epitaxial growth of the bilayers and therefore strong exchange coupling is possible, the deposition of multilayer heterostructures of exchanged couple layers with thin hard magnetic layers is of great interest. Growth and magnetic properties in trilayers with sandwiched FeCo soft magnetic layer between two layers of MnGa hard magnetic phase (with variable thickness ratios) can be studied to investigate the feasibility of deposition with the same out-of-plane epitaxial texture, and to evaluate coherency of exchange coupling and overall magnetic properties in this system. If such approach is successful, one can subsequently engineer epitaxial multilayers to further enhance the magnetic properties.

8.1 Publications

1. **Sareh Sabet**, E. Hildebrandt, F. M. Römer, I. Radulov, H. Zhang, M. Farle, and L. Alff, Low-temperature phase c-axis oriented manganese bismuth thin films with high anisotropy grown from an alloy $Mn_{55}Bi_{45}$ target, IEEE Trans. Magn. 53, 2100306 (2017). doi : 10.1109/TMAG.2016.2636817
2. **Sareh Sabet**, E. Hildebrandt, and L. Alff, Synthesis and magnetic properties of the thin film exchange spring system of MnBi/FeCo, Journal of Physics: Conf. Series 903, 012032 (2017). doi :10.1088/1742-6596/903/1/012032
3. **Sareh Sabet**, A. Moradabadi, S. Gorji, M. Yi, Q. Gong, M. H. Fawey, E. Hildebrandt, D. Wang, H. Zhang, B. -X. Xu, C. Kübel, and L. Alff, The impact of interface structure on magnetic exchange coupling in MnBi/Fe_xCo_{1-x} bilayers, Phys. Rev. B 98, 174440 (2018).doi : 10.1103/PhysRevB.98.174440
4. **Sareh Sabet**, A. Moradabadi, S. Gorji, M. H. Fawey, E. Hildebrandt, I. Radulov, D. Wang, H. Zhang, C. Kübel, and L. Alff, Correlation of interface structure and magnetic exchange in a hard/soft magnetic model nanostructure, Phys. Rev. Appl. 11, 054078 (2019). doi : 10.1103/PhysRevApplied.11.054078

8.2 Conference contributions

1. **Sareh Sabet**, Erwin Hildebrandt and Lambert Alff, Structural and magnetic properties of MnBi thin films grown by magnetron sputtering, poster presentation, **DPG** conference, March 2015, Berlin, Germany
2. **Sareh Sabet**, Erwin Hildebrandt , Florian M. Römer , Michael Farle and Lambert Alff, *c*-axis oriented MnBi thin films with high anisotropy grown from a single $Mn_{55}Bi_{45}$ target, oral presentation, **DPG** conference, March 2016, Regensburg, Germany
3. **Sareh Sabet**, Erwin Hildebrandt , Florian M. Römer, Hongbin Zhang, Michael Farle and Lambert Alff, Structural and magnetic properties of *c*-axis oriented MnBi thin films with high anisotropy grown from a single $Mn_{55}Bi_{45}$ target, oral presentation, **JEMS** conference, August 2016, Glasgow, UK
4. **Sareh Sabet**, Erwin Hildebrandt and Lambert Alff, *c*-axis oriented MnBi thin films with high anisotropy grown from one stoichiometric sputtering target, poster presentation, **REPM** workshop, September 2016, Darmstadt, Germany
5. **Sareh Sabet**, Ashkan Moradabadi, Saleh Gorji, Min Yi, Qihua Gong, Mohammad H. Fawey, Erwin Hildebrandt, Di Wang, Hongbin Zhang, Bai-Xiang Xu, Christian Kübel, and Lambert Alff, Structural and theoretical investigations of MnBi/MnGa-FeCo exchange spring bilayers, poster presentation, **JEMS** conference, September 2018, Mainz, Germany
6. **Sareh Sabet**, Ashkan Moradabadi, Saleh Gorji, Min Yi, Qihua Gong, Mohammad H. Fawey, Erwin Hildebrandt, Di Wang, Hongbin Zhang, Bai-Xiang Xu, Christian Kübel, Lambert Alff, Role of interface properties on magnetic exchange in MnGa/FeCo and MnBi/FeCo bilayer nanostructures, oral presentation, **JEMS** conference, August 2019, Uppsala, Sweden

References

[1] N. Poudyal and J. P. Liu, Advances in Nanostructured Permanent Magnets Research, J. Phys. D: Appl. Phys. 46 (2013) 043001. doi:10.1088/0022-3727/46/4/043001

[2] O. Gutfleisch, Controlling the Properties of High Energy Density Permanent Magnetic Materials by Different Processing Routes, J. Phys. D: Appl. Phys. 33 (2000) R157. doi:10.1088/0022-3727/33/17/201

[3] M. J. Kamer, R. W. McCallum, I. A. Anderson and S. Constantinides, Prospects for Non-Rare Earth Permanent Magnets for Traction Motors and Generators, JOM. 64 (2012) 752. doi:10.1007/s11837-012-0351-z

[4] U.S. Geological Survey, Mineral Commodity Summaries 2018, https://minerals.usgs.gov/minerals/pubs/commodity/rare-earths/, accessed 30.01.2018.

[5] O. Gutfleisch, M. A. Willard, E. Brück, C. H. Chen, S. G. Sankar, and J. P. Liu, Magnetic Materials and Devices for the 21st Century: Stronger, Lighter, and More Energy Efficient, Adv. Mater. 23 (2011) 821. doi:10.1002/adma.201002180

[6] C. Chappert, A. Fert and F. N. V. Dau, The Emergence of Spin Electronics in Data Storage, Nat. Mater. 6 (2007), 813. doi:10.1038/nmat2024

[7] S. Mizukami, T. Kubota, F. Wu, X. Zhang, T. Miyazaki, H. Naganuma, M. Oogane, A. Sakuma, and Y. Ando, Composition Dependence of Magnetic Properties in Perpendicularly Magnetized Epitaxial Thin Films of Mn-Ga Alloys, Phy. Rev. B. 85 (2012) 014416. doi:10.1103/PhysRevB.85.014416

[8] L. J. Zhu, D. Pan, S. H. Nie, J. Lu and J. H. Zhao, Tailoring Magnetism of Multifunctional Mn_xGa Films with Giant Perpendicular Anisotropy, Appl. Phys. Lett. 102 (2013) 132403. doi:10.1063/1.4799344

[9] M. Hosoda, M. Oogane, M. Kubota, T. Kubota, H. Saruyama, S. Iihama, H. Naganuma, and Y. Ando, Fabrication of $L1_0$-MnAl Perpendicularly Magnetized Thin Films for Perpendicular Magnetic Tunnel Junctions, J. Appl. Phys. 111 (2012) 07A324. doi:10.1063/1.3676428

[10] H. Saruyama, M. Oogane, Y. Kurimoto, H. Naganuma, and Y. Ando, Fabrication of $L1_0$-ordered MnAl Films for Observation of Tunnel Magnetoresistance Effect, Jpn. J. Appl. Phys. 52 (2013) 063003. doi:10.7567/JJAP.52.063003

[11] P. Kharel, R. Skomski, R. D. Kirby, and D. J. Sellmyer, Structural, Magnetic and Magneto-transport Properties of Pt-alloyed MnBi Thin Films, J. Appl. Phys. 107 (2010) 09E303. doi:10.1063/1.3360204

[12] W. Zhang, P. Kharel, S. Valloppilly, L. Yue, and D . J. Sellmyer, High-energy-product MnBi Films with Controllable Anisotropy, Phys. Status. Solidi. B. 252 (2015) 1934. doi:10.1002/pssb.201552075

[13] D. Weller, G. Parker,O. Mosendz, E. Champion, B. Stipe, X. Wang, T. Klemmer, G. Ju, and A. Ajan, A HAMR Media Technology Roadmap to an Areal Density of 4 Tb/in^2, IEEE T. Magn. 50 (2014) 3100108. doi:10.1109/TMAG.2013.2281027

[14] H. Pandey, J. Wang, T. Shiroyama, B. S. D. Ch. S. Varaprasad, H. Sepehri-Amin, Y. K. Takahashi, A. Perumal and K. Hono, Structure Optimization of FePt-C Nanogranular Films for Heat Assisted Magnetic Recording Media, IEEE T. Magn. 52 (2016) 3200108. doi:10.1109/TMAG.2015.2477313

[15] J. M. D. Coey, Hard Magnetic Materials: A Perspective, IEEE Trans. Magn. 47 (2011) 4671. doi:10.1109/TMAG.2011.2166975

[16] F. Heusler, Über Manganbronze und über die Synthese Magnetisierbarer Legierungen aus Unmagnetischen Metallen, Angewandte. Chem. 17 (1904) 260. doi:10.1002/ange.19040170903

[17] C. Guillaud, Polymorphisme du composé défini Mn Bi aux températures de disparition et de réapparition de l'aimantation spontanée, J. Phys. Radium. 12 (1951) 143. doi:10.1051/jphysrad:01951001202014300

[18] C. Guillaud, Les points de transformation des composés définis MnAs, MnBi en relation avec un mécanisme probable d'antiferromagnétisme, J. Phys. Radium. 12 (1951) 223. doi:10.1051/jphysrad:01951001203022300

[19] E. Adams, W. M. Hubbard, and A. M. Syelles, A New Permanent Magnet from Powdered Manganese Bismuthide, J. Appl. Phys. 23 (1952) 1207. doi:10.1063/1.1702032

[20] E. Adams, A New Permanent Magnet from Powdered Manganese Bismuthide, Rev. Mod. Phys. 25 (1953) 306. doi:10.1103/RevModPhys.25.306

[21] D. Li, D. Pan, S. Li, and Z. Zhang, Recent Developments of Rare-earth-free Hard-magnetic Materials, Sci. China-Phys. Mech. Astron. 59 (2016) 617501. doi:10.1007/s11433-015-5760-x

[22] B. W. Roberts, Neutron Diffraction Study of the Structures and Magnetic Properties of Manganese Bismuthide, Phys. Rev. 104 (1956) 607. doi:10.1103/PhysRev.104.607

[23] J. Park, Y. K. Hong, J. Lee, W. Lee, S. G. Kim, and C. J. Choi, Electronic Structure and Maximum Energy Product of MnBi, Metals. 4 (2014) 455. doi:10.3390/met4030455

[24] H. J. Williams, R. C. Sherwood, and O. L. Boothby, Magnetostriction and Magnetic Anisotropy of MnBi, J. Appl. Phys. 28 (1957) 445. doi:10.1063/1.1722768

[25] P. A. Albert and W. J. Carr, Jr., Temperature Dependence of Magnetostriction and Anisotropy in MnBi, J. Appl. Phys. 32 (1961) S201. doi:10.1063/1.2000402

[26] T. Chen and W. E. Stutius, The Phase Transformation and Physical Properties of the MnBi and $Mn_{1.08}Bi$ Compounds, IEEE T. Magn. 10 (1974) 581. doi:10.1109/TMAG.1974.1058367

[27] X. Guo, X. Chen, Z. Altounian, and J. O. Ström-Olsen, Magnetic Properties of MnBi Prepared by Rapid Solidification, Phys. Rev. B. 46 (1992) 14578. doi:10.1103/PhysRevB.46.14578

[28] J. B. Yang, Y. B. Yang, X. G. Chen, X. B. Ma, J. Z. Han, Y. C. Yang, S. Guo, A. R. Yan, Q. Z. Huang, M. M. Wu, and D. F. Chen, Anisotropic Nanocrystalline MnBi with High Coercivity at High Temperature, Appl. Phys. Lett. 99 (2011) 082505. doi:10.1063/1.3630001

[29] C. Curcio, E. S. Olivetti, L. Martino, M. Küpferling and V. Basso, Study of the Temperature Dependence of Coercivity in MnBi, Phys. Procedia. 75 (2015) 1230. doi:10.1016/j.phpro.2015.12.135

[30] J. B. Yang, W. B. Yelon, W. J. James, Q. Cai, S. Roy, and N. Ali, Structure and Magnetic Properties of the MnBi Low Temperature Phase, J. Appl. Phys. 91 (2002) 7866. doi:10.1063/1.1451306

[31] J. B. Yang, K. Kamaraju, W. B. Yelon, W. J. James, Q. Cai, and A. Bollero, Magnetic Properties of the MnBi Intermetallic Compound, Appl. Phys. Lett. 79 (2001) 1846. doi:10.1063/1.1405434

[32] J. B. Yang, W. B. Yelon, W. J. James, Q. Cai, M. Kornecki, S. Roy, N. Ali, and P. I. Heritier, Crystal Structure, Magnetic Properties and Electronic Structure of the MnBi Intermetallic Compound, J. Phys. Condens. Matter. 14 (2002) 6509. doi:10.1088/0953-8984/14/25/318

[33] R. G. Pirich and D. J. Larson, Magnetic and Metallurgical Properties of Directionally Solidified Eutectic Bi/MnBi Composites: The Effects of Annealing, J. Appl. Phys. 50 (1979) 2425. doi: 10.1063/1.326974

[34] S. Sabet, E. Hildebrandt, F. M. Römer, I. Radulov, H. Zhang, M. Farle and L. Alff, Low-Temperature Phase *c*-axis Oriented Manganese Bismuth Thin Films with High Anisotropy Grown from an Alloy $Mn_{55}Bi_{45}$ Target, IEEE Trans. Magn. 53 (2017) 2100306. doi:10.1109/TMAG.2016.2636817

[35] G. Q. Di, S. Iwata, and S. Uchiyama, Composition Dependences of Kerr Rotations in MnBi and MnBiAl Films, J. Magn. Magn. Mater. 131 (1994) 242. doi:10.1016/0304-8853(94)90035-3

[36] Y. B. Yang, X. G. Chen, R. Wu, J. Z. Wei, X. B. Ma, J. Z. Han, H. L. Du, S. Q. Liu, C. S. Wang, Y. C. Yang, Y. Zhang, and J. B. Yang, Preparation and Magnetic Properties of MnBi, J. Appl. Phys. 111 (2012) 07E312. doi:10.1063/1.3672086

[37] J. Cui, J. P. Choi, E. Polikarpov, M. E. Bowden, W. Xie, G. Li, Z. Nie, N. Zarkevich, M. J. Kramer, D. Johnson, Effect of Composition and Heat Treatment on MnBi Magnetic Materials, Acta. Mater. 79 (2014) 374. doi:10.1016/j.actamat.2014.07.034

[38] J. Cui, J. P. Choi, G. Li, E. Polikarpov, J. Darsell, N. Overman, M. Olszta, D. Schreiber, M. Bowden, T. Droubay, M. J. Kramer, N. A. Zarkevich, L. L. Wang, D. D. Johnson, M. Marinescu, I. Takeuchi, Q. Z. Huang, H. Wu, H. Reeve, N. V. Vuong, and J. P. Liu, Thermal Stability of MnBi Magnetic Materials, J. Phys. Condens. Mat. 26 (2014) 064212. doi:10.1088/0953-8984/26/6/064212

[39] M. A. McGuire, H. Cao, B. C. Chakoumakos, and B. C. Sales, Symmetry-lowering Lattice Distortion at the Spin Reorientation in MnBi Single Crystals, Phys. Rev. B. 90 (2014) 174425. doi:10.1103/PhysRevB.90.174425

[40] P. Kharel, R. Skomski, and D. J. Sellmyer, Spin Correlations and Electron Transport in MnBi:Au films, J. Appl. Phys. 109 (2011) 07B709. doi:10.1063/1.3537952

[41] P. Kharel, X. Z. Li, V. R. Shah, N. Al-Aqtash, K. Tarawneh, R. F. Sabirianov, R. Skomski, and D. J. Sellmyer, Structural, Magnetic, and Electron Transport Properties of MnBi:Fe Thin Films, J. Appl. Phys. 111 (2012) 07E326. doi:10.1063/1.3675615

[42] T. Suzuki, T. Hozumi, J. Barker, S. Okatov,O. Mryasov, and T. Suwa, Investigation into Magnetic Anisotropy of Low Temperature Phase (LTP) MnBi Thin Films, IEEE Trans. Magn. 51 (2015) 2102804. doi:10.1109/TMAG.2015.2438632

[43] T. Hozumi, P. LeClair, G. Mankey, C. Mewes, H. Sepehri-Amin, K. Hono, and T. Suzuki, Magnetic and Structural Properties of MnBi Multilayered Thin Films, J. Appl. Phys. 115 (2014) 17A737. doi:10.1063/1.4867127

[44] B. Li, W. Liu, X. G. Zhao, W. J. Gong, X. T. Zhao, H. L. Wang, D. Kim, C. J. Choi, and Z. D. Zhang, The Structural and Magnetic Properties of MnBi and Exchange Coupled MnBi/Fe Films, J. Magn. Magn. Mater. 372 (2014) 12. doi:10.1016/j.jmmm.2014.07.027

[45] X.S. Lu, J.K. Liang and M.G. Zhou, ASM Metals Hand Book: Volume 3 - Alloy Phase Diagrams, ASM Internationals, Materials Park, Ohio, USA, 1980.

[46] H. G. Meissner, K. Schubert and T. R. Anantharaman, The Constitution and Structure of Manganese-Gallium Alloys, Proc. Indian Acad. Sci. 61 (1965) 340. doi:10.1007/BF03049257

[47] T. B. Massalski, Binary Alloy Phase Diagrams, 2nd edition, Materials Information Soc., Materials Park, Ohio, 1990.

[48] S. Mizukami, F. Wu, A. Sakuma, J. Walowski, D. Watanabe, T. Kubota, X. Zhang, H. Naganuma, M. Oogane, Y. Ando and T. Miyazaki, Long-Lived Ultrafast Spin Precession in Manganese Alloys Films with a Large Perpendicular Magnetic Anisotropy, Phys. Rev. Lett. 106 (2011) 117201. doi:10.1103/PhysRevLett.106.117201

[49] A. Sakuma, Electronic Structures and Magnetism of CuAu-type MnNi and MnGa, J. Magn. Magn. Mater. 187 (1998) 105. doi:10.1016/S0304-8853(98)00115-2

[50] L J Zhu , S. H. Nie , K. K. Meng , D. Pan , J. H. Zhao and H. Z. Zheng, Multifunctional $L1_0$-$Mn_{1.5}Ga$ Films with Ultrahigh Coercivity, Giant Perpendicular Magnetocrystalline Anisotropy and Large Magnetic Energy Product, Adv. Mater. 24 (2012) 4547. doi:10.1002/adma.201200805

[51] Z. Yang, J. Li, D. Wang, K. Zhang and X. Xie, Electronic Structure and Magnetic Properties of δ-MnGa, J. Magn. Magn. Mater. 182 (1998) 369. doi:10.1016/S0304-8853(97)01029-9

[52] L. J. Zhu and J. H. Zhao, Perpendicularly Magnetized Mn_xGa Films: Promising Materials for Future Spintronic Devices, Magnetic Recording and Permanent Magnets, Appl. Phys. A. 111 (2013) 379. doi:10.1007/s00339-013-7608-4

[53] J. Winterlik, B. Balke, G. H. Fecher, C. Felser, M. C. M. Alves, F. Bernardi and J. Morais, Structural, Electronic, and Magnetic Properties of Tetragonal $Mn_{3-x}Ga$: Experiments and First-principles Calculations, Phys. Rev. B. 77 (2008) 054406. doi:10.1103/PhysRevB.77.054406

[54] S. H. Nie, L. J. Zhu, J. Lu,D. Pan, H. L. Wang, X. Z. Yu, J. X. Xiao and J. H. Zhao, Perpendicularly Magnetized τ-MnAl (001) thin films epitaxied on GaAs, Appl. Phys. Lett. 102 (2013) 152405. doi:10.1063/1.4801932

[55] A. Sakuma, Electronic Structure and Magnetocrystalline Anisotropy Energy of MnAl, J. Phys. Soc. Jpn. 63 (1994) 1422. doi:10.1143/JPSJ.63.1422

[56] L. J. Zhu, S. H. Nie and J. H. Zhao, Recent Progress in Perpendicularly Magnetized Mn-based Binary Alloy Films, Chin. Phys. B. 22 (2013) 118505. doi: 10.1088/1674-1056/22/11/118505

[57] K. M. Krishnan, Ferromagnetic δ-$Mn_{1-x}Ga_x$ Thin Films with Perpendicular Anisotropy, Appl. Phys. Lett. 61 (1992) 2365. doi: 10.1063/1.108245

[58] M. Tanaka, J. P. Harbison, J. DeBoeck, T. Sands, B. Philips, T. L. Cheeks and V. G. Keramidas, Epitaxial MnGa/NiGa Magnetic Multilayers on GaAs, Appl. Phys. Lett. 63 (1993) 696. doi:10.1063/1.109932

[59] E. Lu, D. C. Ingram, A. R. Smith, J. W. Knepper and F. Y. Yang, Reconstruction Control of Magnetic Properties during Epitaxial Growth of Ferromagnetic $Mn_{3-\delta}Ga$ on Wurtzite GaN(0001), Phys. Rev. Lett. 97 (2006) 146101. doi:10.1103/PhysRevLett.97.146101

[60] A. Bedoya-Pinto, C. Zube, J. Malindretos, A. Urban and A. Rizzi, Epitaxial δ-Mn_xGa_{1-x} Layers on GaN(0001): Structural, Magnetic, and Electrical Transport Properties, Phys. Rev. B 84 (2011) 104424. doi:10.1103/PhysRevB.84.104424

[61] A. W. Arins, H. F. Jurca, J. Zarpellon, J. Varalda, I. L. Graff, W. H. Schreiner, and D. H. Mosca, Structure and Magnetism of MnGa Ultra-Thin Films on GaAs(111)B, IEEE Trans. Magn. 49 (2013) 5595. doi:10.1109/TMAG.2013.2272213

[62] K.Wang, E. Lu, J. W. Knepper, F. Yang and A. R. Smith, Structural Controlled Magnetic Anisotropy in Heusler $L1_0$-MnGa Epitaxial Thin Films, Appl. Phys. Lett. 98 (2011) 162507. doi:10.1063/1.3582244

[63] E. Feng, D. V. Thiet, D. D. Dung, Y. Shin and S. Chob, Substrate-modified Ferrimagnetism in MnGa Films, J. Appl. Phys. 108 (2010) 113903. doi:10.1063/1.3517083

[64] K. Wang, A. Chinchore, W. Lin, D. C. Ingram, A. R. Smith, A. J. Hauser and F. Yang, Epitaxial Growth of ferromagnetic δ-phase Manganese Gallium on Semiconducting Scandium Nitride(001), J. Cry. Growth 311 (2009) 2265. doi:10.1016/j.jcrysgro.2009.02.033

[65] M. Glas, D. Ebke, I.-M. Imort, P. Thomas, G. Reiss, Anomalous Hall Effect in Perpendicularly Magnetized $Mn_{3-x}Ga$ Thin Films, J. Magn. Magn. Mater. 333 (2013) 134. doi:10.1016/j.jmmm.2012.12.040

[66] M. A. Angadi and V. Thanigaimani, Hall Effect in MnAl Films, Thin Solid Films, 195 (1991) 7. doi:10.1016/0040-6090(91)90253-T

[67] T. Sands, J. P. Harbison, M. L. Leadbeater, S. J. Allen, G. W. Hull, R. Ramesh, and V. G. Keramidas, Epitaxial Ferromagnetic τMnAl Films on GaAs, Appl. Phys. Lett 57 (1990) 2609. doi: 10.1063/1.103826

[68] E.F. Kneller and R. Hawig, The Exchange-spring Magnet: A New Material Principle for Permanent Magnets. IEEE T. Magn. 27 (1991) 3588. doi:10.1109/20.102931

[69] Eric E. Fullerton, J. S. Jiang, M. Grimsditch, C. H. Sowers, and S. D. Bader, Exchange-spring Behavior in Epitaxial Hard/Soft Magnetic Bilayers, Phys. Rev. B 58 (1998) 12193. doi:10.1103/PhysRevB.58.12193

[70] Eric E. Fullerton, J. S. Jiang, and S. D. Bader, Hard/Soft Magnetic Heterostructures: Model Exchange-Spring Magnets, J. Magn. Magn. Mater. 200 (1999) 392. doi:10.1016/S0304-8853(99)00376-5

[71] T. Leineweber and H. Kronmüller, Micromagnetic Examination of Exchange Coupled Ferromagnetic Nanolayers, J. Magn. Magn. Mater. 176 (1997) 145. doi:10.1016/S0304-8853(97)00601-X

[72] R. Skomski and J. M. D. Coey, Giant Energy Product in Nanostructured Two-phase Magnets, Phys. Rev. B. 48 (1993) 15812. doi:10.1103/PhysRevB.48.15812

[73] R. Skomski, Aligned Two-phase Magnets: Permanent Magnetism of The Future?(invited), J. Appl. Phys. 76 (1994) 7059. doi:10.1063/1.358027

[74] Laura H Lewis and Félix Jiménez-Villacorta, Perspectives on Permanent Magnetic Materials for Energy Conversion and Power Generation, Metall. Mater. Trans. A. 44 (2013) 2. doi:10.1007/s11661-012-1278-2

[75] T. R. Gao, L. Fang, S. Fackler, S. Maruyama, X. H. Zhang, L. L. Wang, T. Rana,P. Manchanda, A. Kashyap, K. Janicka, A. L. Wysocki, A. T. N'Diaye, E. Arenholz, J. A. Borchers, B. J. Kirby, B. B. Maranville, K. W. Sun, M. J. Kramer, V. P. Antropov, D. D. Johnson, R. Skomski, J. Cui, and I. Takeuchi, Large Energy Product Enhancement in Perpendicularly Coupled MnBi/CoFe Magnetic Bilayers, Phys. Rev. B. 94 (2016) 060411. doi: 10.1103/PhysRevB.94.060411

[76] Y. Yan, J. Guo, J. Li, and R. Li, Magnetically Exchange Coupled MnBi/FeCo Thin Film Composites with Enhanced Maximum Energy Products, Mater. Lett. 184 (2016) 13. doi: 10.1016/j.matlet.2016.08.015

[77] Q. L. Ma, S. Mizukami, T. Kubota, X. M. Zhang, Y. Ando, and T. Miyazaki, Abrupt Transition from Ferromagnetic to Antiferromagnetic of Interfacial Exchange in Perpendicularly Magnetized $L1_0$-MnGa/FeCo Tuned by Fermi Level Position, Phys. Rev. Lett. 112 (2014) 157202. doi: 10.1103/PhysRevLett.112.157202

[78] J. M. D. Coey, Magnetism and Magnetic Materials, Cambridge University Press, NY, USA, 2009.

[79] B. D. Cullity and C. D. Graham, Introduction to Magnetic Materials, John Wiley and Sons, Inc., Hoboken, NJ, 2009.

[80] R. C. O'Handley, Modern Magnetic Materials: Principles and Applications, Wiley-Interscience, John Wiley and Sons Inc., NY, 2000.

[81] P. Weiss, L'hypothése du champ moléculaire et la propriété ferromagnétique (The Molecular Field Hypothesis and the Ferromagnetic Property), J. Phys. Theor. Appl. 6 (1907) 661. doi: 10.1051/jphystap:019070060066100

[82] T. Miyazaki and H. Jin, The Physics of Ferromagnetism, Springer-Verlag Berlin Heidelberg, 2012.

[83] H. Kronmüller H., S. Parkin (Eds.), Handbook of Magnetism and Advanced Magnetic Materials. Volume 1, Wiley-Interscience, 2007.

[84] S. Chikazumi, Physics of Ferromagnetism, Oxford University Press Inc., NY, 1997.

[85] W. Z. Heisenberg, Zur Theorie des Ferromagnetismus, Physik 49 (1928) 619. doi: 10.1007/BF01328601

[86] E. Pavarini, E. Koch, F. Anders, and M. Jarrell (Eds.), Correlated Electrons: From Models to Materials, Forschungszentrum Jülich GmbH, Jülich, Germany 2012.

[87] Mathias Getzlaff, Fundamentals of Magnetism, Springer-Verlag Berlin Heidelberg, 2008.

[88] H. Ibach, H. Lüth, Festkörperphysik, Springer Berlin Heidelberg, 1985.

[89] J. C. Slater, Electronic Structure of Alloys, J. Appl. Phys. 8 (1937) 385. doi:10.1063/1.1710311

[90] L. Pauling, The Nature of the Interatomic Forces in Metals, Phys. Rev. 54 (1938) 899. doi:10.1103/PhysRev.54.899

[91] M. A. Ruderman, C. Kittel, Indirect Exchange Coupling of Nuclear Magnetic Moments by Conduction Electrons, Phys. Rev. 96 (1954) 99. doi:10.1103/PhysRev.96.99

[92] C. Kittel, Quantum Theory of Solids, John Wiley and Sons, USA, 1987.

[93] T. Kasuya, A Theory of Metallic Ferro- and Antiferromagnetism on Zener's Model, Prog. Theor. Phys. 16 (1956) 45. doi:10.1143/PTP.16.45

[94] K. Yosida, Magnetic Properties of Cu-Mn Alloys, Phys. Rev. 106 (1957) 893. doi:10.1103/PhysRev.106.893

[95] H. A. Kramers, L'interaction Entre les Atomes Magnétogénes dans un Cristal Paramagnétique (Interaction Between Magnetogenic Atoms in a Paramagnetic Crystal), Physica (Utrecht) 1 (1934) 182. doi:10.1016 S0031-8914(34)90023-9

[96] P. W. Anderson, Antiferromagnetism. Theory of Superexchange Interaction. Phys. Rev. 79 (1950) 350. doi:10.1103/PhysRev.79.350

[97] J. B. Goodenough, Theory of the Role of Covalence in the Perovskite-Type Manganites [La, M(II)] MnO_3, Phys. Rev. 100 (1955) 564. doi:10.1103/PhysRev.100.564

[98] J. B. Goodenough, An Interpretation of the Magnetic Properties of the Perovskite-type Mixed Crystals $La_{1-x}Sr_xCoO_{3-\lambda}$, J. Phys. Chem. Solids 6 (1958) 287. doi:10.1016/0022-3697(58)90107-0

[99] J. Kanamori, Superexchange Interaction and Symmetry Properties of Electron Orbitals, J. Phys. Chem. Solids 10 (1959) 87. doi:10.1016/0022-3697(59)90061-7

[100] M. T. Johnson, P. J. H. Bloemen, F. J. A. den Broeder, and J. J. de Vries, Magnetic Anisotropy in Metallic Multilayers, Rep. Prog. Phys. 59 (1996) 1409. doi:10.1088/0034-4885/59/11/002

[101] L. Néel, Magnetic Surface Anisotropy and Superlattice Formation by Orientation, J. Phys. Radium 15 (1954) 225. doi: 10.1051/jphysrad:01954001504022500

[102] H. Zabel and S. D. Bader, Magnetic Heterostructures, Springer-Verlag Berlin Heidelberg, 2008.

[103] F. J. A. den Broeder, W. Hoving a and P.J.H. Bloemen, Magnetic Anisotropy of Multilayers, J. Magn. Magnet. Mater. 93 (1991) 562. doi:10.1016/0304-8853(91)90404-X

[104] S. Constantinides, Demand for Rare Earth Materials in Permanent Magnets, Presented at the 51st Annual Conference of Metallurgists, Niagara Falls, Ontario, October 2012 (COM 2012). https://www.magmatllc.com/publications.html (accessed December 2016)

[105] M. Humphries, Rare Earth Elements: The Global Supply Chain,CRS Report for Congress, Congressional Research Service, December 2013. https://archive.org/details/R41347RareEarthElementsTheGlobalSupplyChain-crs (accessed November 2016)

[106] S. Sabet, A. Moradabadi, S. Gorji, M. Yi, Q. Gong, M. H. Fawey, E. Hildebrandt, D. Wang, H. Zhang, B. -X. Xu, C. Kü bel, and L. Alff, The Impact of Interface Structure on Magnetic Exchange Coupling in MnBi/Fe$_x$Co$_{1-x}$ Bilayers, Phys. Rev. B 98 (2018) 174440. doi:10.1103/PhysRevB.98.174440

[107] P. Siebe, Die Legierungen: Mangan-Wismut, Mangan-Zink und Mangan-Silber, ZAAC 108 (1919) 161. doi:10.1002/zaac.19191080113

[108] A. F. Andresen, W. Hälg, P. Fischer and E. Stoll, The Magnetic and Crystallographic Properties of MnBi Studied by Neutron Diffraction, Acta Chemica Scandinavica 21 (1967) 1543. doi:10.3891/acta.chem.scand.21-1543

[109] A. U. Seybolt, H. Hansen, B. W. Roberts, P. Yurcisin, Contribution to the Bi-Mn System, J. Metals. 8 (1956) 606.

[110] H. Yoshida, T. Shima, T. Takahashi, H. Fujimori, Preparation of Highly Pure MnBi Intermetallic Compounds by Arc-Melting, Mater. Trans. 40 (1999) 455. doi:10.2320/matertrans1989.40.455

[111] X. Guo, A. Zaluska, Z. Altounian and J. O. Ström-Olsen, The Formation of Single-phase Equiatomic MnBi by Rapid Solidification, J. Mater. Res. 5 (1990) 2646. doi:10.1557/JMR.1990.2646

[112] X. Guo, Z. Altounian and J. O. Ström-Olsen, Formation of MnBi Ferromagnetic Phases through Crystallization of the Amorphous Phase, J. Appl. Phys. 69 (1991) 6067. doi:10.1063/1.347771

[113] N. V. R. Rao, A. M. Gabay and G. C. Hadjipanayis, Anisotropic Fully Dense MnBi Permanent Magnet with High Energy Product and High Coercivity at Elevated Temperatures, J. Phys. D: Appl. Phys. 46 (2013) 062001. doi:10.1088/0022-3727/46/6/062001

[114] N. V. R. Rao, A. M. Gabay, W. F. Li and G. C. Hadjipanayis, Nanostructured Bulk MnBi Magnets Fabricated by Hot Compaction of Cryomilled Powders, J. Phys. D: Appl. Phys. 46 (2013) 265001. doi:10.1088/0022-3727/46/26/265001

[115] K. Momma and F. Izumi, VESTA 3 for Three-dimensional Visualization of Crystal, Volumetric and Morphology Data, J. of Appl. Crystallogr. 44 (2011) 1272. doi:10.1107/S0021889811038970

[116] D. Chen, J. F. Ready, and E. Bernal G., MnBi Thin Films: Physical Properties and Memory Applications, J. Appl. Phys. 39 (1968) 3916. doi:10.1063/1.1656875

[117] R. R. Heikes, Magnetic Transformation in MnBi, Phys. Rev. 99 (1955) 446. doi:10.1103/PhysRev.99.446

[118] Q. M. Lu, M. Yue, H. G. Zhang, M. L. Wang, F. Yu, Q. Z. Huang, D. H. Ryan and Z. Altounian, Intrinsic magnetic properties of single-phase $Mn_{1+x}Ga$ (0<x<1) alloys, Sci. Rep. 5 (2015) 17086. doi:10.1038/srep17086

[119] E. Krén and G. Kádár, Neutron Diffraction Study of Mn_3Ga, Solid State Commun. 8 (1970) 1653. doi:10.1016/0038-1098(70)90484-9

[120] J. S. Wu and K. H. Kuo, Decagonal Quasicrystal and Related Crystalline Phases in Mn-Ga Alloys with 52 to 63 a/o Ga, Metall. Mater. Trans. A 28 (1997) 729. doi:10.1007/s11661-997-1000-y

[121] T. A. Bither and W. H. Cloud, Magnetic Tetragonal δ Phase in the Mn-Ga Binary, J. Appl. Phys. 36 (1965) 1501. doi:10.1063/1.1714349

[122] H. Niida, T. Hori,H. Onodera, Y. Yamaguchi and Y. Nakagawa, Magnetization and Coercivity of $Mn_{3-\delta}Ga$ Alloys with a $D0_{22}$-type Structure, J. Appl. Phys. 79 (1996) 5946. doi:10.1063/1.362115

[123] H. Kurt, K. Rode, M. Venkatesan, P. Stamenov and J. M. D. Coey, $Mn_{3-x}Ga$ (0≤x≤1): Multifunctional Thin Film Materials for Spintronics and Magnetic Recording, Phys. Status. Solidi B 248 (2011) 2338. doi:10.1002/pssb.201147122

[124] Y. Huh, P. Kharel, V. R. Shah, X. Z. Li, R. Skomski, and D. J. Sellmyer, Magnetism and Electron Transport of Mn_yGa (1<y<2) Nanostructures, J. Appl. Phys. 114 (2013) 013906. doi:10.1063/1.4812561

[125] F. Wu, S. Mizukami, D. Watanabe, H. Naganuma, M. Oogane, Y. Ando, and T. Miyazaki, Epitaxial $Mn_{2.5}Ga$ Thin Films with Giant Perpendicular Magnetic Anisotropy for Spintronic Devices, Appl. Phys. Lett. 94 (2009) 122503. doi:10.1063/1.3108085

[126] F. Wu, E. P. Sajith , S. Mizukami, D. Watanabe, T. Miyazaki, H. Naganuma, M. Oogane, and Y. Ando, Electrical Transport Properties of Perpendicular Magnetized Mn-Ga Epitaxial Films, Appl. Phys. Lett. 96 (2010) 042505. doi: 10.1063/1.3298363

[127] K. Seshan, Handbook OF Thin-Film Deposition Processes and Techniques: Principles, Methods, Equipment and Applications, NOYES PUBLICATIONS, WILLIAM ANDREW PUBLISHING, Norwich, New York, USA, 2002.

[128] J. Sarkar, Sputtering Materials for VLSI and Thin Film Devices, William Andrew, Elsevier Inc., USA, 2014.

[129] K. Wasa, M. Kitabatake, H. Adachi, Thin Film Materials Technology: Sputtering of Compound Materials, William Andrew, Inc., USA, 2004.

[130] K. S. Sree Harsha, Principles of Physical Vapor Deposition of Thin Films, Elsevier, Oxford, UK, 2006.

[131] M. Ohring, The Materials Science of Thin Films, Academic Press, London, 1991.

[132] M. A. Lieberman and A. J. Lichtenberg, Principles of Plasma Discharges and Materials Processing, John Wiley & Sons Inc, Hoboken, NJ, USA, 2005.

[133] D. Depla and S. Mahieu, Reactive Sputter Deposition, Springer-Verlag Berlin Heidelberg, 2008.

[134] P. Sigmund, Theory of Sputtering. I. Sputtering Yield of Amorphous and Polycrystalline Targets, Phys. Rev. B. 184 (1969) 383.

[135] B. A. Movchan and A. V. Demchishin, Investigations of the Structure and Properties of Thick Nickel, Titanium, Tungsten, Aluminum Oxide and Zirconium Dioxide Vacuum Condensates, Fiz. Metall. Metalloved., 28 (1969) 83.

[136] J. A. Thornton, Influence of Apparatus Geometry and Deposition Conditions on the Structure and Topography of Thick Sputtered Coatings, J. Vac. Sci. Technol. 11 (1974) 666. doi:10.1116/1.1312732

[137] A. Anders, A Structure Zone Diagram Including Plasma-based Deposition and Ion Etching, Thin Solid Films 518 (2010) 4087. doi:10.1016/j.tsf.2009.10.145

[138] R. Messier, A. P. Giri, and R. A. Roy, Revised Structure Zone Model for Thin Film Physical Structure, J. Vac. Sci. Technol. A 2 (1984) 500. doi:10.1116/1.572604

[139] P. Barna , M. Adamik, Fundamental Structure Forming Phenomena of Polycrystalline Films and the Structure Zone Models, Thin Solid Films, 317(1998) 27. doi:10.1016/S0040-6090(97)00503-8

[140] J. Pelleg, L. Z. Zevin, S. Lungo, Reactive-sputter-deposited TiN films on glass substrates, Thin Solid Film, 197 (1991) 117. doi:10.1016/0040-6090(91)90225-M

[141] J. E. Greene, J.-E. Sundgren, L. Hultman, I. Petrov, and D. B. Bergstrom, Development of Preferred Orientation in Polycrystalline TiN Layers Grown by Ultra-High-Vacuum Reactive Magnetron Sputtering, Appl. Phys. Lett. 67 (1995) 2928. doi:10.1063/1.114845

[142] I. Petrov, P. B. Barna, L. Hultman and J. E. Greene, Structural Evolution During Film Growth, J. Vac. Sci. and Technol. A 21 (2003) S117. doi:10.1116/1.1601610

[143] E. Alfonso, G. Cubillos, J. Olaya, Thin Film Growth Through Sputtering Technique and Its Applications, INTECH Open Access Publisher, 2012. doi:10.5772/35844

[144] W. Ensinger, Ion Bombardment Effects During Deposition of Nitride and Metal Films, Surf. Coat. Technol. 99 (1998) 1. doi:10.1016/S0257-8972(97)00410-6

[145] P. Losbichler, C. Mitterer, Non-reactively Sputtered TiN and TiB_2 films: Influence of Activation Energy on Film Growth, Surf. Coat. Technol. 97 (1997) 567. doi:10.1016/S0257-8972(97)00331-9

[146] J. Musil, S. Kadlec, Reactive Sputtering of TiN Films at Large Substrate to Target Distances, Vacuum, 40 (1990) 435. doi:10.1016/0042-207X(90)90241-P

[147] P. Ziemann, E. Kay, Correlation Between the Ion Bombardment During Film Growth of Films and Their Structure and Electrical Properties, J. Vac. Sci. Technol., A 1 (1983) 512. doi:10.1116/1.571920

[148] D. L. Smith, Thin-Film Deposition: Principles and Practice, USA McGraw-Hill Education, NY, USA, 1995.

[149] Z. Y. Zhang and M. G. Lagally, Atomistic Processes in the Early Stages of Thin-Film Growth, Science 276 (1997) 377. doi:10.1126/science.276.5311.377

[150] A. Rockett (Ed.), The Materials Science of Semiconductors, Springer US, Boston, MA, 2008.

[151] J. E. Greene (R. Bunshah,ed.), Nucleation, Film Growth, and Microstructural Evolution, Deposition Processes for Films and Coating, Handbook of Deposition Technologies for Films and Coatings, Noyes Publications, NJ, USA, 1994.

[152] I. V. Markov, Crystal Growth for Beginners: Fundamentals of Nucleation, Crystal Growth, and Epitaxy, World Scientific Publishing Co., Singapore, 2003.

[153] J. Als-Nielsen and D. McMorrow, Elements of Modern X-ray Physics, Wiley., NY, USA, 2001.

[154] N. W. Ashcroft and N. D. Mermin, Solid State Physics, Holt, Rinehart and Winston, 1976.

[155] W. H. Bragg and W. L. Bragg, X-Rays and Crystal Structure, G. Bell, London, 1915.

[156] W. L. Bragg, The Development of X-ray Analysis, G. Bell and Sons, Reprinted by Dover Publications, London, 1975.

[157] Y. Waseda, E. Matsubara, K. Shinoda, X-Ray Diffraction Crystallography, Introduction, Examples and Solved Problems, Springer-Verlag, Berlin Heidelberg, 2011.

[158] Mario Birkholz, Thin Film Analysis by X-ray Scattering ,WILEY-VCH Verlag, Weinheim, Germany, 2006.

[159] B. D. Cullity, Elements of X-ray Diffraction, ADDISON-WESLEY Publishing Company, USA, 1956.

[160] P. Debye and P. Scherrer, Interferenzen an Regellos Orientierten Teilchen im Röntgenlicht, Phys. Z. 17 (1916) 277.

[161] D. B. Williams and C. B. Carter, Transmission Electron Microscopy: A Textbook for Materials Science, Springer, NY, USA, 2008.

[162] B. D. Josephson, Possible New Effects in Superconductive Tunneling, Phys. Lett. 1 (1962) 251. doi:0031-9163(62)91369-0

[163] J. M. Rowell, Magnetic Field Dependence of the Josephson Tunnel Current, Phys. Rev. Lett. 11 (1963) 200. doi:10.1103/PhysRevLett.11.200

[164] R. C. Jaklevic, J. Lambe, A. H. Silver and J. E. Mercereau, Quantum Interference Effects in Josephson Tunneling, Phys. Rev. Lett. 12 (1964) 159. doi:10.1103/PhysRevLett.12.159

[165] J. Clarke and A. I. Braginski (Eds.), The SQUID Handbook Vol. I, Fundamentals and Technology of SQUIDs and SQUID Systems, WILEY-VCH Verlag GmbH & Co., Weinheim, Germany, 2004.

[166] W. Buckel and R. Kleiner, Superconductivity: Fundamentals and Applications, Wiley-VCH, Weinheim, Germany, 2004.

[167] Magnetic Property Measurement System User Manual, Quantum Design, San Diego, CA, 2004.

[168] J. Worst, J. C. Lodder and T. Wielinga, R.F.-Sputtered Co-Cr Layers for Perpendicular Magnetic Recording II: Magnetic Anisotropy, Thin Solid Films 101 (1983) 75. doi:10.1016/0040-6090(83)90494-7

[169] H. Miyajima, K. Sato and T. Mizoguchi, Simple Analysis of Torque Measurement of Magnetic Thin Films, J. Appl. Phys. 47 (1976) 4669. doi:10.1063/1.322398

[170] A. Lisfi, C. M. Williams, L. T. Nguyen, J. C. Lodder, A. Coleman, H. Corcoran, A. Johnson, P. Chang, A. Kumar and W. Morgan, Reorientation of Magnetic Anisotropy in Epitaxial Cobalt Ferrite Thin Films, Phys. Rev. B 76 (2007) 054405. doi:10.1103/PhysRevB.76.054405

[171] I. S. Jacobs and F. E. Luborsky, Magnetic Anisotropy and Rotational Hysteresis in Elongated Fine-Particle Magnets, J. Appl. Phys. 28 (1957) 467. doi:10.1063/1.1722773

[172] A. Lisfi and j. C. Lodder, Curling Mode in Barium Ferrite Films with Perpendicular Anisotropy, IEEE Trans. Magn. 35 (1999) 2754. doi:10.1109/20.800975

[173] S. Tumanski, Handbook of Magnetic Measurements, CRC Press Taylor and Francis Group, Boca Raton, FL, USA, 2011.

[174] F. B. Humphrey and A. R. Johnston, Sensitive Automatic Torque Balance for Thin Magnetic Films, Rev. Sci. Instrum. 34 (1963) 348. doi:10.1063/1.1718362

[175] Physical Property Measurement System User Manual (Torque Magnetometer Option User Manual), Quantum Design, San Diego, CA, 1999.

[176] P. Hohenberg and W. Kohn, Inhomogeneous electron gas, Phys. Rev. 136 (1964) 864. doi:10.1103/physrev.136.b864

[177] W. Kohn and L. J. Sham, Self-consistent equations including exchange and correlation effects, Phys. Rev. 140 (1965) 1133. doi:10.1103/PhysRev.140.A1133

[178] A. Moradabadi, Theoretical Study of Charge Transport in Li-based Batteries, Doctoral Dissertation, Freie Universität Berlin, Berlin, 2017.

[179] E. Schrödinger, Quantisierung als Eigenwertproblem, Annalen der Physik 384 (1926) 361. doi:10.1002/andp.19263840404

[180] M. Longair, Quantum Concepts in Physics: An Alternative Approach to the Understanding of Quantum Mechanics, Cambridge University Press, Padstow, UK, 2013.

[181] M. Born and R. Oppenheimer, Zur Quantentheorie der Molekeln, Annalen der Physik 389 (1927) 457. doi:10.1002/andp.19273892002

[182] V. Fock, Näherungsmethode zur Lösung des quantenmechanischen Mehrkörperproblems, Zeitschrift für Physik 61 (1930) 126. doi:10.1007/BF01340294

[183] D. Hartree and W. Hartree, Self-consistent Field, with Exchange, for Beryllium, Proceedings of the Royal Society of London. Series A, Mathematical and Physical Sciences 150 (1935) 9. doi:10.1098/rspa.1935.0085

[184] G. Kresse and J. Furthmüller, Efficient Iterative Schemes for *ab initio* Total-energy Calculations Using a Plane-wave Basis Set, Phys. Rev. B. 54 (1996) 11169. doi:10.1103/PhysRevB.54.11169

[185] J. P. Perdew, K. Burke, and M. Ernzerhof, Generalized Gradient Approximation Made Simple, Phys. Rev. Lett. 77 (1996) 3865. doi:10.1103/PhysRevLett.77.3865

[186] V. P. Antropov, V. N. Antonov, L. V. Bekenov, A. Kutepov, and G. Kotliar, Magnetic Anisotropic Effects and Electronic Correlations in MnBi Ferromagnet, Phys. Rev. B. 90 (2014) 054404. doi:10.1103/PhysRevB.90.054404

[187] N. Umetsu, Y. Toga, and A. Sakuma, First-Principles Study of Interface Magnetic Structure in $Nd_2Fe_{14}B$/(Fe,Co) Exchange Spring Magnets, Phys. Rev. B 93 (2016) 014408. doi:10.1103/PhysRevB.93.014408

[188] Y. Toga, H. Moriya, H. Tsuchiura, and A. Sakuma, First Principles Study on Interfacial Electronic Structures in Exchange-Spring Magnets, J. Phys. Conf. Ser. 266 (2011) 012046. doi:10.1088/1742-6596/266/1/012046/meta

[189] M. J. Donahue and D. G. Porter, Oommf Software Package, 2016.

[190] T H Rana, P Manchanda, B Balamurugan, A Kashyap, T R Gao, I Takeuchi, J Cun, S Biswas, R F Sabirianov, D J Sellmyer, and R Skomski, Micromagnetism of MnBi:FeCo Thin Films, J. Phys. D: Appl. Phys. 49 (2016) 075003. doi:10.1088/0022-3727/49/7/075003

[191] S. Mao, J. Lu, X. Zhao, X. Wang, D. Wei, J. Liu, Ji. Xia, and J. Zhao, MnGa-based Fully Perpendicular Magnetic Tunnel Junctions with Ultrathin Co_2MnSi Interlayers, Sci. Rep.7 (2017) 43064. doi:10.1038/srep43064

[192] S. Sabet, E. Hildebrandt, and L. Alff, Synthesis and Magnetic Properties of The Thin Film Exchange Spring System of MnBi/FeCo, J. Phys. Conf. Ser. 903 (2017) 012032. doi:10.1088/1742-6596/903/1/012032

[193] S. Sabet, A. Moradabadi, S. Gorji, M. H. Fawey, E. Hildebrandt, I. Radulof, D. Wang, H. Zhang, C. Kübel, and L. Alff, Correlation of Interface Structure with Magnetic Exchange in a Hard/Soft Magnetic Model Nanostructure, Phys. Rev. Appl. 11 (2019) 054078. doi:10.1103/PhysRevApplied.11.054078

[194] D. J. Dunlop, The Rock Magnetism of Fine Particles, Phys. Earth Planet. Inter. 26 (1981) 1. doi:10.1016/0031-9201(81)90093-5

[195] M. Farle, Ferromagnetic Resonance of Ultrathin Metallic Layers, Rep. Prog. Phys. 61 (1998) 755. doi:10.1088/0034-4885/61/7/001

[196] N. A. Zarkevich, L. L. Wang, and D. D. Johnson, Anomalous Magneto-structural Behavior of MnBi Explained: a Path towards an Improved Permanent Magnet, APL Mat. 2 (2014) 032103. doi:10.1063/1.4867223

[197] P. Toson, A. Asali, G. A. Zickler, and J. Fidler, Ab-Initio Study on the Hard Magnetic Properties of MnBi, Phys. Procedia. 75 (2015) 1410. doi:10.1016/j.phpro.2015.12.159

[198] V. P. Antropov, V. N. Antonov, L. V. Bekenov, A. Kutepov, and G. Kotliar, Magnetic Anisotropic Effects and Electronic Correlations in MnBi Ferromagnet, Phys. Rev. B. 90 (2014) 054404. doi:10.1103/PhysRevB.90.054404

[199] X. Guo, X. Chen, Z. Altounian, and J. O. Ström-Olsen, Temperature Dependence of Coercivity in MnBi, J. Appl. Phys. 73 (1993) 6275. doi:10.1063/1.352668

[200] M. D. Kuz'min, Shape of Temperature Dependence of Spontaneous Magnetization of Ferromagnets: Quantitative Analysis, Phys. Rev. Lett. 94 (2005) 107204. doi:10.1103/PhysRevLett.94.107204

[201] C. Kuhrt and L. Schultz, Formation and Magnetic Properties of Nanocrystalline Mechanically Alloyed Fe-Co and Fe-Ni, J. Appl. Phys. 73 (1993) 6588. doi:10.1063/1.352573

[202] C. Kittel, Introduction to Solid State Physics, Wiley, NY, USA, 1953.

[203] R. Skomski, Nanomagnetics, J. Phys. Condens. Matter. 15 (2003) R841. doi:10.1088/0953-8984/15/20/202/meta

[204] M. Yi, O. Gutfleisch, and B.-X. Xu, Micromagnetic Simulations on The Grain Shape Effect in Nd-Fe-B Magnets, J. Appl. Phys. 120 (2016) 033903. doi:10.1063/1.4958697

[205] M. Yi, H. Zhang, O. Gutfleisch, and B.-X. Xu, Multiscale Examination of Strain Effects in Nd-Fe-B Permanent Magnets, Phys. Rev. Appl. 8 (2017) 014011. doi:10.1103/PhysRevApplied.8.014011

[206] S. G. Fishman, D. Gupta, and D. S. Lieberman, Diffusivity and Isotope-Effect Measurements in Equiatomic Fe-Co, Phys. Rev. B 2 (1970) 1451. doi:10.1103/PhysRevB.2.1451

[207] J. S. Jiang, J. E. Pearson, Z. Y. Liu, B. Kabius, S. Trasobares, D. J. Miller, S. D. Bader, D. R. Lee, D. Haskel, G. Srajer, and J. P. Liu, Improving Exchange-spring Nanocomposite Permanent Magnets, Appl. phys. lett. 85 (2004) 5293. doi:10.1063/1.1828225

[208] Y. Liu, S. G. E. Te Velthuis, J. S. Jiang, Y. Choi, S. D. Bader, A. A. Parizzi, H. Ambaye, and V. Lauter, Magnetic Structure in Fe/Sm-Co Exchange Spring Bilayers with Intermixed Interfaces, Phys. Rev. B 83 (2011) 174418. doi:10.1103/PhysRevB.83.174418

[209] A. K. Patra, F. Fleischhauer, S. Oswald, L. Schultz and V. Neu, Coercivity Mechanism in Hard Magnetic $SmCo_5$/$PrCo_5$ Bilayers, J. Phys. D: Appl. Phys. 47 (2014) 215001. doi:10.1088/0022-3727/47/21/215001/meta

[210] J. Schoenes, K.-U. Harder, D. Menzel and T. Widmer, Epitaxial Growth of MnBi Films and Characterization, J. Magn. Soc. Jpn. 23 (1999) 95. doi:10.3379/jmsjmag.23.S1-95

Acknowledgement

First, I would like to thank my supervisor, Prof. Dr. Lambert Alff, for giving me the opportunity to perform research in his group. This three and a half years has been a truly great experience for me both professionally and personally.

I am also grateful to Dr. Erwin Hildebrandt for all his assistance and support during my work on this thesis.

I thank all the members of ATFT group for their continuous help and support with all the challenges on the way. I would not be able to overcome the technical or scientific issues without your extra help and our daily discussions.

I thank Dr. Imants Dirba from the group of Prof. Dr. Gutfleisch for all his help regarding magnetron sputtering unit and the time he took to give me instructions on how to use and maintain the system. Special thanks to our ATFT technician Herr. Jürgen Schreeck for all his support for repairing and maintenance of the sputtering unit during several times that the unit was down due to technical issues.

I thank all my fellow RESPONSE project members specially from group of Prof. Dr. Gutfleisch, Dr. Simon Sawatski, Dr. Tim Helbig, Dr. Iliya Radulov, Dr. Semih Ener, Dr. Leopold Diop and Dr. Konstantin Skokov for all our fruitful discussions during or extracurricular to our RESPONSE seminars and for all the valuable scientific collaborations. I additionally thank Dr. Iliya Radulov for Torque magnetometery measurements.

I am also thankful to Jun. Prof. Dr. Hongbin Zhang and Dr. Min Yi for discussions and support regarding theoretical calculations performed as part of this study. Special thanks to Jun. Prof. Dr. Hongbin Zhang for his comments on my thesis.

My special thanks of gratitude to Dr. Ashkan Moradabadi for the DFT calculations and micromagnetic simulations of the exchange interface and all the fruitful endless discussions.

I thank the group of Prof. Dr. Christian Kübel from Karlsruhe Institute of Technology, especially M. Sc. Saleh Gorji and Dr. Mohammed Fawey, for the HR-TEM measurements of my samples and for their scientific help and support regarding evaluation of the data.

I thank the group of Prof. Dr. Farle from Universität Duisburg-Essen and in particular Dr. Florian M. Römer for their collaboration and for all the effort regarding FMR measurements.

I thank my husband, my friends and my family for continuously encouraging me and believing in me, without your trust I would not be able to finish this work.

I thank Dr. Olga Bauder and Dr. Maximilian Hödl for their kind help regarding the german translation of my thesis abstract.

Finally I thank the LOEWE project RESPONSE funded by the Ministry of Higher Education, Research and Arts (HMWK) of the state of Hessen for funding my doctoral work.

Curriculum Vitae

Sareh EsmaeilySabetRoudsari (Sareh Sabet), born on 20th of September 1986 in Tehran, IRAN.

- **School education** :
  - 1992-1997: Primary school
  - 1997-2000: Secondary school
  - 2000-2003: High School, Nedaie Azadi high school, Tehran, IRAN
  - 2003-2004: Pre-university, Shahid Mehrab College, Tehran, IRAN

- **University education** :
  - 09/2004-12/2009: **B.Sc.** in Material Science and Engineering, IRAN University of Science and Technology (IUST), Tehran, IRAN
  - 10/2010-09/2013: **M.Sc.** Advanced Materials/Nanomaterials, Universität Ulm, Ulm, Germany
  - 01/2014 - 08/2019 (experiments finished until 06/2017): **Doctoral Studies**, Technische Universität Darmstadt, Institute of Materials Science, Advanced Thin Film Technology, Darmstadt, Germany
  - Supervisor: Prof. Dr. Lambert Alff
  - Thesis: "*Investigation of structural and magnetic properties in MnBi/FeCo and MnGa/FeCo exchange spring bilayers*"

- **Teaching and supervision assignments** :
  - Bachelor Grundpraktikum II: Solid state synthesis and energy-dispersive X-ray analysis of superconducting $YBa_2Cu_3O_{7-\delta}$ (Summer semester module: 11-01-1026, during years: 2015 and 2016)
  - Master Research Lab I: Thin film growth by Pulsed Laser Deposition (PLD) and *mathitin situ* RHEED monitoring (Winter semester module: 11-01-4101, during years: 2015 and 2016)
  - Bachelor thesis supervision: "*Growth of MnBi thin films by RF—magnetron sputtering*" (Student: Tayyab Ahmad, SoSe 2014)

- **Work experience** :
  - 01/2014 - 05/2017: Wissenschaftliche Mitarbeiterin, Institute of Materials Science, TU Darmstadt (LOEWE project RESPONSE funded by the Ministry of Higher Education, Research and Arts (HMWK) of the state of Hessen)
  - 06/2017 - present: Application Scientist, SUSS MicroTec Lithography GmbH